Metal Oxide Nanostructures and Their Applications

A thesis
Submitted to the Department of Materials Science, School of Natural Sciences, University of Patras, in partial fulfilment of the requirements for the degree of

Doctor of Philosophy

BY

Ghulam Nabi Dar

University of Patras

Department of Materials Science
University of Patras
Greece
February, 2015

Advisory Committee

Associate Professor Sotirios Baskoutas (Supervisor)
Department of Materials Science, University of Patras, Greece

Associate Professor Umar Ahmad (Co-supervisor)
Promising Center for Sensors and Electronic Devices, Najran University, Saudi Arabia

Associate Professor Nikolaos Bouropoulos
Department of Materials Science, University of Patras, Greece

Examination Committee

Professor Nikolaos Vainos

Department of Materials Science, University of Patras, Greece

Associate Professor Ahmad Umar

Promising Center for Sensors and Electronic Devices, Najran University, Saudi Arabia

Associate Professor Sotirios Baskoutas

Department of Materials Science, University of Patras, Greece

Associate Professor Nikolaos Bouropoulos

Department of Materials Science, University of Patras, Greece

Assistant Professor Ioannis Koutselas

Department of Materials Science, University of Patras, Greece

Lecturer Emmanuel Topoglidis

Department of Materials Science, University of Patras, Greece.

Lecturer Aristides Bakandritsos

Department of Materials Science, University of Patras, Greece

Examination date: 9.00 AM, 16th February 2015

ACKNOWLEDGEMENTS

الحمد لله

I would like to express my special appreciation and thanks to my advisor Dr. Sotirios Baskoutas, Department of Materials Sciences, University of Patras, Greece and Co- Advisor Dr. Ahmad Umar, Deputy Director, Promising Center for Sensors and Electronic Devices, Najran University, Saudi Arabia, for their support and encouragement during this program. I would like to thank both of my research guides for allowing me to grow as a research scientist. Both of your advices, support, co-operation on both research as well as on my career have been invaluable.

I would also like to thank Prof. N.A. Vainos, Chairman Department of Materials Sciences, University of Patras, Greece for his friendly and full supportive approaches. Special thanks to my committee member Professor N. Bouropoulos, Department of Materials Scienc, University of Patras, Greece.

Special thanks to Prof. Ali Al-Hajry, Prof. Mohammad Sultan Al-Assiri and Dr. Saleh Al-Sayari, colleagues and friends like Dr. Shabi Abbas Zaidi, Dr. Shamoon, Dr. Abdullah, Dr. Faisal, Dr. S.H. Kim, Dr. S.W. Hwang, Dr. Adil, Dr. Farid, Dr. Ayman, Mr. Houcine Bouzid, Mr. Mohamed Eisa A. Abaker, Mr. Saleh Al-Abbas, Mr. Mohamad Maliki and Mr. Musfir Ahmad. Mr. Abdul Baqi. I would like to express my special thanks to one of our beloved member, well known as Raju.

Great thanks to the Vice-Chancellor, Registrar, University of Kashmir, and HoD, department of Physics KU, India for granting me study leave to carry out this research work. Special thanks to Dr. Manzoor Malik, who was always there whenever needed for any support and encouragement. Dr. Waseem and Dr. Altaf Pandith from chemistry department KU who pushed me to pursue this research and I extend these many thanks to my friends Mr. Farooq Husain Bhat, Arafat Firdous and Mir Tariq, Tariq Ahmad, Yaqub and few of local friends like Dar Nazir, Gulzar, Nazir Bhat etc.

I extend special thanks to my family. Words cannot express how grateful I am to my mother, father, mother-in law, father-in-law (a deported soul, who loved and cared me like a father), brothers and sisters, sisters-in-law for all of the sacrifices that you’ve made on my behalf. Your prayer for me was what sustained me thus far. I would also like to thank my beloved wife who stands the main force for my academic advancements specially this PhD thesis.

Thanks specially to my two beloved kids Ahanan Nabi & Faizan Nabi.

Ghulam Nabi Dar

Abstract

Recently, researchers on nanoparticles and nanostructures has received a great deal of attention not only in the area of synthesis and characterization but also in their potential application in various high-technological applications. Nanomaterials are widely used not only for environmental and biological applications but also for electronic and sensing applications. Among various classes of nanomaterials, the metal oxide nanostructures possess particular important because of their significant physical and chemical properties which allowed them to be used for the fabrication of highly an efficient nanodevices. The metal oxide nanomaterials are widely used for catalysis, sensing, and electronic devices, and so on. Due to the high-efficient applications, researchers have developed several synthesis strategies to prepare metal oxide nanostructures with tailored geometry and utilize them for a variety of applications. However, it is still desirable to prepare metal oxide nanomaterials with environment-friendly precursors and processes with varied size and morphology for their effective utilization in specific applications.

This thesis focuses on the synthesis, characterizations and specific applications of two undoped and doped metal oxide nanostructures like ZnO and iron oxide (α-Fe_2O_3). The thesis highlights the development of novel synthesis techniques/procedures which are rapid, consume less energy and time, and are less cumbersome, more economical, especially because of the low temperature process. The other aspect of the thesis is to use the as-synthesized nanomaterials for several important applications such as sensors, photovoltaic, and photocatalysis.

The thesis is divided into several chapters. Chapter 1 starts with a brief introduction of the metal oxide nanostructures and their various synthetic methods. In addition to this, a short review on the targeted applications, i.e. sensing, photovoltaic and photocatalytic, of this thesis was also discussed in this chapter. Finally, the chapter describes the objective and importance of the thesis.

Chapter 2 deals with the details of the synthesis and characterization techniques used in this thesis. Two specific techniques, i.e. hydrothermal and thermal evaporation, have been used for the synthesis of various undoped and doped nanomaterials explored in this thesis. The synthesized nanomaterials were examined by variety of techniques in terms of the morphological, structural, optical, compositional and electrical properties. Moreover the prepared nanomaterials together were used for various applications such as sensing, photovoltaic and photocatalytic applications. In a word, this chapter provides all the detailed procedures for the synthesis, characterizations and applications of targeted nanomaterials in this thesis.

Chapter 3 describes the main results and discussion of the thesis. This chapter is divided into several sections and each section describes the synthesis, detailed characterizations and particular application of a single metal oxide nanomaterial. Section 1 describes the growth, characterization and ammonia chemical sensing applications of well-crystalline ZnO nanopencils grown via facile and simple hydrothermal process using commonly used laboratory chemicals. Importantly, the fabricated ammonia chemical sensor exhibited ultra-high sensitivity. Section 2 demonstrates the use of ZnO balls made of intermingled nanocrystalline nanosheets (NS) for photovoltaic device application. Successful growth, characterizations and phenyl hydrazine chemical sensing applications based on Ag-doped ZnO nanoflowers was demonstrated in section 3 of this chapter. Section 4 describes the Ce-doped ZnO nanorods for the detection of hazardous chemical; hydroquinone. Section 5 exemplifies the facile growth and detailed structural and optical characterizations of In-doped ZnO hollow spheres composed of NS networks and nanocones. Finally, section 6 illustrates the utilization of α-Fe_2O_3 hexagonal nanoparticles for environmental remediation and smart sensor applications. Moreover the synthesized α-Fe_2O_3 hexagonal nanoparticles were characterized in detail in terms of their morphological, structural, compositional and optical properties.

Chapter 4 briefly highlights the overall conclusion and an outlook for further investigations suggested by the work undertaken here for this thesis.

KEYWORDS: Metal Oxides, Nanostructures, Zinc Oxide, Silver doped Zinc Oxide, Cerium doped Zinc Oxide, Indium doped Zinc Oxide, Iron Oxide, Chemical Sensors, Photovoltaic Devices, Photocatalyst

Περίληψη

Τα τελευταία χρόνια τα νανοσωματίδια και οι νανοδομές έχουν προσελκύσει μεγάλο ερευνητικό ενδιαφέρον λόγω των σημαντικών δυνατοτήτων που προσφέρουν για εφαρμογές υψηλής τεχνολογίας. Τα νανοϋλικά χρησιμοποιούντα ευρέως τόσο για περιβαλλοντικές και βιολογικές εφαρμογές όσο και για εφαρμογές στην ηλεκτρονική και τους αισθητήρες. Μεταξύ των διάφορων κατηγοριών νανοϋλικών, οι νανοδομές μεταλλικών οξειδίων παρουσιάζουν ιδιαίτερο ενδιαφέρον λόγω των φυσικών και χημικών ιδιοτήτων τους, που τους επιτρέπουν να χρησιμοποιούνται για την κατασκευή νανοσυσκευών υψηλής απόδοσης, με χαρακτηριστικά πεδία εφαρμογών την κατάλυση, την ηλεκτρονική και τους αισθητήρες. Για τους σκοπούς αυτούς, έχει αναπτυχθεί πληθώρα μεθόδων για την σύνθεση και προετοιμασία νανοδομών μεταλλικών οξειδίων με επιθυμητές γεωμετρίες, ώστε να είναι κατάλληλα για διαφορετικές εφαρμογές. Παρόλα αυτά, εξακολουθεί να υπάρχει έντονο ενδιαφέρον για την παραγωγή τέτοιων υλικών σε διάφορα μεγέθη και μορφολογίες, με περιβαλλοντικά φιλικές μεθόδους, με απώτερο σκοπό την χρησιμοποίησή τους σε συγκεκριμένες εφαρμογές.

Η παρούσα διατριβή εστιάζει στην σύνθεση, τον χαρακτηρισμό και τις εφαρμογές των νανοδομών δύο συγκεκριμένων μεταλλικών οξειδίων (ZnO και α-Fe_2O_3) με ή χωρίς προσμείξεις. Η διατριβή δίνει έμφαση σε νέες τεχνικές σύνθεσης, οι οποίες είναι γρήγορες, καταναλώνουν λιγότερη ενέργεια και είναι πιο οικονομικές κυρίως λόγω χαμηλότερης θερμοκρασίας επεξεργασίας. Οι δομές των νανοϋλικών που προκύπτουν, χρησιμοποιούνται σε διάφορες σημαντικές εφαρμογές, όπως είναι οι αισθητήρες, τα φωτοβολταϊκά και η φωτοκατάλυση.

Η διατριβή χωρίζεται σε 4 κεφάλαια. Στο κεφάλαιο 1 δίνεται μία σύντομη εισαγωγή στις νανοδομές των μεταλλικών οξειδίων και τις διάφορες μεθόδους σύνθεσης. Παρουσιάζονται συνοπτικά τα είδη των εφαρμογών τα οποία θα αποτελέσουν αντικείμενο μελέτης και τέλος περιγράφονται οι αντικειμενικοί στόχοι και η σημασία της διατριβής.

Το κεφάλαιο 2 πραγματεύεται λεπτομερώς τις τεχνικές σύνθεσης και χαρακτηρισμού που υιοθετούνται στο μεγαλύτερο μέρος της μελέτης. Συγκεκριμένα, για την σύνθεση των νανοϋλικών (με ή χωρίς προσμίξεις) χρησιμοποιούνται οι τεχνικές της υδροθερμικής και της θερμικής εξάχνωσης. Τα παραγόμενα νανοϋλικά μελετήθηκαν ως προς την σύνθεσή τους, καθώς επίσης και τις μορφολογικές, δομικές, οπτικές και ηλεκτρικές ιδιότητες. Στην συνέχεια, χρησιμοποιούνται για τα διάφορα είδη εφαρμογών που αναφέρθηκαν παραπάνω. Με άλλα

λόγια, στο κεφάλαιο αυτό περιέχονται όλες οι λεπτομέρειες των διαδικασιών παραγωγής και των εφαρμογών.

Το κεφάλαιο 3 περιλαμβάνει την παρουσίαση και συζήτηση των αποτελεσμάτων. Αποτελείται από διάφορες παραγράφους η κάθε μία εκ των οποίων περιγράφει την σύνθεση, τον χαρακτηρισμό και τις εφαρμογές ενός εκ των υλικών. Στην Παράγραφο 1 περιγράφονται η ανάπτυξη, ο χαρακτηρισμός των κρυσταλλικών ZnO νανομολυβδιών μέσω μίας απλής και εύκολης υδροθερμικής διαδικασίας, χρησιμοποιώντας συνηθισμένα εργαστηριακά υλικά, καθώς επίσης και η εφαρμογή τους ως χημικοί αισθητήρες αμμωνίας. Αξίζει να σημειωθεί ότι οι αισθητήρες που κατασκευάστηκαν επέδειξαν υπέρ-υψηλή ευαισθησία. Η παράγραφος 2 επιδεικνύει την χρήση ZnO σφαιρών που είναι κατασκευασμένες απο αναμιγμένα νανοκρυσταλλικά νανοφύλλα για φωτοβολταϊκές εφαρμογές. Η επιτυχής ανάπτυξη και χαρακτηρισμός ZnO νανολουλουδιών εμπλουτισμένα με Άργυρο καθώς επίσης και η χρήση τους σε εφαρμογές αισθητήρων φαινυλο-υδραζίνης παρουσιάζονται στην παράγραφο 3. Στην παράγραφο 4 περιγράφεται η χρήση ZnO νανοράβδων εμπλουτισμένων με Δημήτριο για την ανίχνευση της επικίνδυνης χημικής ουσίας υδροκινόνης. Στην Παράγραφο 5 παρουσιάζεται η ανάπτυξη και ο λεπτομερής δομικός και οπτικός χαρακτηρισμός κοίλων σφαιρών ZnO εμπλουτισμένων με Ίνδιο που αποτελούνται απο δίκτυα νανοφύλλων και νανοκώνους. Τέλος στην παράγραφο 6 περιγράφεται η χρήση εξαγωνικών νανοσωματιδίων α-Fe_2O_3 για περιβαλλοντική αποκατάσταση και εφαρμογές ευφυών αισθητήρων. Οι δομές αυτές χαρακτηρίστηκαν λεπτομερώς ως προς τη σύνθεση τις μορφολογικές, τις δομικές και τις οπτικές ιδιότητες.

Στο κεφάλαιο 4 παρουσιάζονται τα συμπεράσματα της παρούσας διατριβής καθώς επίσης και προστάσεις για την περεταίρω διερεύνηση των υπό μελέτη συστημάτων.

Λέξεις Κλειδιά: Οξείδια μετάλλων, Νανοδομές, Οξείδιο του Ψευδαργύρου, Οξείδιο του Ψευδαργύρου εμπλουτσμένο με Άργυρο, Οξείδιο του Ψευδαργύρου εμπλουτσμένο με Δημήτριο, Οξείδιο του Ψευδαργύρου εμπλουτσμένο με Ίνδιο, Οξείδιο του Σιδήρου, Χημικοί Αισθητήρες, Φωτοβολταϊκά, Φωτοκατάλυση.

Abbreviations

CFCVD:	Cyclic chemical vapor deposition
DSSC:	Dye sensitized solar cell
EDS:	Energy dispersive spectroscopy
EELS:	Electron energy-loss spectrometry
FESEM:	Field emission scanning electron microscopy
FTIR:	Fourier transform infrared spectroscopy
HRTEM:	High-resolution transmission electron microscope
IV:	Current voltage
MOCVD:	Metal organic chemical vapor deposition
MOVPE:	Metal-Organic Vapor Phase Epitaxy
NS:	Nanosheets
PBS:	Phosphate buffer solution
PL:	Photoluminescence
PLD:	Pulsed laser deposition
RhB:	Rhodamine B
TEM:	Transmission electron microscope
UV-Vis:	Ultraviolet –visible
VLS:	Vapor-Liquid-Solid
VS:	Vapor-Solid
XRD:	X-ray diffraction.
ZnO:	Zinc oxide
0D:	Zero dimensional
1D:	One dimensional
2D:	Two dimensional

Contents

List of tables

List of figures

CHAPTER-1

Chapter 1 starts with a brief introduction of the metal oxide nanostructures and their various synthetic methods. In addition to this, a short review on the targeted applications, i.e. sensing, photovoltaic and photocatalytic, of this thesis was also discussed in this chapter. Finally, the chapter describes the objective and importance of the thesis.

Nanotechnology is an interdisciplinary field of the sciences of physics, chemistry and materials sciences, meant for the design and fabrication of nanomaterials and their application. This branch of science is meant to understand the fundamental physical and chemical properties and the phenomenon of nanomaterials and nanostructures, and because of the novel application of nanomaterials, the science of nanomaterials has evolved as a frontline research area [**1,2**]. Feynman pointed out the importance of nanotechnology at the annual meeting of the American Physical Society in 1959, in the classic science lecture entitled ‘‘There is plenty of room at bottom”. In the last three decades, many discoveries and inventions have been made in the field of nanosciecne in terms of fabricating new materials and utilizing them for applications. Various new experimental techniques, with unique and desired properties of nanomaterials fabrication have been discovered.

Considerable research efforts with different synthesis methods have given brith to different class of nanomaterials, typically classified into three categories based on their dimensionality: 0 dimensional, one dimensional, two and three dimensional. Quantum dots and the individual molecules fall in the 0-dimensional structures where the nanoparticles are isolated from each other [**3-5**]. One dimensional nanostructures where atleast one of the dimension goes in the range of nanoscale order are being highly utilized and have versatile application in the nanodevice fabrications. Thin nano films lie in the two dimensional structures and are studied extensively for the utilization of nanodevice application [**6-8**]. Three-dimensional nanomaterials include powders, fibrous, multilayer and polycrystalline materials in which the 0D, 1D and 2D structural elements are in close contact with each other and form interfaces. An important type of three-dimensional nanostructured materials is a compact or consolidated (bulk) polycrystal with nanosize grains, whose entire volume is filled with those nanograins.

Semiconductor nanomaterials is one of the richest class of nanomaterials. A semiconductor is a material with electrical conductivity due to electron flow intermediate in magnitude between that of an insulator and a conductor. Semiconductor has governed a significant role in progressing research in nanoscience and nenotechnology, which results in novel classes of semiconductor materials. Usually in conductors current is considered to flow due to electrons only but here in semconductor materials it is caused by both electron as well as hole movements. Semiconductor materials do not belong only to crystal solids but are of the nature of amorphous and liquids too. A pure semiconductor is called as intrinsic semiconductor. The electronic properties and the conductivity of semiconductor can be changed in a controlled manner by addinig very small quantities of other materials called dopants.

The field is expected to open new avenues for science and technology. Preparation and applications of the metal oxide nanostructures is one of the classes belonging to Semiconducting nanomaterials and nanotechnology. Metal oxide proved to be very promising for a variety of practical applications. The good thermal and chemical stability of these inorganic materials enable them to be widely used. Metal oxides play a very important role in many areas of chemistry, physics, and materials science [**9-12**].

1.1. Metal oxide nanomaterials

Metal oxides because of their electronic structure differences, exhibit metallic, semiconductor, or insulator character. Preparation of these materials through the novel synthesis procedures can be described as physical and chemical methods. In general, two approaches have been used for the synthesis of these metal oxide nanostructures, top-down and bottom-up fabrication techniques. These approaches involve liquid–solid or gas–solid transformations. [**1,2,13-18**]. Metal oxide nanostructures among the most versatile groups of semiconductor nanostructures stand out as one of the most common, most diverse and most probably richest class of materials due to their extensive structural, physical and chemical properties and functionalities. In recent times metal oxides have been at the heart of many dramatic advances in the materials science. These materials display most fascinating and widest range of properties.

Due to the unique and tunable properties of these metal oxides such as optical, optoelectronic, magnetic, electrical, mechanical, thermal, catalytic, photochemical etc. made themselves excellent candidates for various high level technological applications. For instance, fuel cells, secondary battery materials, ceramics, chemical sensors, gas sensors and biosensor, solar cells, alkaline and lithium ion batteries, pyroelectric, piezoelectric, ferroelectric, magnetic, actuator, super capacitors, optical devices, lasers, waveguides, infrared(IR) and solar absorbers, gate dielectric, dielectrics in dynamics random access memories, High TC superconductivity, decoupling capacitors, magneto- resistance and so on. Hence metal oxide nanostructure materials have been actively studied in a broader perspective by the researchers. Therefore it is essential to explore its understanding in great details interms of their synthesis, properties and applications.

Thus this thesis is planned to study in particular ZnO, doped ZnO and Iron oxide metal oxide nanostructures. Here in this thesis, we will investigate the synthesis of the above mentioned metal oxide nanostructures through two routes, hydrothermal as well thermal evaporation. Until now a number of metal oxides nanostructures have been synthesized such as zinc oxide (ZnO) [**19-21**], copper oxide (CuO) [**22-24**], nickel oxide (NiO) [**25-27**] gallium oxide (Ga_2O_3) [**28,29**] etc.Variety of metal oxide morphogoies such as nanorods, nanowires, nanocubes, nanocones ,nanobelts and nanotubes have been observed. These nanostructures have been prepared by different methods, such as thermal evaporation,[**30-32**] chemical vapor deposition, [**33**] chemical synthesis, [**20**,**34,35**] etc. The only two metal oxides we study here in this work are pure and doped ZnO and an iron oxide nanomaterials.

1.2. Synthesis techniques of metal oxide nanomaterials

Synthesis of nanomaterials with desired morphology and composition is the most challenging task in the field of nanoscience and nanotechnology. In last several decades, the synthesis of metal oxides nanostructures have stimulated the great interest because of their novel properties which provide intense research efforts to fabricate the efficient miniaturized devices for the application in various nanoelectonics and photonics. So a variety of fabrication techniques have been explored in the literature for the synthesis of these metal oxide nano-structures such as thermal evaporation [**36-55**] metal organic and chemical vapor deposition [**56-61**], hydrothermal synthesis [**62-68**] template-based synthesis [**69**]etc. The synthesis methods can be classified into spontenous as well as template – based synthesis category [**69]**. In the spontenous synthsis, the crystal structures and surface properties grow along a particular direction [**69**] , while as in the case of template based –synthesis , different tempates are used to facilitate the growth of nanostructures [**69**]. The spontaneous class of synthesis is further divided into three classes: dissolution-condensation growth, evaporation-condensation growth and vapor-liquid-solid(VLS) growth [**69**]. In the dissolution –condensation process, the precursors are used to be first dissolved into a solvent or a solution and diffused latter on the surface resulting the formation of nanostructures, while as the evaporation-condensation growth process differs a little in the sense that one or more precursors used to be first evaporated to vapor at high temperature and then the resultant are condensed to solid at lower temperature. In the VLS classification, the materials used to go through three different phases; wherein some catalysts are usually needed to control the growth direction and growth area of nanostructures [**69**]. The detailed discussion on the used synthesis techniques for metal oxide nanostructures is presented in chapter 2, where a special space is given to the hydrothermal and thermal evaporation techniques as we synthesized all the metal oxide nanostructure through these two routes only here.

Nanoparticle research, includes synthesis, characterization of the structural, chemical and physical properties, assembly into 1-, 2- and 3-dimensional architectures and application in various fields of technology. Various different synthesis techniques used for the fabrication of nanomaterials with a wide range of compositions and well-defined and uniform crystallite sizes. Two ways for the synthesis of nanomaterials are gas phase and the liquid phase. Although gas-phase processes are successfully employed for the low-cost production of large quantities of nanopowders [**70,71**]. A liquid-phase synthesis is flexible with regard to the controlled variation of structural, compositional, and morphological features of the final nanomaterials. The significance of nanoparticle synthesis is clear from the fact that many groundbreaking findings that can be regarded as milestones in the history of nanoscience are directly related to synthetic work, for example the discovery of carbon nanotubes [**72**], the synthesis of well-defined quantum dots [**73**] , or the shape control of CdSe nanocrystals (NC) [**74**]. The size- and shape-dependent physical and chemical properties of semiconductor nanoparticles [**75-77**] as well as the increased surface-to-volume ratio of nanoscale materials in general raised expectations for a better performance of nanomaterials compared to their bulk counterparts.

Two strategies are generally pursued to prepare nanostructures: the “top-down”approach, using physical methods such as photolithography and related techniques, and the “bottom-up” employing physical and chemical approaches. For the miniaturization of electronic devices and the fabrication of complex 3D architectures, the bottom-up approach, making use of both specific and non-covalent interactions (e.g. hydrogen bonding, electrostatic and Van der Waals interactions) between molecules or colloidal particles to assemble discrete nanoscale structures, represents a valuable way [**78,79].** The bottom-up approach for the assembly of nanoparticles seems to prove a solution to the technological challenges faced by the semiconductor industry [**80**].

In this chapter, an overview is given on the experimental techniques used for synthesis and the characterization of nanomaterials. Synthesis of nanomaterials with desired morphology and composition is the most challenging task in the fields of nanoscience and nanotechnology. In several decades, the synthesis and characterization of metal oxides nanostructures have stimulated great interest because of their novel properties which provide intense research efforts to fabricate efficient miniaturized devices for the application in various nanoelectonics and photonics. Therefore, a variety of fabrication techniques have been explored in the literature for the synthesis of these metal oxide nano-structures but typically, they can be divided into two categories: (1) vapor phase growth and (2) solution phase growth processes.

a) Vapor Phase growth Process

For the growth of a versatile group of nanostructures, the vapor phase deposition is the most versatile technique. In vapor-phase synthesis of nanoparticles, conditions are created where the vapor phase mixture is thermodynamically unstable relative to formation of the solid material to be prepared in nanoparticulate form. This includes the usual situation of a supersaturated vapor. It also includes a third process ‘chemical supersaturation’ in which it is thermodynamically favorable for the vapor phase molecules to react chemically to form a condensed phase. If the degree of supersaturation is sufficient, and the reaction/condensation kinetics permit, particles will nucleate homogeneously. Once nucleation occurs, remaining supersaturation can be relieved by condensation or reaction of the vapor-phase molecules on the resulting particles, and particle growth will occur rather than further nucleation. Therefore, to prepare small particles, one wants to create a high degree of supersaturation by inducing a high nucleation density, and then immediately quench the system, either by removing the source of supersaturation or slowing the kinetics, so that the particles do not grow. In most cases, this happens rapidly (milliseconds to seconds) in a relatively uncontrolled fashion, and lends itself to continuous or quasicontinuous operation.

In order to control the diameter, aspect ratio and crystallinity, diverse techniques have been explored including the thermal evaporation, pulse laser deposition (PLD), metal organic chemical vapor deposition (MOCVD), sputtering process, thermal chemical vapor deposition, cyclic chemical vapor deposition (CFCVD), etc. Generally two growth mechanism have been explored for the formation of these metal oxide nanostructures by the aforesaid techniques: (a) Vapor-Liquid-Solid (VLS) and (b)Vapor-Solid(VS) process.

Vapor-Liquid-Solid (VLS): The VLS technique is one of the most successful techniques used for the growth of crystalline one dimensional nanostructures. This method was proposed by Wagner and Ellis in 1964 [**81**]. They observed the growth of silicon whiskers [**82**]. Wu et al. when demonstrated the direct Ge nanowire growth by the VLS mechanism observed by the means of real time in situ transmission electron microscope(TEM; JEM-2100F) [**83**]. The VLS mechanism is a catalyst assisted process in which the metal nanoclusters or metal nanoparticles have been used as a nucleation sited for the growth of one dimensional nanostructures.

In this process, the gaseous reactants dissolve with the catalytic particles and form the alloy liquid droplets which play an important role in the growth of one dimensional nanostructures. Precipitation occurs when the liquid droplet becomes supersaturated with the source material and under appropriate gas flow with increasing the time, and hence precipitation increases which leads to the formation of metal oxide crystals. Normally the grown crystal is along one particular crystallographic orientation and hence corresponds to the minimum atomic stacking energy and results the one dimensional structure formation. VLS technique have been extensively used for a variety of nanostructure formations and is not limited to metal oxides only but to other elements and different semiconductors. The synthesized metal oxides followed the VLS process are ZnO, MgO, CdO, TiO_2, SnO_2, In_2O_3, WO_3 etc. [**36-43**].

Vapor-Solid Mechanism (VS): The VS mechanism is another Important mechanism for the formation of nanostructures. This mechanism occurs in many catalyst free growth processes. Although exact phenomenon of this mechanism is not known but it is generally accepted that the control of supersaturation is a prime consideration for the growth of nanostructures specially the one dimensional nanostructures. As the degree of supersaturation factor determines the prevailing growth morphology, hence a low supersaturation is required for whiskers growth; a medium supersaturation is required for bulk growth while the high supersaturation leads to the powder growth [**73**]. In a typical process under high temperature, the source materials are vaporized and then directly condensed onto the substrate placed at a low temperature region. After initial condensation, the condensed molecules form seed crystals which serve as nucleation sites for further growth of nanostructures. This VS process has been widely used for the growth of various nanostructures which not only restrict to metal oxides but also to other elements and semiconductors. Several metal oxides produced by VS method are including more particularly ZnO, Ga_2O_3, SnO_2, MgO, WO_3, CdO, TiO_2, etc [**39**,**45-55**].

b) Thermal Evaporation Process

Various materials nanostructures are grown up by thermal evaporation process. For this technique, there is a need of high temperature thermal furnace, used for vaporizing the source material and facilitates the deposition of the nanostructures at relatively low temperatures. Here in this process, the vapor species of source materials are generated first by physical or chemical methods, and subsequently are condensed under certain conditions such as temperature, pressure, on silicon substrate. Numerous nanomaterials have been grown by this method that range from elemental nanowires to a variety of semiconductor materials [**20**,**34-55**]. Generally, the thermal evaporation process contains a horizontal quartz tube furnace with rotary pump and gas supply system. The details of thermal evaporation process are presented in chapter 2.

c) Pulsed Laser deposition Process (PLD)

The interaction of laser radiation with solid materials are primarily determined by the nature of the materials and the properties of the laser radiation. The use of a pulsed laser to induce the stoichiometric transfer of a material from a solid source to a substrate, simulating earlier flash evaporation methods, is reported in the literature as early as 1965 [**84**].

A pulsed-laser beam leads to a rapid removal of material from a solid target and to the formation of an energetic plasma plume, which then condenses onto a substrate. In contrast to the simplicity of the technique, the mechanisms in PLD—including ablation, plasma formation, and plume propagation, as well as nucleation and growth are rather complex. In the process of laser ablation, the photons are converted first into electronic excitations and then into thermal, chemical, and mechanical energy [**85,86**], resulting in the rapid removal of material from a surface. This process has been studied extensively because of its importance in laser machining. Heating rates as high as 1011 Ks^{-1} and instantaneous gas pressures of 10–500 atm are observed at the target surface [**87**].

PLD has been used extensively in the growth of high-temperature cuprates and numerous other complex oxides, including materials that cannot be obtained via an equilibrium route. Early on, it has been shown that the processes in the growth of materials from a PLD plume are fundamentally different from those found in thermal evaporation [**88**]. The method has been successful for the film synthesis of Y-type magnetoplumbite (with a c-axis lattice parameter of 43.5 Å) [**89**] and garnets with 160 atoms per unit cell [**90**]. Some other recent examples include the preparation of magnetic oxide nanoparticles, titania nanoparticles and hydrogenated-silicon nanoparticles [91-93].

d) Sputtering Process

A final means of vaporizing a solid is via sputtering with a beam of inert gas ions.
Urban et al.in 2002 demonstrated formation of nanoparticles of a dozen different metals using magnetron sputtering of metal targets [94]. They formed collimated beams of the nanoparticles and deposited them as nanostructured films on silicon substrates. This process must be carried out at relatively low pressures (~1 mTorr), which makes further processing of the nanoparticles in aerosol form difficult. It is largely driven by momentum exchange between ions and atoms in the material, due to collision. Surface diffusion is usually used for explanation of nanoscale islands or rods growth during the sputtering process. Recently this method has been used for the synthesis of variety of nanostructures like ZnO, W, Si, B, CN, etc. [**95-97**]

e) Metal- organic chemical vapor deposition (MOCVD) process

This technique (MOCVD) is also called as Metal-Organic Vapor Phase Epitaxy (MOVPE) and is widely used for preparing epitaxial structures by depositing atoms on a wafer substrate. For various thin film growths, this method has been extensively used. The operational principle is very simple. For the specific crystal growth, the desired atoms, which are bind with a particular complex organic gas molecules are passed over a hot semiconductor wafer. Due to heat, the complex organic molecules breakup and deposit the desired atoms layer by layer onto the substrate surface. The undesired remnants are removed or deposited on the walls of the reactor. By varying the composition of the gas, the crystal properties at almost atomic scale can be changed. Using this technique, layers of the precisely controlled thickness can be obtained, which is important for the fabrication of materials with specific optical and electrical properties.

By MOCVD, it is possible to build a range of semiconductor photodetectors and lasers. Furthermore, recently scientists inclined to grow nanostructures with this technique too in addition to application of thin film growth. Varieties of semiconductor nanostructures have been synthesized by this technique as reported in the literature [**56-61**].

f) Cyclic feeding chemical vapor deposition (CFCVD) process

This technique was first developed by Umar et al in 2005 [**49,50**]. It differs from other chemical vapor deposition techniques in the way that it is based on cyclic feeding of reactant gases and precursor of the deposited materials. Therefore each precursor required for the growth, is introduced into the reaction chamber only after a certain interval of time. This dosing sequence of precursors inhibits the gas phase reactions on the deposited material. This technique (CFCVD) yields the growth of low impurities content and is relative faster than the other conventional deposition techniques.

g) Spark discharge generation

Another means of vaporizing metals is to charge electrodes made of the metal to be vaporized in the presence of an inert background gas until the breakdown voltage is reached. The arc (spark) formed across the electrodes then vaporizes a small amount of metal. This produces very small amounts of nanoparticles, but does so relatively reproducibly. Weber et al. in 2001 used this method to prepare well-characterized nickel nanoparticles for studies of their catalytic activity in the absence of any support material [98]. By preparing the nanoparticles as a dilute aerosol they were able to carry out reactions on the freshly prepared particles while they were still suspended. Metal-oxides or other compounds can be prepared by using oxygen or another reactive background gas. Rather than having the background gas present continuously, it can be pulsed between the electrodes at the same time that the arc is initiated, as in the pulsed arc molecular beam deposition system described by Rexer et al. in 2000 [**99**].

h) Solution Phase Growth Process

Solution phase growth process is the successful and generic method for synthesis of variety of nanostructures. Unlike to the vapor phase synthesis, this method provides much different environment for the growth of the nanostructures. Thus it considerably reduces the cost and complexity for the fabrication of nanostructures. Although large yield of desired nanomaterial's are produced based on solution method but and however it considerably produces large amount of impurities as well; Which in turn can hamper the applications of so obtained products. The so obtained products however can be cleaned and hence the impurities can be decreased by the filtration and by washing of the obtained products. In this way getting pure products makes this technique commercially applicable for the nanostructure formations.

To develop strategies that guides and confine the growths, a number of approaches have been used and is reported in the literature, such as Sol-Gel technique, Electrochemical Deposition, Surfactant Assisted Growth Process, Sonochemical Method, and Solvothermal Methods, Chemical precipitation method and so on.

i) Sol-gel deposition process

Sol-gel chemistry has recently evolved into a general and powerful approach for preparing inorganic materials [**100-102**]. This method typically entails hydrolysis of a solution of a precursor molecule to obtain first a suspension of colloidal particles (the sol) and then a gel composed of aggregated sol particles. The gel is then thermally treated to yield the desired material. This method is a versatile solution process for making ceramic and glass materials. A variety of nanostructures are also synthesized by this route such as ZnO, MnO_2, ZrO_2, TiO_2, CuO, V_2O_5 etc [**103-107**].

j) Electrochemical deposition process

This method has been widely used for the fabrication of metallic nanowires in the porous structures. This method is convenient for the fabrication of metal oxide nanostructures. This method, from dissolved precursors, especially in aqueous solution, is a low cast and a scalable technique, well suited for a large scale of semiconductor thin film production. Recently, the electrochemical method attracted much attention due to its short reaction times and low cost. Yang et al. in 2007 reported the synthesis of highly ordered ZnO ultrathin nanorod and hierarchical nanobelt arrays on zinc substrate with an electrochemical route in the mixed H_2O_2 and NaOH solution [**108**]. Different materials so produced with this method using the porous or non porous structures, substrates and metal foils etc. are reported in the literature [**109**].

k) Surfactant and capping agent assisted process

This method is an effective way for the synthesis of nanostructures. For obtaining a desired product, careful selection of precursor and surfactant species as well as controlling other parameters such as pH, concentration and temperature of the reactants are needed. In this regard, the surfactant assisted method is a trial and error based procedure, and it requires endeavor to choose proper capping agents and reaction environment. The capping reagents are used to confine the lateral growth of the desired product. It serves as a soft template which can change the free energies of the various surfaces and thus alter their growth rates. Earlier this method was used to control the morphology of the nanoparticles and now it is extensively used to for the synthesis of nanomaterials. Variety of nanomaterials such as ZnO, SnO_2, NiO, $PbCrO_4$, CeO_2 etc have been synthsised by this process and are reported in the literature [**110-114**].

l) Sonochemcial method

Sonochemical processing has been proven as a useful technique for generating novel materials with unusual properties. Sonochemistry arises from acoustic cavitation phenomenon which involves the formation, growth, and collapse of many bubbles in the aqueous solution [**115**]. Under extreme reaction conditions, for instance extremely high temperatures more than 5000 k, pressures larger than 500 atm, and very high cooling rates higher than 1010 k/s attained during cavity collapse. It leads to many unique properties of the irradiated solution, results the formation of nanostructures via chemical reaction. A variety of nanostructures are already prepared and reported in the literature [**116,117**].

m) Chemical precipitation method

Chemistry has been taking the leading role in developing new materials with novel properties for technological applications. It is comparatively easy to design materials of varied morphology and composition with a better control through chemical synthesis routes. Since properties of a nanomaterial are very sensitive to the resulting shape, size, and composition of the material, synthesizing nanomaterials through chemical route is gaining popularity. The potential of large scale synthesis of nanomaterials by chemical routes, in a cost-effective manner, is also one of the reasons behind its popularity.

Metal oxides are prepared using chemical precipitation route. Selection of proper reactants is the most important factor in any chemical synthesis process. For this purpose extensive knowledge on chemical reactivities of the reagents, and the reaction steps that reactants supposed to undergo is required. The morphology and the composition of a nanomaterial can be controlled in a better way if each reaction step is known and controlled. The chemical reaction can start just by mixing the reactants in a beaker or in a round-bottom flask. Concentration of reactants, time and order of addition of reactants to the solution, temperature, pH, viscosity, and surface tension of the solution are the parameters to control. When reaction products get supersaturated, spontaneous nucleation occurs. Subsequently, it goes through the growth mechanism. Nanomaterials, with different morphology, can be prepared during this step if proper care is taken. The major difficulty in the chemical precipitation method is to get rid of the contamination, particularly due to the by-product generated in chemical reaction. The optimization procedure is really a tedious job. So many experiments at different parameters need to be carried out in order to get the desired result. For any chemical method other working conditions like stirring speed, vibration, exposure to light, cleanliness of glassware etc. can significantly affect the quality of nanomaterial formed. Hence, synthesis of nanomaterials of desired morphology and composition through chemical methods is considered to be an art, to some extent [**118**].

n) Hydrothermal growth process

Hydrothermal synthesis can be defined as a method of synthesis of single crystals that depends on the solubility of minerals in hot water under high pressure. The crystal growth is performed in an apparatus consisting of a steel pressure vessel called autoclave, in which a nutrient is supplied along with water. A gradient of temperature is maintained at the opposite ends of the growth chamber so that the hotter end dissolves the nutrient and the cooler end causes seeds to take additional growth. Hydrothermal research was initiated in the middle of the 19th century by geologists and was aimed at laboratory simulations of natural hydrothermal phenomena. In the 20th century, hydrothermal synthesis was clearly identified as an important technology for materials synthesis, predominantly in the fields of hydrometallurgy and single crystal growth [**119**]. Details of this method will come in the chapter 2.

Advantages of the hydrothermal synthesis method include the ability to synthesize crystals of substances which are unstable near the melting point, and the ability to synthesize large crystals of high quality. The solubility of many oxides in hydrothermal solutions of salts is much higher than in pure water; such salts are called mineralizers. Disadvantages are the high cost of equipment and the inability to monitor crystals in the process of their growth [**120**].

1.3.Importance of Metal Oxide Nanostructures

Nanoparticles of metal oxides have attracted increasing technological and industrial interest due to the changes in their optical, magnetic, electrical and catalytic properties accompanied with improved physical properties of stability or chemical passivity. Many physical properties of nanoparticles differ drastically from that of a single crystal of the same chemical composition. At nanoscale size, due to the confinement effect of electronic states and large number of surface atoms, many physical properties are influenced compared to their bulk phases.

Metal oxide nanoparticles have technological applications in areas such as catalysts, passive electronic components and high performance ceramics. These materials play important role in the selective surface modification of different substrates in the form of coatings. In comparison to that of bulk metaloxide phase nanomaterial metal oxides contain large fraction of total atoms as surface atoms, which makes a distinct contribution to the free energy and results in the large changes in the thermodynamic properties (melting temperature depression, solid-solid phase transition elevation). Also the intrinsic properties of metal oxide are transferred by quantum size effect, that is changes in the optical and electrical properties with size arises because of the transformation in the density of electronic energy levels. Specific importance of used metal oxide nanostructures in this thesis will be presented in the results and discussion section of chapter 3.

1.4. Applications of metal Oxide Nanostructures

Among the functionalized nanomaterials synthesized, metal oxide nanostructures are particularly attractive candidates, from a scientific as well as technological point of view. The unique characteristic of metal oxides make them the most diverse class of materials, with most of the properties covering from solid state physics to materiasls science. The great variety of structures and properties of metal oxide nanostructures makes them an important target of materials science. The crystal structure of metal oxide nanostructures range from simple rock salt to highly complex modulated structures. The nature of the metal – oxygen bonding varies from ionic to covelent or metallic [**121,122**]. Related to the change in structure as well as the bonding of metal oxide nanomaterials, these materials exhibit fascinating magnetic and electronic properties. For example $BaTiO_3$ is an insulator while as RuO_2 or ReO_3 are metallic. The magnetic properties of metal oxides include ferro, ferri and antiferromagnetic.

The potential applications for metal oxide nanomaterials include paint pigments, cosmetics, pharmaceuticals, catalysis and supports, medical diagonotics, magnetic and optical devices, flat panel displays, batteries and fuel cells, electronic and magnetic devices, biomaterials, structured materials and protective coatings. Oxide nanomaterials are finding a wide range of applications in a vaierty of fields by virture of their unique property like high reactivity, due to their high specific surface area, controlled size and distribution. Much attention has been paid for the preparation of nanomaterial oxides due to their application in optical and electrical properties and are well proposed for wide range of applications. Due to the restricted scope of this research thesis, we will report our work in chapter 3.

1.5. Targeted metal oxide nanomaterials in this thesis

1.5.1. Zinc Oxide (ZnO):

A representative of II-VI semiconductor compounds, is a technologically important material. Having unique positions in the semiconducting oxide class due to its piezoelectric and transparent conducting properties, optical transmittance and high electrical conductivity. These properties make it ideal for applications in window layers, in thin film hetero junction solar cells and transparent conducting electrodes in flat panel displays. In metal oxides family, the wurtzite hexagonal-shaped ZnO possess special place due to its own properties and wide range of applications. The various exotic properties of ZnO include its direct and wide band gap (~3.37 eV), high exciton binding energy (60 meV) much larger than other semiconductor materials, biocompatibility, easy and cost effective synthesis, high electron features, optical transparency, non-toxicity and so on [**89-93**] exhibiting many potential applications in areas such as laser diodes, gas sensors, optoelctronic devices and devices for solar energy conversion. The ZnO structures have an enhanced gas sensing properties due to its high surface area.

Properties of ZnO:

Crystal structure of ZnO: There are three forms of ZnO crystals, hexagonal wurtzite, cubic zincblende, and the rarely observed cubic rocksalt. The wurtzite structure is most stable at ambient conditions and thus most common. The zincblende form can be stabilized by growing ZnO on substrates with cubic lattice structure. In both cases, the zinc and oxide centers are tetrahedral. The rocksalt (NaCl-type) structure is only observed at relatively high pressures about 10 GPa.

Hexagonal and zincblende polymorphs have no inversion symmetry (reflection of a crystal relatively any given point does not transform it into itself). This and other lattice symmetry properties result in piezoelectricity of the hexagonal and zincblende ZnO, and in pyroelectricity of hexagonal ZnO. A more stable state of ZnO is wurtzite structure having hexagonal unit cell with the lattice parameters a = 0.3296, and c = 0.52065 nm. The oxygen anions and Zn cations form a tetrahedral unit. The entire structure lacks central symmetry. The structure of ZnO can be simply described as a number of alternating planes composed of tetrahedrally coordinated O^{2-} and Zn^{2+} ions, stacked alternatively along the c-axis [**94-106**] as shown in the figure 1.1.

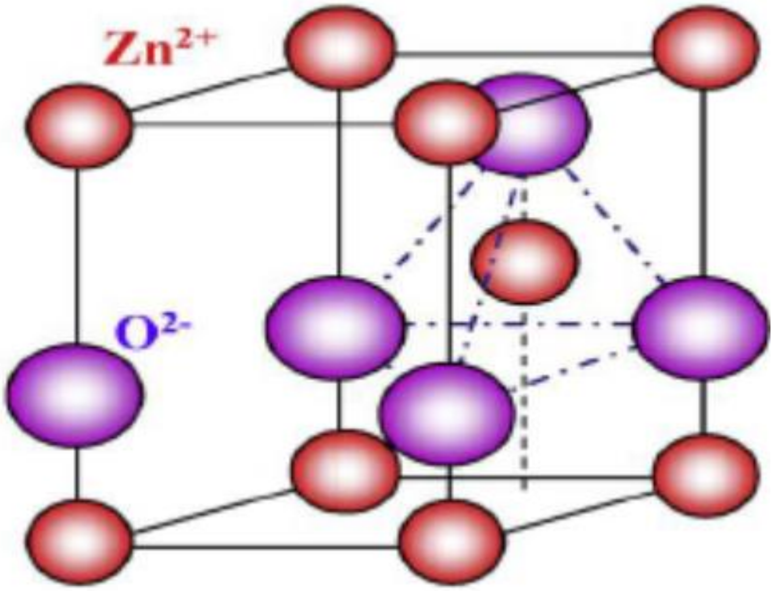

Figure1.1. Crystal structure of Zinc oxide (ZnO)

Mechanical properties**:** It is relatively a soft material having a hardness of 4.5 on the Mohs scale approximately. Its high heat capacity and heat conductivity with low thermal expansion and high melting temperatures makes it beneficial for ceramics. It has one of the highest piezoelectric tensor compared to other III-V semiconductors such as GaN and An. This property makes it important for many piezoelctircal applications, which require a large electromechanical coupling.

Eectronic properties:Having a relatively large direct band gap of ~3.7 eV and large excitation binding energy of 60 meV compared to themal energy which is of the order of ~ 26 meV at room temperature. Due to this very important property of large band gap, it has an advantage to sustain at large electric fiels, and can have lower electronic noise and will operate at high temperatures. Usually most of the ZnO materials are of n- type character, p-type doping of ZnO is relatively difficult. But these limitations of p-type doping does not restrict the applications of ZnO in electronic and optoelectronic cases which usually require junctions of n-type and p-type materials.

Optical properties:These materials have wide applications in the optical field, such as ZnO nanorods can be used in lasers for fast optical pumping and hence produce high power laser beams. In the near ultra violet and in visible regions, due to its wide band gap charater, ZnO material dispays uminescent properties.

The Photoluminescence (PL) spectra of ZnO structures have been widely reported. Excitonic emissions have been observed from the PL spectra of ZnO materials. It has been also observed that on the confinement of quantum size of ZnO nanomaterials, the exciton binding energy increases but it has also been observed at the same time that the intensity of green emission increases very much due the decrease in the diameter of the ZnO nanorod diameters. This is due to large ratio of surface to volume factor of nanowires favouring higher level of defects and surface combinations. Quantum confinement was also reported to be responsible for blue shift in the near UV emission peak in the ZnO nanobelts. Other application include and are not limited to optical fibres, solar cells , surface acoustic devices etc. [**105-107**]. The physical properties of the ZnO material are given as in the table 1.1 below [**108,109**].

Table 1.1. Properties of ZnO

Property	Value
Molecular formula	ZnO
Molar mass	81.4084 g/mol
Appearnece	Amorphous white or yellowish white powder
Odour	Odourless
Density	5.606 g/cm^3
Boiling point	2360 ^{0}C
Solubility in water	0.16 mg/100 mL
Melting point	1975 ^{0}C
Refractive index	-2.0041
Lattice Constants	a_0=0.32469 A c_0=0.52069
Relative Dielectric Constant	8.66
Energy Gap	3.4 eV Direct

Property	Value
Intrinsic Carrier Concentration	< 10^6/cc
Exiton Binding Energy	60 meV
Electron effective mass	0.24
Electron mobility(at 300K)	200 cm^2/Vsec.
Hole Effective mass	0.59
Hole mobility (at 300K)	5.50 cm^2/Vsec.

Applications of ZnO:

It has tremendous applications in many fields such as Rubber manufacture, medical uses, food additives anti corrosive coatings and in various ways in electronics. Most applications exploit the reactivity of the oxide as a precursor. ZnO has a high refractive index, good thermal , binding, antibacterial and UV protection properties, used in materials science applications. Also this material is added into various materials and products like ceramics, glass, rubber, lubricants, paints, ointments adhesive foods, batteries, ferrites , fire retardants etc.

1.5.2. Iron Oxide: Properties and applications

Iron oxides are chemical compounds composed of iron and oxygen. All together, there are sixteen known iron oxides and oxyhydroxides[**110-114**]. Iron oxide NPs are found naturally in the environment as particulate matter in air pollution and in volcanic eruptions. Either magnetite or maghemite – the two most commonly studied iron oxides − particles can be generated as emissions from traffic, industry and power stations but can also be specifically synthesised chemically for a wide variety of applications (so-called engineered nanoparticles).

Iron oxides play an important role in many geological and biological processes, and are widely utilized by humans, e.g., as iron ores, pigments, catalysts, in thermite , Hemoglobin. Common rust is a form of iron(III) oxide. Iron oxides are widely used as inexpensive, durable pigments in paints, coatings and colored concretes. Colors commonly available are in the "earthy" end of the yellow/orange/red/brown/black range.

Various phases in which irox oxide exists are as Iron(II) oxide as wustite (FeO), Iron(II,III) oxide, magnetite (Fe_3O_4) and Iron(III) oxide (Fe_2O_3) as alpha (α-Fe_2O_3), beta (β-

Fe_2O_3), gamma (γ-Fe_2O_3) and epsilon phase (ε-Fe_2O_3). It is clear from above that Iron oxides are technologically relevant metal oxides because they possess multivalent oxidation states that can be tuned specifically for an application, such as a catalytic template in sensor development or a substrate for drug delivery. Magnetite (Fe_3O_4), which is naturally found in the magnetosomes of MTB or other iron - reducing bacteria, is a well recognized example of controlled biomineralization [**115-117**]. Once crystallized intracellularly, magnetite nanoparticles align with the Earth's magnetic field to serve as a navigational compass for a number of aquatic animals [**118**]. Salmon, for example, utilize the magnetite located in their head for magnetic navigation that can last up to three years over tens of thousands of kilometers [**116-117]**. Although Iron oxide is found in nature in different forms, Magnetite (Fe_3O_4), Maghemite (γ-Fe_2O_3) and Hematite (α-Fe_2O_3) are the most common among them.

Hematite α-Fe_2O_3 is the oldest known Fe oxide mineral and is widespread in rocks and soils. It is extremely stable and is often the final stage of transformations of other iron oxides. The blood-red-coloured hematite is an important pigment and a valuable ore. Other names for hematite include iron(III)oxide, ferric oxide, red ochre and kidney ore.

Magnetite Fe_3O_4 is a black, ferromagnetic mineral containing both Fe(II) and Fe(III). Magnetite is an important iron ore. Together with titanomagnetite, it is responsible for the magnetic properties of rocks. It is formed in various organisms in which it serves as an orientation aid. Other names for magnetite include black iron oxide, magnetic iron ore, iron(II,III)oxide and ferrous ferrite.

Maghemite, γ-Fe_2O_3, is a red-brown, ferromagnetic mineral isostructural with magnetite, but with cation deficient site. It occurs in soils as a weathering product of magnetite or as the product of heating of other Fe oxides, usuallay in the presence of organic matter.

Iron oxide magnetic nanoparticles differ with their atoms and bulk counter parts in their physical and chemical properties [**118]**. As each nanoparticle is considered a single magnetic domain, large surface area and quantum size effects lead to some dramatic change in magnetic properties resulting in super paramagnetic phenomena and quantum tunnelling of magnetization. Based on their unique physical, chemical, thermal and mechanical properties, super para-magnetic nanoparticles offer a high potential for different applications [**119-124**]. These applications demand nanomaterials of specific sizes, shapes, surface characteristics, and magnetic properties, fields of high- density data storage, ferrofluids, magnetic resonance imaging, waste water treatment, bio separations and biomedicines.

1.6. Targeted applications of ZnO and iron oxide nanomaterials presented in this thesis

a) Sensor applications of targeted metal oxide nanostrutures

Sensor is a device that can measure the physical quantity of analyte of interest and convert it to readable signals. Part of this thesis focuses on chemical sensor applications of ZnO based and iron oxide nanomaterials. Most of the fabricated sensors belong to the environmental remediation applications. The environmental pollution caused by various ways such as agricultural sectors, industrial leakages of toxic chemicals, combustion from vehicles has created serious concerns in the scientific community [**125,126**] and now the scientists are developing various ways to fabricate efficient sensors which can effectively detect these alarming and highly toxic pollutants. The leakage of such toxic chemicals contaminates the environment and shows adverse effects to human beings, animals and other living organisms.

Therefore, there is a great demand to fabricate highly sensitive chemical sensors which are capable to detect the toxic chemicals and contaminants in an efficient way. This thesis reports on several highly sensitive chemical sensors fabricated based on the utilization of undoped and doped ZnO nanomaterials and iron oxide nanoparticles. For the fabrication of chemical sensors, the nanomaterials were used as supporting matrixes to modify the electrodes and these modified electrodes were used as the working electrode for the chemical sensor applications. In this thesis, we have fabricated several highly sensitive chemical sensors for the detection of ammonia, phenyl hydrazine, hydroquinone and 4-nitrophenol. The fabrication details and sensor performances of the fabricated sensors are demonstrated in detail in chapter 3.

b) Photovoltaic device (dye sensitized solar cell) applications of ZnO nanomaterials

A solar cell is a source of electricity which converts light into electricity. The commonly known solar cell fabricated based on oxide nanomaterials is dye-sensitized solar cells (DSSCs). A DSSC is also composed of a nano-crystaline oxide semiconductor, visible light sensitizer, redox electrolyte, transparent conducting oxide and a counter electrode. In 1991, Michael Gratzel and his coworkers from EPFL in Switzerland discovered the first DSSC with a photo conversion efficiency of 7% using metal oxide nanoparticles and visible light sensitizing materials [**127**]. This is the reason that DSSC is also known as Gratzel cell. Many scientists paid special attention towards this aspect and were successful to improve photo conversion efficiency and an understanding of the working principle of the cell. This made scientists able to develop DSSCs with an efficiency of photo to electricity conversion as high as 10-11% [**128-131**]. Although the conversion efficiency reached to 11% but demand goes for as high as 15% to compete the conventional solar cell. With this regard, new metal oxides with high photoconductivity, defect free surfaces and higher conduction band (CB) edge energy than TiO_2, as well as panchromatic and high molar extinction coefficient sensitizers need to be developed. This DSSC is now considered to be the most promising alternative candidate to expensive conventional solar cells.

Due to the almost identical properties of the II-VI semiconductor ZnO compared to TiO_2, such as electron affinity and band gap (3.37 eV at 298 K), higher electronic mobility (115–155 $cm^2\ V^{-1}\ s^{-1}$) than TiO_2($>10^{-5}$ $cm^2\ V^{-1}\ s^{-1}$), the ZnO nanomaterials are considered as an alternative material to be used as efficient photo-electrode material for the fabrication of dye-sensitized solar cells. Therefore, so far, several works have already been reported on the variety of ZnO nanostructured based DSSCs. In this thesis, we are reporting the successful synthesis and characterization of ZnO balls made of intermingled nanocrystalline NS and utilization of as-synthesized ZnO balls for DSSC applications. The fabricated DSSC exhibited an overall light-to-electricity conversion efficiency of 2.1%. The details of the fabricated DSSC based on ZnO balls is presented in chapter 3.

c) Photocatalyst applications of targeted metal oxide nanomaterials

The disposal of colored organic waste water from the textile industries causes serious problems to the aquatic ecosystem and because of this the aquatic environment is contaminated which created a serious threat to the living organisms. Therefore, it is highly desirable to develop a simple but effective way to degrade these colored organic wastes. Conventionally, a biological treatment or degradation process is utilized to decolorize the dyes, but it is ineffective for the complete removal and degradation of dyes. In last few years, the catalytic process derived by solar energy or other radiation energy has been studied for the successful degradation of harmful organic dyes into environmental friendly materials. Recently, nanomaterials are effectively used as active catalysts for the degradation/oxidation of organic dyes. The photocatalytic degradation occurs due to the effective separation of excited electron in conduction band (CB) and hole in valance band (VB) under the light illumination, which could capture by some surface species in the surroundings such as hydroxyl or O_2 groups. Various reports are already published in the literature which show that the nanomaterials are effective candidates for the photocatalytic degradation of organic dyes and toxic chemicals. In this thesis, we have synthesized α-Fe_2O_3 hexagonal nanoparticles and utilized them as efficient photocatalysts for the degradation of the hazardous Rhodamine B (RhB) dye. The details of photocatalytic degradation of α-Fe_2O_3 hexagonal nanoparticles towards RhB dye are presented in chapter 3.

1.7. Objective and Importance of the thesis

The objective of this thesis is to synthesize and characterize metal oxide nanomaterials for various sensing, photovoltaic and photocatalytic applications. The metal oxide nanomaterials were prepared by two techniques, i.e. hydrothermal process and thermal evaporation process and characterized in detail in terms of their morphological, structural, compositional and optical properties. The prepared metal nanomaterials were examined by FESEM and TEM in order to check the general morphologies while the structural characterizations were studied by using high-resolution TEM (HRTEM) and X-ray diffraction (XRD; PANanalytical Xpert Pro.) with Cu-Kα radiation (λ=1.54178 Å). The elemental and chemical compositions were evaluated by energy dispersive spectroscopy (EDS) attached with FESEM and Fourier transform infrared (FTIR) spectroscopy. Raman-scattering spectroscopy was used to determine the scattering properties of prepared metal oxide nanomaterials. UV-vis spectroscopy (Perkin Elmer-UV/VIS-Lambda 950) was used to examine the optical properties of the targeted nanomaterials. After detailed characterizations, finally, the nanomaterials were used for the fabrication of efficient chemical sensors, photovoltaic devices and photocatalytic applications.

The structure of the thesis is as follows: Chapter 2 comprise the general experimental methodologies used in our research works. Chapter 3 deals with the growth, properties and applications of undoped and doped ZnO nanostructures and iron oxide nanomaterials synthesized using different techniques. Finally, the general conclusions about all the presented work are reported in chapter 4.

CHAPTER-2

EXPERIMENTAL DETAILS

Chapter 2 deals with the details of the synthesis and characterization techniques used for the prepared metal oxide nanomaterials targeted in this thesis. Two specific techniques, i.e. hydrothermal and thermal evaporation, have been used for the synthesis of various undoped and doped nanomaterials explored in this thesis. The synthesized nanomaterials were examined by variety of techniques in terms of the morphological, structural, optical, compositional and electrical properties. Moreover the prepared nanomaterials were used for various applications such as sensing, photovoltaic and photocatalytic. In a word, this chapter provides all the detailed procedures for the synthesis, characterizations and applications of targeted nanomaterials in this thesis.

The targeted metal oxide nanomaterials in this thesis are pure ZnO, In, Ag- and Ce-doped ZnO and iron oxide. The targeted metal oxide nanomaterials were prepared by two specific techniques, i.e. simple and facile low-temperature hydrothermal process and thermal evaporation process. The synthesized ZnO nanostructures were extensively characterized in terms of their morphological, structural, optical, compositional and electrical properties. The general morphologies of the prepared nanomaterials were examined by field emission scanning electron microscopy (FESEM; JEOL-JSM-7600F) and transmission electron microscopy (TEM; JEOL-JEM-2100F). To examine the structural properties, the prepared nanomaterials were characterized by high-resolution TEM (HRTEM) and XRD pattern. The elemental and chemical compositions of prepared nanomaterials were investigated by energy dispersive x-ray spectroscopy (EDS) and FTIR spectroscopy, respectively. The optical properties were examined by UV-visible spectroscopy and PL spectroscopy at room-temperature. The scattering properties of synthesized nanomaterials were examined by Raman-scattering at room-temperature.

Finally, the synthesized nanomaterials were used for sensing, photovoltaic and photocatalytic applications.

2.1. Details of synthetic techniques

Two different synthesis techniques have been used to prepare the nanomaterials presented in this thesis. The synthesis techniques are:

a) Hydrothermal growth process
b) Thermal evaporation process

a) Hydrothermal growth process

Hydrothermal synthesis can be defined as a method of synthesis of single crystals that depends on the solubility of minerals in hot water under high pressure. The crystal growth is performed in an apparatus consisting of a steel pressure vessel called autoclave, in which a nutrient is supplied along with water. A gradient of temperature is maintained at the opposite ends of the growth chamber so that the hotter end dissolves the nutrient and the cooler end causes seeds to take additional growth. Hydrothermal research was initiated in the middle of the

19th century by geologists and was aimed at laboratory simulations of natural hydrothermal phenomena. In the 20th century, hydrothermal synthesis was clearly identified as an important technology for materials synthesis, predominantly in the fields of hydrometallurgy and single crystal growth [**119**].

The hydrothermal process is well known technique for the synthesis of nanostructures. Hydrothermal crystallization processes afford excellent control of morphologies (such as spherical, cubic, fibrous, and plate-like), sizes (from a couple of nanometers to tens of microns), and degree of agglomeration. These characteristics can be controlled in wide ranges using thermodynamic variables, such as reaction temperature, types and concentrations of the reactants, in addition to non-thermodynamic (kinetic) variables, such as stirring speed. Moreover, the chemical composition of the powders can be easily controlled from the perspective of stoichiometry and formation of solid solutions. Finally, hydrothermal technology affords the ability to achieve cost effective scale-up and commercial production. This process begins with the aqueous mixture of soluble metal salt (metal and /or metal organic) of the precursor material under temperature and pressure above its critical point to increase the solubility of a solid and to increase the reaction intensity between solids. Typically, the precursor's solution are mixed and placed in an autoclave under elevated temperature and pressure. Hydrothermal synthesis can be affected both under temperatures and pressures below the critical point for a specific solvent above which differences between liquid and vapor disappear, and under supercritical conditions. Using hydrothermal synthesis process, variety of metal oxide nanostructures such as ZnO, Ag doped ZnO, CuO, CeO_2, TiO_2, In_2O_3, Fe_3O_4, MnO_2, Ga_2O_3 etc. were synthesized and reported in the literature [**62-68**].

For the hydrothermal growth process, autoclaves are used which are made of thick-walled steel cylinders with a hermetic seal which must withstand high temperatures and pressures for prolonged periods of time. Furthermore, the autoclave material must be inert with respect to the solvent. In most cases steel-corroding solutions are used in hydrothermal experiments. To prevent corrosion of the internal cavity of the autoclave, protective inserts such as closed Teflon beakers are generally used. These may have the same shape of the autoclave and fit in the internal cavity (contact-type insert) and occupies only part of the autoclave interior. The sizes of the autoclaves can be controlled depending upon the amount of materials needed. Figures 2.1 and

2.2 exhibited the typical autoclaves reactors used for the synthesis of metal oxide nanomaterials studied in this thesis.

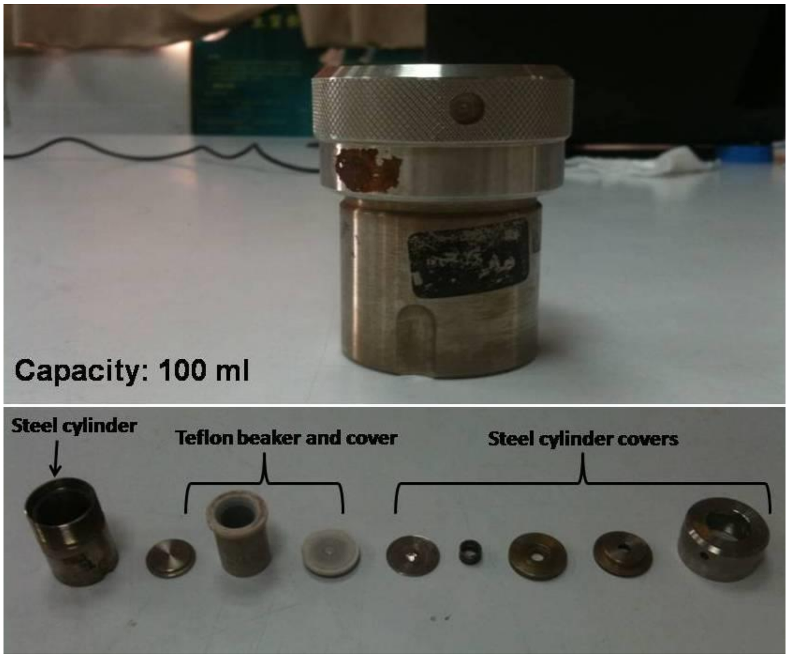

Figure 2.1. Typical picture of hydrothermal reactor (autoclave; capacity = 100 ml) for the synthesis of metal oxide nanostructures presented in this thesis.

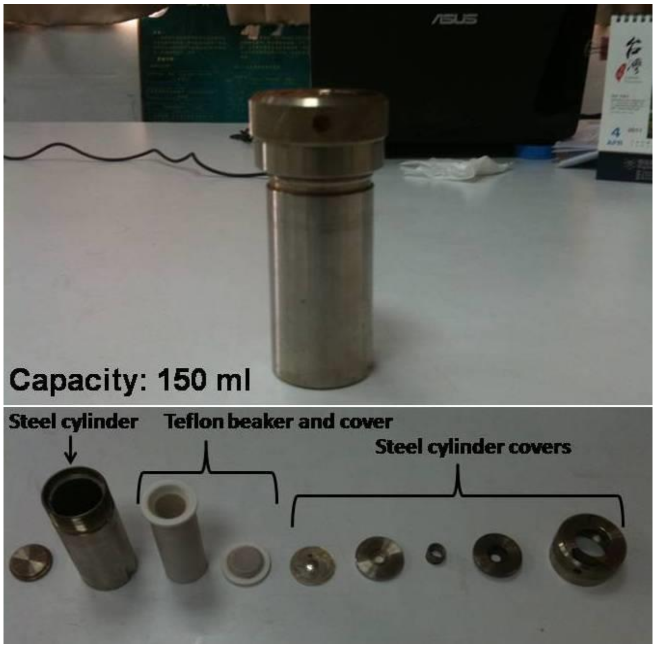

Figure 2.2. Typical picture of hydrothermal reactor (autoclave; capacity = 150 ml) for the synthesis of metal oxide nanostructures presented in this thesis.

For the hydrothermal growth of metal oxide nanomaterials studied in this thesis, in a typical reaction process, appropriate metal salt was dissolved in de-ionized (DI) water and stirred for 20 min. After stirring, normally ammonium hydroxide (NH_4OH) or sodium hydroxide (NaOH) was added in the solution to maintain the pH= 9-12 of the prepared solution. The final solution was vigorously stirred for 30 min and consequently transferred to teflon lined autoclave which was then sealed and heated upto an appropriate temperaure for certain time. After terminating the reaction, the autoclave was allowed to cool at room-temperature and the obtained products were washed several times with DI water and ethanol, sequentially and dried at appropriate temperature. The as-synthesized products were investigated in terms of their morphological, structural, and optical properties. Finally, the prepared nanomaterials were used for sensing, photovoltaic and photocatalytic properties.

b) Thermal evaporation process

The thermal evaporation or vapor phase synthesis process is the simplest and most versatile method for the synthesis of a variety of nanostructures. This technique needs a high temperature furnace which is used for vaporizing the source material and facilitates the deposition of the nanostructures at relatively low-temperatures. Here in this process, the vapor species of source materials are generated first by physical and subsequently are condensed under certain conditions such as temperature, pressure, substrate and atmosphere etc. Numerous nanomaterials have been grown by this method that range from elemental nanowires to a variety of semiconductor materials. The schematic instrumental setup for the thermal evaporation or vapor-phase deposition process for the growth of nanostructures is shown in the figure 3.3. As can be seen, the thermal evaporation process is made of horizontal long quartz tube, rotary pump and gas supply systems. Gas inlet is connected to one side while the rotary vacuum pump is attached to another side of the quartz tube. Both the ends of the quartz tube are sealed with rubber rings with vacuum grease. High purity metallic powders and oxygen gases are used as source materials for the growth of nanostructures. The nitrogen gas is used to create an inert atmosphere as well as for the carrier gas to transport the reactant vapors inside the quartz tube during reaction. The temperature and gas flow is controlled by temperature controller and mass-flow meters, respectively. Variety of metal oxide nanomaterials are made by using this technique and reported in the literature [**36-55**].

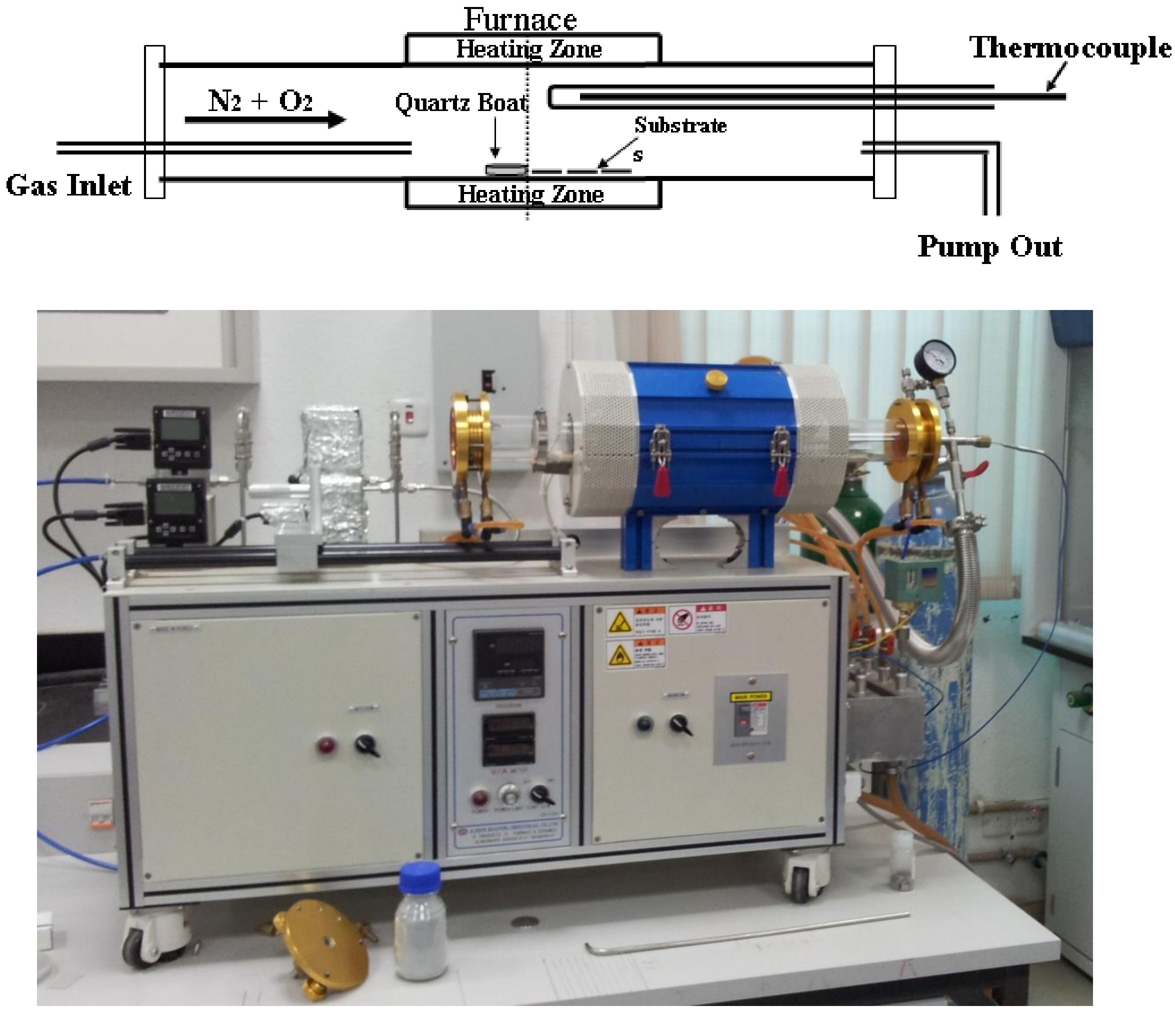

Figure 2.3. Schematic for the instrumental setup and real picture of the horizontal quartz tube furnace used for the growth of In-doped ZnO nanostructures, Ajeon Company,Korea based in Najran University Saudi Arabia

In this thesis, In-doped ZnO hollow spheres composed of NS networks and nanocones were prepared on silicon substrate by simple and facile non-catalytic thermal evaporation process. For this, commercially available metallic zinc and Indium (In) powders and high-purity oxygen gas were used as sources for zinc, Indium and oxygen, respectively. In a typical reaction process, zinc and In powders were thoroughly mixed and put into a ceramic boat which was placed at the centre of the quartz tube furnace. Several pieces of Si(100) were placed adjacent to the source boat and after this arrangement, the quartz tube chamber pressure was down to 1 torr using a rotary vacuum pump and the furnace was heated up to 850 ºC under the continuous flow of highly-pure nitrogen and oxygen gases. The reaction was terminated in 1.5 h. After completing the reaction for desired time, the furnace was allowed to cool at room temperature and the deposited materials on Si(100) substrate was characterized in detail in terms of their morphological, structural and optical properties.

2.2. Characterization of prepared metal oxide nanomaterials

The prepared metal oxide nanomaterials presented in this thesis were characterized in detail in terms of their morphological, structural, compositional and optical properties. The morphological properties of the synthesized metal oxide nanomaterials were characterized by FESEM and TEM; JEM-2100F) equipped with high-resolution TEM (HRTEM). The structural properties were examined by XRD in the range of 10-80°. The elemental and chemical compositions were examined by using EDS, attached with FESEM and FTIR spectroscopy, respectively. The optical properties were examined by using UV-visible spectroscopy and PL spectroscopy at room-temperature.

2.2.1. Field emission scanning electron microscopy (FESEM)

The FESEM is an incredible tool for seeing the unseen world of micro and nano dimension. Conventional light microscope use a series of glass lenses to bend light waves and create a magnified image. The FESEM creates the magnified images by using electrons instead of light waves. These electrons are liberated by a field emission source. The object is scanned by electrons according to zigzag patterns.

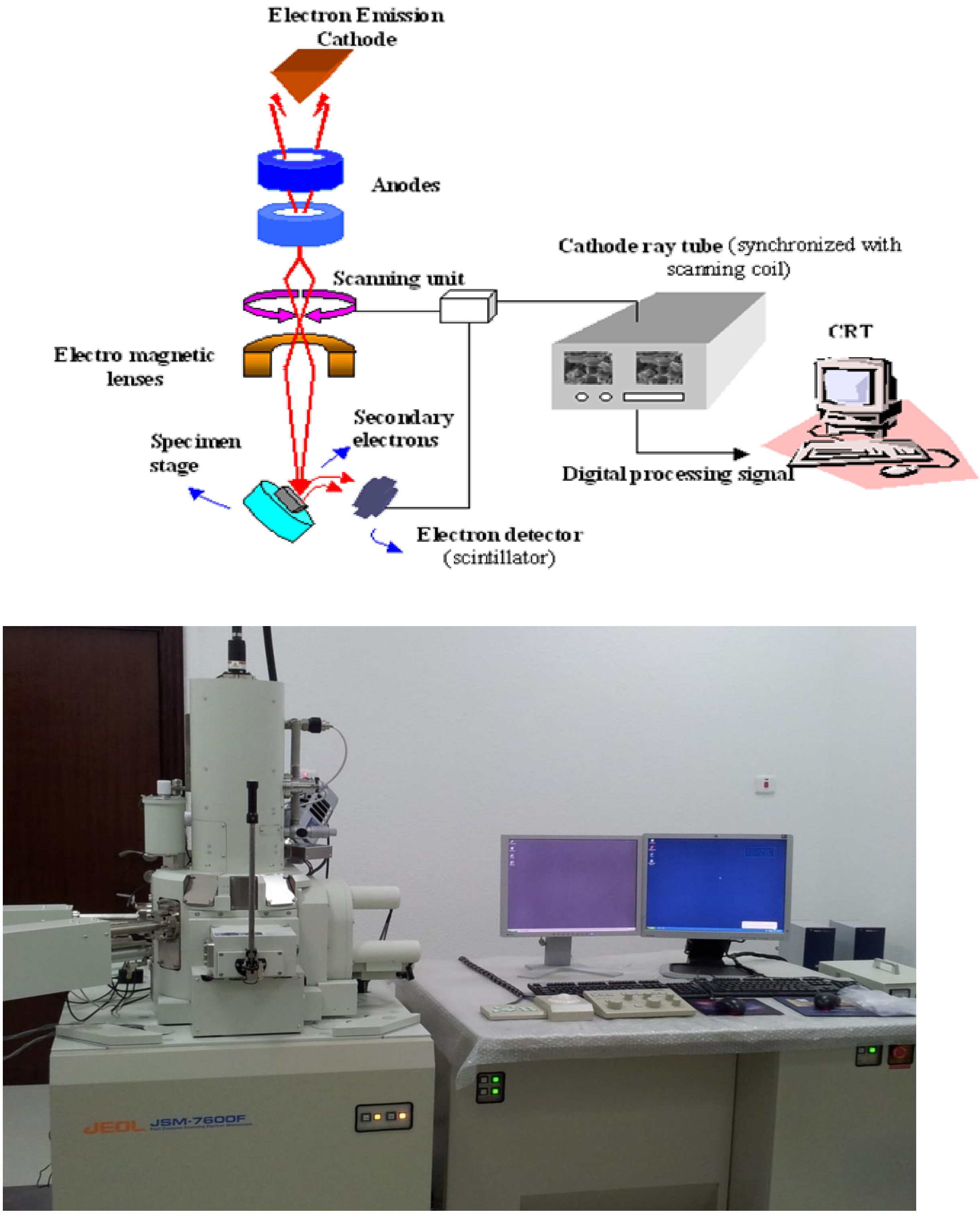

Figure 2.4. Schematic block diagram and real picture of field emission scanning electron microscope (FESEM; JEOL-JSM-7600F), based in Najran University Saudi Arabia

The internal arrangement of SEM of which the block diagram is shown as figure 2.4 has following components

a) Electron Source ("Gun")
b) Electron Lenses
c) Sample Stage
d) Detectors for all signals of interest
e) Display / Data output devices
f) Infrastructure Requirements which include as
i) Power Supply
ii) Vacuum System
iii) Cooling system
iv) Vibration-free floor
v) Room free of ambient magnetic and electric fields.

Electrons are liberated from a field emission source and accelerated in a high electrical field gradient. In the high vacuum columns these primary electrons so called are focused and deflected by electronic lenses to produce a narrow scan beam that bombards the object. As a result secondary electrons are emitted from each spot on the object. Since the energy of the secondary electrons is very small, those generated at deep region of the specimen are quickly absorbed by the specimen itself while as only those generated at the top of the surfaces are emitted out of the specimen. It means secondary electrons are very sensitive to the surfaces. Also the angle and velocity of these secondary electrons relates to the surface structure of the object. A detector catches the secondary electrons and produces an electronic signal. This signal is amplified and transformed to a video scan-image that can be seen on a monitor or to a digital image which can be saved and processed further. In fact FESEM can produce very high-resolution images of a sample surface, revealing details about less than 1 to 5 nm in size. Due to the very narrow electron beam, SEM micrographs have a large depth of field yielding a characteristic three-dimensional appearance useful for understanding the surface structure of a sample. Nowadays, three-dimensional features can be observed due to the large Depth of Field available in the FESEM. The addition of energy dispersive X-ray detector combined with digital image processing is a powerful tool in the study of materials, allowing good chemical analysis of the material. The FESEM is a major tool in materials science research and development.

In most of the applications, the data collected is over a pre-selected area of the sample surface and following this, a 2D image is generated that shows the various spatial variations. Conventional SEMs with a magnification range of 20X to 30000X with a spatial resolution of 50-100 nm can scan areas which vary from 1 cm to 5µm in width. SEMs also have the ability to analyze particular points as can be seen during EDX operations which help in determining the chemical composition of the sample concerned [**121**].

For observational purposes using the FESEM, objects are first made conductive with the help of coating with an extremely thin layer (1.5 - 3.0 nm) of gold or gold-palladium. Further objects must sustain and maintain (not to lose water or gasses molecules) a high vacuum. For structural analysis, a small piece of substrate which contains the deposited products are pasted on the sample holder using the carbon tape. Silver paste was used to stick the sample to the sample holder and a thin layer of gold or gold platinum or platinum was coated on the surface of the sample using an ion beam sputtering to avoid charging of the specimen. The object is inserted through an exchange chamber into the high vacuum part of the microscope and anchored on a moveable stage. The object can be moved in horizontal and vertical directions, and can also be tilted, rotated and translated.

2.2.2. Transmission electron microscopy (TEM)

The TEM has become the premier tool for the microstructural characterization of materials. In practice, the diffraction patterns measured by x-ray methods are more quantitative than electron diffraction patterns, but electrons have an important advantage over x-rays electrons can be focused easily. The optics of electron microscopes can be used to make images of the electron intensity emerging from the sample. For example, variations in the intensity of electron diffraction across a thin specimen, called “diffraction contrast,” is useful for making images of defects such as dislocations, interfaces, and second phase particles. Beyond diffraction contrast microscopy, which measures the intensity of diffracted waves, in “high-resolution” transmission electron microscopy (HRTEM or HREM) the phase of the diffracted electron wave is preserved and interferes constructively or destructively with the phase of the transmitted wave. This technique of “phase contrast imaging” is used to form images of columns of atoms. TEM is such a powerful tool for the characterization of materials that some microstructural features are defined largely in terms of their TEM images.

Besides diffraction and spatial imaging, the high-energy electrons in TEM cause electronic excitations of the atoms in the specimen. Two important spectroscopic techniques make use of these excitations.

(a) In energy-dispersive x-ray spectrometry (EDS), an x-ray spectrum is acquired from small regions of the specimen illuminated with a focused electron beam, usually using a solid-state detector. Characteristic x-rays from each element are used to determine the concentrations of the different elements in the specimen.

(b) In electron energy-loss spectrometry (EELS), energy losses of the electrons are measured after the high-energy electrons have traversed the specimen. Energy loss mechanisms such as plasmon excitations and core electron excitations provide distinct and useful features in EELS spectra.

TEM is the most powerful tool to study nanomaterials. It gives a direct evidence of formation of nanostructures, and is routinely used for determining shape, size, and crystal structure of nanomaterials. TEM is carried out for all our synthesized metal oxide nanomaterials. A TEM is analogous to a conventional optical microscope. Instead of visible light, an electron beam is used as illuminating source in TEM. Electromagnetic and electrostatic lenses are used to control the electron beam to focus it at a specific plane relative to the sample in a manner optical lenses are used to focus light on or through a specimen to form an image in an optical microscope. The ultimate small dimension seen by the optical microscope is limited due to the wavelength restriction of the “light source” while as TEM using electrons as “source” and their much lower wavelength makes it possible to get a resolution of thousand times better than of a light microscope. One can see the objects to the order of few angstroms [**123,124**].

A schematic of TEM is shown in Fig. 2.5. Due to much smaller wavelength of electron beam (as compared to the normal visible light) a much higher magnification and resolution is obtained in TEM. A stream of electrons, from an electron gun, is focused to a small, thin, and coherent beam by the use of condenser lenses.

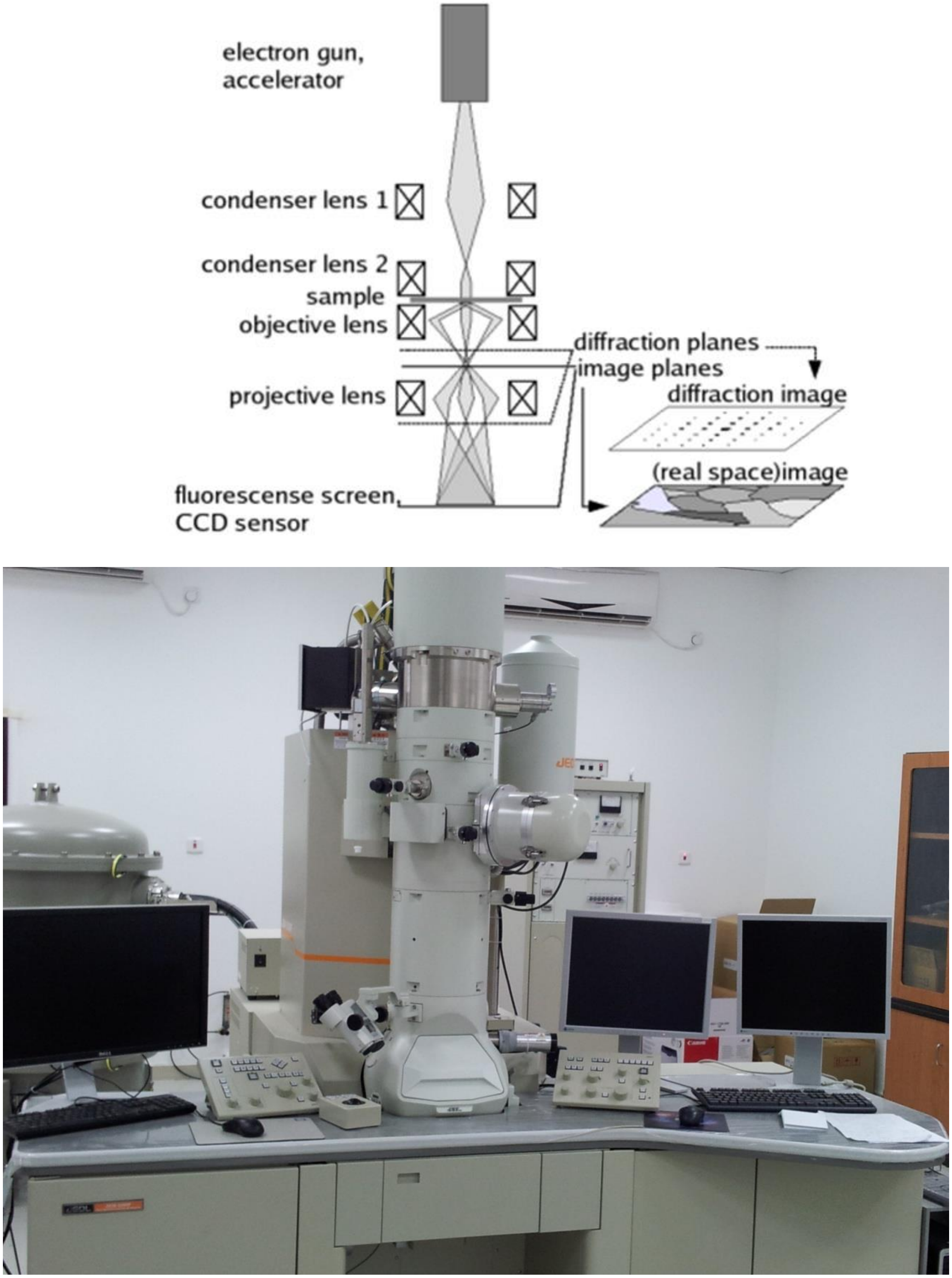

Figure 2.5. Schematic block diagram and real picture of high-resolution transmission electron microscope (TEM; JEM-2100F), based in Najran University Saudi Arabia

It then passes through the sample when some of the electrons are scattered and disappears from the beam. The original beam is focused by the objective lens. The intermediate lens is adjusted in such a way that the image plane of the objective lens becomes its object plane. So it forms a magnified shadow image of the specimen on the phosphor screen. The different parts of the specimen are displayed in varied darkness depending on their density or thickness, from which a lot of information about the material can be obtained.

If intermediate lenses are adjusted in such a way that the back focal plane of the objective lens acts as its object plane, then a diffraction pattern is projected onto the viewing screen. Since the basic principle of electron diffraction (ED) is almost similar to that of XRD.

2.2.3. X-ray diffraction (XRD)

A crystal lattice is a regular three-dimensional distribution of atoms in space. These are arranged so that they form a series of parallel planes separated from one another by a distance (d), which varies according to the nature of the material. For any crystal, planes exist in a number of different orientations, each with its own specific d-spacing.

XRD technique have played crucial role in the identification and evaluation of crystalline perfection of crystals. It is one of the oldest and non-destructive methods of analysis of samples and is still valid for all branches of solid state analysis. The XRD pattern obtained from the crystal sample depends on the shape and size of basic unit cell of the crystal [**132-136**]. Therefore, properties of a material are very much dependent on its structure. For example, HgS in the trigonal structure is a wide band gap semiconductor (E_g = 2.0 eV) but in zincblende modification it becomes a narrow band gap semi-metal (E_g = 0.5 eV). Therefore, it is essential to determine the structure of a material after its synthesis. XRD and ED experiments are the major techniques to determine the crystal structure of a material.

When a material gets irradiated with a monochromatic light of wavelength around the inter-atomic distance of the material, light gets scattered by atoms of the material and interfere to give rise to a diffracted light with higher intensity. The intensity distribution of scattered light in space is related to the arrangement of atoms in the material. If the wavelength of light is $\boldsymbol{\lambda}$ and the angle of incidence is $\boldsymbol{\theta}$ then constructive interference will be observed at an angle $2\boldsymbol{\theta}$ from the incidence beam if Bragg's equation gets satisfied [**137-140**], Bragg's equation can be written as equation (2.1)

$$2d_{hkl}\sin\theta_B = n\lambda \qquad (2.1)$$

Where d is the d-spacing of hkl planes. $\theta_B$is the Bragg angle and n is the diffraction order. It should be noted that d-spacing of planes is related to its Miller indices [**141**]. For example as shown in equation (2.2), in a hexagonal system,

$$d_{hkl} = \frac{1}{\sqrt{\frac{4}{3}\left(\frac{h^2+hk+k^2}{a^2}\right)+\frac{l^2}{c^2}}} \qquad (2.2)$$

Since wavelength of incident light is known and θ_B is measured from the experiment, d-spacing can be calculated and diffraction peak can be indexed with the Miller indices of planes. Joint committee on powder diffraction standards (JCPDS) has collected diffraction data on thousands of crystalline substances. Since lattice parameters are unique for a particular substance, comparison of the peak positions (search/match) with the data base helps in identifying the material and its crystalline phase.

Usually, in XRD, Cu-Kα line is used as the incident light for which λ= 0.154 nm. For a sample having large number of randomly oriented nanocrystals, certain planes of some particles would satisfy Bragg's equation and the diffracted beam will travel over the surface of a cone that makes $2\theta_B$angle with the axis (direction of the beam). Unlike placing a recording film/phosphor screen normal to the beam direction as in the case of ED, in XRD experiments, the angle between incident X-ray beam and the detector ($2\theta_B$) is directly measured by moving the detector. A rise in the intensity is observed when detector moves across the diffracted beam. The d-spacing is calculated according to eqn.(2.1) and indexed by comparing with the standard d-spacing of the material from the JCPDS data base.

It is worthwhile to mention here that the mean crystallite size of nanomaterials can also be obtained from the XRD spectrum, along with identification of the material, and its crystalline phase. For an infinite size crystal a complete destructive interference will take place at all direction except at $2\theta_B$. But for a finite crystallite, destructive interference is incomplete at slightly away from $2\theta_B$ and this leads to a peak broadening. Figure 2.6 exhibits the typical block diagram and real picture of XRD.

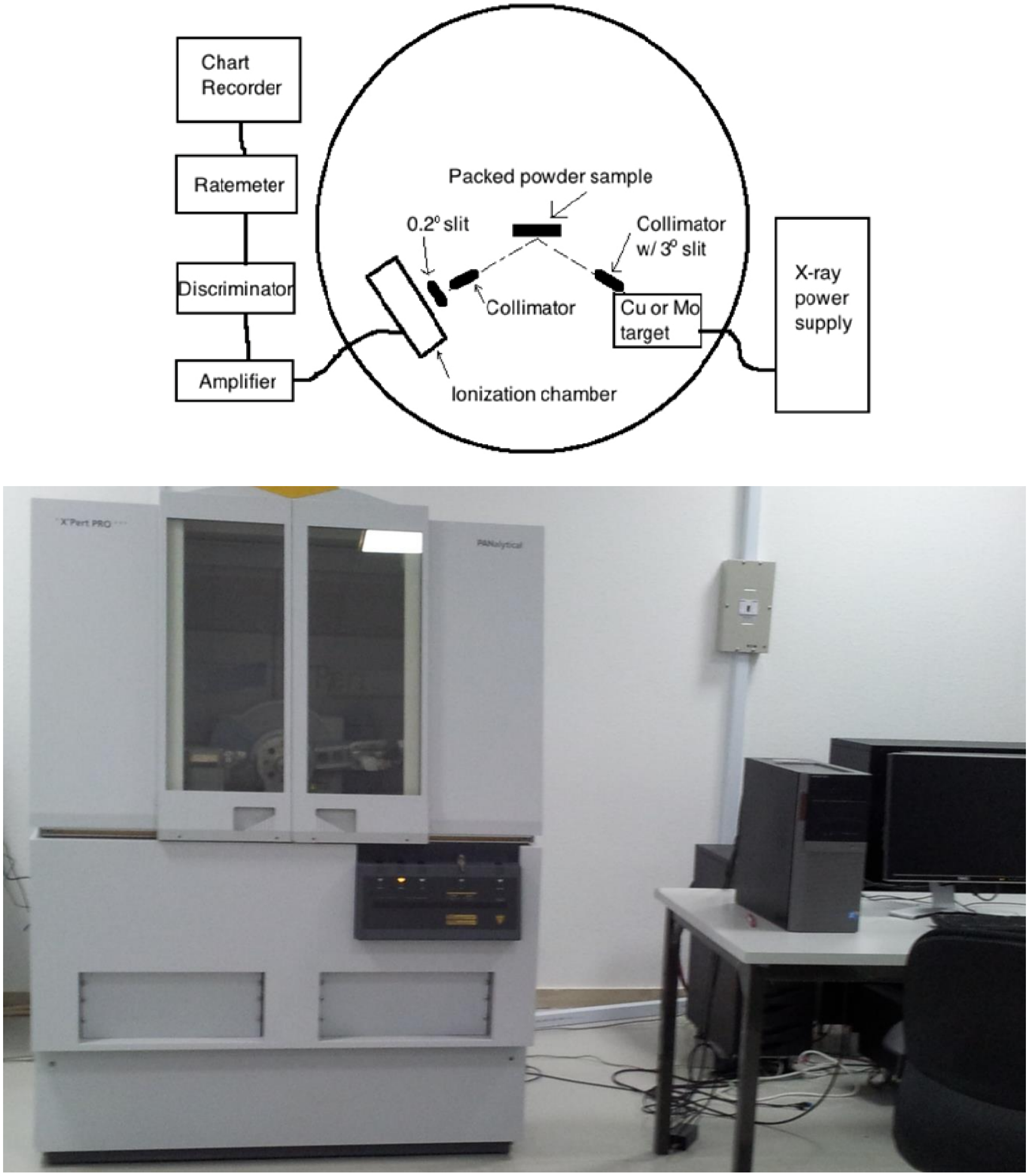

Figure 2.6. Typical block diagram and real picture of X-ray diffractometer (XRD; PANanalytical Xpert Pro.) with Cu-Kα radiation (λ=1.54178 Å), based in Najran University Saudi Arabia

2.2.4. Energy dispersive X-ray spectroscopy (EDS)

Energy-dispersive X-ray spectroscopy (EDS or EDX) is an analytical technique used for the elemental analysis or chemical characterization of a sample. It is one of the variants of X-ray fluorescence spectroscopy which relies on the investigation of a sample through interactions between electromagnetic radiation and matter, analyzing X-rays emitted by the matter in response to being hit with charged particles. Its characterization capabilities are due in large part to the fundamental principle that each element has a unique atomic structure allowing X-rays that are characteristic of an element's atomic structure to be identified uniquely from one another [**122**].

In EDS, an x-ray spectrum is acquired from small regions of the specimen illuminated with a focused electron beam, usually using a solid-state detector. Characteristic x-rays from each element are used to determine the concentrations of the different elements in the specimen. In the present investigation, elemental analysis was carried out using energy dispersive X-ray spectrometer.

2.2.5. Fourier Transform Infrared (FTIR) Spectroscopy

The physics of the individual atoms and simple molecules can be understood by studying their interaction with electromagnetic radiations. This study is called as spectroscopy. In spectroscopy, electromagnetic radiation of a particular frequency or a range of frequencies is allowed to fall on a sample understudy. The radiation coming out of the sample is then analyzed in terms of the intensity at different frequencies. This indicates about the line absorbed or emitted by the molecule, and hence giving a picture of the molecular energy levels.

Here the term FTIR refers to Fourier transform Infrared spectroscopy, when intensity time output of the interferometer is subjected to a Fourier transform to convert it to a familiar infrared spectrum (intensity frequency). The energy of infrared radiation corresponds to the difference of vibrational energy modes in a molecule. Infrared spectroscopy is therefore a probe of vibrational motion of a molecule. The technique works on the fact bonds and groups of bonds vibrate at characteristic frequencies. FTIR analysis provides information about the chemical bonding or molecular structure of materials, whether organic or inorganic. Figure 2.7 exhibits the real picture of FTIR instrument.

Figure 2.7. Real picture of Fourier transform Infrared spectrometer (FTIR; Perkin Elmer-FTIR Spectrum-100), based in Najran University Saudi Arabia

2.2.6. Raman-Scattering Spectroscopy

Raman scattering exhibits high specificity and requires no special sample preparation. It is being carried out in a short experimental scale. In the Raman measurement a beam of laser light is incident on the sample (viewed by the video facility), scattered photons are collected at the detector, sample surface is being refreshed by the XYZ translation stage, and hence no direct contact with the sample is needed during the experiment. This makes Raman Spectroscopy a non-destructive effective analysis tool.

Raman modes are like Infra-red modes but the IR modes are due to the change in dipole moment where as the Raman modes are due to the change in polarizibility. The modes which are inactive in IR due to the reason of zero change in their dipole moments can be easily observed by Raman spectroscopy. A Raman spectrum is a plot of intensity of scattered photons as a function of change of its (scattered photons) frequency. This difference is called Raman shift (usually expressed in units of wave numbers cm-1). In the Raman spectroscopy, difference in the scattered photon is important so it is independent of incident frequency and hence gives a broader choice of the laser sources [**142,143**]. A typical Raman spectrometer is made of three basic parts: the laser, the collection device, and the spectrograph. A laser beam which is coherent and mono-chromatic is used to excite Raman spectra, Collective device filters out the Rayleigh scattered photons (same frequency as the incident one) and any other back ground signal from the fiber-optic cables and sends only the Raman scattered photons to the spectrograph. And finally, a detector which records the intensity profile corresponding to each Raman scattered photon. The scattering property of as-prepared metal oxide materials were examined by using Raman-scattering spectroscopy (Perkin Elmer-Raman Station 400 series) at room-temperature. Figure 2.8 exhibits the real picture of Raman instrument.

Figure 2.8. Real picture of Raman scattering spectrometer (Perkin Elmer-Raman Station 400 series), based in Najran University Saudi Arabia

2.2.7. UV-Visible (UV-vis.) Spectroscopy

The structure of the compounds prepared in the lab are verified by spectroscopic techniques. These techniques are usually non-destructive and generally requires small amount of sample for the investigation. UV Vis spectrometer is a tool used for the investigation of electronic transitions and hence to determine the electronic bonding in a molecule. In a standard UV-Vis spectrometer, the beam of light is split into two parts by a partial mirror; one half of the beam (the sample beam) is directed through a transparent cell containing a solution of the compound being analyzed, and one half (the reference beam) is directed through an identical cell that does not contain the compound but contains the same solvent wherein the compound is dissolved. The solvents are must to be taken care of to be transparent for the interested light. The difference of light intensities scanned over a range of wavelength are taken and compared. The intensity profile over a range of wavelengths are observed. In complex molecules the energy levels are more closely spaced and photons of near ultraviolet and visible light can affect the transition. These substances, therefore, will absorb light in some areas of the near ultraviolet and visible regions.

UV-Vis. spectroscopy was used to examine the optical properties of prepared metal oxide nanomaterials. Figure 2.9 exhibits the real picture of UV-Visible spectrophotometer.

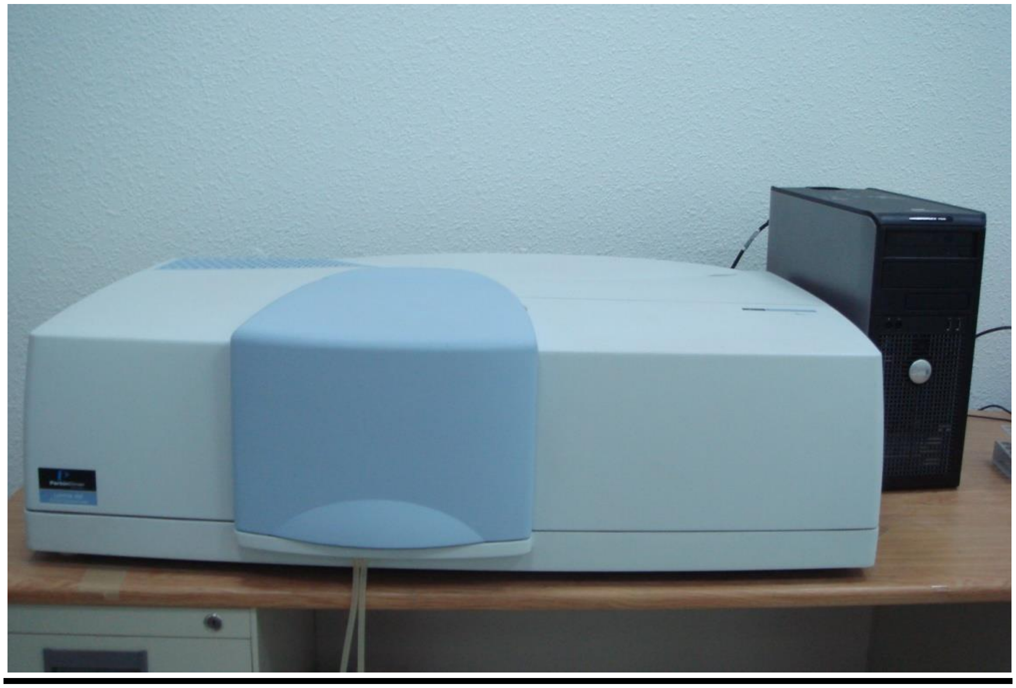

Figure 2.9. Real picture of UV-Visible spectrophotometer (Perkin Elmer-UV/VIS-Lambda 950), based in Najran University Saudi Arabia

2.3. Applications of prepared metal oxide nanomaterials

The synthesized metal oxide nanomaterials were efficiently used for the fabrication of sensing, photovoltaic and photocatalytic applications.

2.3.1. Sensing applications of metal oxide nanomaterials

To fabricate the sensor, slurry of as grown metal oxide nanomaterials is prepared by addition of conducting binders and coated on silver (AgE, Surface area 0.0214 cm^2) or gold (AuE, surface area 0.0214 cm^2) or on glassy carbon electrode (GCE, surface area 0.0316 cm^2). Prior to the modification of electrodes, the surface of given electrodes is polished with alumina-water slurry on a polishing cloth, followed by washing them with water thoroughly. In order to modify the electrode surface, the optimized amounts of as synthesized nanomaterials powder (~ 85-90%) and conducting agent (Butyl carbital acetate) were mixed well to make slurry. Finally, a certain amount of the slurry was casted on the electrode. The modified electrode is then dried and aged at 60 ± 5 ºC for 5-6 hrs to get a uniform and dry layer over active electrode surface. To evaluate the sensing performance, a simple two electrode system (current-voltage, *I-V* technique) was used in which the modified electrode is used as working electrode and Pd wire as counter electrode. An electrometer (Keithley, 6517A, USA) is used as a voltage source for I-V measurement. The current response is measured over a small potential ranging from almost 0 to 2.0 volts while the time delaying can be fixed to 1.0 second. Various analytes concentrations were prepared in a phosphate buffer solution (PBS, pH-7.0, 0.1M). The sensitivity is considered as the vital indicator of the sensing performance of any chemical sensor. Therefore, the sensitivity of the proposed chemical was calculated by slope of the current-concentration calibration profile.

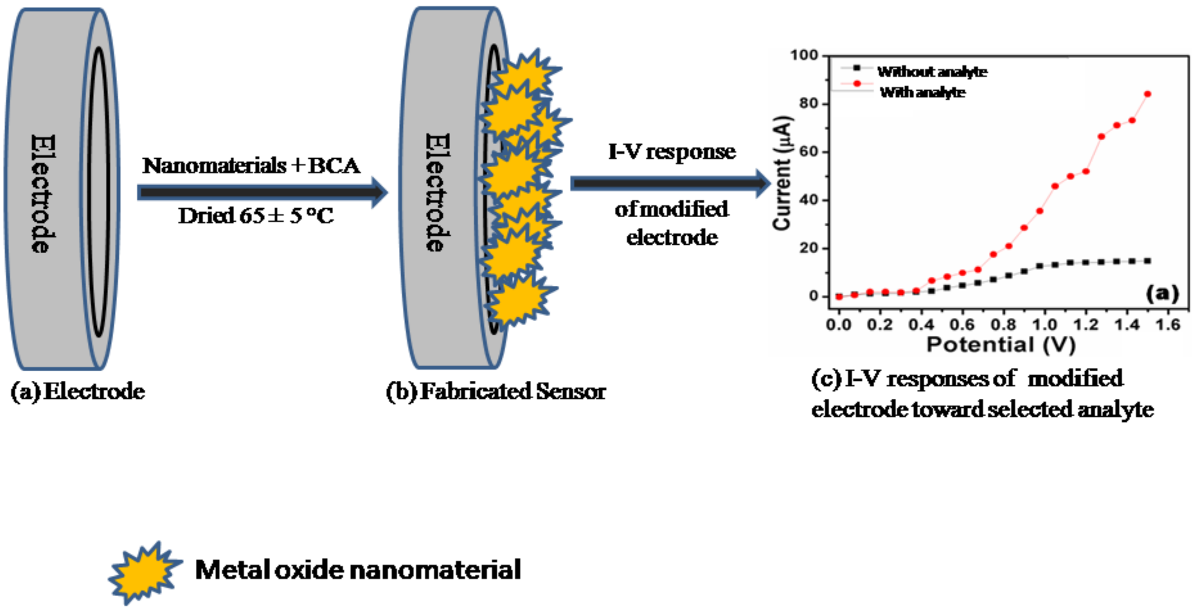

Figure 2.10. Schematic representation of the fabricated chemical sensor fabrication based on metal oxide nanomaterial coated specific electrode and its characterization by simple and facile I-V technique

The sensitivity was obtained when the slope of the current-concentration calibration profile was divided by the active surface area of working electrode according to the following equation:

Sensitivity=Slope of calibration profile / Surface area of electrode

Figure 2.10 presents the schematic representation of the fabricated chemical sensor fabrication based on metal oxide nanomaterial coated specific electrode and its characterization by simple and facile I-V technique.

2.3.2. Photovoltaic (dye-sensitized solar cell) application of ZnO nanomaterials

The photovoltaic device was fabricated as reported in the literature [**144**]. In a typical fabrication process of photovoltaic device, i.e. dye sensitized solar cells, the slurry of as-synthesized ZnO nanomaterial was made by adding appropriate amount of material in PEG solution and then coated as a film on fluorine-doped tin oxide (FTO) glass substrates. Finally, the prepared thin film was calcined at 450 °C for 1h. The prepared film electrodes were immersed in the 0.3 M ethanolic solution of *cis*–bis (isothiocyanato) bis (2,2`-bipyridyl-4,4`-dicarboxylato)-

ruthenium(II) bis-tetrabutyl ammonium dye (N719) for 3h at room-temperature. Thus, the dye absorbed electrode was attached with counter electrode of Pt layer on FTO glass substrate, and edges were sealed using thick sealing sheet. The liquid electrolyte, made of 0.5 M LiI, 0.05 mM I_2, and 0.2 M tert-butyl pyridine in acetonitrile, was introduced into the cell through one of two small holes drilled in the counter electrode. The active layer of the resulting cell was approximately 0.25 cm^2 (0.5 cm x 0.5 cm). The photocurrent density – voltage (*J–V*) curve was measured using computerized digital multi-meters. The light source was 1000-W metal halide lamp and its radiant power was adjusted with respect to Si reference solar cell to about one-sun-light intensity (100 mW/cm^2).

2.3.2. Photocatalytic decomposition of Rhodamine B using as-synthesized α-Fe_2O_3 hexagonal nanoparticles

The photocatalytic degradation of RhB dye was carried out in a three neck pyrex flask reactor using α-Fe_2O_3 nanoparticles as photocatalyst under UV illumination of xenon arc lamp (300W, Hamamatus: L 2479). For the photocatalytic degradation of RhB dye, 10ppm dye solution was prepared in 100ml DI water in which 0.15g photocatalyst (α-Fe_2O_3nanoparticles) was added and the resultant mixture was purged with Ar gas under continuous stirring. Consequently, the obtained suspension was equilibrated for 30min to stabilize the absorption of RhB dye over α-Fe_2O_3nanoparticles prior to the light exposure. The photocatalytic degradation of the RhB dye was estimated by measuring the absorbance of dye solution in the presence of photocatalyst exposed at different time intervals (10min). The absorbance was measured by UV-vis. spectrophotometer. The degradation rate of RhB dye was estimated according to the following equation [**145,146**]**:**

$$\textbf{Degradation rate (\%)} = (C_o\text{-}C/C_o) \times 100 = (A_o\text{-}A/A_o) \times 100$$

Where C_o represents the initial concentration, C the variable concentration, A_o the initial absorbance, and A the variable absorbance.

CHAPTER-3

RESULTS AND DISCUSSION

Chapter 3 describes the main results and discussion of the thesis. This chapter is divided into several sections and each section describes the synthesis, detailed characterizations and particular application of a single metal oxide nanomaterial. Section 3.1 describes the growth, characterization and ammonia chemical sensing applications of well-crystalline ZnO nanopencils grown via facile and simple hydrothermal process using commonly used laboratory chemicals. Importantly, the fabricated ammonia chemical sensor exhibited ultra-high sensitivity. Section 3.2 demonstrates the use of ZnO balls made of intermingled nanocrystalline NS for photovoltaic device application. Successful growth, characterizations and phenyl hydrazine chemical sensing applications based on Ag-doped ZnO nanoflowers was demonstrated in section 3.3 of this chapter. Section 3.4describes the Ce-doped ZnO nanorods for the detection of hazardous chemical; hydroquinone. Section 3.5 exemplifies the facile growth and detailed structural and optical characterizations of In-Doped ZnO hollow spheres composed of NS networks and nanocones. Finally, section 3.6 illustrates the utilization of α-Fe_2O_3 hexagonal nanoparticles for environmental remediation and smart sensor applications. Moreover the synthesized α-Fe_2O_3 hexagonal nanoparticles were characterized in detail in terms of their morphological, structural, compositional and optical properties.

Here in this chapter we will investigate the used nanomaterial metal oxide nanostructures, we present the part of experimental details related to each nanomaterial as synthesized via hydrothermal or chemical vapour deposition method. Detailed characterizations in terms of their morphology and crystallite structures using standard techniques will be presented. We will report the explored application as used here towards the detection of hazardous chemical applications. In fact this chapter will be divided into various sections. Each section will consist of systematic synthesis and growth of the nanomaterial metal oxide, their characterization and the explored application and the necessary conclusion.

Section 3.1: Ultra-high Sensitive ammonia chemical sensor based on ZnO Nanopencils

This section reports a very simple, reliable and facile methodologyto fabricate ultra-high sensitive liquid ammonia chemical sensor using well-crystalline hexagonal-shaped ZnO nanopencils as an efficient electron mediator. A low-temperature facile hydrothermal technique was used to synthesize ZnO nanopencils. The synthesized nanopencils were characterized in detail in terms of their morphological, structural and optical properties which confirmed that the synthesized nanomaterial is well-crystalline, possessing wurtzite hexagonal phase and possessing very good optical properties. A very high sensitivity of ~26.58μA cm^{-2} $mM^{-1}$and experimental detection limit of ~5 nM with a correlation coefficient (R) of 0.9965 were observed for the fabricated liquid ammonia by I-V technique. To the best of our knowledge, by comparing the literature, it is confirmed that the fabricated sensor based on ZnO nanopencils exhibits highest sensitivity and lowest experimental detection limit for liquid ammonia. This research opens a way that simply synthesized nanomaterials could be used as efficient electron mediators for the fabrication of efficient liquid ammonia chemical sensors.

3.1.1. Introduction

In recent years, numerous intensive reseacrh efforts in the field of nanotechnology hasshown great potential. There has been a significant improvement for the synthesis of desired inorganic nanomaterials as reported by vast literature reported so far. Being at the dimension between approximately 1 – 100 nm, nanomaterial enabled the various useful applications in diverse fields of the scientific areas.

Nowadays, environmental pollution caused by combustion from vehicles, agricultural sector and industrial leakages of toxic chemical and gases at very alarming rate created havoc in the scientific community [**147,148**]]. Among various environmental pollutants, the liquid ammonia (i.e. ammonium hydroxide) is one of the highly toxic chemicals for human being and wildlife produced in fertilizer and chemical factories. The dissolution of this chemical into running and drinking water may cause severe health problems such as skin, throat, and lung cancer and permanent blindness. Therefore, early detection and monitoring of leakage of liquid ammonia in the environment is highly desirable for public safety. In this regard, there have been reports for the detection of ammonia (gas and liquid both) in various forms such as electrochemical sensor, optical sensor, chemiresistive sensor, polyaniline and metal oxide based sensors, biomaterials (L-glutamic acid.HCl) based sensors, I-V technique based sensor and so on [**149-159**]. Among various detection techniques, the I-V technique is one of the simplest and easy technique for the efficient detection of various hazardous chemicals and environmental pollutants. For this, various nanostructures were used as efficient electron mediators to modify the electrodes for the fabrication of efficient I-V technique based chemical sensor [**160-164**]]. Among various nanostructures, metal oxide nanostructures possess excellent properties and hence used for wide applications [**151-156, 158-162,164-167**]. In metal oxides family, the II-VI wurtzite hexagonal-shaped ZnO possess special place due to its own properties and wide applications. The various exotic properties of ZnO include its direct and wide band gap (~3.37 eV), high exciton binding energy (60 meV) much larger than other semiconductor materials, biocompatibility, easy and cost effective synthesis, high electron features, optical transparency, non-toxicity and so on [**168-172**]. Although, ZnO have excellent properties, there are very few reports of this material as ammonia chemical sensor.

In this work, we report the fabrication of highly sensitive chemical sensor for the efficient detection of liquid ammonia simply by using ZnO nanopencils. For this, a layer of ZnO nanopencils was coated over the active surface of Glassy carbon electrode (GCE) followed by thermal treatment in an oven in order to obtain a uniform and stable layer. Later, the ZnO modified GCE was used to detect the liquid ammonia sensor by I-V technique. Due to well-crystallinity and higher surface area of the synthesized ZnO nanopencils, the fabricated sensor offers ultra-high sensitivity towards the efficient detection of liquid ammonia. In addition to this, the fabricated sensor also exhibited high regression coefficient and very low experimental detection limit, i.e. in the nanomolar range. Furthermore, it was observed that the proposed ammonia sensor is highly reproducible and stable over a long period of time.

3.1.2. Experimental Details

3.1.2.1. Synthesis of ZnO nanopencils by low-temperature hydrothermal process

Large-quantity synthesis of ZnO nanopencils was done by simple and facile hydrothermal process by using zinc acetate dihydrate ($Zn(CH_3COO)_2.2H_2O$) and ammonium hydroxide (NH_4OH) at low-temperature of 125 ºC. All the chemicals utilized for the synthesis of ZnO nanopencils were purchased from Sigma-Aldrich and used as received without further purification. In a typical reaction process, 0.05M zinc acetate was mixed with 0.05M ammonium hydroxide solution, both made in 50 mL DI water, under contineous stirring. Few drops of ammonium hydroxide were added to maintain the pH of the solution =10.0. The final solution was vigorously stirred for 30 min and consequently transferred to teflon lined autoclave which was then sealed and heated upto 125 ºC for 8 hrs. After terminating the reaction, the autoclave was allowed to cool at room-temperature and the obtained products were washed several times with DI water and ethanol, sequentially and dried at 45 ºC. The as-synthesized products were investigated in terms of their morphological, structural and optical properties.

3.1.2.2. Characterizations of ZnO nanopencils by low-temperature hydrothermal process

The as-synthesized products were extensively characterized by various analytical techniques. The general and detailed morphologies were examined by using FESEM and TEM equipped with high-resolution TEM (HRTEM). The crystallinity and crystal phases of the synthesized products was examined by using XRD measured with Cu-Kα radiation (λ=1.54178 Å) in the range of 20-65°. The chemical composition was examined by using EDS and elemental mapping, both attached with FESEM, and FTIR spectroscopy in the range of 465-3750 cm^{-1}. The optical properties of the prepared nanomaterial were examined by using UV-visible spectroscopy and Raman-scattering spectroscopy at room-temperature.

3.1.2.3. Fabrication and characterization of aqueous ammonia chemical sensor by I-V technique

To fabricate the aqueous ammonia chemical sensor, slurry of as-prepared ZnO nanopencils was made with the addition of conducting binders and coated on glassy carbon electrode (GCE, surface area 0.0316 cm^2). Prior to the modification, GCE surface was polished with alumina-water slurry on a polishing cloth, followed by rinsing with distilled water thoroughly. For the electrode surface modification, firstly, an appropriate composition of nanomaterial (ZnO nanopencils) and conducting agent (Butyl carbital acetate) were mixed together and ground to obtain a fine powder using a mortal and a pestle. Later, a slurry was produced by dispersing of as prepared powder in a solvent (acetyl acetate). Finally, a certain amount of the slurry was casted on GCE carefully. The modified GC electrode was then dried and aged at 60 ± 5 ºC for 4-6 hrs to get a uniform and dry layer over active electrode surface. The modified GCE was employed as working electrode. A simple two electrode system was used to evaluate the sensing performance of ZnO in which the modified electrode was used as working electrode and Pd wire as the counter electrode. An electrometer (Keithley, 6517A, USA) was used as a voltage source for I-V measurement. The current response was measured from 2.0 to +5.0 volts while the time delay was fixed of 1.0 second. The concentration and volume of PBS were kept constant of 0.1M and 10.0 mL, respectively. A wide concentration range of ammonium hydroxide (5 mM to 50 nM) was used for all the experiments. The sensitivity of the fabricated aqueous ammonia chemical sensor was estimated from the slope of the current vs concentration from the calibration plot divided by the value of active surface area of sensor/electrode.

3.1.3.Results and Discussion

3.1.3.1. Morphological, structural and optical properties of as-synthesized ZnO nanopencils

The morphological, structural and optical properties of as-synthesized ZnO nanopencils were examined by various techniques and discussed in this section. To evaluate the general morphologies, the as-synthesized products were characterized by FESEM and the micrographs are reported in figure 3.1.1. The FESEM images clearly confirm that the synthesized materials are pointed nanorods which are grown in large quantity. Interestingly, it is seen that the pointed nanorods are assembled in bunches and each bunch has hundreds of nanorods in it. The lengths of the nanorods are in the range of 6 ± 2 μm. Figure 3.1.1 (b)-(d) exhibits the typical high-magnification images of as-synthesized pointed nanorods. It is clear from high-resolution images that the nanorods formed pencil like morphology and this is the reason why these nanorods are called "Nanopencils". The nanopencils exhibit very uniform, smooth and clear hexagonal surfaces throughout their length. The characteristic hexagonal surfaces of as-synthesized nanopencils confirm the good crystallinity and wurtzite hexagonal phase for synthesized product. The diameters of the nanopencils at their tips and surfaces are in the range of 45 ± 10 nm and 250 ± 50 nm, respectively (figure 3.1.1 (c) and (d)).

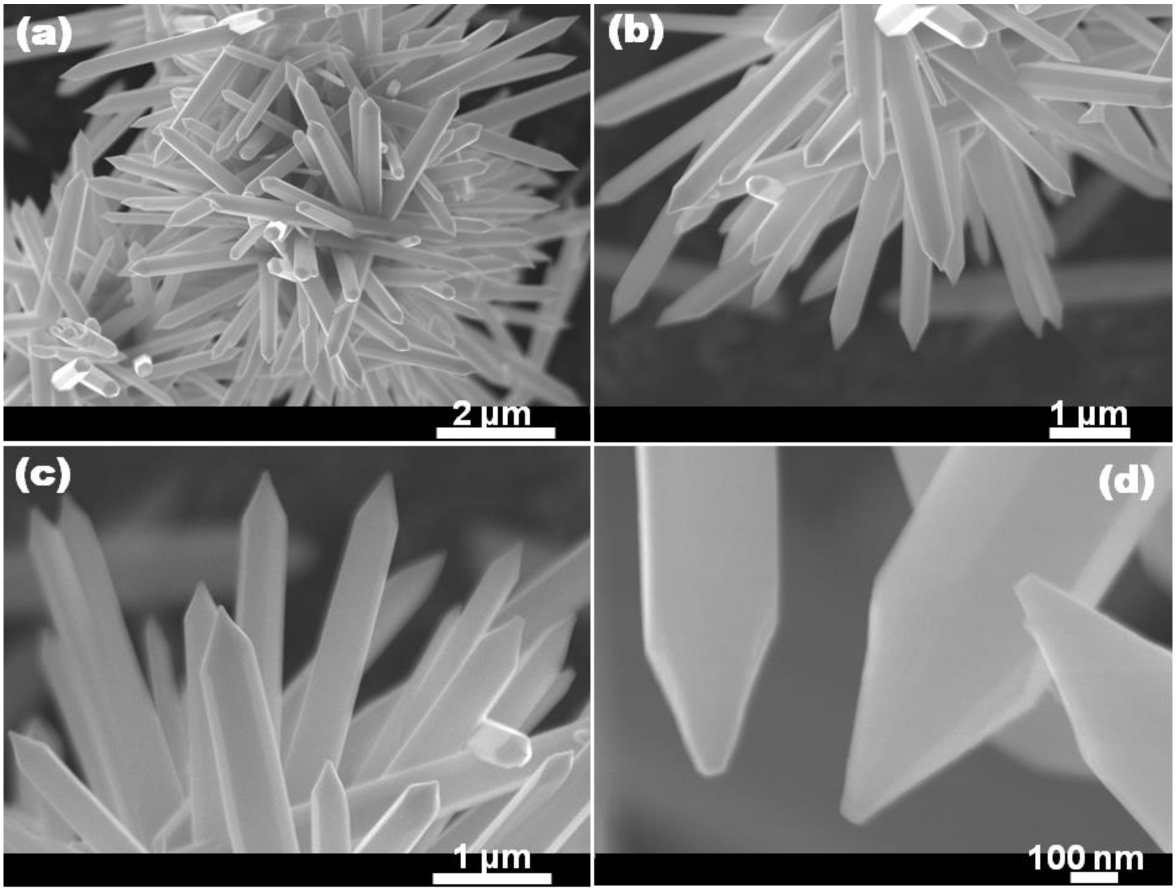

Figure 3.1.1. Low magnification ((a) and (b)) and high-resolution (c) and (d) FESEM micrographs of as-synthesized ZnO nanopencils

To examine the crystallinity and crystal quality of the as-synthesized ZnO nanopencils, XRD technique was used and the pattern is reported in figure 3.1.2. Several well-defined diffraction reflections are observed which are well matched with the pure wurtzite hexagonal phase. The calculated lattice parameters for the synthesized ZnO nanopencils were a= 3.249 Å, c= 5.205 Å which are similar to the reported data in Joint Committee on Powder Diffraction Standards (JCPDS), card no. 36-1451. In addition to this, the obtained results are well consistent with the already reported literature [**171,172**]**.**No other peak related with any impurity was detected in the observed pattern, upto the detection limit of XRD, confirming that the synthesized nanopencils are made of pure ZnO and possess wurtzite hexagonal structure. For detailed structural investigations, the as-synthesized nanopencils were characterized by TEM equipped with HRTEM and the results are presented in figure 3.1.3.

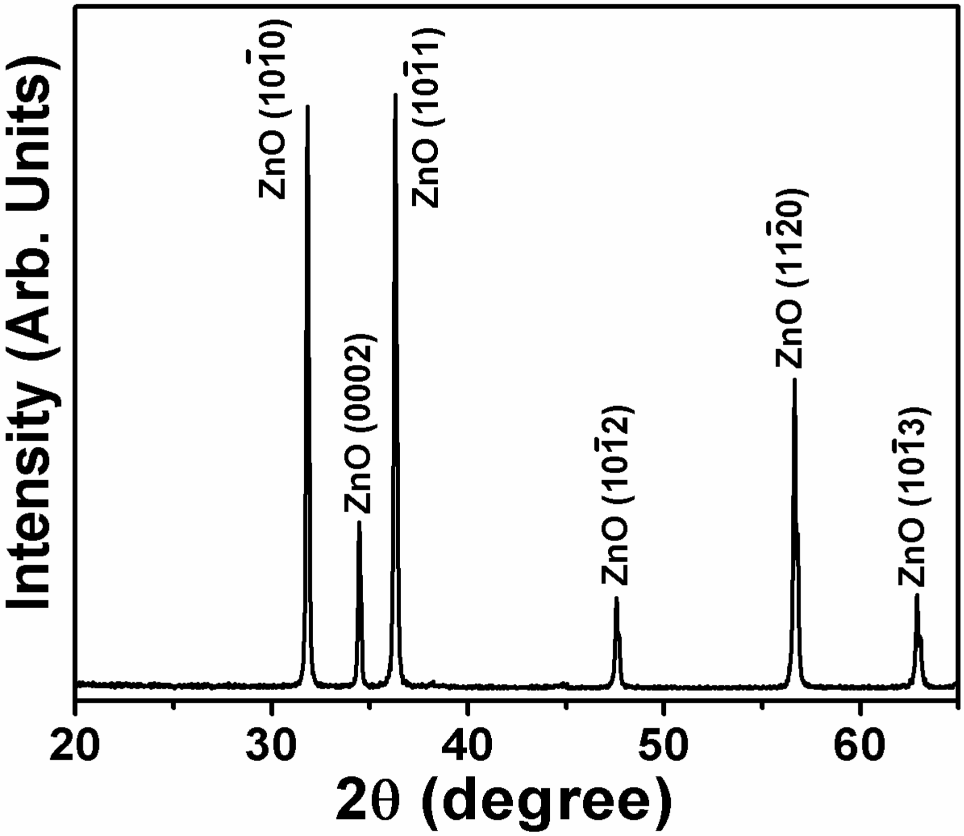

Figure 3.1.2. XRD pattern of as-synthesized ZnO nanopencils

Figure 3.1.3 (a) exhibit the low-magnification TEM images, which exhibits the full consistency with the obtained FESEM results in terms of the morphology, shape and size of the nanopencils. To check more elaborately, a high-resolution TEM (HRTEM) was done for as-synthesized nanopencils which clearly exhibits that the lattice fringes are organized in such a proper manner that no dislocation is seen which clearly confirms that the synthesized nanorods are almost defect free and possess good crystallinity (figure 3.1.3 (b)). In addition to this, the distance between two lattice fringes along the longitudinal axis direction, corresponding to the d-spacing of ZnO (0002) crystal planes, was measured and found to be ~ 0.52 nm which confirms that the synthesized nanopencils are well-crystalline and having wurtzite hexagonal phase. The inset of figure 3.1.3 (a) exhibits the typical crystallographic growth habit of as-synthesized ZnO nanopencils. It is well known that the shape of any ZnO crystal depends on the relative growth velocities of its different crystal planes [Laudise et al., 1960]. In case of wurtzite hexagonal ZnO, the ideal growth rates in the various crystal facets should be in the order of $[0001] > [01\bar{1}\bar{1}] > [01\bar{1}0] > [01\bar{1}1] > [000\bar{1}]$ under hydrothermal condition [**173**]. According to the ideal growth rates in various crystal facets, the growth along the [0001] direction is maximum and the synthesized nanorods contains $\pm\{0001\}$ crystal planes at their top and bottom and enclosed by the six equivalent $\{01\bar{1}0\}$ crystal facets**[174]**. It is known that the fastest growing plane generally tends to disappear and leaving behind the slower growing forms with lower surface energy. Hence, the (0001) face is not an equilibrium surface and it is bounded by the growth facets of $\{01\bar{1}1\}$ whichhas higher Miller indices but lower specific surface energy compared to the (0001) facets. As the specific surface free energy of (0001) faces are higher than other growth facets, hence after the growth of $\{01\bar{1}1\}$ facets, the (0001) planes are the most likely remaining facets which appear on the ZnO crystals. Interestingly, it is observed that our as-synthesized ZnO nanopencils follow the same growth pattern as reported in the literature for the growth of ideal wurtzite hexagonal ZnO crystals **[144,175].**

To check the composition and purity, the as-synthesized ZnO nanopencils were examined by using EDS and elemental mapping, both attached with FESEM. Figure 3.1.4 (a) exhibits the typical FESEM image of as-synthesized nanopencils and (b) illustrates the typical EDS spectrum of the corresponding nanopencils shown in (a). As can be seen from the obtained FESEM images, the nanopencils are grown in very high density. The corresponding EDS spectrum confirms that the synthesized nanopencils are made of zinc and oxygen. No other impurity peak was observed in the spectrum, up to the detection limit of EDS.

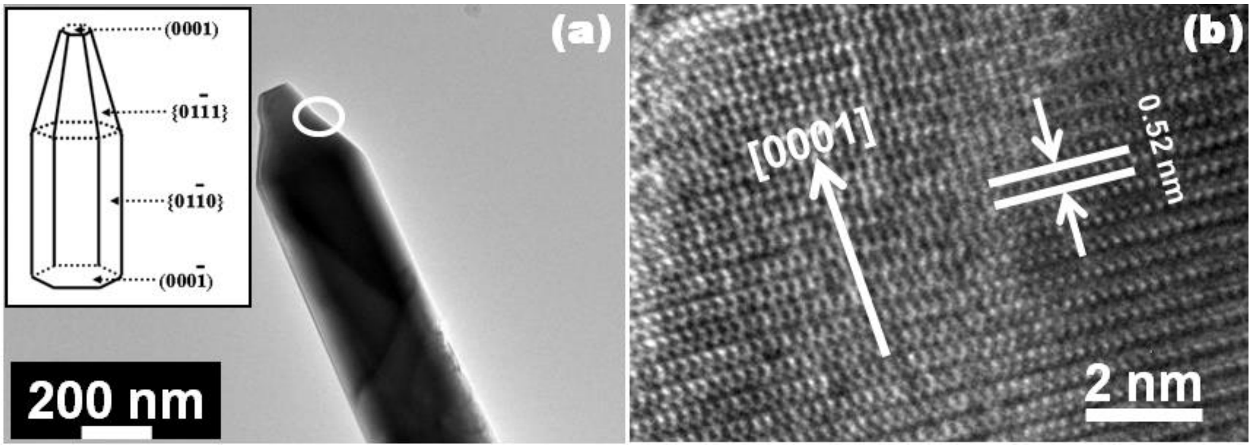

Figure 3.1.3. High-resolution TEM micrographs of as-synthesized ZnO nanopencils. Inset of(c) exhibits the schematic of typical crystal habits of as-synthesized ZnO nanopencils by Hydrothermal process

The quality and chemical composition of the as-synthesized ZnO nanopencils were examined by FTIR spectroscopy at room temperature in the range of 465-3750 cm^{-1} and shown in figure 3.1.5. Several well-defined peaks at 559, 1627 and 3439 cm^{-1} have been observed in the obtained FTIR spectrum. A sharp peak appeared at 559 cm^{-1} is related with metal-oxygen (Zn-O)bond and confirms that the synthesized material is ZnO [31, 32]. In addition to the Zn-O band, a very short band appeared at 1627 cm^{-1} and a broad peak at 3439 cm^{-1} was also seen in thespectrum. The appearance of a very short band at 1627 cm^{-1} is due to the bending vibration of absorbed water and surface hydroxyl, while the broad peak 3439 cm^{-1} is due to the O-H stretching mode [**176, 177**]. In addition to the observed peaks, no other peak related with any functional group was detected in the spectrum which reveals that the synthesized nanopencils are pure ZnO without any significant impurities.

To evaluate the optical properties, the as-synthesized ZnO nanopencils were examined by using a UV-visible (UV-Vis) spectrophotometer after dispersion in water by means of ultrasounds at room-temperature. Figure 3.1.6 illustrates the typical UV-Vis. spectrum of as-synthesized ZnO nanopencils and a well-defined absorption peak at 374 nm is clearly visible.

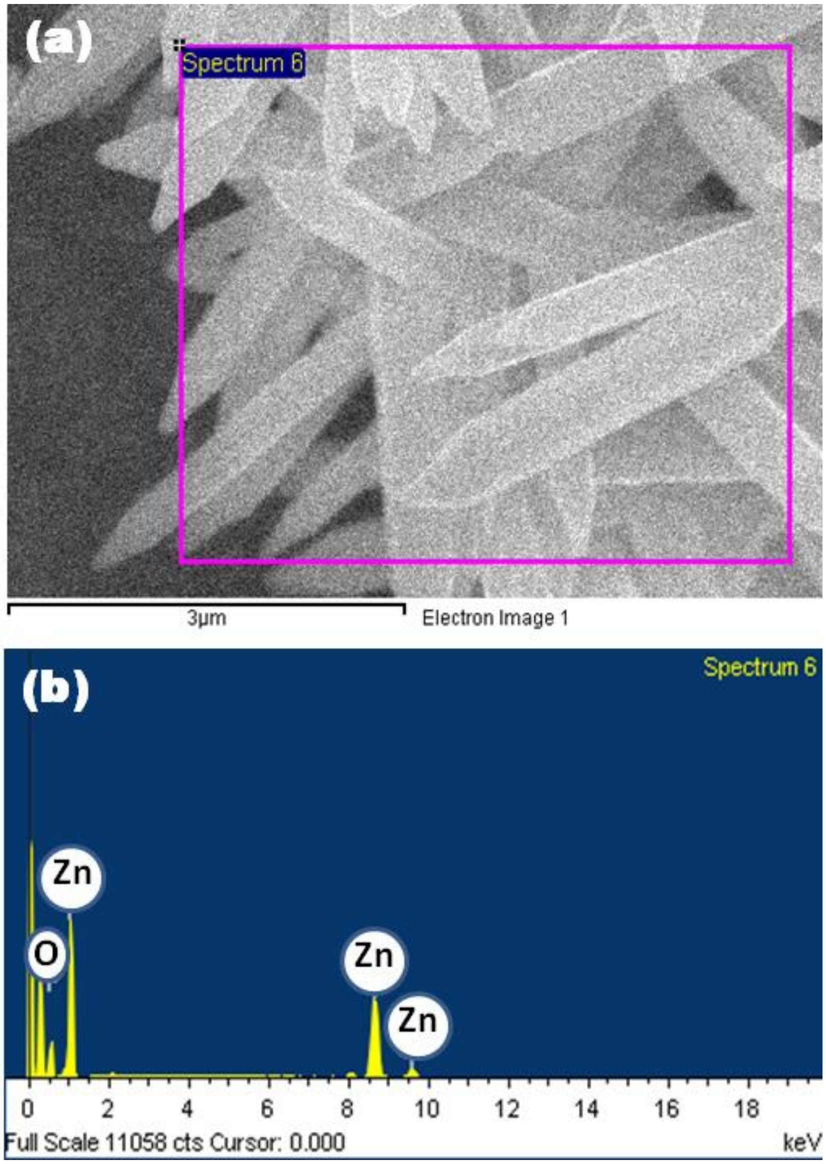

Figure 3.1.4. Typical (a) FESEM image and (b) its corresponding EDS spectrum of as-synthesized ZnO nanopencils

The optical band gap of as-synthesized ZnO nanopencils can be observed by using the Tauc's equation which demonstrates a relationship between absorption coefficient and the incident photon energy of semiconductors. The Tauc's equation is as follows (equation 3.1.1):

$$(\alpha h\nu) = A(h\nu - E_g)^n \qquad (3.1.1)$$

where α is the absorption coefficient, A is constant, and n is equal to ½ for a direct transition semiconductor and 2 for indirect transition semiconductor. According to the equation 3.1.1, the calculated optical band gap for as-synthesized nanopencils was found to be ~3.33 eV. The observed optical band gap for the synthesized nanopencils shows fully consistency with the already reported literature [**171**].

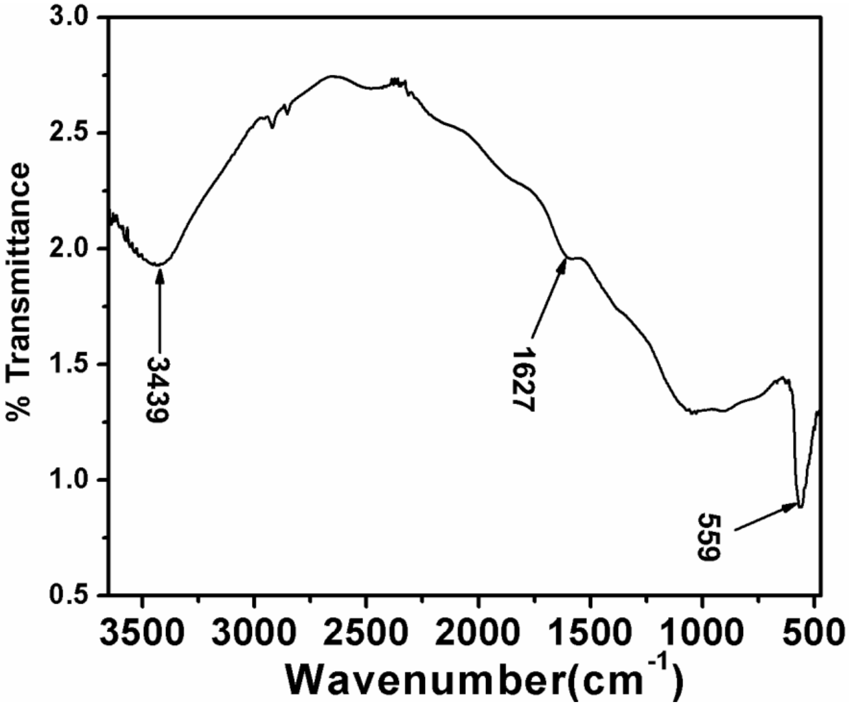

Figure 3.1.5. FTIR spectrum of as-synthesized ZnO nanopencils

The scattering properties of as-synthesized ZnO nanopencils were characterized by Raman-scattering measurements. ZnO with wurtzite hexagonal crystal structure belongs to C^4_{6V} space group with two formula units per primitive cell. According to the group theory, various Raman active phonon modes exists which are denoted as $\Gamma = A_1 + E_1 + 2E_2$ [**178,179**]. Among various phonon modes, the A_1 and E_1 modes are polar and split into transverse optical (TO) and longitudinal optical (LO) branches. The E_2 modes are non-polar modes. Figure 3.1.7 shows the typical Raman-scattering spectrum of ZnO nanopencils which exhibits two defined bands, i.e. a sharp and strong band appeared at 437 cm^{-1} and a suppressed and short band at 331 cm^{-1}. The peak appeared at 437cm^{-1} is attributed to the Raman-active non-polar optical phonon E_2 (high) mode and is a significant band for the wurtzite hexagonal phase of pure ZnO [**174**].

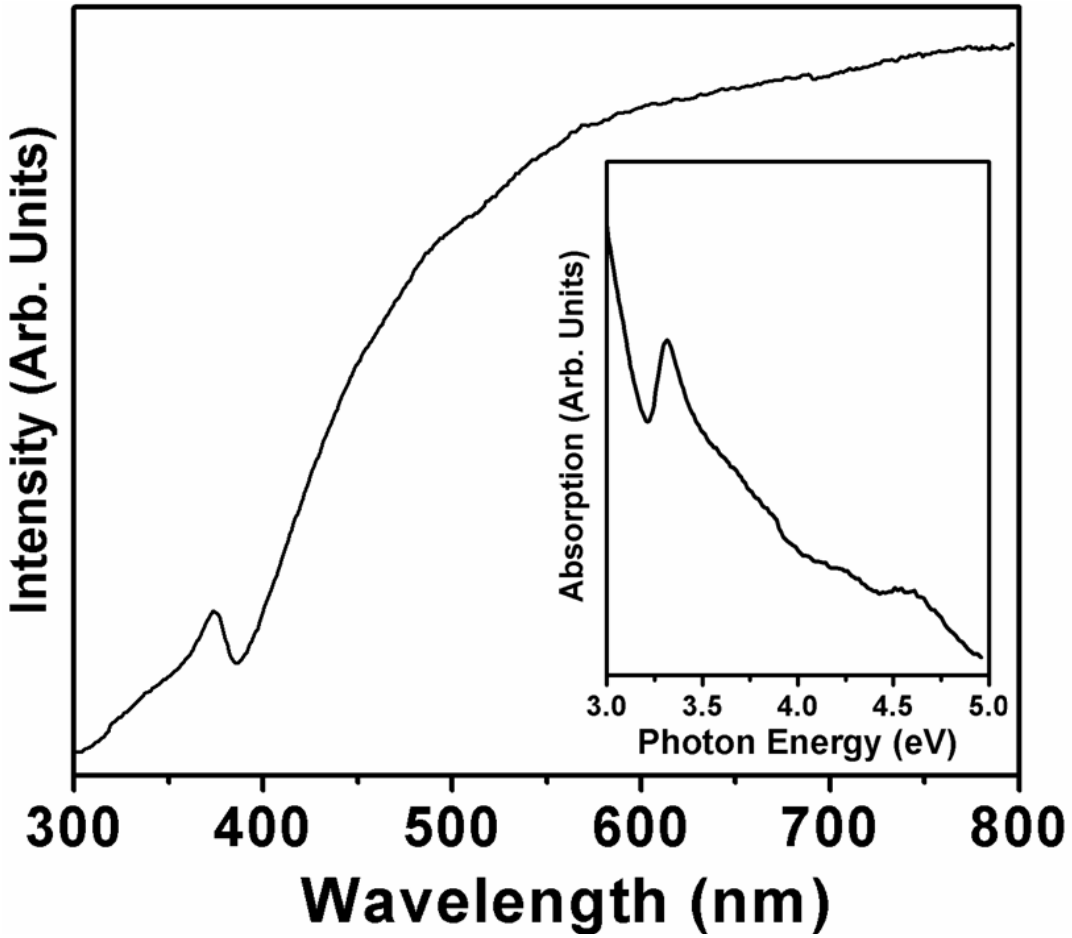

Figure 3.1.6. UV-Vis. spectrum of as-synthesized ZnO nanopencils

The other observed short band at 331 cm^{-1} is assigned as $E_{2H} – E_{2L}$ (multi-phonon process) and can be found only when the ZnO is very well crystallized [**180**]. No other band related with any other optical phonon is seen in the spectrum. Therefore, due to the presence of sharp and strong Raman-active optical phonon E_2 (high) mode and small $E_{2H} – E_{2L}$ mode clearly confirmed that the as-synthesized ZnO nanopencils have good crystal quality with the wurtzite hexagonal phase.

3.1.3.2. Ammonia chemical sensor application of as-synthesized ZnO nanopencils

The proposed ZnO nanopencils based chemical sensor was used to detect ammonia in liquid phase which is considered one of the potential hazardous compounds to living beings and wildlife directly or indirectly. The methodology for the detection of ammonia through a typical I-V technique has been extensively described in the fabrication part.

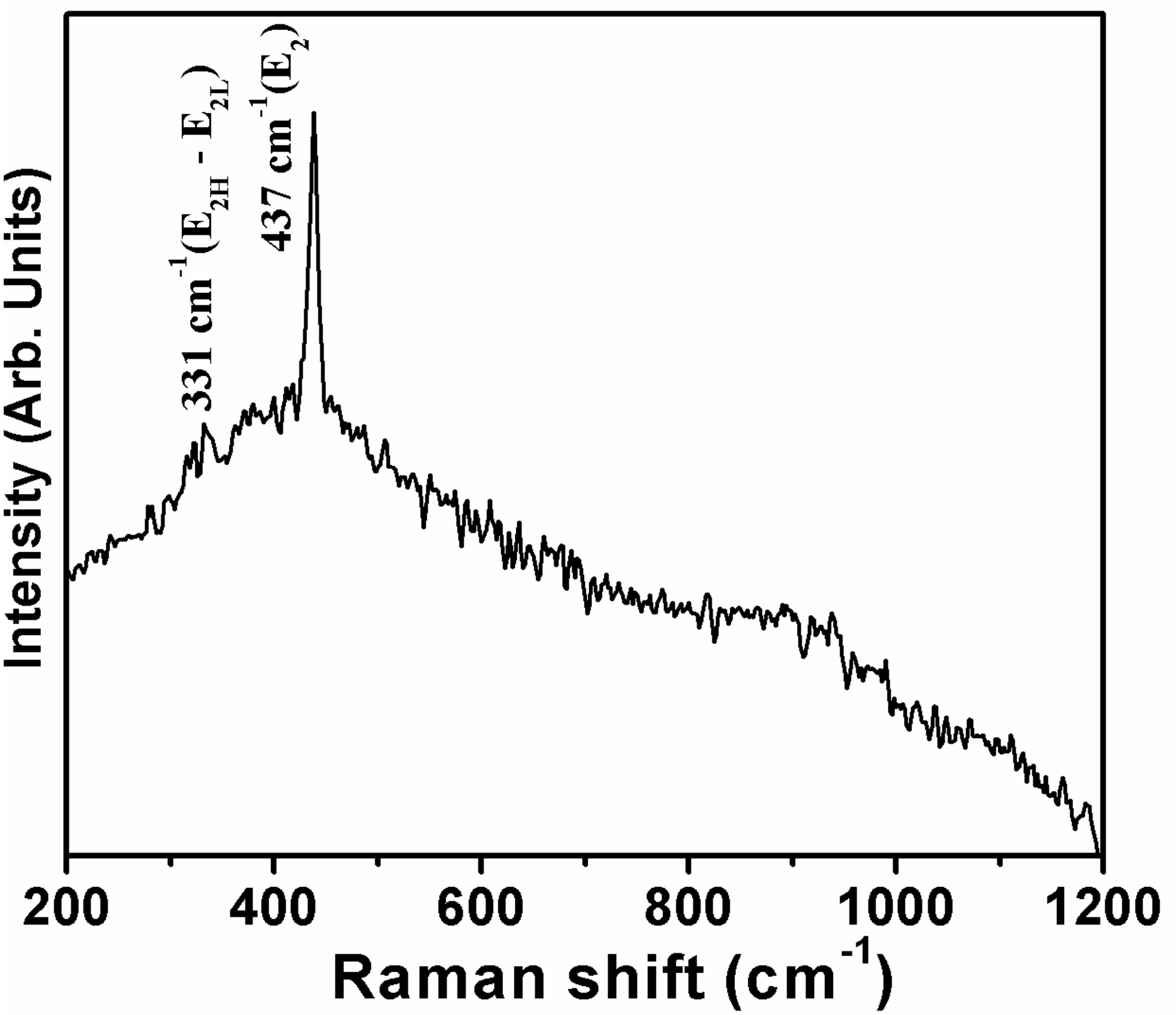

Figure 3.1.7. Raman-scattering spectrum of as-synthesized ZnO nanopencils

The schematic representation of sensor fabrication is illustrated in Figure 3.1.8. The ZnO nanopencils based ammonia sensors possess various advantages which include their stability in air and normal environments, biosafety and biocompatibility, high-electrochemical features, non-toxicity, easy fabrication, reliability and many more. Figure 3.1.9 exhibits the typical I-V electrical response of the fabricated ammonia chemical sensor based on ZnO nanopencils modified GCE in the absence and presence of 50 nM ammonia in 10.0 mL of PBS solution. It is obvious from the figure 3.1.9 that by injecting the target analyte, i.e. ammonium hydroxide, a significant enhancement in current was observed which reflects the high sensitivity of ZnO nanopencils to the analyte. As ZnO possesses good electrocatalytic and fast electron exchange properties, hence it is believed that due to these properties a rapid increase in the current was observed in presence of ammonium hydroxide. In addition to this, the increase in the current could be attributed to the discharge of the trapped electrons into the conduction band.

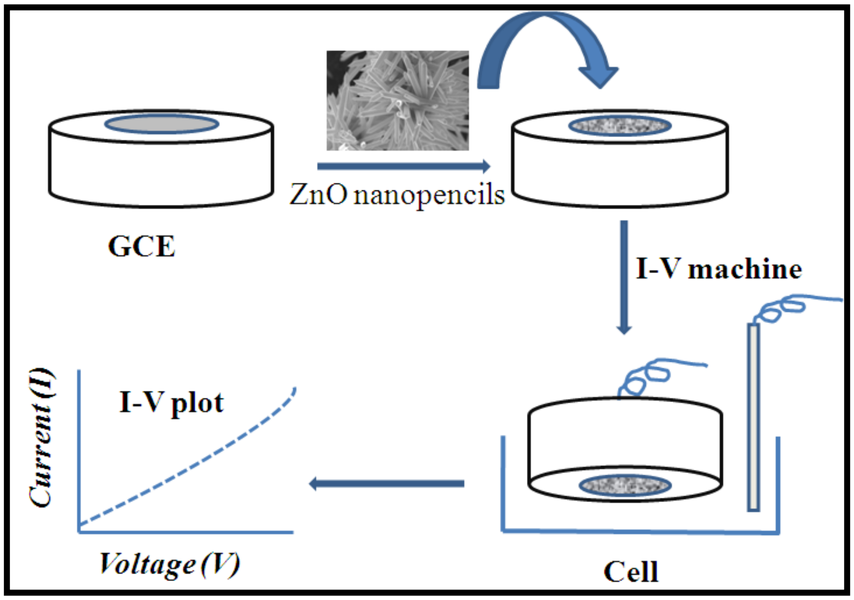

Figure 3.1.8. Schematic representation of ammonia chemical sensor fabrication based on ZnO nanopencils coated GCE electrode and its response by a simple and facile I-V technique

Furthermore, the decomposition of liquid ammonia (Eq. 3.1.2) molecules is an exothermic reaction, releasing the sufficient amount of energy to the electrons to overcome the barrier.

$$NH_4OH_{liquid} \rightarrow NH^4 + OH^- \qquad (3.1.2)$$

In other words, a catalytic and rate determining reaction occurs on the surface of the ZnO modified electrode. In case of catalytic reaction, the ammonia is first adsorbed on a catalyst, gets split up into ions and then spreads over on the surface and reacts with surface oxygen ions of functional material thereby decreasing the resistance of the sensor and enhancing the current response, because of the ZnO n-type semiconducting behavior.

In general, the detection of any target analyte using metal oxide semiconductors is based upon the oxidation of analyte of interest on sensor surface by the ionized oxygen from the liquid /air interface and subsequent emission of an electron from the ionized species into the conduction band **[181].** It has been elucidated in the literature that oxygen plays a vital role in the change of electrical behavior of ZnO nanostructures. As shown in Eq. (3.1.3), oxygen is adsorbed at nanostructure surface and gets ionized into dynamic oxygen species, such as O^- and O^{2-} by extracting the electron from conduction band of nanostructure surface and hence leading to decrease in the conductance (or increase in resistance).

$$\frac{1}{2} O\,(g) + ne^- \rightarrow O^{n-}\,ads \qquad (3.1.3)$$

Where O^{n-} ads is adsorbed oxygen (n = 0, 1, 2) and e^- is electronic charge.

However, introduction of analyte in the sensor system results into a catalytic reaction described in Eq. (3.1.4). The produced ions react with the adsorbed oxygen species and subsequently emit the trapped electrons into the conduction band of nanomaterial. Consequently, this process increases the conductance of nanomaterials and exhibits in the form of electrical signal.

$$A\,(liquid\,) \rightarrow B^+ + C^- \qquad (3.1.4)$$

For further sensor performance investigations, the I-V electrical response of the fabricated ammonia chemical sensor based on ZnO nanopencils modified GCE was investigated in various concentrations of ammonium hydroxide in 10.0 mL of PBS solution. For concentration studies, the stock solution of ammonia was prepared by adding the appropriate amount of ammonia in the 0.1M pH 7.0 buffer. Then, concentrations of ammonia were varied from 5 nM to 5 mM by diluting the stock solution further with the same buffer accurately. Figure 3.1.10 (a) exhibits the typical I-V response of the fabricated ammonia sensor as a function of ammonium hydroxide concentration at room-temperature. It is observed that the current response increases rapidly with the increase in concentration. Therefore, at lower to higher concentrations of target analyte, the current increases gradually. It can be deduced from current behavior that the number of ions are increased with the increase of the concentration of ammonia corresponding to the rapid electrons transfer relay into conduction band. This results into the enhancement of the sensor response [**169,182**].

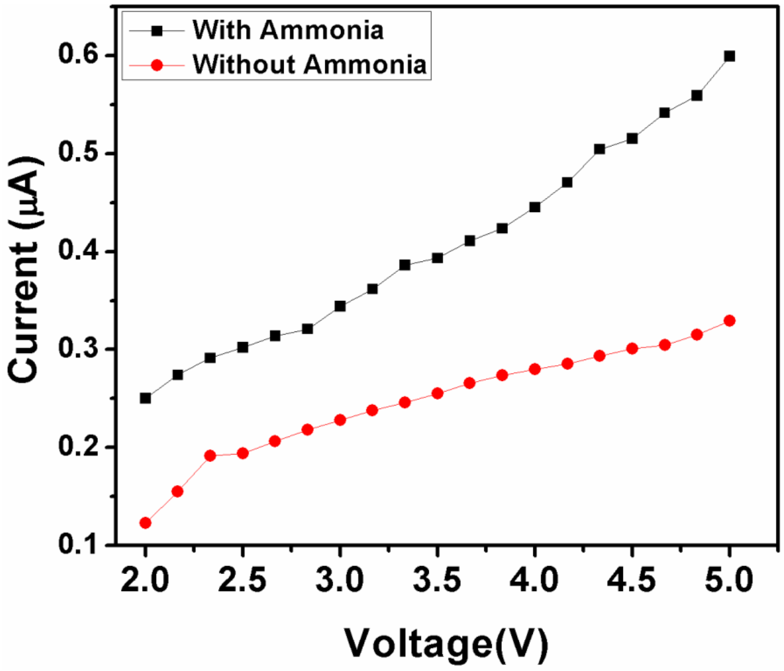

Figure 3.1.9. Typical I-V response of Glassy Carbon Electrode (GCE) in 10 mL, 0.1 M PBSsolution: (■) with 50 nM ammonia and (●) without the presence of liquid ammonia

The fabricated sensor sensitivity was estimated from the slope of the current vs concentration from the calibration plot shown in Figure 3.1.10(b). The fabricated aqueous ammonia sensor based on ZnO nanopencils exhibits good and reproducible sensitivity of ~26.58 μA/mMcm^2 and experimental detection limit of ~5 nM with a correlation coefficient (R) of 0.9965. The linear dynamic range was in the range between 50 nM to 0.5mM. To the best of our knowledge, the fabricated liquid ammonia chemical sensor exhibits the highest sensitivity ever reported in the literature [**157,163,165**]. In addition to this, the obtained experimental detection limit of the fabricated sensor is ~5 nM which is lower than the previously reported literature values (Table-3.1.1).The proposed sensor exhibited prominent stability over long period of time. The stability of the present ammonia sensor was determined by measuring the response once a day for 4 weeks. After each measurement, the sensor was stored in a PBS (pH=7.0). No significant decrease in ammonia detection was observed for 3 weeks. After 3 weeks, the response of sensor was gradually reduced due to the weak interaction of ZnO nanopencils electrode and liquid ammonia. This indicates that the fabricated sensor showed not only high but also long term stability.

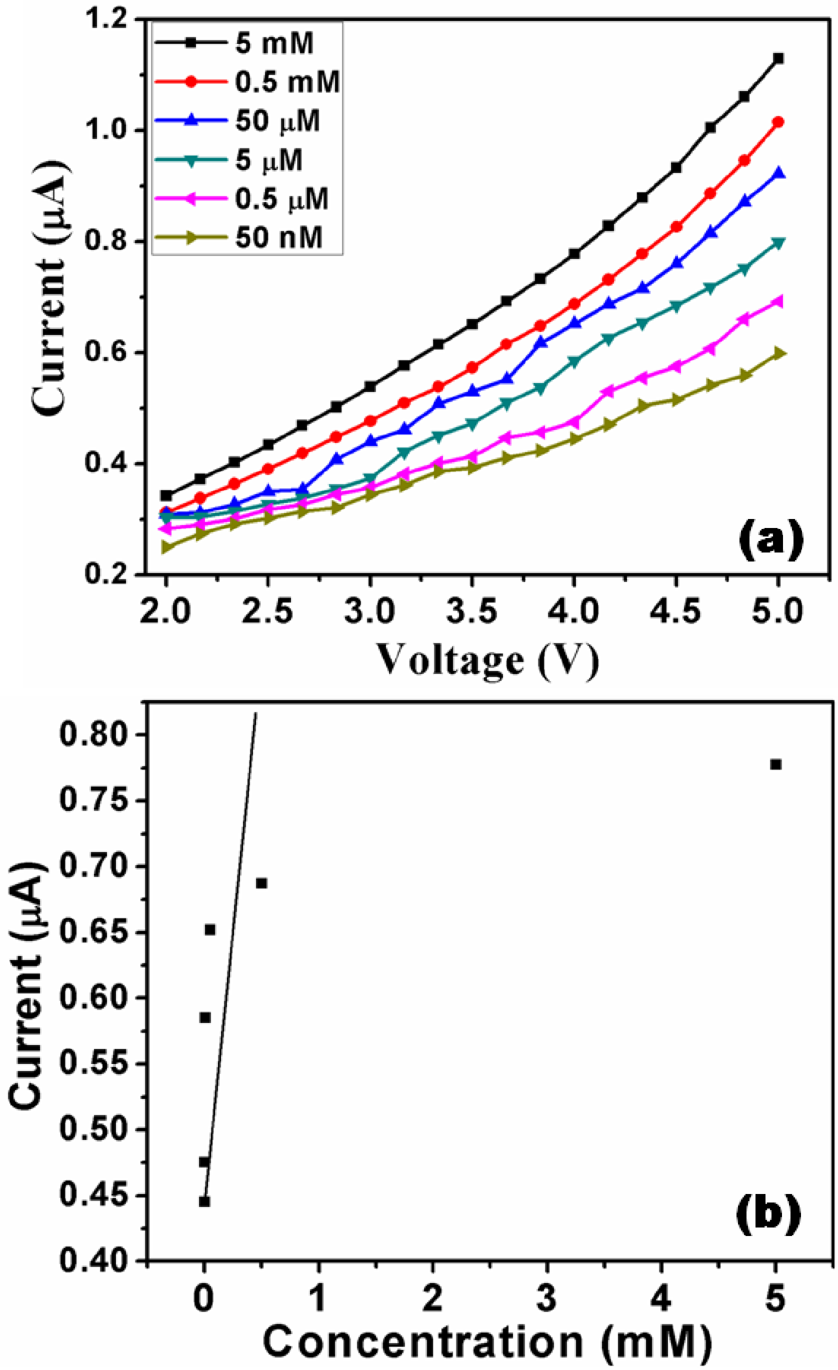

Figure 3.1.10. (a) Typical I-V response of ZnO nanopencils modified GCE towards variousconcentrations (from 50 nM to 5 mM) of liquid ammonia into 0.1 M PBS solution (pH=7) and**(b)** Calibration curve

Furthermore, the proposed ammonia sensor showed reproducible behavior too. It is noticeable that the estimated sensitivity of the fabricated sensor is relatively higher than previously reported ammonium hydroxide sensor fabricated based on the utilizationof various nanomaterials and/or composite materials modified electrodes [**163**,**165**,**182**]. The observed high-sensitivity and low-experimental detection limit of the fabricated liquid ammonia sensor based on ZnO nanopencils modified electrode was mainly due to the good adsorption ability, rapid catalytic activity and biocompatible nature of as-prepared ZnO nanopencils. A concise table 3.1.1 has been shown to compare the performances of ammonia sensor presented in this study with the already reported values for ammonia sensor fabricated based on the utilization of various electron mediator materials.

Table-3.1.1: Comparison of the performances of the ammonia chemical sensors fabricated based on the utilization of various nanomaterials as electron mediators:

Materials/electrodes	**Sensitivity ($\mu A.cm^{-2}\,mM^{-1}$)**	**Detection limit**	**Linear Range**	**References**
ZnO nanopencils	**~26.5822**	**~5.0 nM**	**50 nM ~ 0.5 mM**	**Present work**
Polyurethane acrylate	8.5254	0.018 µM	0.05µM ~ 0.05M	**[157]**
β-Fe_2O_3 Nanoparticles	0.5305	21.8 µM	77 µM- 0.77 M	**[163]**
CuO codoped ZnO nanorods	1.549	8.9 µM	-	**[165]**

3.1.4. Conclusion

In summary, a very simple, reliable, reproducible and facile method has been presented to fabricate ultra-high sensitive liquid ammonia chemical sensor. Low-temperature grown, well-crystalline hexagonal-shaped ZnO nanopencils were used as efficient electron mediators for the fabrication of proposed chemical sensor. The fabricated liquid ammonia chemical sensor exhibits ultra-high sensitivity of ~26.58 $\mu A\ cm^{-2}\ mM^{-1}$ and very low experimental detection limit of ~ 5nM . To the best of our knowledge, the fabricated chemi-sensor exhibits highest sensitivity for liquid ammonia. This research opens a way that simply synthesized nanomaterials could be used as efficient electron mediators for the fabrication of various effective chemical sensors.

Section 3.2: ZnO balls made of intermingled nanocrystalline nanosheets for photovoltaic device application

This work reports the facile synthesis of well-crystalline ZnO balls made of intermingled nanocrystalline NS by hydrothermal process using zinc nitrate hexahydrate, hydroxylamine hydrochloride and sodium hydroxide. The prepared ZnO balls were examined using several techniques in terms of their morphological, structural, compositional, optical and photovoltaic properties. The detailed morphological studies revealed that the synthesized material possessed ball-shaped morphologies which were made of intermingled NS. The detailed compositional, structural and optical properties confirmed that the synthesized material was pure ZnO and possessed well-crystalline wurtzite hexagonal phase and exhibited good optical properties. The as-synthesized ZnO balls were used as photo-anode materials to fabricate efficient DSSCs. The fabricated DSSCs exhibited an overall light-to-electricity conversion efficiency of 2.1 % with a short-circuit current of 6.28 mA/cm^2, open-circuit voltage of 0.659 V and fill factor of 0.51. The obtained results revealed that simply synthesized ZnO nanomaterials can efficiently be used for the fabrication of high-efficient dye-sensitized solar cell applications.

3.2.1. Introduction

The II-VI metal oxide semiconductor ZnO has attracted a great attention worldwide due to its various excellent properties and wide applications [**183**]. The remarkable properties of ZnO include its wide band gap (3.37 eV), higher exciton binding energy (60 meV), excellent thermal and chemical stability, piezoelectricity, biocompatibility, high electronic carrier mobility, high breakdown voltage, large saturation velocity, cost effective syntheses and so on [**183-192**]. Due to these intriguing properties, ZnO is widely used in variety of high-technological applications such as electronics and optoelectronics, photonics, piezoelectric nanogenerators, piezoelectric sensors and actuators, field emission devices, energy storage and conversion, chemical and biosensors, cancer detection and cancer therapy, antibacterial and antimicrobial agents, photocatalysis and catalysis, solar cells, light emitting diodes (LEDs), acoustic wave filters, photonic crystals and so on [**183-197**].Because of various exotic properties and wide applications, ZnO has extensively been studied by several researchers and variety of ZnO nanomaterials were synthesized and reported in the literature [**183-202**].

Recently, due to serious energy problems around the world, great attentions have been paid to new and renewable energy research [**203-210**]. In this regard, the one of the widely studied photovoltaic device, i.e. DSSCs have recently gained much attentions due to their relatively low-cost, ease of manufacturing and reasonable high solar to electricity conversion efficiency [**127,211-217**]. Generally, the DSSCs are comprises of nanocrystalline semiconductor metal oxides (normally TiO_2) electrode modified with dye fabricated on FTO/ITO glass substrate, Pt counter electrode, and electrolyte solution. Using TiO_2 nanocrystalline thin films, the DSSC devices with high power conversion efficiencies greater than 10% have been reported in the literature [**218-220**]. Because of almost identical properties of the II-VI semiconductor ZnO compared to TiO_2, such as electron affinity and band gap (3.37 eV at 298 K), higher electronic mobility (115–155 $cm^2\ V^{-1}\ s^{-1}$) than TiO_2 ($>10^{-5}\ cm^2\ V^{-1}\ s^{-1}$), the ZnO nanomaterials are considered as an alternative materials to be used as efficient photo-electrode material for the fabrication of dye-sensitized solar cells [**221-229**].So far, several works have already been reported on the variety of ZnO nanostructured based DSSCs[**221-229**]. Baxter et al. manufactured the branch-structured ZnO nanowires thin film prepared by a MOCVD method to fabricate DSSCs which achieved the low conversion efficiency of ~0.5% [**230]**. Law et al. prepared ZnO nanowire arrays based photoanode for DSSCs and obtained 1.5% conversion efficiency [**231**].Al-Hajry presented the DSSC application of solution grown flower-shaped ZnO nanostructures reported in the literature [**232**].Suh et al. reported the DSSC applications of pillar and branched shaped ZnO nanowires grown on FTO substrates and obtained the conversion efficiency of ~0.46% from the branched ZnO nanowires [**233**].

This paper reports the successful synthesis and characterization of ZnO balls made of intermingled nanocrystalline NS and utilization of as-synthesized ZnO balls for DSSC applications. The grown nanosheets were characterized in terms of their morphological, structural, optical and compositional properties. The fabricated DSSC exhibited an overall light-to-electricity conversion efficiency of 2.1 %.

3.2.2. Experimental details

ZnO balls made by intermingled nanocrystalline NS were synthesized by facile low-temperature process by using zinc nitrate hexahydrate ($Zn(NO_3)_2.6H_2O$), hydroxylamine hydrochloride ($NH_2OH.HCl$) and sodium hydroxide (NaOH). All chemical used for the synthesis of ZnO balls were purchased from Sigma Aldrich and utilized as received without any further purification. In a typical synthesis process of ZnO balls, aqueous solutions of 0.1M zinc nitrate and 0.1M hydroxylamine hydrochloride was mixed under contineous stirrring for 30 min at room-temperature. After vigerous stirring, aqueous solution of 1M NaOH, made in 25 ml DI water, was added in the previous solution and the resultant solution was again stirred for 30 min. After vigerous stirring, extra few drops of NaOH was added to maintain the pH=11.0 of the resultant solution. Consequently, the resultant solution was then transferred to teflon lined autoclave which was then sealed and heated upto 110 ºC for 3 h. The possible chemical reaction for the synthesis of ZnO balls was as follows:

$$3Zn(NO_3)_2.6H_2O + NH_2OH.HCl + 6NaOH$$

$$\downarrow$$

$$3Zn(OH)_2 + 6NaNO_3 + NH_3 + HCl + H_2O + 5H_2O \qquad (3.2.1)$$

$$Zn(OH)_2 \rightarrow ZnO + H_2O \qquad (3.2.2)$$

After terminating the reaction, the autoclave was allowed to cool at room-temperature and the obtained products were washed with DI water and dried at 50 ºC.

The as-synthesized ZnO material was characterized in detail by using various techniques in terms of their morphological, structural, compositional, optical and photovoltaic properties. The morphological properties were investigated by using FESEM and TEM equipped with high-resolution TEM (HRTEM). The structural properties of the prepared material was examined by XRD in the range of 10-80°. The elemental and chemical compositions of the prepared ZnO materials were examined by using EDS, attached with FESEM and FTIR spectroscopy in the range of 450-4000 cm^{-1}, respectively. The optical properties of the prepared ZnO balls were examined by UV-visible spectroscopy and Raman-scattering measurements at room-temperature.

The fabrication and characterizations of dye-sensitized solar cell (DSSC) based on as-synthesized ZnO balls made by intermingled nanocrystalline NS was done according to the reported literature [**234**]. Photocurrent–Voltage (I–V) measurements was performed under AM 1.5G and one sun light intensity of 100 mW cm^{-2} (PV Measurements Inc.). The amount of the dye absorbed was measured by UV-Vis. Spectrophotometer.

3.2.3. Results and discussion

3.2.3.1. Detailed properties of ZnO balls made of intermingled nanocrystalline nanosheets

The as-synthesized ZnO materials were examined by FESEM to examine the general morphologies. Figure 3.2.1 (a) and (b) exhibit the typical low-magnification FESEM images of as-synthesized ZnO materials which reveal that the prepared material possess spherical ball-shaped and grown in large quantity.

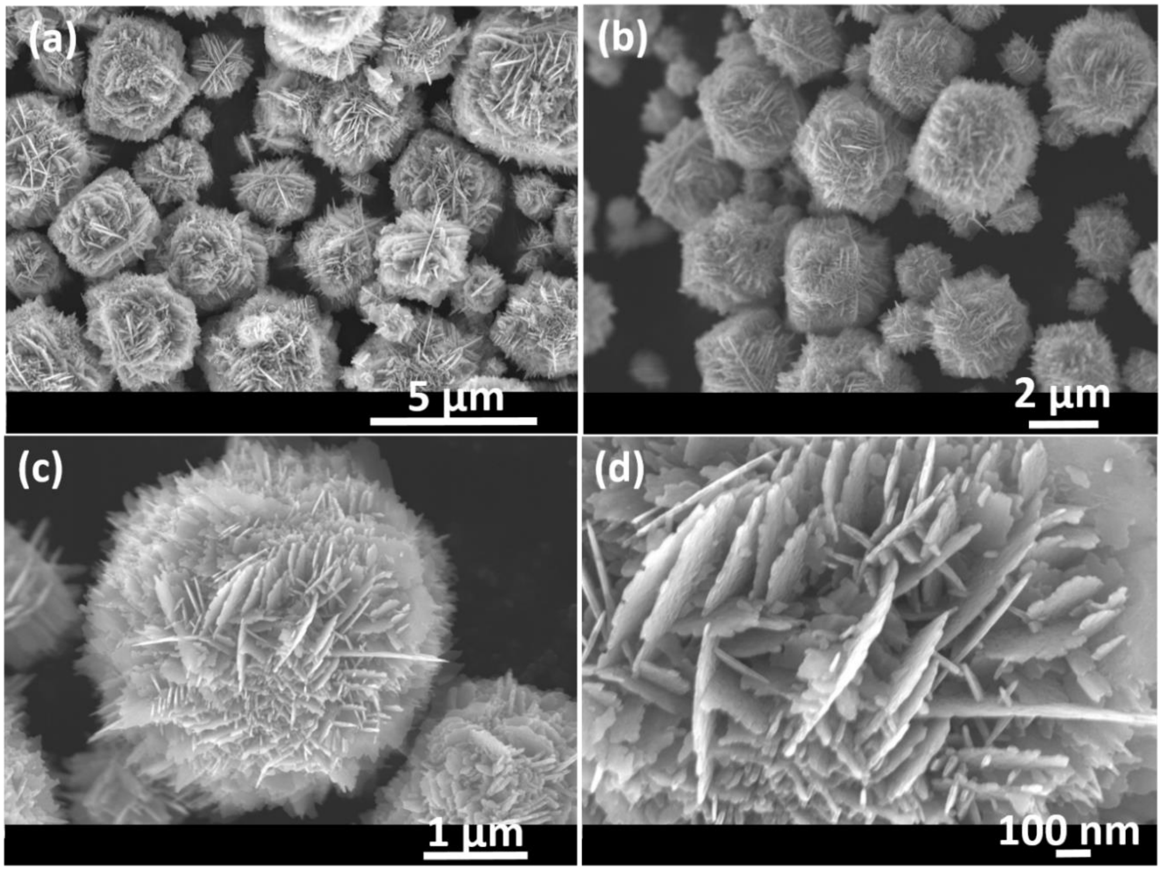

Figure 3.2.1. (a and b) Low-magnification and **(c and d)** high-resolution FESEM images of as-synthesized ZnO balls made of intermingled nanocrystalline nanosheets

Figure 3.2.1 (c) shows typical FESEM image of a single ZnO ball which confirmed that the synthesized balls are made by the accumulation of several thin 2D ZnO NS which are interconnected and intermingled with each other in such a manner that finally they made ball-shaped morphologies. The sizes of synthesized ZnO balls are not uniform and vary from 600 nm to 3 µm.

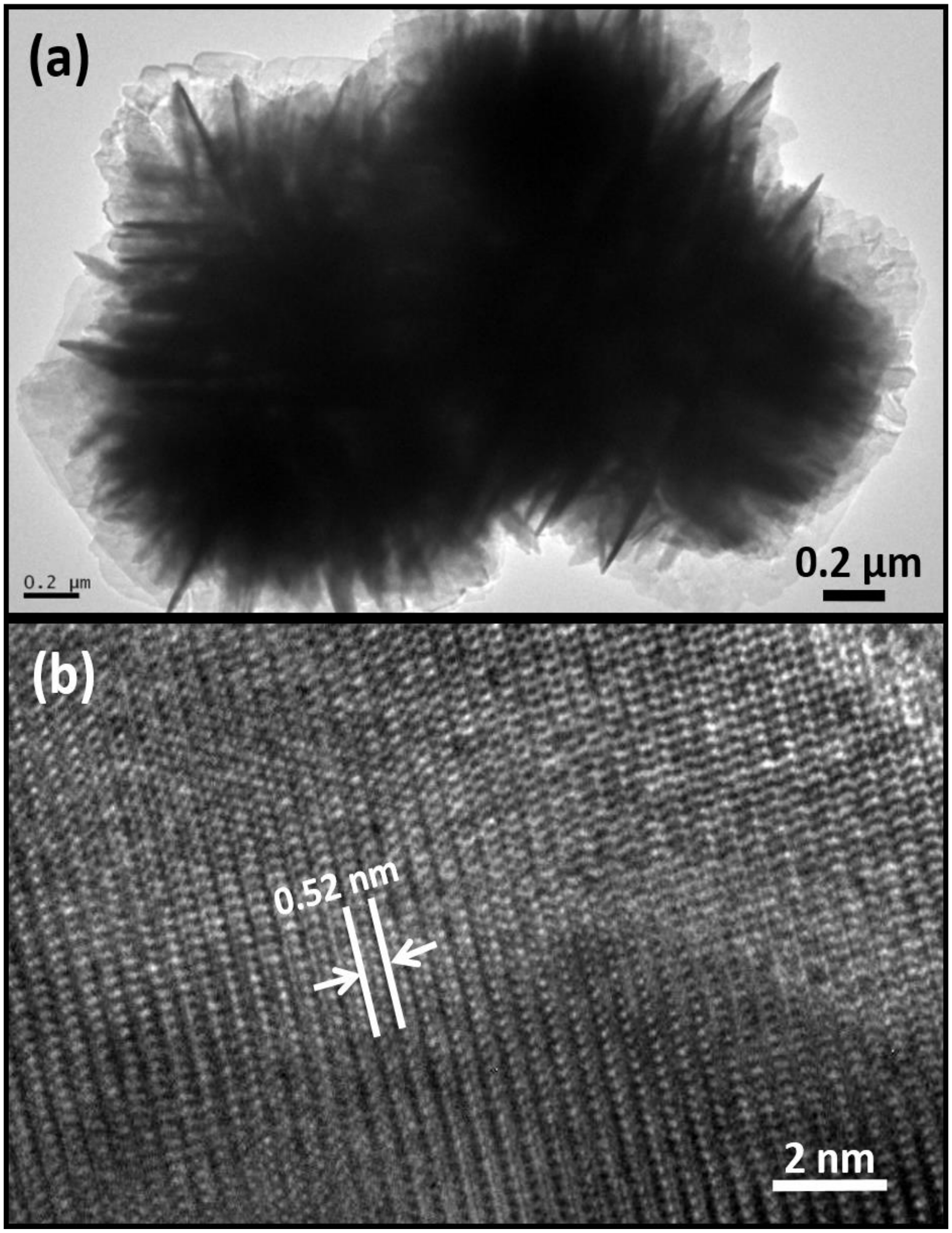

Figure 3.2.2. (a) Low-magnification and **(b)** high-resolution TEM images of as-synthesized ZnO balls made of intermingled nanocrystalline nanosheets

Interestingly, the NS do not possess smooth and clean surfaces and outer surfaces of the NS show rough boundaries (figure 3.2.1 (d)). The thicknesses of NS are in the range of ~ 35 ± 10 nm. The detailed morphological and structural properties of as-synthesized ZnO balls were examined by TEM and HRTEM analysis

Figure 3.2.2 (a) exhibits the typical TEM image of as-prepared ZnO balls which clearly shows that the synthesized ZnO balls are made of thin ZnO NS which are arranged in such a special manner that they made ball shaped morphologies. The TEM observations of the ZnO balls are well-consistent with the FESEM investigations in terms of its morphologies and dimensionalities. Figure 3.2.2 (b) demonstrates the typical HRTEM image of as-synthesized ZnO balls. Very well-defined lattice fringes are seen in the micrograph in which two lattice fringes along the longitudinal axis direction, corresponds to the *d*-spacing of ZnO (0002) crystal planes are separated with 0.52 nm. The well-defined lattice fringes and distance between two fringes confirmed that the synthesized structures are well-crystalline and possessing wurtzite hexagonal phase.

To examine the elemental composition, the as-synthesized ZnO balls were investigated by EDS attached with FESEM. Figure 3.2.3 (a) exhibits the typical EDS spectrum of as-synthesized ZnO balls. The EDS spectrum exhibits well-defined peaks for zinc and oxygen which revealed that the prepared materials are made of zinc and oxygen. Except Zn and O, no other peak related with any impurity was detected in the spectrum which further confirmed that the prepared materials are pure ZnO. To investigate the crystallinity and crystal phases, the as-synthesized ZnO balls were examined by XRD pattern.

The optical properties of the as-prepared ZnO balls were investigated by UV-Vis. spectroscopy. Figure 3.2.4 (a) exhibits the typical UV-Vis. spectrum of as-prepared ZnO balls. A well-defined excitonic absorption peak at ~367 nm, corresponding to 3.37 eV, was seen in the observed spectrum. The obtained spectrum is well-matched with the wurtzite hexagonal phase bulk and pure ZnO [**234**]. Except the well-defined absorption peak, no other band was observed in the spectrum which confirmed that the as-synthesized balls are pure ZnO and possessing good optical properties.

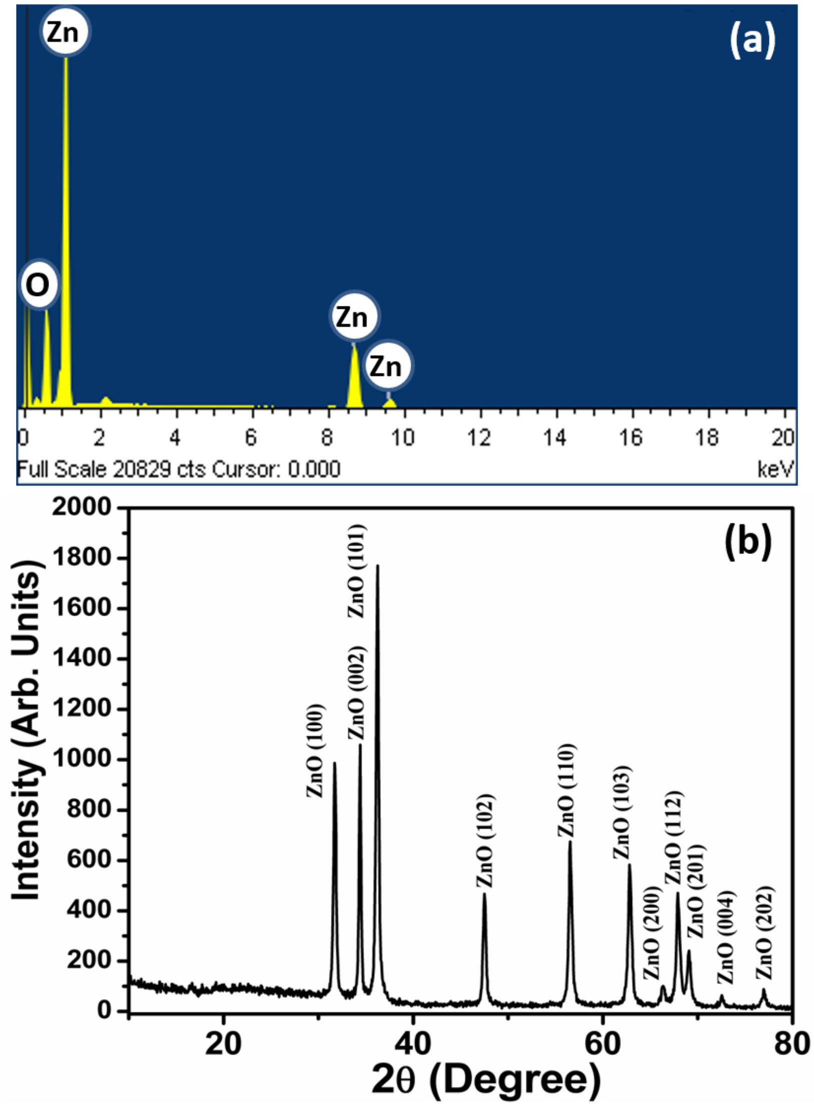

Figure 3.2.3. (a) Typical EDS spectrum and (b) XRD pattern ofas-synthesized ZnO balls made of intermingled nanocrystalline nanosheets.

To examine the chemical compositions, the as-synthesized ZnO balls were examined by FTIR spectroscopy in the range of 400-4000 cm^{-1}. Several well-defined bands were seen in the observed FTIR spectrum at ~531, 889, 1385, 1639 and 3421 cm^{-1}. The band appeared at ~531 cm^{-1} is related with the formation of metal-oxygen (Zn-O) bond [**235**]. The peaks appeared at 1385 cm^{-1} and 889 cm^{-1} are correlated to the presence of NO_3^- group[**236**]. The presence of two small bands appeared at ~1639 cm^{-1} and ~3421 cm^{-1}, are related with the O-H stretching and bending modes of vibrations, respectively. Therefore, the presence of well-defined Zn-O band in the FTIR spectrum confirmed that the prepared balls are pure ZnO without any significant impurity.

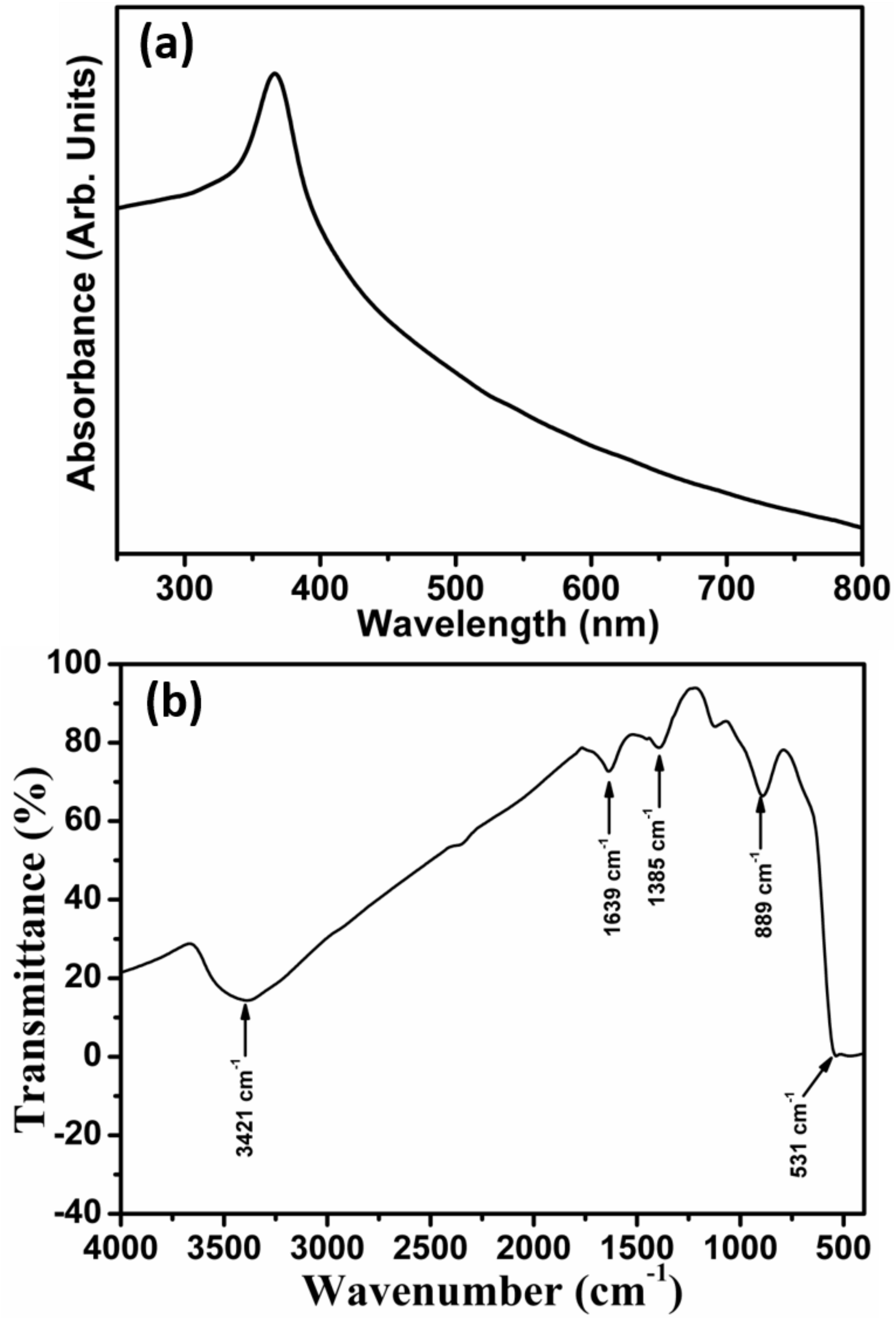

Figure 3.2.4. (a) Typical UV-Vis. spectrum and (b) FTIR spectrum ofas-synthesized ZnO balls made of intermingled nanocrystalline nanosheets

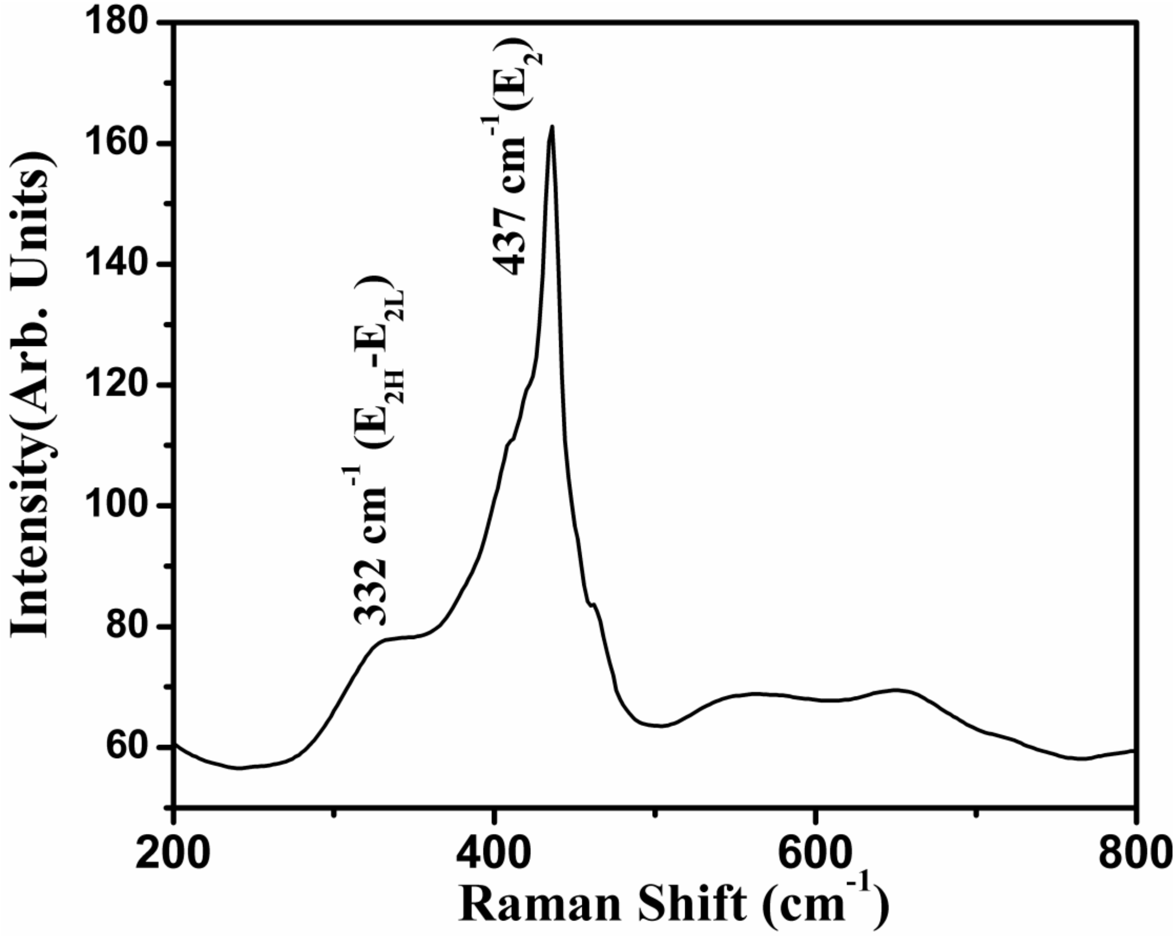

Figure 3.2.5. Typical Raman-scattering spectrum ofas-synthesized ZnO balls made of intermingled nanocrystalline nanosheets

To further investigate the crystallization, structural disorders and defects, the as-prepared ZnO balls were characterized by Raman-scattering spectroscopy. Figure 3.2.5 exhibits the typical Raman-scattering spectrum of as-synthesized ZnO balls made of intermingled nanocrystalline NS. The Raman-scattering spectrum exhibits a well-defined and sharp peak at 437 cm^{-1}, which can be assigned as optical phonon E_2 mode, a characteristic peak for the wurtzite hexagonal phase of ZnO [**197**]. In addition to the well-defined optical phonon E_2 mode, a small band at 332 cm^{-1} is also seen in the spectrum which can be assigned as $E_{2H} - E_{2L}$ (multi phonon) mode. Therefore, due to the presence of a sharp and strong optical phonon E_2 mode in the observed spectrum reveals that the as-synthesized balls are pure ZnO without any significant impurity.

3.2.3.2. Dye-sensitized solar cell application of as-synthesized ZnO balls made of intermingled nanocrystalline nanosheets

The thin film of as-synthesizedZnO balls made of intermingled nanocrystalline NS were used as photo-anode material for the fabrication of efficient dye-sensitized solar cell. For the fabrication of dye-sensitized solar cells, it is important to estimate the amount of dye absorption/desorption through the photo-anode materials.

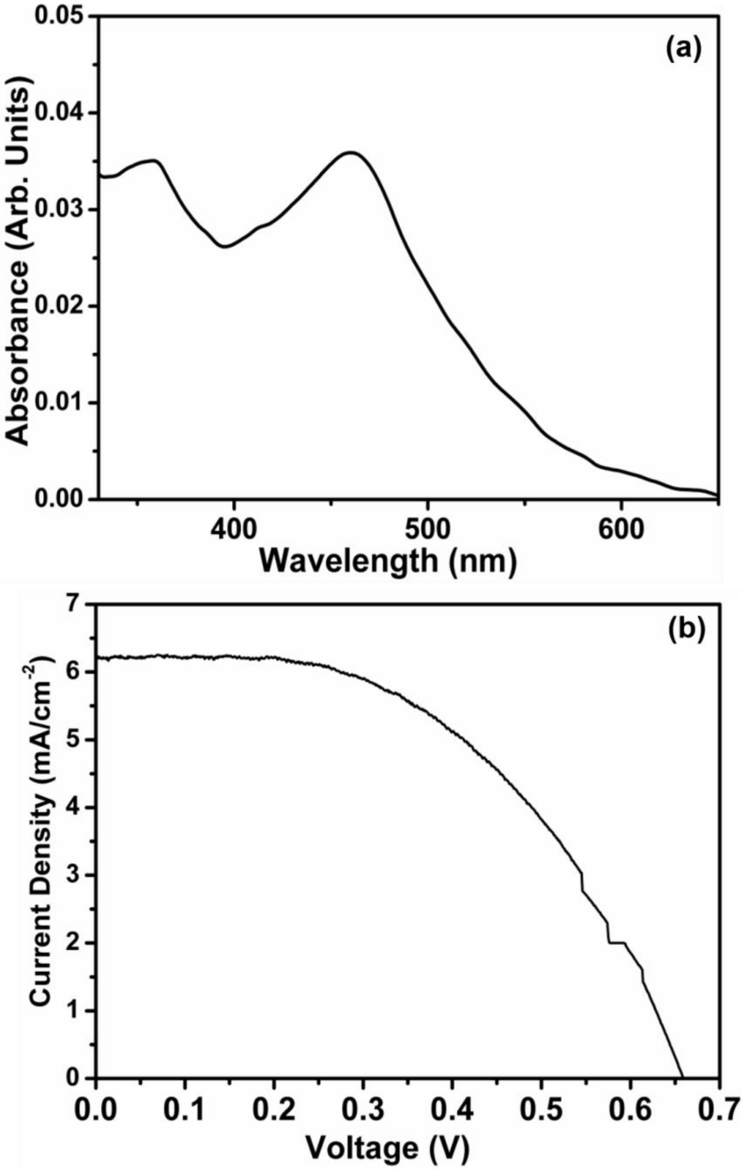

Figure 3.2.6. (a) Typical UV-Vis absorption spectra of the desorbed dye (N719) from the ZnO balls made of intermingled nanocrystalline nanosheets based electrode. **(b)** Typical current-voltage (*J-V*) characteristics of ZnO balls made of intermingled nanocrystalline nanosheets based DSSC.

Normally, it is considered that the amount of dye absorption by photo-anode material is directly related with the photocurrent density and conversion efficiencies of the fabricated dye-sensitized solar cells (DSSCs). Hence, high-dye absorption leads high light harvesting efficiencies and finally the high photocurrent density and conversion efficiencies for the fabricated DSSCs. To examine the desorption of dye, the dye-absorbed ZnO balls electrode was dipped into 0.1 mM NaOH solution for 5-10 minutes. The desorbed dye was examined by UV-Vis. spectrum and results are shown in figure 3.2.6 (a). The observed spectrum shows two absorption bands at particular wavelengths which are corresponding to typical UV-visible spectrum of N710 dye used for the fabrication of DSSCs. The estimated dye absorption for the fabricated DSSC was 2.8 x 10^{-7} mol/cm^2.The observed surface area of the ZnO balls made of intermingled nanocrystalline NS was ~12.74 m^2/g.

For the fabrication of DSSC based on ZnO balls made of intermingled nanocrystalline NS, briefly, the slurry of as-prepared ZnO material was coated on the fluorine-doped tin oxide (FTO) glass substrates, dried at room-temperature and calcined at 450 °C for 1h. The prepared electrode was immersed in 0.3 M ethanolic solution of *cis*–bis (isothiocyanato) bis (2, 20-bipyridyl- 4, 40- dicarboxylato) - ruthenium (II) bis-tetrabutyl ammonium dye (N719) for 5 hrs at room-temperature. After rinsing with ethanol, the dye-absorbed ZnO balls based electrode was attached with Pt counter electrode, prepared on FTO glass substrate, and edges were sealed using thick sealing sheet. The liquid electrolyte was used for the fabrication of solar cells which was introduced into the cell through one of two small holes drilled in the counter electrode. The active layer of the resulting cell was approximately 0.25 cm^2 (0.5 cm x 0.5 cm). The photocurrent density – voltage (*J*–*V*) curve was measured using computerized digital multi-meters.

Figure 3.2.6 (b) exhibits the typical *J*-*V* characteristics of the fabricated DSSC. The *J*-*V* characteristics of the fabricated DSSC were measured under a simulated illumination with the light intensity of 100 mW/cm^2 (AM 1.5G). The *J*-*V* curve provides the typical information for the fabricated DSSC such as the short circuit current (J_{SC}), open circuit voltage (V_{OC}), fill factor (*FF*), overall conversion efficiency, and so on. According to the observed *J*-*V* curve, the calculated short circuit current (J_{SC}) and open circuit voltage (V_{OC}) are to be 6.28 mA/cm^2 and0.659 V, respectively. The fill factor of the fabricated DSSC was estimated using the following equation:

$$FF = \frac{J_{\max}V_{\max}}{J_{SC}V_{OC}} \qquad (3.2.3)$$

Where $J_{max}$and $V_{max}$are the voltage and current density, respectively at maximum power output; J_{SC} is short circuit current and V_{OC} is an open circuit voltage.

According to the mentioned above equation, the calculated *FF* for the fabricated DSSC based on ZnO balls made of intermingled nanocrystalline NS was 0.51. It is reported that the value of *FF* can be increased by reducing the recombination between the photoexcited carriers at the nanostructured electrode and the tri-iodide ions in the electrolyte [**237**].

Further, the photovoltaic conversion efficiency (η) of the fabricated DSSC based on ZnO balls made of intermingled nanocrystalline NS was also estimated from the obtained *J-V* curve. The conversion efficiency (η) was calculated according to the equation mentioned below:

$$\eta = \frac{J_{SC}V_{OC}FF}{P_{in}} \qquad (3.2.4)$$

Where P_{in} is the power density of incident radiation.

According to the mentioned above equation, the calculated overall light-to-electricity conversion efficiency of the fabricated DSSC was 2.1 %. The high light-to-electricity conversion efficiency of the fabricated DSSC based on ZnO balls is due to special morphologies of the synthesized ZnO balls which possess high surface area ZnO NS and porous morphologies. Hence, the high surface area and porous morphologies lead higher dye absorption capabilities and therefore direct to high conversion efficiencies for the fabricated DSSC.

The incident photon-to-current conversion efficiency (IPCE) has been performed to investigate the photocurrent density of fabricated DSSC based on ZnO balls made of intermingled nanocrystalline NS photo-anode. The IPCE provides the ratio between the number of generated charge carriers contributing to the photocurrent and the number of incident photons. The IPCE at a particular wavelength can be calculated by the equation mentioned below [**238**].

$$IPCE(\%) = \frac{1240(eV.nm) \times J_{SC}(\frac{\mu A}{cm^2})}{\lambda(nm) \times \phi(\frac{mW}{cm^2})} \times 100 \qquad (3.2.5)$$

where J_{SC} is the short-circuit photocurrent density for mono-chromatic incident light and λ and P_{in} are the wavelength and the intensity of the monochromatic light, respectively. Figure

3.2.7 shows the IPCE plot for the fabricated DSSC based on balls made of intermingled nanocrystalline NS photo-anode. A reasonable IPCE of ∼17.8 % was obtained in the broad absorption range of 400–650 nm. The occurrence of reasonable IPCE is related to the relatively good dye absorption through the surface of the ZnO balls made of intermingled nanocrystalline NS based photoanode. The obtained IPCE result is well consistent with the *J*-*V* results of the fabricated DSSC based on ZnO balls made of intermingled nanocrystalline NS based photoanode [**239**]. The IPCE results clearly confirmed that the utilized photoanode material, i.e. ZnO balls, present excellent platform for the efficient dye absorption which results the high photon to current conversion efficiencies for the fabricated DSSC.

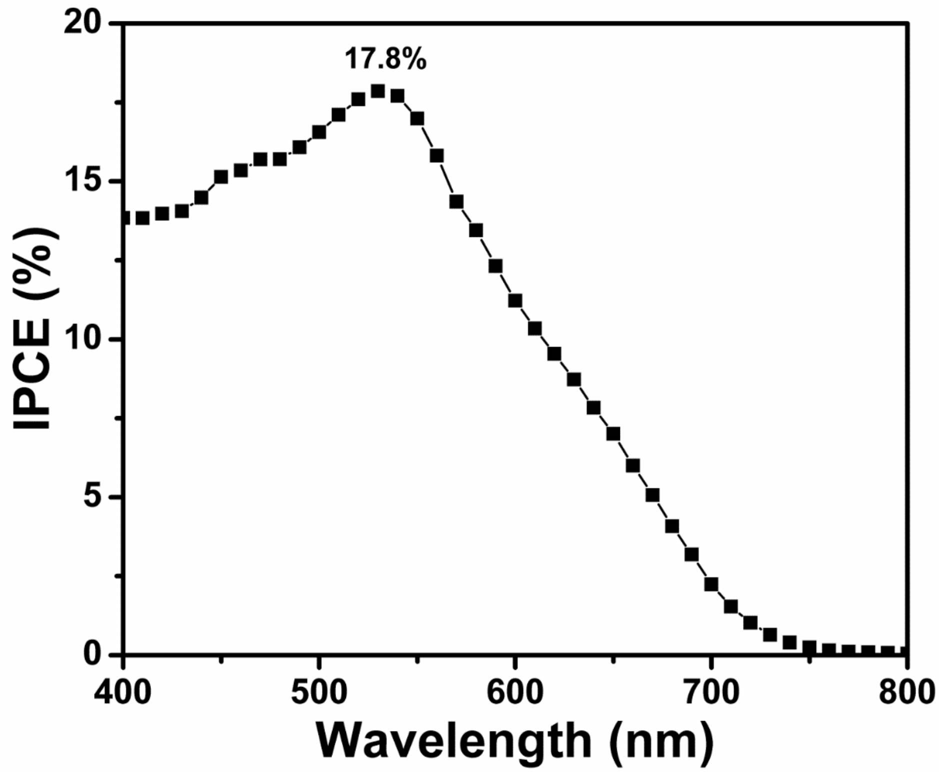

Figure 3.2.7. Typical incident photon-to-current conversion efficiency (IPCE) characteristics of ZnO balls made of intermingled nanocrystalline nanosheets based electrode.

3.4. Conclusion

In summary, ZnO balls made of intermingled nanocrystalline NS were synthesized by facile hydrothermal process and characterized in detail using various analytical tools in terms of their morphological, structural, optical, compositional and photovoltaic properties. The detailed studies confirmed that the prepared ZnO balls are pure and possess well-crystalline wurtzite hexagonal phase and exhibiting good optical properties. Furthermore, the prepared ZnO balls were used as photo-anode materials to fabricate DSSCs which exhibited an overall light-to-electricity conversion efficiency of 2.1 % with a short-circuit current of 6.28 mA/cm^2, open-circuit voltage of 0.659 V and fill factor of 0.51.

Section 3.3: Growth and properties of Ag-doped ZnO nanoflowers for highly sensitive phenyl hydrazine chemical sensor application

This section reports the fabrication of a robust, highly sensitive, reliable and reproducible phenyl hydrazine chemical sensor using Ag-doped ZnO nanoflowers as efficient electron mediators. The Ag-doped ZnO nanoflowers were synthesized by facile hydrothermal process at low-temperature and characterized in detail in terms of their morphological, structural, compositional and optical properties. The detailed morphological and structural characterizations revealed that the synthesized nanostructures were flower-shaped, grown in very high-density, and possessed well-crystalline structure. The chemical composition confirmed the presence of Ag into the lattices of Ag-doped ZnO nanoflowers. High sensitivity of ~557.108 ± 0.012 $\mu A.cm^{-2}.mM^{-1}$and experimental detection limit of ~10 nM with correlation coefficient (R) of 0.97712 were observed for the fabricated chemical sensor towards the detection of phenyl hydrazine by using a simple current-voltage (I-V) technique. Due to high sensitivity and low-experimental detection limit, it can be concluded that Ag-doped ZnO nanoflowers could be an effective candidate for the fabrication of phenyl hydrazine chemical sensors.

3.3.1. Introduction

Environmental pollution caused by various means such as automobiles, agricultural run offs and industrial leakages of toxic chemicals and gases at very alarming rate pose a direct threat to human beings and animals by accumulation, entrapment, and suffocation inside their body [**240-245]**. The leakage of such toxic chemicals contaminates the environment and shows adverse effects to human beings, animals and other living organisms. Among various toxic chemicals, the phenyl hydrazine is one of the most emerging environmental pollutants used in the preparation of pesticides, pharmaceutical, photography chemicals and aerospace fuel. Thus, release of phenyl hydrazine in the environment may cause a severe damage to ecosystem [**242-245**]. The exposure of this chemical, even at lower concentration, may cause adverse effect to the human body such as skin irritation, dermatitis, hemolytic anemia, liver and kidney injury. In addition to this, phenyl hydrazine is also considered as a carcinogen and thus it is necessary to detect phenyl hydrazine in an effective manner to prevent its side effects towards human and other living organism [**240-245**]. There are few reports regarding the determination of phenyl hydrazine through electrochemical techniques where different types of redox mediators were utilized to reduce the high over potential problems in phenyl hydrazine [**240-245**]. However, these methods lack high sensitivity, good stability and reproducibility. Therefore, a reliable and robust approach for the determination of phenyl hydrazine is still in demand.

Recently, the nanomaterials are utilized as efficient electron mediators for the fabrication of high sensitive chemical and biosensors. Among various nanostructured materials, ZnO, a II-VI semiconductor material, presents itself as one of the most important functional material with numerous remarkable properties favorable for fabrication of various electronic, optoelectronic, sensors and other nanodevices [**240**]. The properties which are responsible to make ZnO a multifunctional material are the wide band gap (~3.37 eV), high exciton binding energy (60 meV), biocompatibility, high electron feature and good electrochemical properties, simple and cost effective synthesis, non-toxicity, optical transparency, and so forth [**168,169,171,172,246-255**].

It is observed that the properties of ZnO nanostructures can be tailored for desired applications through doping, coating and surface modification [**172,246-253**]. Therefore, thus far, several metals such as Ga [**256**], Mn [**257**], In [**258**], Mg [**259**], Al[**260**], Sb [**261**], Sn [**262**], Ag [**263-265**], etc have been utilized to dope the ZnO nanostructures for specific applications and reported in the literature.

Among various metals doped in ZnO nanostructures, the Ag has attracted particular interest due to its various properties. The doping of noble metal (Ag) into semiconductors (ZnO) enhances the optical properties of the resulting nanomaterials [**263-265**]. Therefore, it was found that the light absorption ability of Ag-doped ZnO thin films was enhanced [**266**]. In another report, an improved gas sensing property was observed by Ag-doped ZnO nanostructures [**265,-267**]. Even though Ag-doped ZnOpossesses excellent properties and have been used in variety of applications, but, to the best of our knowledge, the use of Ag-doped ZnOnanostructures as efficient electron mediator for the fabrication of phenyl hydrazine chemical sensor is not reported yet in the literature.

This research focuses on the fabrication of a phenyl hydrazine chemical sensor based on Ag-doped ZnOnanoflowers. The fabricated chemical sensor showed very high sensitivity and low experimental detection limit. This work offers few important advantages such as facile synthesis of Ag-doped ZnOnanoflowers, simple electrode modification and rapid detection of phenyl hydrazine using the simple current-voltage (I-V) technique.

3.3.2. Experimental Details

3.3.2.1. Synthesis of Ag-doped ZnO nanoflowers

Ag-doped ZnO nanoflowers were synthesized by simple hydrothermal process using zinc nitrate hexahydrate ($Zn(NO_3)_2.6H_2O$), silver nitrate ($AgNO_3$) and ammonium hydroxide (NH_4OH) at low-temperature. All the chemicals utilized for the synthesis of Ag-doped ZnO nanoflowers were purchased from Sigma-Aldrich and used as received. To synthesize the Ag-doped ZnO nanoflowers, aqueous solutions of 0.01mol L^{-1}zinc nitrate and 0.001 mol L^{-1} $AgNO_3$, were mixed under contineous stirrring for 45 min at room-temperature. The pH of the solution was maitained to 9.5 by adding few drops of ammonium hydroxide. The final solution was vigorously stirred for 30 min and consequently transferred to teflon lined autoclave which was then sealed and heated upto 150 ºC for 5 h. After terminating the reaction, the autoclave was allowed to cool at room-temperature and the obtained products were washed several times with DI water and ethanol, sequentially and dried at 45 ºC. The as-synthesized products were investigated in terms of their morphological, structural, optical and sensing properties.

3.3.2.2. Characterization of Ag-doped ZnO nanoflowers

The as-synthesized Ag-doped ZnO nanoflowers were characterized in details using various analytical techniques. FESEM was used to investigate the general morphologies of as-synthesized nanoflowers. The crystallinity and crystal phases of the as-synthesized nanoflowers were examined by XRD; PANanalytical Xpert Pro.) with Cu-Kα radiation (λ=1.54178 Å) in the range of 10-80°. The chemical composition was examined by using EDS, attached with FESEM and FTIR spectroscopy in the range of 450-4000 cm^{-1}. UV-visible spectroscopy was done at room-temperature to determine the optical properties of as-synthesized ZnO nanoflowers.

3.3.2.3. Fabrication and characterization of phenyl hydrazine chemical sensor by using current-voltage (I-V) technique

For the fabrication of phenyl hydrazine sensor, the as-synthesized Ag-doped ZnO nanoflowers were coated on glassy carbon electrode (GCE, surface area 0.0316 cm^2). Before coating, the GC electrode surface was polished with alumina-water slurry on a polishing cloth, followed by thorough rinsing with distilled water. For the electrode surface modification, slurry was made by adding an appropriate composition of Ag-doped ZnO nanoflowers and binder (butyl carbitol acetate). Finally, a certain amount of the slurry was casted on GCE carefully and dried at 60 ± 5 ºC for 4-6 h to get a uniform and dry layer over active electrode surface. A simple two electrode system (an electrometer; Keithley, 6517A, USA) was used to evaluate the sensing performance in which the modified electrode was used as working electrode and Pt wire as counter electrode. The current response was measured from 0.0 to + 2.0 V while the time delaying were 1.0 second. The concentration and volume of PBS were kept constant to 0.1 mol $L^{-1}$and 10.0 mL, respectively. A wide concentration range of phenyl hydrazine (1 mol $L^{-1}$to 10^{-8} mol L^{-1}) was used to check the sensing performance of fabricated phenyl hydrazine chemical sensor.

3.3.3. Results and Discussion

3.3.3.1. Morphological, structural and optical properties of as-synthesized Ag-doped ZnO nanoflowers

The general morphologies of as-synthesized Ag-doped ZnO nanomaterials were investigated by using FESEM and results are shown in Figs. 3.3.1 (a)-(c). Figure 3.3.1 (a) exhibits the typical low-magnification FESEM image, which confirms that the as-synthesized nanomaterials are flower shaped and grown in very high density. The as-synthesized nanoflowers are made up of several triangular –shaped petals and possess sharp tips and wider bases. These wider bases are connected with each other in such a special fashion that they make beautiful flower-like morphologies. The typical diameters at the tips and bases of petals are ~70 ± 20 nm and 200 ± 50 nm, respectively. The lengths of petals are in the range of 400-450 nm. The typical dimension of a single flower is ~400 ± 50 nm.

To examine the structural properties and crystal phase identifications, powder XRD in the range of 10 - 80° with 2°/min scanning speed. The observed XRD pattern exhibits well crystalline nature and mixed phases of Ag and ZnO for as-synthesized nanoflowers (Fig. 3.3.1

(d)). Several well-defined diffraction reflections related with ZnO were observed in the obtained pattern. The observed diffraction reflections for ZnO (100), (002), (101), (102), (103), (200), (112), (201), (004) and (202) are similar to bulk ZnO and corresponding to wurtzite hexagonal phase of ZnO.

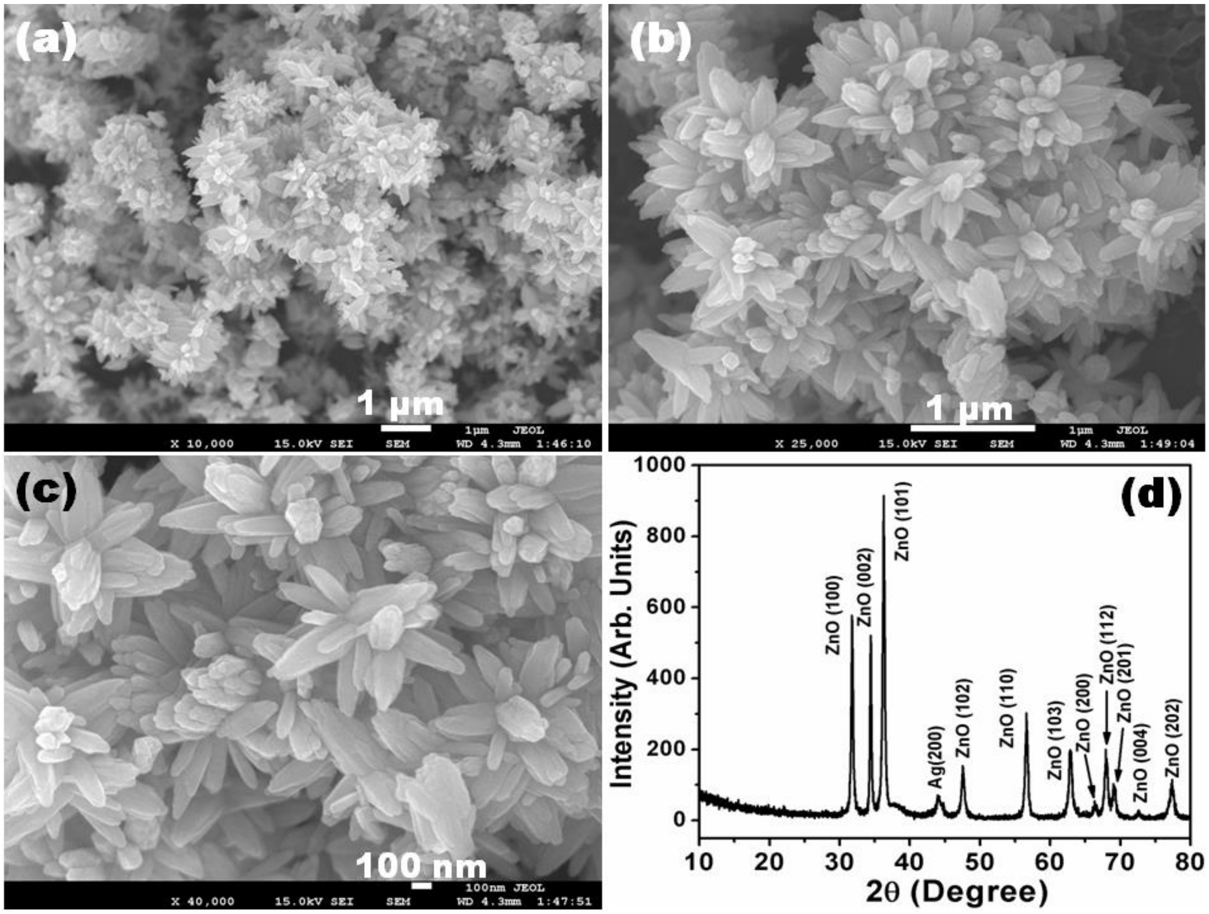

Figure 3.3.1. Low magnification ((a) and (b)) and high-resolution (c) FESEM images and (d) XRDpattern of as-synthesized Ag-doped ZnO nanoflowers

The obtained results are in good agreement with standard JCPDS data card No 36-1451. In addition to the ZnO reflections, a small peak corresponding to Ag (200) is also appeared at 44.04°. Except ZnO and Ag, no other reflections related to impurities such as Zn and Ag_2O were found in the pattern.

To check the composition and purity of the as-synthesized Ag-doped ZnO nanoflowers, the nanoflowers were investigated by using EDS and elemental mapping, both attached with FESEM, and shown in Figs. 3.3.2 and 3.3.3, respectively.

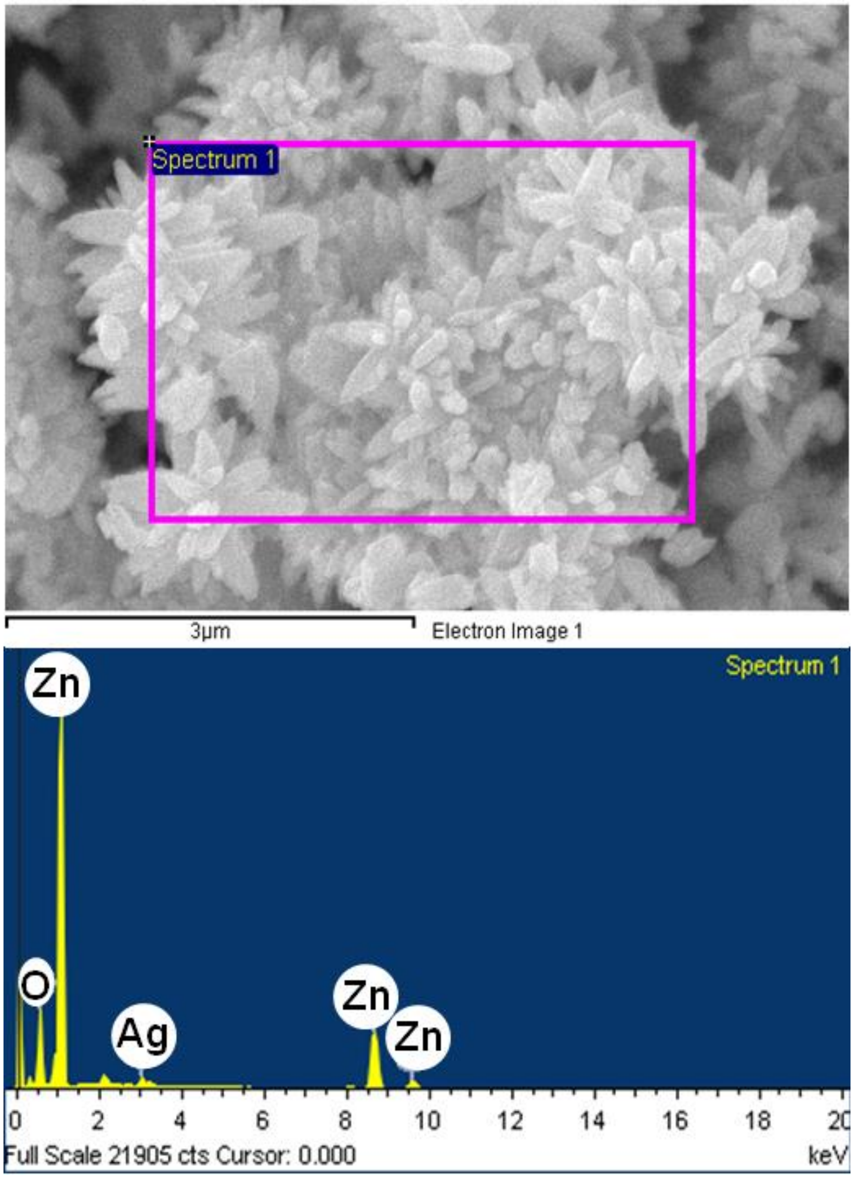

Figure 3.3.2. Typical (a) FESEM image and (b) its corresponding EDS spectrum of as-synthesizedAg-doped ZnO nanoflowers

Figure 3.3.2 (a) exhibits the typical FESEM image of as-synthesized Ag-doped ZnO nanoflowers and confirmed that the nanoflowers are grown in very high density. To investigate the composition, a selected area of EDS spectrum from Fig. 3.3.2 (a) has been taken and result is demonstrated in Fig. 3.3.2 (b). The EDS spectrum shows various well-defined peaks of Zn, O, and Ag. No peak related to any other impurity was detected in the spectrum. This clearly shows that the synthesized nanoflowers are Ag-doped ZnO.

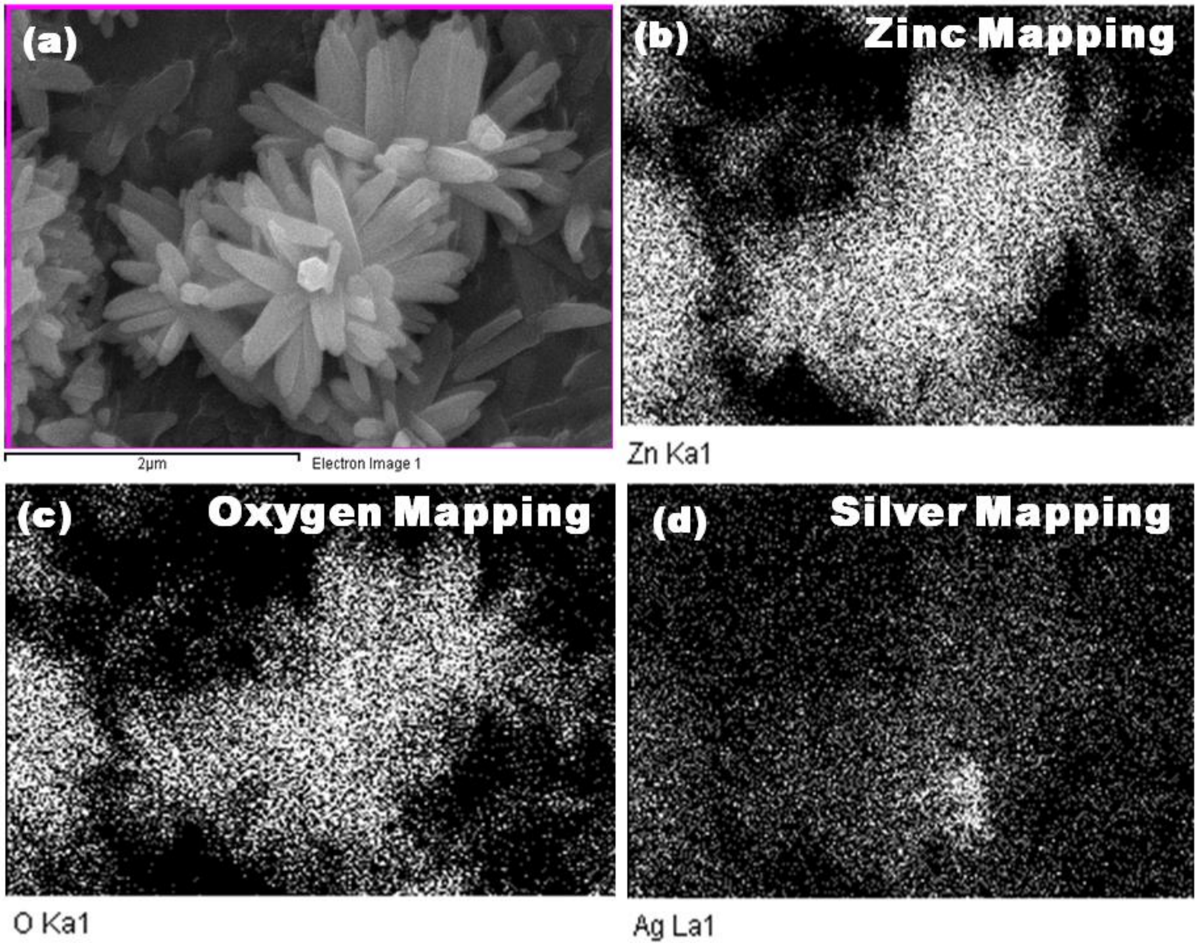

Figure 3.3.3. Typical (a) FESEM image and its corresponding elemental mapping images for (b) zinc, (c) oxygen and (d) silver of as-synthesized Ag-doped ZnO nanoflowers

It is important to examine the distribution of different ions such as Zn, O and Ag into the lattices of as-synthesized nanoflowers in order to confirm that the substituted metal is distributed homogeneously over the whole crystal. Figure 3.3.3 (a) exhibits the typical FESEM image of as-synthesized Ag-doped ZnO nanoflowers while the Figs. 3.3.3 (b)-(d) depict the corresponding elemental mapping (elemental distribution along the whole crystal) for Zn, O and Ag. It is evident from Figs. 3.3.3 (b)-(d) that the number of spots corresponding to Zn and

O are higher in density and the homogenous distribution of Zn and O is evident (Figs. 3.3.3 (b) and 3.3.3(c)). The smaller number of spots for Ag as compared to those for Zn and O are due to the less amount of Ag metal doping into the lattices of as-synthesized nanoflowers (Fig. 3.3.3(d)). Thus, the elemental mapping further confirmed that the synthesized nanoflowers are Ag-doped ZnO.

The quality and chemical composition of as-synthesized Ag-doped ZnO nanoflowers were investigated by FTIR spectroscopyat room-temperature in the range of 450-4000 cm^{-1} and demonstrated in Fig. 3.3.4. Several absorption peaks at 481, 891, 1382, 1623 and 3425 cm^{-1} were observed in the obtained FTIR spectrum. The absorption peak appeared at about 481 cm^{-1} is related to a typical FTIR absorption peak of ZnO which originates from stretching mode of the Zn–O bond [**33-35**]. Two very small peaks originated at ~891 cm^{-1} and ~1382 cm^{-1} are probably due to the nitrate (NO_3^-) group [**270,271**]. Appearance of another small absorption peak at 1623cm^{-1} could be ascribed to the bending vibration of absorbed water and surface hydroxyl [**177**]. Furthermore, a well-defined absorption peak appeared at 3425 cm^{-1} is related to the O-H stretching mode [**177**]. Except above mentioned absorption bands, no other distinguished peak related to any other functional group is detected in the FTIR spectrum which clearly reflects that the synthesized product is without any significant impurity.

UV-Vis spectroscopy was performed to examine the optical property of as-synthesized Ag-doped ZnO nanoflowers at room-temperature and result is reported in Fig. 3.3.5. The as-synthesized Ag-doped ZnO nanoflowers exhibits a single and well-defined absorption band at 377 nm, which is the characteristic band for the wurtzite hexagonal structure of ZnO [**176**]. The obtained UV-Vis spectrum for Ag-doped ZnO nanoflowers does not show any significant change in the absorption spectrum due to the doping of Ag into ZnO lattices. The observed results are almost similar with the already reported literature [**272**].

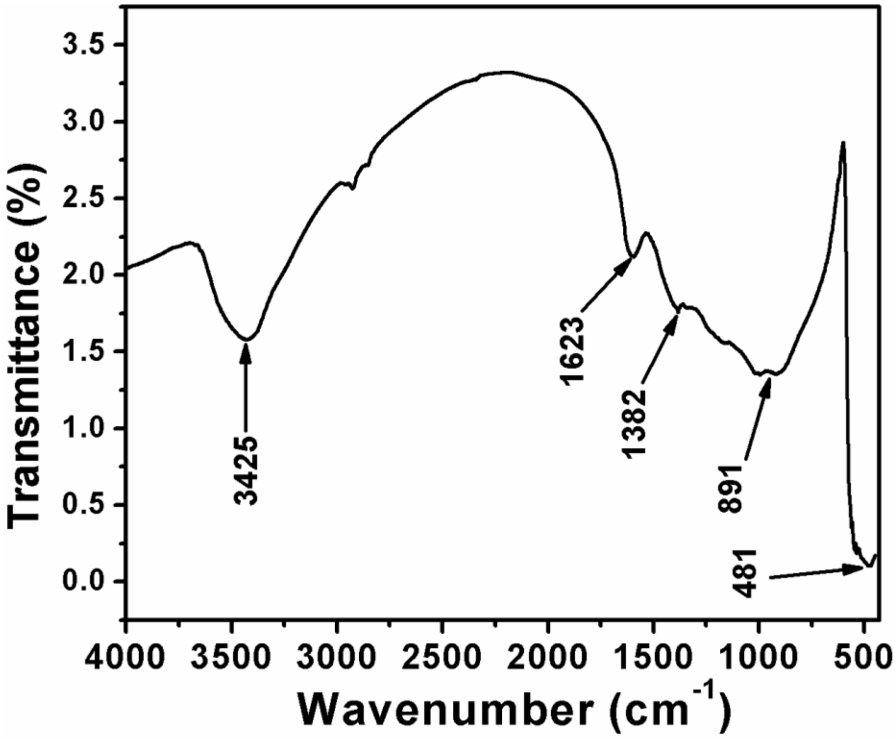

Figure 3.3.4. FTIR spectrum of as-synthesized Ag-doped ZnO nanoflowers

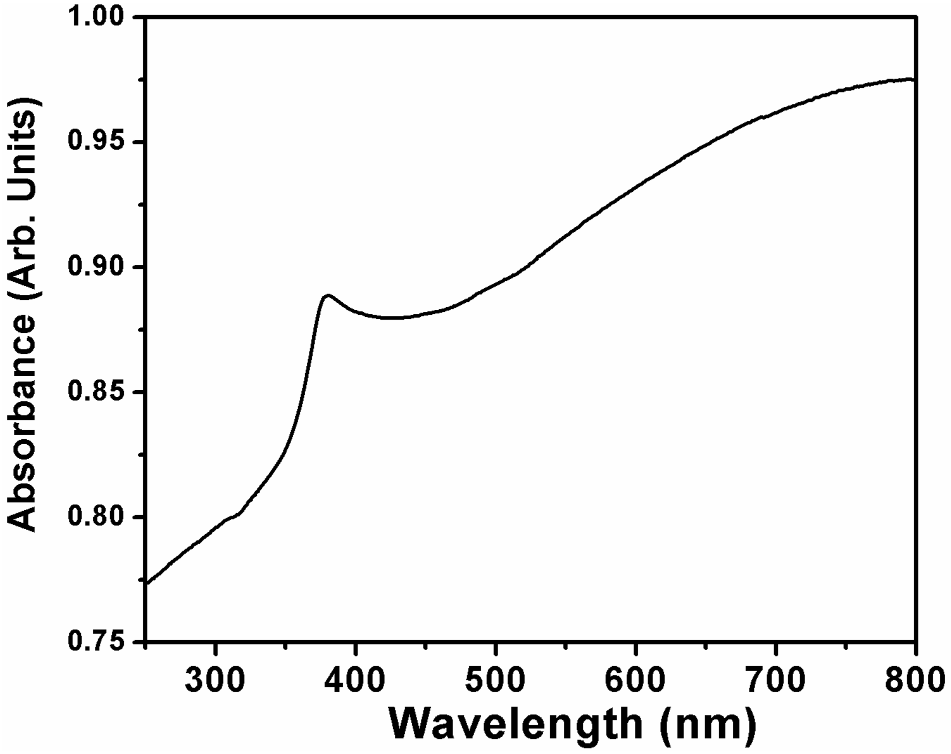

Figure 3.3.5. UV-Vis. spectrum of as-synthesized Ag-doped ZnO nanoflowers

3.3.3.2. Phenyl hydrazine chemical sensor application of as-synthesized Ag-doped ZnO nanoflowers

The methodology for the detection of phenyl hydrazine using the typical current-voltage (I-V) technique has been extensively described in the experimental detail section. In short, slurry of as-grown Ag-doped ZnO mixed with certain amount of binder was casted on GC electrode and dried. In two electrode I-V system, the modified GCE was used as working electrode while Pt wire was employed as a counter electrode. The current response was measured from 0.0 to + 2.0 V and the time delaying were 1.0 second.

The schematic for the fabrication of Ag-doped ZnO nanoflowers based phenyl hydrazine chemical sensor and its mechanism has been illustrated in Fig. 3.3.6. The proposed Ag-doped ZnO nanoflowers modified sensor was applied to detect phenyl hydrazine in liquid phase. The detection of phenyl hydrazine with this modified sensor is typically attributed to the oxidation and reduction properties of metal oxides nanostructures (Ag-doped ZnO in the present case). The oxygen is very essential part of the sensing mechanism and the adsorption of the oxygen at nanomaterial surface depends on the structural properties of doped material. Firstly, the oxygen is adsorbed chemically at liquid surface boundary while the physiosorption of oxygen monolayer takes place at Ag-doped ZnO nanomaterial surface from the bulk solution. The number of defects in the Ag-doped ZnO nanomaterial surface, due to doped metal, enhanced the oxygen adsorption. It is also known that oxidizing behavior of nanomaterial is increased due to increase in the amount of adsorbed oxygen. The oxygen which takes part in the detection procedure is subsequently converted into dynamic oxygen species i.e. O_2^- and O^- depending on the available energy bands after extracting the electrons from Ag-doped ZnO nanoflowers surface. These procedures occur according to following reactions (3.3.1) and (3.3.2).

$$\mathbf{2O_{2(g)} \longrightarrow 2O_{2\,(ads)}} \qquad \textbf{(3.3.1)}$$

$$\mathbf{O_{2(ads)} + 2e^- \text{ (Ag-doped ZnO)} \longrightarrow 2O^-_{(ads)}\ (O^- / O_2^-)} \qquad \textbf{(3.3.2)}$$

The emission of the electrons from according to reaction (3.3.2) decreases the conductance properties and increases the resistance of Ag-doped ZnO nanoflowers, thus, creating the holes for conduction that play pivotal role in phenyl hydrazine sensing. Due to the decrease in conductance, the value of current is reduced. In second step, the phenyl hydrazine is oxidized to diazenyl benzene in the presence of dynamic oxygen species and emits two free electrons simultaneously as shown in reaction (3.3.3).

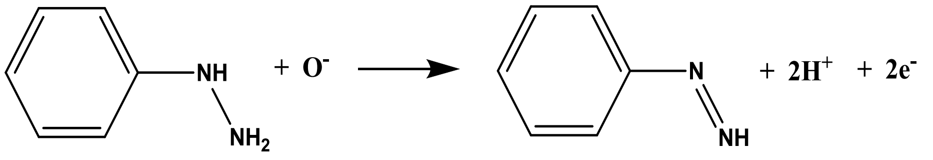

(3.3.3)

Phenyl hydrazine **Diazenyl benzene**

According to reaction (3.3.3), the oxygen ions are consumed and the doped nanoflowers surface captures the released electrons, consequently the conducting behavior of doped nanomaterial surface is amplified [**273**].

The current responses of the sensor with and without coating of Ag-doped ZnO nanoflowers material over GCE are shown in Fig. 3.3.7. The lower current value was observed with nanomaterial modified GCE compared to non-modified (no coating) GCE in 0.1 mol L^{-1}PBS buffer. The decrease in current response may be due to the increase in the surface resistance of modified electrode surface. To observe the sensor behavior in different concentration of phenyl hydrazine solutions, the I-V signals were measured. This is clear from Fig. 3.3.8 (a) that the values of current increases substantially from lower to higher concentrations (10^{-8} mol L^{-1} to 1 mol L^{-1}) of phenyl hydrazine. The reason of observed current behavior lies in the fact that the ionic strength of the solution was increased by increasing the phenyl hydrazine concentration, thus producing more number of ions.

The sensitivity of the fabricated phenyl hydrazine chemical sensor was acquired by slope of the current-concentration calibration profile. The sensitivity was obtained when the slope was divided by the active surface area of electrode according to the equation**:** "Sensitivity=Slope/Surface area of electrode" (surface area of GCE is 0.0316 cm2). The calibration curve was plotted by taking average of currents over a range of potentials spanning from 0.5- 1.1 V. The calibration data was fitted well linearly at smaller scale concentration range (10 nM – 1 mM), from which the slope was calculated. The calibration (sensitivity) curve of the fabricated sensor is shown in Fig. 3.3.8 (b).

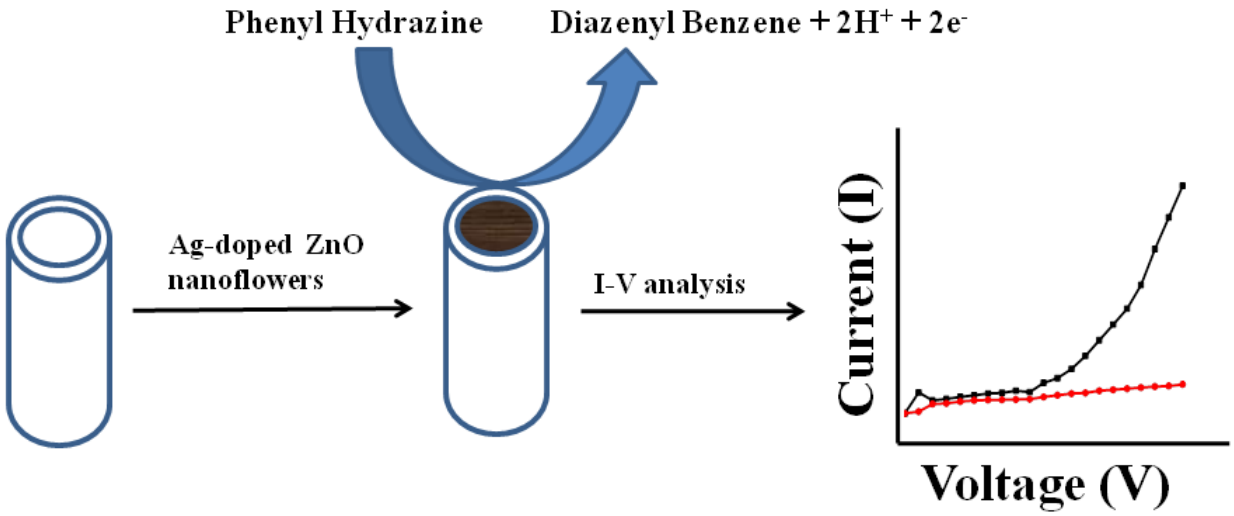

Figure 3.3.6. Schematic representation of Phenyl Hydrazine chemical sensor fabrication based on Ag-doped ZnO nanoflowers coated GCE electrode and its sensing mechanism by simple and facile I-V technique

According to the calibration curve, the calculated sensitivity of the fabricated phenyl hydrazine chemical sensor was found to be ~~557.108 ± 0.012 µA.cm^{-2}.mM^{-1}. The observed sensitivity of the fabricated chemi-sensor is higher than the fabricated phenyl hydrazine sensor based on modified carbon paste electrode [**241**]. The experimental detection limit of the fabricated phenyl hydrazine sensor was determined to be ~10 nM which is lower than previously fabricated phenyl hydrazine chemical sensors based on modified carbon paste electrode [**241**], lectin glycoenzyme multilayer film modified sensor [**243**], horseradish peroxidase (HRP) inhibition biosensor for determination of phenyl hydrazine [**244**]and ferrocene-carbon nanotubes modified carbon paste electrode [**245**]. The correlation coefficient (R) of the fabricated chemical sensor was found to be ~0.97712 and the current exhibited the linearity in the range of 10 nM – 1 mM.

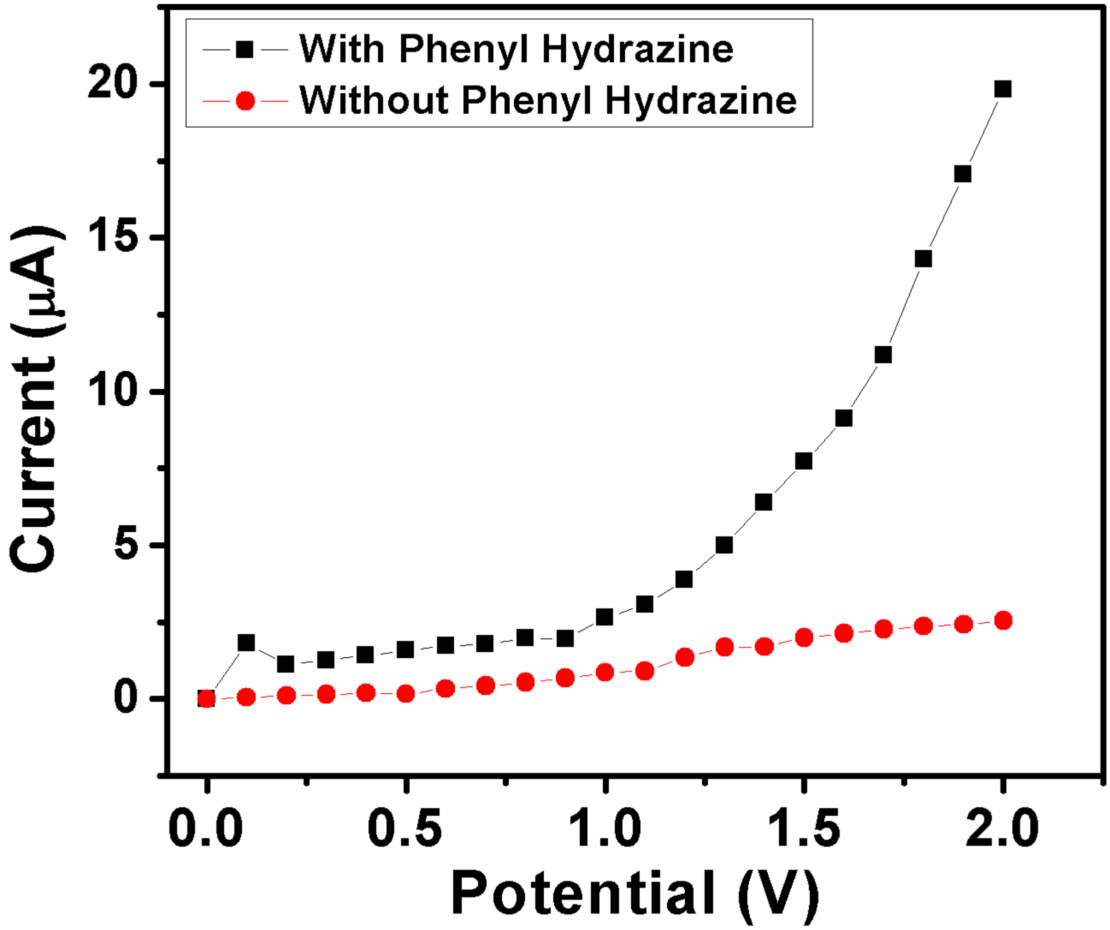

Figure 3.3. 7. Typical I-V response of Glassy Carbon Electrode (GCE) in 10 ml, 0.1 M PBS solution: (■) with 10 nM Phenyl Hydrazine and (●) without the presence of Phenyl Hydrazine

The proposed phenyl hydrazine chemical sensor showed good stability and reproducibility. The stability of the present phenyl hydrazine sensor was determined by the repetitive measurements once a day for 5 weeks. After each measurement, the sensor was stored in a PBS (pH=7.0). No significant decrease in phenyl hydrazine detection was observed for 5 weeks. After 5 weeks, the response of sensor was gradually reduced due to the weak interaction of phenyl hydrazine and nanomaterial surface.

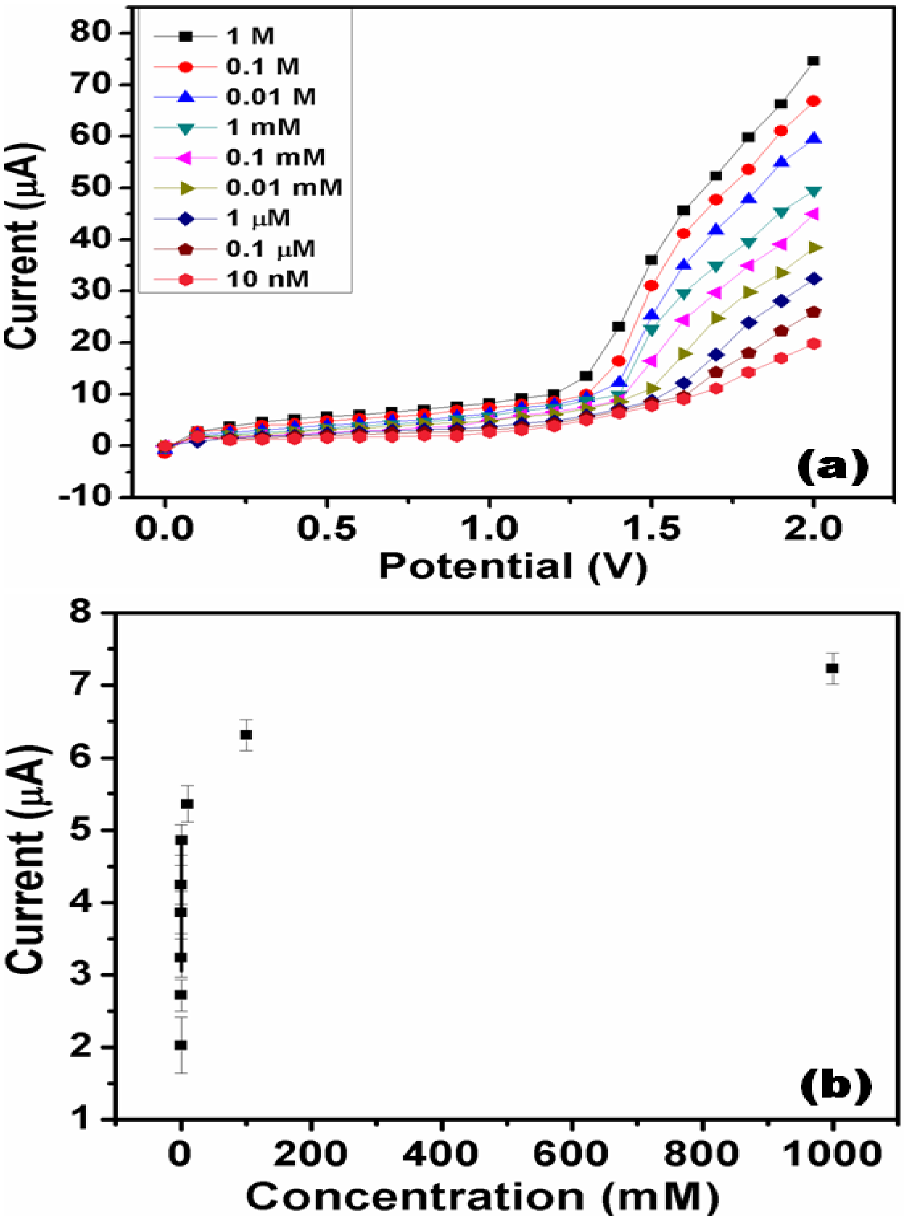

Figure 3.3.8. (a)Typical I-V response of Ag-doped ZnO nanoflowers modified GCE towards various concentrations (from 10 nM to 1M) of phenyl hydrazine into 0.1 M PBS solution (pH=7) and (b) calibration curve

3.3.4. Conclusion

In summary, a robust, highly sensitive, reliable and reproducible phenyl hydrazine chemical sensor was fabricated by utilizing simply synthesized Ag-doped ZnO nanoflowers as efficient electron mediator. The as-synthesized nanoflowers were characterized in terms of their structural and optical properties which revealed the well-crystalline nature and good optical properties for as-synthesized products. A very high sensitivity of ~557.108 ± 0.012 $\mu A.cm^{-2}.mM^{-1}$,and experimental detection limit of ~10 nM with a correlation coefficient (R) of 0.97712 were observed for the fabricated chemical sensor towards the detection of phenyl hydrazine by simple current-voltage (I-V) technique. This research opens a way that simply synthesized Ag-doped ZnO nanomaterials could be used as efficient electron mediators for the fabrication of various effective chemical sensors.

Section 3.4: Ce-doped ZnO nanorods for the detection of hazardous chemical

This section reports a successful synthesis, characterizations and an efficient chemical sensor application of as-synthesized Ce-doped ZnO nanorods. The Ce-doped ZnO nanorods were synthesized by simple low-temperature hydrothermal process. The as-synthesized nanorods were characterized in terms of their morphological, structural and compositional properties. The morphological and structural studies revealed that the synthesized nanorods were grown in high-density and possessed well-crystallinity. The as-synthesized nanorods were used as an effective electron mediator for the fabrication of an efficient hydroquinone chemical sensor. The fabricated sensor exhibited high and reproducible sensitivity of ~10.218±0.01 $mA.cm^{-2}.mM^{-1}$ and experimental detection limit of ~10 nM. To the best of our knowledge, this is the first ever report on the fabrication of hydroquinone chemical sensor using Ce-doped ZnO nanostructures. This work demonstrates that simply synthesized Ce-doped ZnO nanostructures can be used as an effective electron mediator for the fabrication of chemical sensors.

3.4.1. Introduction

The detection of analytes using modified electrodes has always been the focus of the various researchers over a decade. The modification of electrodes brings numerous advantages for the determination of different chemicals such as improved electro-catalysis reactions, prevention of undesirable surface reactions and untoward fouling effects of electrodes. The ever increasing need of various simple, cost effective, rapid and reproducible analytical techniques for the determination of hazardous and toxic chemicals has pushed the scientific community to search new and more effective materials which could be utilized to fabricate the simple and sensitive sensors.

In recent years, the environmental pollution has increased greatly due to the toxic chemicals as reacting species in most of the industries, vast use of fertilizers in agriculture sector, combustion from automobiles and so on [**249,274-280**]. Hydroquinone, a phenolic compound, is used in various manufacturing units such as paper industries, coal-tar production, photographic developing areas and so on. It is one of the highly hazardous polluting chemical, usually absorbed through the skin and mucous membranes and can cause damage to the lungs, liver, kidney and urinary tract in the living beings [**281-283]**]. Furthermore, hydroquinone is considered to be a potential carcinogen candidate and as an effective xenobiotic micropollutant. The environmental monitoring agencies have tightened the norms in order to prevent or reduce the pollution caused by it. In this context, it becomes highly desirable to detect and quantify the leakage of hydroquinone to avoid untoward effects on human health. After exhaustive literature survey, few reports concerning the hydroquinone sensors were found such as Hathoot et. al. used poly 1,8 - diaminonaphtalene derivatives modified electrodes for electrocatalytic oxidation of hydroquinone [**283**], while in another report, Wang et. al. prepared a self-assembled gold monolayers modified electrode (L-Cys/Au SAMs) of L-Cysteine and performed voltametric sensing of hydroquinone [**284**]. A biomimetic sensor based on dinuclear copper (II) complex combined with a ligand was used to determine the hydroquinone in cosmetics using square wave voltammetry by Oliviera et.al. [**285**]. Kong et. al synthesized a composite of β-Cyclodextrin/Poly(N-Acetylaniline)/Carbon Nanotube modified Glassy Carbon Electrode (GCE) and conducted voltammteric determination of hydroquinone [**286**]. In a very recent report, a hybrid material composed of graphene was synthesized by Li et.al. using microwave-assisted chemical reduction process and used for electrochemical detection of hydroquinone [**287-290**]. All the mentioned reports presented satisfactory results for the evaluation of hydroquinone, however, the discussed procedures were tedious. In addition, the synthesized materials in those works were not suitable for trace determination of hydroquinone in complex pollution sample.

Among various materials used for modification of electrodes for the determination of hazardous chemicals, semiconductors metal oxide nanomaterials have contributed significantly [**291**]. Across the range of many excellent metal oxides nanomaterials, ZnO has offered multitude of applications as a result of its remarkable properties such as wide and direct band gap (~3.37 eV), high exciton binding energy (60 meV) at room temperature, ease of fabrication, and biocompatibility [**172, 291-298**]. Due to its promising qualities, ZnO has been extensively studied in the areas of catalysis, field-emission devices, optoelectronics, and chemical sensors [**248, 299,300**]. In particular, ZnO has been proved to be a highly sensitive material as the modification material for electrodes in the determination of various toxic and hazardous chemicals and gases [**301-304**]. Many scientific and technological efforts have been made to improve its response, reaction speed, and stability [**305-308**].

Doping is considered an effective way to mend the properties of ZnO in order to enhance the structural properties of ZnO for various applications. There have been numerous reports on the utilization of several metals such as Ga [**256**], Mn [**257**], In [**258**], Mg [**259**], Al [**260, 309,310**], Sb [**261**], Ag [**311**], Co [**312**] and so on to tailor the desirable properties of ZnO. In addition to these metal doping reports, the rare earth metal, such as cerium (Ce) [**313-315**] has also been included in lattice structure of ZnO nanomaterials. Thus, the Ce-doped ZnO nanomaterials exhibited versatile properties and have been explored to assess the PL, photoelectrochemical activity under visible light and gas sensing properties so far [**316-319**]. Even though Ce-doped ZnO nanostructures are utilized for variety of applications but yet, to the best of our knowledge, there is no report on application of this material for determination of toxic chemicals in liquid phase.

In the present research, we attempt to synthesize the Ce-doped ZnO nanomaterial by low temperature-hydrothermal method and employed the as-synthesized nanomaterial for highly sensitive and reproducible trace determination of hydroquinone chemical in liquid phase after electrode modification. The sensing experiments were conducted using current-voltage (I-V, 2-electrodes system) technique. The fabricated chemical sensor offered high sensitivity and low experimental detection limit. The proposed approach offered few important advantages such as robust and facile synthesis of Ce-doped ZnOnanorods, simple electrode modification, trace determination and rapid detection of hydroquinone through a simple current-voltage (I-V) technique.

3.4.2. Experimental Details

3.4.2.1. Synthesis of Ce-doped ZnO nanorods

For the growth of Ce-doped ZnO nanorods, ($Zn(NO_3)_2.6H_2O$), cerium chloride heptahydrate ($CeCl_3.7H_2O$) and sodium hydroxide (NaOH) were used. All the chemicals were obtained from Sigma-Aldrich and used as purchased without further purification. The synthesis was performed by hydrothermal approach and distilled water (DW) was used as a solvent. In a typical reaction process, for the synthesis of Ce-doped ZnO nanorods, solutions of 0.01M zinc nitrate and 0.001M $CeCl_3.7H_2O$, both made in 50 mL DW, were mixed and the stirrring was continued for 30 min at room-temperature. After stirring, the pH of the solution was maintained at ~8.0 by adding appropritae amount NaOH solution. The resultant solution was again stirred with slight heating for 30 min. The obatined solution was then transferred to teflon lined autoclave, sealed and heated upto 130ºC for 7 h. After completion of the reaction, the autoclave was allowed to cool at room-temperature followed by washing with DW, ethanol and acetone sequentially and dried at room-temperature. The as-synthesized Ce-doped ZnO nanorods were further subjected to characterization in terms of their morphological, compositional and structural properties. Finally, the experiments were carried out to obtain the information of sensing properties using I-V technique.

3.4.2.2. Characterizations of Ce-doped ZnO nanorods

The as-synthesized Ce-doped ZnO nanorods were investigated in terms of their morphological, structural and compositional properties by using various analytical techniques. The morphologies of as-prepared nanorods were determined using FESEM while the crystallinity and crystal phases were examined by XRD in the range of 10-80° with 2°/min scanning speed. The elemental composition of as-synthesized nanorods was examined by using EDS attached with FESEM, whereas the chemical composition was determined by FTIR spectroscopy in the range of 450-4000 cm^{-1} at room-temperature.

3.4.2.3. Electrode fabrication using as-synthesized Ce-doped ZnO nanorods

For the fabrication of hydroquinone chemical sensor, a glassy carbon electrode (GCE, surface area 0.0316 cm^2) was modified and used as a working electrode. For the GCE modification, paste of the functional nanomaterial (i.e. Ce-doped ZnO nanorods) was prepared by adding a particular amount of functional nanomaterial and butyl carbitol acetate. Before coating, the electrode surface was cleaned and polished with alumina-water slurry on a polishing cloth and washed with DW thoroughly. A certain amount of prepared slurry was coated on the GCE and dried at 60 ± 5 ºC for 4-6 h. After drying, a uniform Ce-doped ZnO nanorods layer covering the active area of the electrode surface was obtained. For the sensing measurements, a simple two electrode system (an electrometer; Keithley, 6517A, USA) was used. The Ce-doped ZnO nanorods modified electrode was used as working electrode and Pt wire as counter electrode in the two electrode system. The current response was measured from 0.0 to + 1.5 V. The time delaying were 1.0 second. For all the experiments, 0.1M PBS was used. Various concentrations of hydroquinone, from 100 mM to 10 nM were used to examine the sensing performances.

3.4.3. Results and Discussion

3.4.3.1. FESEM analysis of as-synthesized Ce-doped ZnO nanorods

Figure 3.4.1 (a) and (b) show the low-magnification and high-resolution FESEM images of as-synthesized Ce-doped ZnO nanorods, respectively. As can be seen from the low-magnification FESEM image that the nanorods are grown in very high density and distributed randomly. The diameters of most of them are almost same throughout their length and all exhibited a slight reduction in the diameters at their tips. The typical length of the nanorods are in the range of 1.5- 2 μm while the diameters are in the range of 100-120 nm.

3.4.3.2. EDS analysis of as-synthesized Ce-doped ZnO nanorods

To assess the elemental composition of as-synthesized nanorods, the EDS analysis was done and the result is mentioned in Figure 3.4.1 (c). In EDS spectrum, numerous well-defined peaks were evident related to Zn, O and Ce which clearly support that the synthesized nanorods are made of Zn, O and Ce. No other peak related to impurities was detected in the spectrum which further confirms that the synthesized nanorods are Ce-doped ZnO.

3.4.3.3. X-ray Diffraction (XRD) characterization of as-synthesized Ce-doped ZnO nanorods

To determine the crystal phases and structures of as-synthesized Ce-doped ZnO nanorods, XRD was performed. Figure 3.4.1 (d) exhibits the typical XRD pattern of as-synthesized Ce-doped ZnO nanorods. The observed diffraction reflections i.e. (100), (002), (101), (102), (110), (103), (200), (112), (201), (004) and (202) were similar to bulk ZnO and corresponded to wurtzite hexagonal phase of ZnO. The obtained results are in good agreement with standard JCPDS data card No 36-1451. No reflections related to Ce and other related impurities such as CeO_2, Ce_2O_3 or other crystalline forms were detected in the pattern which confirms that Ce ions were uniformly substituted by Zn sites into the lattices of ZnO crystals. Moreover, the obtained reflections are sharp and high in intensity which reveal that the synthesized Ce-doped ZnO nanorods are well-crystalline.

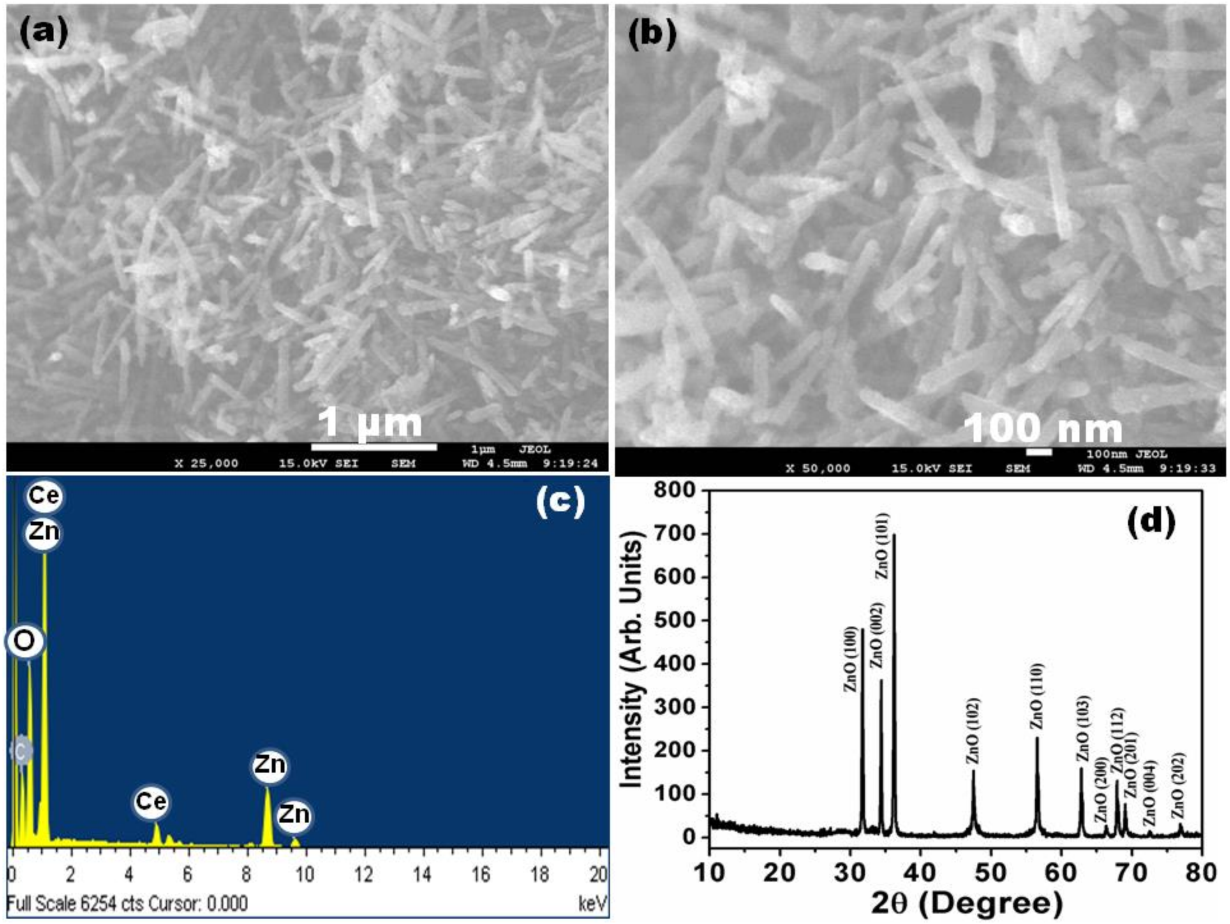

Figure 3.4.1. Typical (a) low and (b) high- magnification FESEM images, (c) EDS spectrumand (d) XRD pattern of as-synthesized Ce-doped ZnO nanorods.

3.4.3.4. Chemical composition analysis using FTIR spectroscopy of as-synthesized Ce-doped ZnO nanorods

To confirm the chemical compositions, the as-synthesized Ce-doped ZnO nanorods were characterized by FTIR spectroscopy at room-temperature in the range of 450-4000 dcm^{-1}. The typical FTIR spectrum of as-synthesized Ce-doped ZnO nanorods is shown in Figure 3.4.2. Various well-defined peaks at 511, 881, 1381, 1619 and 3425 cm^{-1} were observed in the spectrum. The peak appeared at 511 cm^{-1} could be attributed to the Metal-oxygen (Zn-O) bonds and verified the formation of doped ZnO [**318,319**]. Appearance of two very small peaks at ~881 cm^{-1} and 1381 cm^{-1} were may be due to the nitrate (NO_3^-) group [**270, 271**]. Origin of two well-defined absorption bands at 1619 cm^{-1} and 3425 cm^{-1} were due to the bending vibration of absorbed water and surface hydroxyl and O-H stretching mode, respectively [**271**]. No other absorption band except mentioned here was detected in the FTIR spectrum which substantiates that the synthesized nanorods are almost pure without any significant impurity.

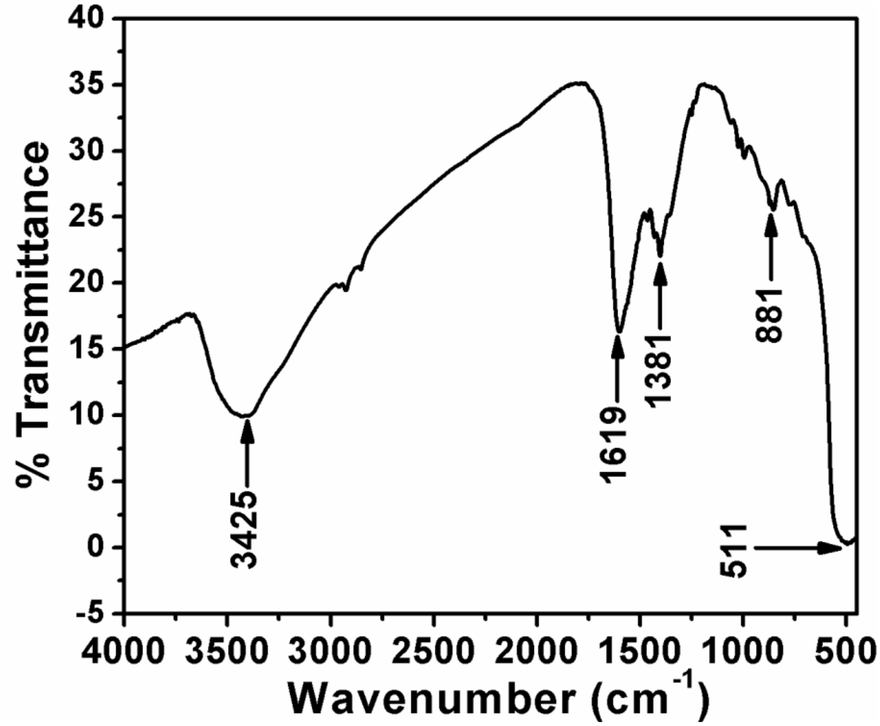

Figure 3.4.2. Typical Fourier transform infrared (FTIR) spectrum of as-synthesized Ce-doped ZnO nanorods.

3.4.3.5. Ce-doped ZnO nanorods application for hydroquinone chemical sensor

The detection of hydroquinone and electrode modification procedure using the typical current-voltage (I-V) technique has been discussed in the experimental section. In brief, the modification of GCE was carried out by mounting a certain amount of as-synthesized Ce-doped ZnO nanorods and butyl carbitol acetate followed by drying it in an oven. The modified GCE electrode was employed as a working electrode while Pt wire was used as a counter electrode in an electrometer (I-V technique) for sensor studies. For all the sensor measurements, the current response range was 0.0 to + 1.5 V. The Ce-doped ZnO nanorods modified GCE was employed to detect toxic hydroquinone in liquid phase. Figure 3.4.3 outlines the fabrication of hydroquinone sensor based on Ce-doped ZnO nanorods and its sensing mechanism.

Figure 3.4.4 (a) illustrates the current responses of the hydroquinone sensor with and without hydroquinone using modified Ce-doped ZnO GCE electrode. It can be deduced from Figure 3.4.4 (a) that the current value was enhanced with hydroquinone compared to without it (i,e in 0.1 MPBS). This increase in current response is considered to be due to the amplified interaction between hydroquinone moieties and the active sites available at Ce-doped ZnO nanorods. To explore the sensing properties of fabricated hydroquinone in different concentrations, several hydroquinone solutions with different concentrations were prepared and the I-V signals were measured. It is evident from Figure 3.4.4 (b) that the values of current increase substantially from lower to higher concentrations (10 nm to 100 mM) of hydroquinone due to increase in the ionic strength of the hydroquinone solution.

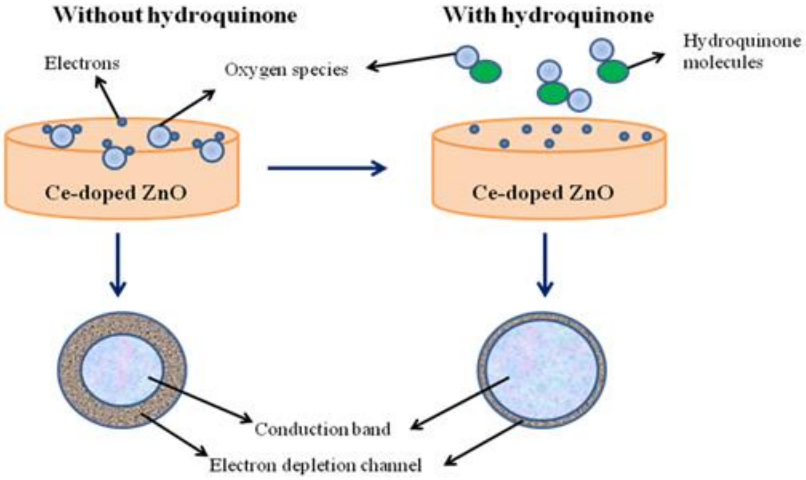

Figure 3.4.3. Schematic design and mechanism for the fabrication of hydroquinone chemicalsensor based on Ce-doped ZnO nanorods by I-V technique using GCE electrode

The oxygen present at nanomaterial and liquid surface boundary plays a vital role in the sensing mechanism of hydroquinone. The amount of oxygen adsorption depends on the structural properties of doped material which in turn affects the variation of the sensor resistance. It is found generally that doped nanomaterial is capable to adsorb greater amount of oxygen due to the existence of high number of defects [**311**]. The increase in the sensing ability (decrease in the resistance of the sensor) of the sensor is caused due to the additional adsorption of the oxygen.

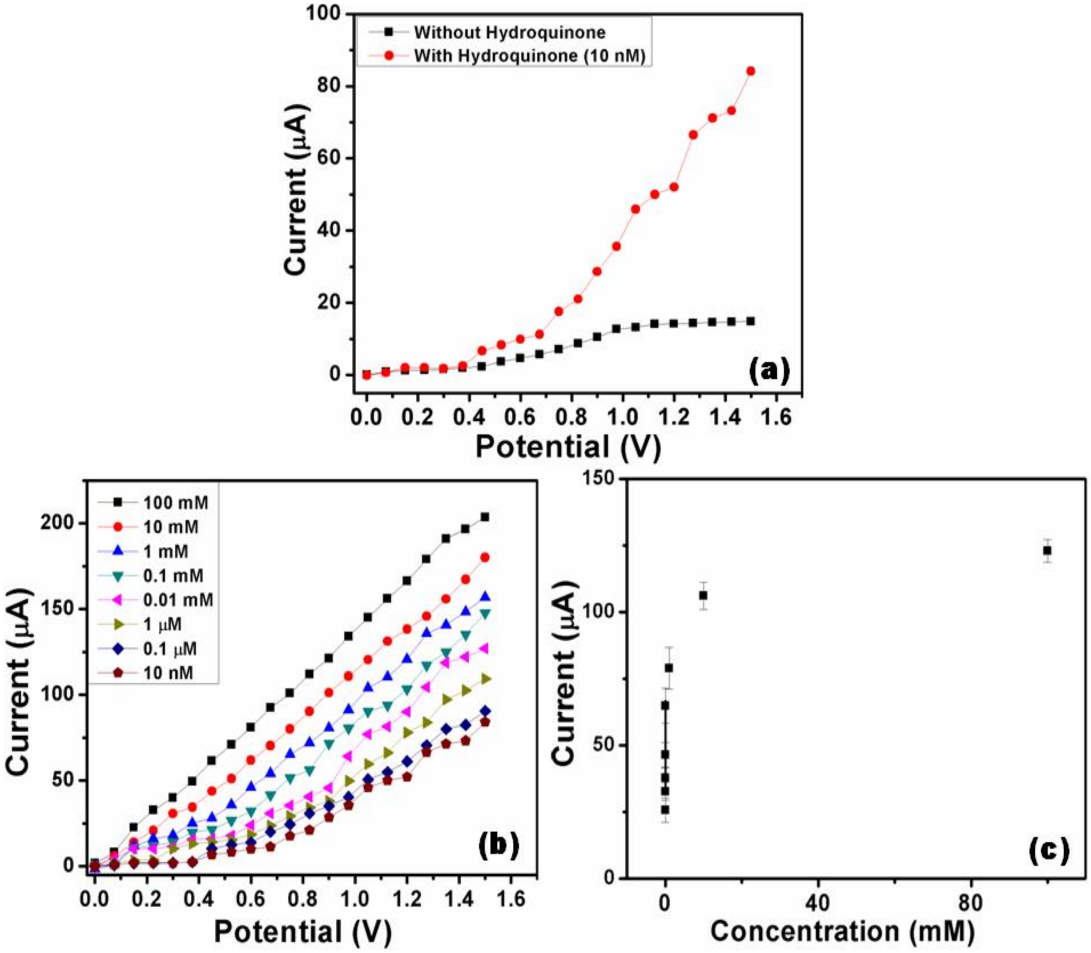

Figure 3.4.4. (a)Typical I-V responses of Ce-doped ZnO nanorods in (GCE) in 10 ml, 0.1 M PBS solution (pH=7.2): (●) with 10 nM hydroquinone and (■) without hydroquinone; (b) I-Vresponse for various concentrations (from 10 nM ~ 100 mM) of hydroquinone and (c) calibration curve.

The exact sensing mechanism of hydroquinone over Ce-doped ZnO depends on the surface reactions involving adsorbed oxygen ions. The change in resistance of the Ce-doped ZnO nanorods is caused by the oxygen which is adsorbed chemically at liquid surface boundary whereas the physiosorption of oxygen occurs at Ce-doped ZnO nanomaterial surface from thebulk solution according to the two successive surface reactions (3.4.1) & (3.4.2) depicted below. The oxygen which takes part in the detection procedure is subsequently ionized into dynamic oxygen species i.e. O_2^- and O^- while moving from site to site by capturing electrons from active surface sites of Ce-doped ZnO nanorods. Due to the emission of electrons from Ce-doped ZnO, the barrier height for electron transport will increase that subsequently increases the resistance of nanomaterials surface. As is found in the literature, the ionization of oxygen species to O_2^- and O^- is dependent on the available energy (or temperature). Thus, in our case, all the sensor studies were performed at room temperature where the O^- is the dominant species.

$$O_{2\,(\text{Liq.})} \longrightarrow O_2\,(\text{absorbed}) \qquad (3.4.1)$$

$$O_2(\text{absorbed}) + 2e^-\,(\text{Ce-doped ZnO}) \longrightarrow 2O^-(\text{absorbed}) \qquad (3.4.2)$$

From equation (3.4.2), the emission of 2 electrons from the Ce-doped ZnO increases the resistance (decrease in conductance) of Ce-doped ZnO nanorods. Due to the decrease in conductance, the value of current is reduced. In Final step, the oxygen species (O-) assist in the oxidation of the hydroquinone into 1,4-benzoquinone and emits 2 free electrons simultaneously as shown in reaction (3.4.3). The Ce-doped ZnO nanomaterial surface accepts the released electrons, resulting into the enhanced conducting behavior of doped nanomaterial.

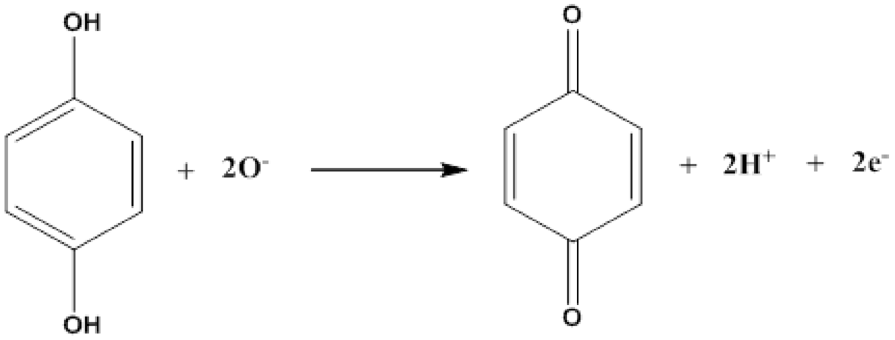

(3.4.3)

The sensitivity is considered as the vital indicator of the sensing performance of any chemical sensor. Therefore, the sensitivity of the proposed hydroquinone chemical sensor was calculated by slope of the current-concentration calibration profile. The sensitivity was obtained when the slope was divided by the active surface area of GCE according to the following equation:

Sensitivity=Slope/Surface area of electrode

where the surface area of GCE is 0.0316 cm2

The calibration curve was plotted by taking average of currents over a range of potentials spanning from 0.75- 0.975 V. The calibration data was fitted well linearly at smaller scale concentration range (10 nM – 0.1mM), from which the slope was calculated. The calibration (sensitivity) curve of the fabricated sensor is shown in Figure 3.4.4 (c). The sensitivity of the fabricated hydroquinone chemical sensor was calculated to be of ~10.218±0.01 mA.cm^{-2}.mM^{-1}. The experimental detection limit of the proposed hydroquinone chemical sensor based on Ce-doped ZnO nanorods was found to ~10 nM. The linear dynamic range (LDR) was from 10 nM to 0.1 mM. In order to examine the suitability of the present research for the assessment of hydroquinone using a simple synthesis method of nanomaterial and experimental technique, the present work is compared with other methods reported in literature for the hydroquinone detection and assembled in Table 3.4.1. A very good sensitivity for the fabricated hydroquinone chemical sensor was achieved which may be due to the existence of Ce which accelerates oxidation of hydroquinone into 1,4-hydroquinone in a very short response time. Furthermore, the improved sensitivity can also be attributed to the decreased diameter of Ce-doped ZnO nanorods caused by Ce doping resulting into an increase in hydroquinone adsorption [**320**].

To test the stability of prepared hydroquinone chemical sensor, repetitive measurements were performed once a day for several weeks. The hydroquinone sensor was kept in a PBS (pH=7.0) after each experiment. It was found that there was no significant reduction in the current response for hydroquinone determination for ~4 weeks however; the current response for hydroquinone was decreased with time.

Table.3.4.1. Comparison summary of the performances of hydroquinone chemical sensors fabricated based on the utilization of various materials as electron mediators:

Electrode Materials	Sensitivity	Detection Limit	LDR	Ref.
Ce-doped ZnO nanorods	**~10.218±0.01 mA.cm^{-2}.mM^{-1}**	**~ 10 nM**	**10 nM to 0.1 mM**	**This work**
L-Cys/Au SAMs	-	4.0×10^{-7}M	2.0×10^{-6}~2.0×10^{-4}M	[**284**]
Dinuclear copper (II) complex in carbon paste	-	3.0×10-^{7} mol L^{-1}	6.0×10^{-5} to 2.5×10^{-3} mol L^{-1}	[**285**]
β-Cyclodextrin/Poly(N-Acetylaniline)/Carbon Nanotube Composite modified GCE	-	8×10^{-7} mol l^{-1}	1×10^{-6} to 5×10^{-3} mol l^{-1}	[**286**]
Graphene modified GCE	1.38 μA μM^{-1} cm^{-2}	12 μM	20–115 μM	[**287-290**]
Graphene modified GCE	-	1.5×10^{-8}M	1.0×10^{-6} to 5.0×10^{-5}M	[**319**]

3.4.4. Conclusion

In summary, by utilizing Ce-doped ZnO nanorods, an efficient, robust, and highly sensitive with low-experimental detection limit hydroquinone chemical sensor was fabricated for the first time. The Ce-doped ZnO nanorods were synthesized by low-temperature simple hydrothermal process. The nanorods were grown in high-density and possessing well-crystalline structure as confirmed from the detailed morphological and structural characterizations. The as-synthesized nanorods were used as an effective electron mediator for the fabrication of an efficient hydroquinone chemical sensor which exhibits a high and a reproducible sensitivity of ~10.218±0.01 mA.cm^{-2}.mM^{-1} with experimental detection limit of ~10 nM. This research opens a way out that a simply synthesized Ce-doped ZnO nanomaterials can efficiently be used as an effective electron mediator for the fabrication of an efficient hydroquinone chemical sensors.

Section 3.5: Growth of In-Doped ZnO Hollow Spheres Composed of Nanosheets Networks and Nanocones: Structural and Optical Properties

Section 3.5 reports the facile growth and characterizations of In-doped ZnO hollow spheres composed of NS networks and nanocones. The In-doped ZnO hollow spheres composed of NS networks and nanocones were grown on Si (100) substrate by simple and non-catalytic thermal evaporation process using metallic zinc and indium powders in the presence of oxygen. The prepared materials were examined in terms of their morphological, compositional, structural and optical properties. The detailed morphological studies revealed that the synthesized products are hollow spheres composed of NS networks and nanocones and grown in high-density. The observed structural properties exhibited well-crystallinity and wurtzite hexagonal phase for the grown materials. The room-temperature PL spectrum showed a broad band in the visible region with a suppressed UV emission and hence due the enhancement in the green emission, the prepared materials exhibits a great interest in the area of ZnO phosphors, such as field emissive display technology, etc.

3.5.1.Introduction

Due to excellent properties and wide applications, the II-VI wurtzite hexagonal phase ZnO presents itself as one of the most promising and exotic materials in the metal oxide family. The properties of ZnO include its direct and wide band gap energy (3.37 eV at room-temperature), large exciton binding energy (60 meV), high surface-to-volume ratio, high mechanical strength and thermal stability, biocompatibility, optical transparency in the visible region, piezoelectricity and so on[**172,183,321-323**]. Due to its wide band gap and large exciton binding energy, ZnO is widely used for the fabrication of efficient short-wavelength optoelectronic devices such as light-emitting diodes (LEDs) and laser diodes (LDs)[**324,325**]. Due to the optical transparency of ZnO, this material can be widely used as transparent conductors in many applications[**326**]. By exploring the piezoelectric properties, recently, ZnO nanostructures based nano-generators, which are able to convert mechanical energy into electric power, were fabricated and reported in the literature[**327-329**]. Because of the biocompatibility nature, ZnO is also used for several biological applications such as cancer detection and therapy, biosensors, anti-bacterials and so on[**330-332**]. In addition to these, ZnO is also used for various other applications such as photocatalysis, solar cells, field emission displays (FED), optical waveguides, optical switches, chemical and gas sensors, actuators, catalysts, hydrogen storage, electronic and photovoltaic devices, transparent conductive films, and so on[**172,183, 321-336**].

Recently, to enhance the electrical and optical properties, ZnO was doped with various elements such as As, Ga, In, Sn, Ce, Sb, W, Ag and so on.[1] Among various dopants, the doping of In in ZnO has particular interest as In-doped ZnO show similar electrical conductivity and better transparency in both, visible and infrared, regions as compared to ITO. Therefore, the In-doped ZnO can be used in many electronic and optoelectronic device applications. Due to this, various In-doped ZnO nanomaterials were synthesized by different techniques and reported in the literature[**258,337,338**].

In this work, we present the facile growth of In-doped ZnO hollow spheres composed of NS networks and nanocones on silicon substrate by non-catalytic thermal evaporation process. The synthesized materials were characterized in detail in terms of their morphological, compositional, structural and optical properties.

3.5.2. Experimental Details

In-doped ZnO hollow spheres composed of NS networks and nanocones were prepared on silicon substrate by simple and facile non-catalytic thermal evaporation process. Commercially available metallic zinc and Indium (In) powders and high-purity oxygen gas were used as sources for zinc, Indium and oxygen, respectively. In a typical reaction process, zinc and In powders (10:2) were thoroughly mixed and put into a ceramic boat which was placed at the centre of the quartz tube furnace. Several pieces of Si(100) were placed adjacent to the source boat, however, before loading, the Si(100) substrates were cleaned with DI water, ethanol and acetone, sequentially and dried with nitrogen gas. After loading the source materials and substrates, the quartz tube chamber pressure was down to 1 torr using a rotary vacuum pump and this pressure was maintained during the whole reaction process. The furnace was heated up to 850 ºC under the continuous flow of highly-pure nitrogen and oxygen gases with the flow-rates of 40 and 100 sccm, respectively. The reaction was terminated in 1.5 h. After completing the reaction for desired time, the furnace was allowed to cool at room temperature and the deposited materials on Si (100) substrate was characterized in detail in terms of their morphological, structural and optical properties.

To examine the general morphologies, the as-deposited materials were investigated by FESEM. The structural property was examined by XRD in the range of 20-65°. The elemental composition of the prepared material was checked by using EDS, attached with FESEM. The crystal and optical properties of the deposited material was examined by Raman-scattering and room-temperature PL, measured with the Ar^+ (513.4 nm) and He-Cd (325nm) laser lines as the exciton sources, respectively.

3.5.3. Results and Discussion

The general morphologies of as-grown In-doped ZnO material was examined by FESEM and results are demonstrated in figure 3.5.1. Figure 3.5.1 (a) and (b) exhibit the low-magnification images and confirmed that the as-prepared materials are possessing spherical shape with hollow interiors and grown in high density on the silicon substrate. It is clear from the images that most of the spheres are hollow with different sizes, i.e. in the range of 3-10 µm. Most of the spheres showed an opening on their surfaces, probably because of thin oxide sheath and confirm that the spheres have hollow interiors. Figure 3.5.1 (c) ad (d) shows the high-resolution FESEM images of as-grown hollow spheres. Interestingly, it is seen from the high-resolution images that the spheres are composed of thin NS networks and nanocones.

To closely examine the morphologies of as-prepared In-doped hollow spheres, a single hollow sphere was chosen and examined by using high-resolution FESEM. Figure 3.5.2 (a) shows the typical FESEM image of single hollow sphere structure which clearly revealed that the outer surface of the sphere is covered by the NS which are randomly distributed in partially aligned manner and interconnected with adjacent NS in such a way that they form the network like structures (figure 3.5.2 (b)-(d)). The average lengths of the grown NS are in the range of 1.5–2 µm, however some shorter length NS were also seen in the micrograph (Figure 3.5.2 (c) and (d)). The average thicknesses of the NS are in the range of 80-110 nm. Interestingly, it was also observed that the NS are penetrated to their adjacent NS and form trenches which were filled with some other specific kind of nanostructures (figure 3.5.2 (d)). To narrowly examine the morphologies of these nanostructures, high-resolution FESEM was done and results are demonstrated in figure 3.5.2 (e) and (f).

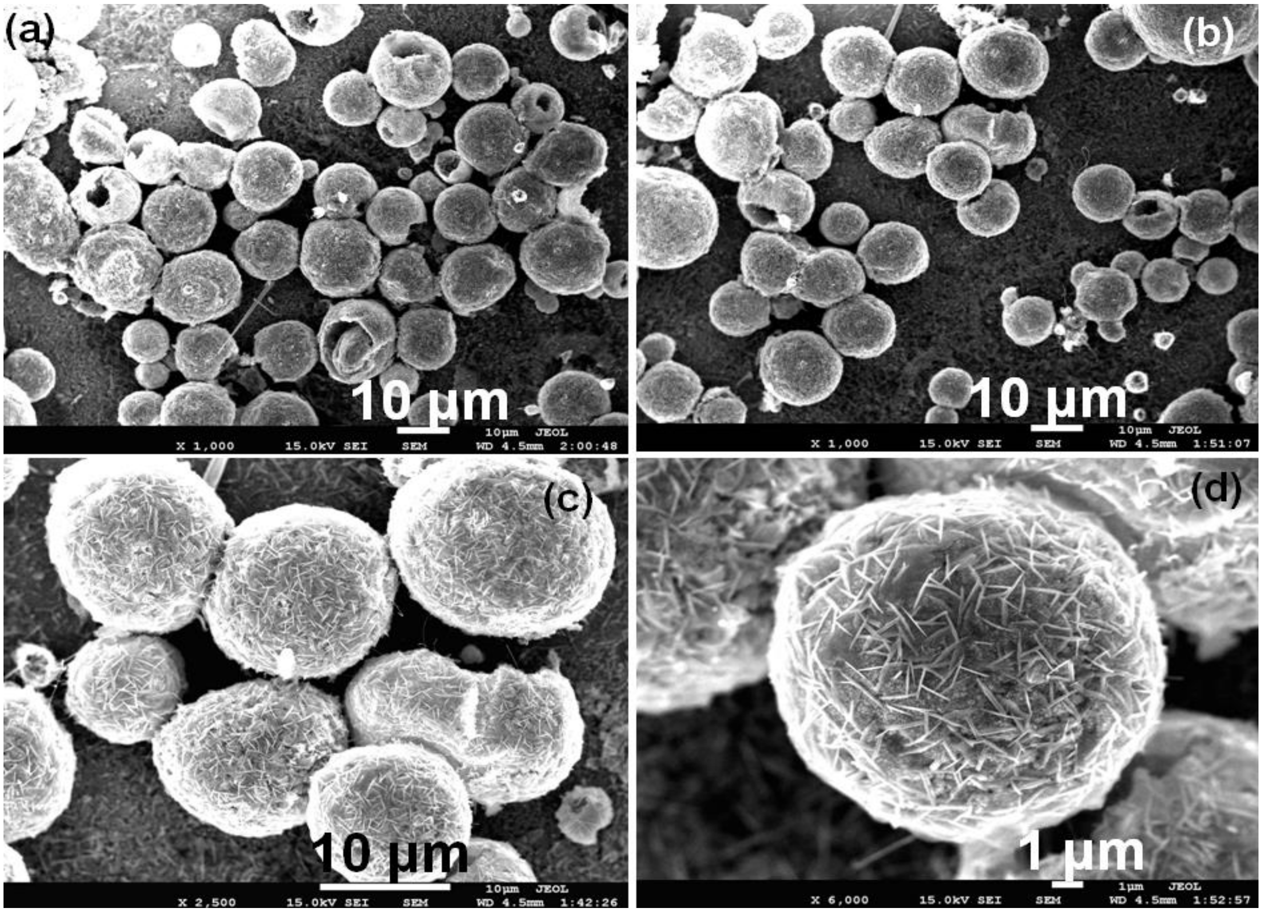

Figure 3.5.1.(a and b) Low magnification and (c and d) high-resolution FESEM images of In-doped ZnO hollow spheres composed of nanosheets networks and nanocones prepared bythermal evaporation process

By the close view, it was observed that trenches of the NS were filled with small nanocone. The nanocones possess narrow tips and wide bases and the shapes and sizes of most of the nanocones are uniform. The typical lengths of the nanocones are in the 70 ± 10 nm. The typical diameters of the nanocones at their bases and tips are ~25 ± 5 nm and 10 ± 2 nm, respectively (figure 3.5.2 (f)). Moreover, large quantity nanocones are randomly and densely distributed in the trenches.

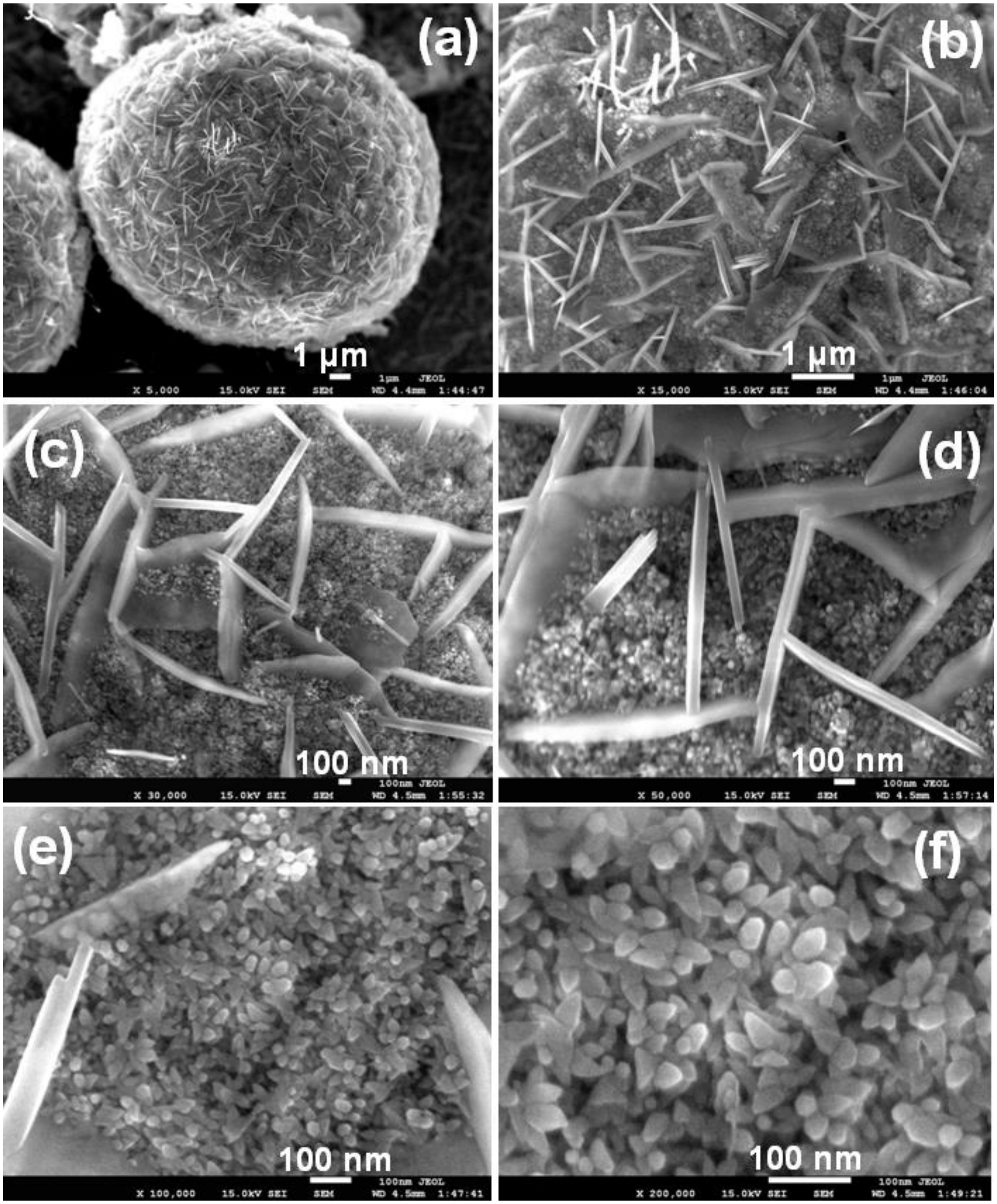

Figure 3.5.2. Typical FESEM images of (a) a single sphere; (b-d) high-magnification images of nanosheet networks, (e and f) nanocones prepared by thermal evaporation process

To examine the elemental compositions, the as-prepared In-doped ZnO hollow spheres were examined by EDS attached with FESEM. Figure 3.5.3 (a) exhibits the typical EDS spectrum of as-prepared In-doped hollow spheres and reveals the appearance of several well defined peaks for zinc, oxygen and In which clearly verify that the synthesized products are made of these elements. To determine the crystallinity and crystal phases, the as-prepared In-doped ZnO spheres were examined by XRD. Figure 3.5.3 (b) shows the typical XRD pattern of as-prepared In-doped ZnO spheres which exhibits several well-defined diffraction reflections at 30.6°, 31.3°, 34.4°, 36.1°, 47.8°, 56.6° and 62.8°. Except 30.6° diffraction reflection, all other peaks appeared in the pattern can be indexed as those from the known wurtzite-structured hexagonal phase well-crystalline bulk ZnO. In addition to this, the origination of a small peak at 30.6º was due to the presence of In in the lattices of ZnO. The presence of a small In peak with other wurtzite ZnO reflections in the pattern confirmed that the In atoms are available in the lattices of ZnO in the grown structures. Furthermore, no characteristic diffraction reflections related with any impurities were detected in the pattern within the detection limit of the x-ray diffractometer, which in turn further revealed the purity of the In-doped ZnO hollow spheres.

Interestingly, it was observed that doping of In in ZnO play an important role for the formation of hollow spheres composed of NS networks and nanocones. To verify this, some experiments have been done for the formation of pure ZnO hollow sphere. For these experiments, all the experimental parameters such as temperature, pressure, amount of zinc powder, flow of oxygen and nitrogen gases were kept constant. Figure 3.5.4 exhibits the typical FESEM images of pure ZnO hollow spheres. It is interesting to note that the prepared ZnO hollow spheres and cages exhibit smooth and clean surfaces unlike to the In-doped ZnO hollow spheres which show the formation of NS networks and nanocones on their outer surfaces. The observed FESEM images revealed that most of the spheres are hollow with different sizes, i.e. in the range of 3-13 μm.

To examine the optical properties, the grown In-doped ZnO hollow spheres composed of NS networks and nanocones were examined by room-temperature PL spectroscopy. Figure 3.5.5 exhibits the typical room-temperature PL spectrum of as-deposited In-doped ZnO hollow spheres. Normally two bands are appearing in the room-temperature PL spectrum of ZnO based nanomaterials; a band in the UV region also called as near band edge emission originated due to the free-exciton recombination and another band in the visible range, also known as deep level emission (DPE), and appear caused by the impurities and structural defects such as oxygen vacancies and interstitials of zinc[**339,340**].

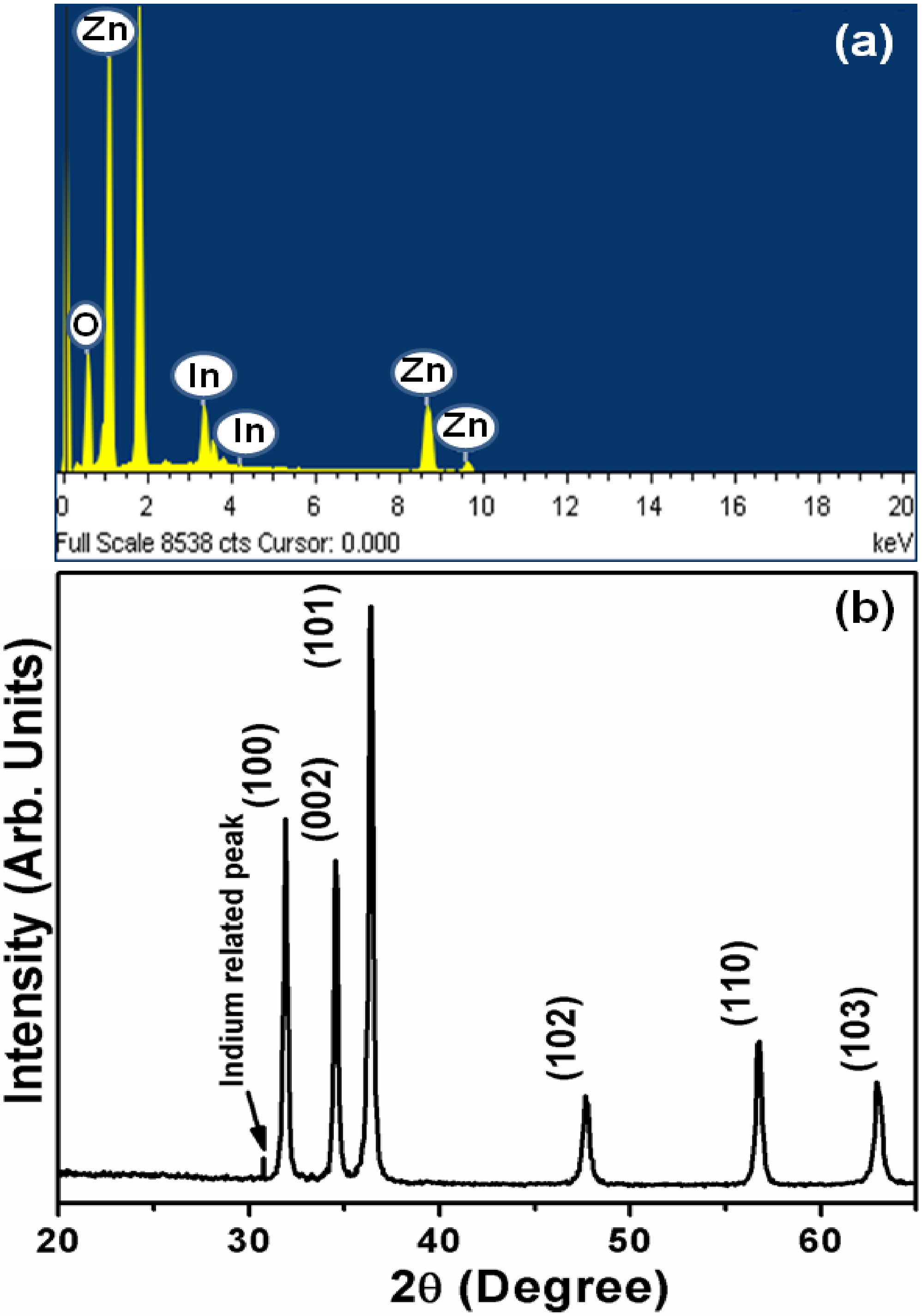

Figure 3.5.3. (a) EDS spectrum and (b) XRD pattern of In-doped ZnO hollow spheres composed of nanosheets networks and nanocones prepared by thermal evaporation process

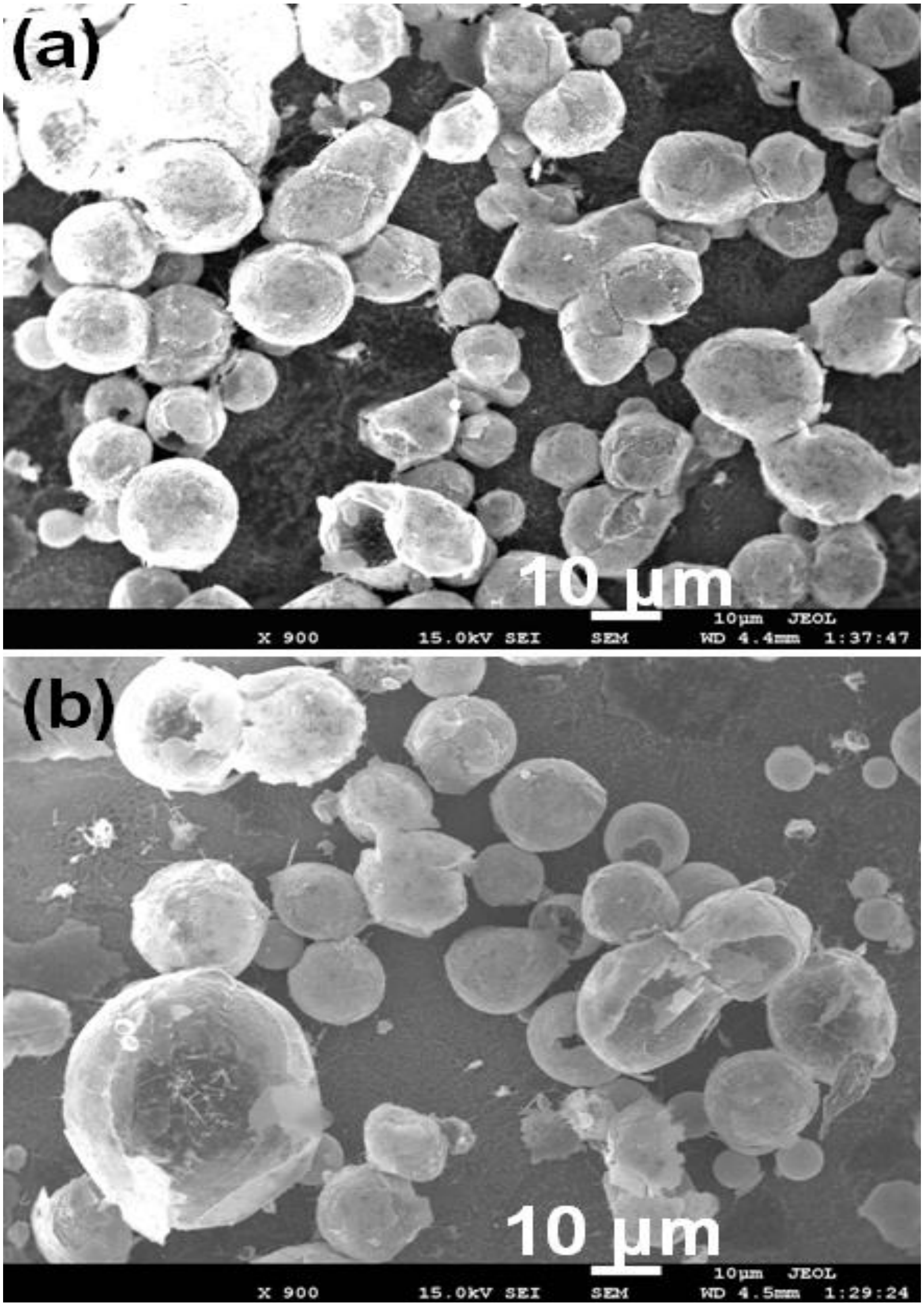

Figure 3.5.4. (a) Low magnification and (b) high-resolution FESEM images of ZnO hollow spheres prepared by thermal evaporation process

Interestingly, it is seen that the observed PL spectrum exhibits two well-defined bands, i.e. a short but sharp band at 385 nm in the UV region and broad and strong band at 521 nm in the visible region. It is also reported that with increasing the structural defects and impurities in the lattices of ZnO, the intensity of deep level emission increases while decreasing the defects and impurities, the intensity of the near band emission increases[**341**]. Therefore, it can be concluded that the appearance of strong deep level emission in the observed PL spectrum are due to Indium doping into the lattices of ZnO which create some defects in the lattices of ZnO and hence enhance the green emission.

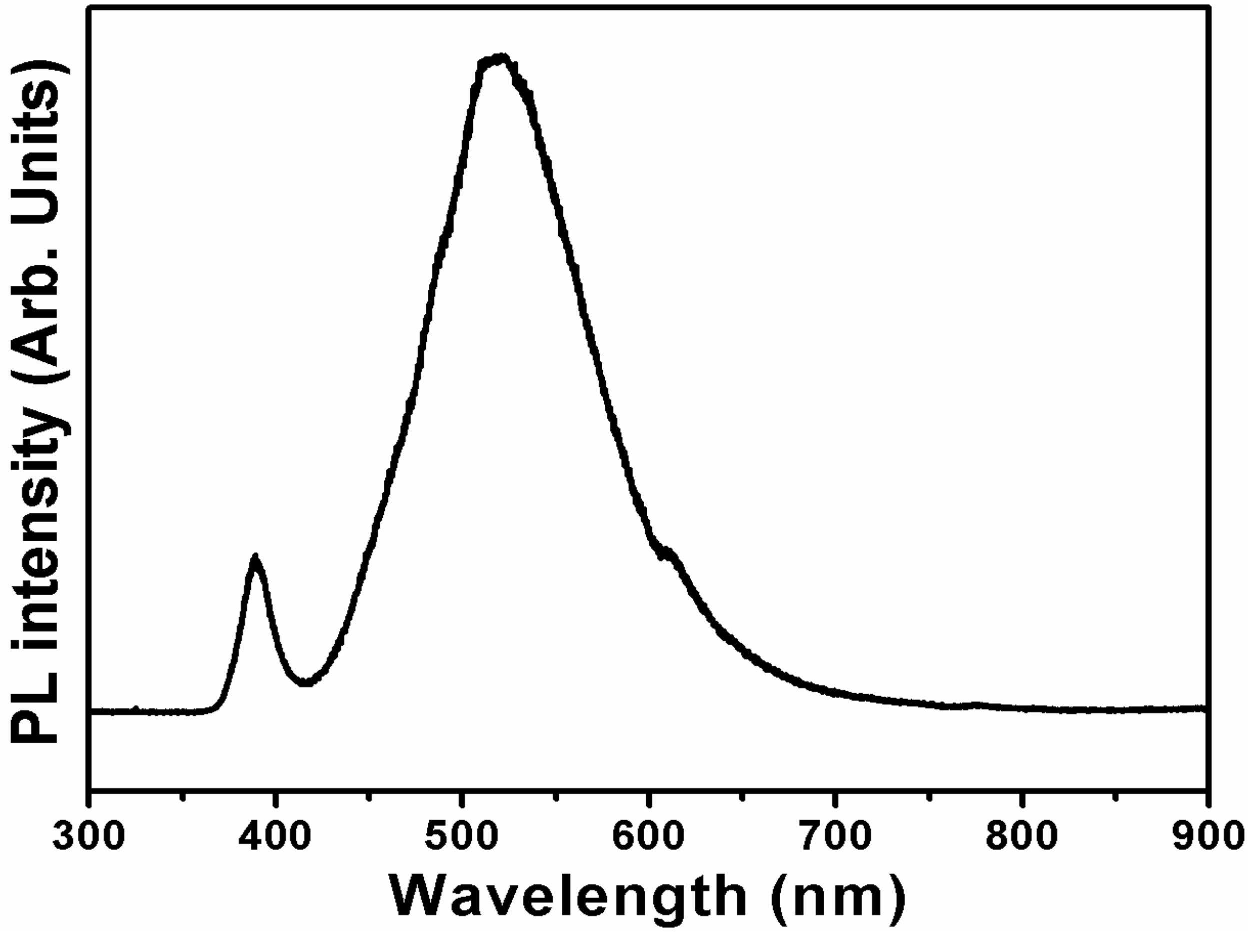

Figure 3.5.5. Room-temperature photoluminescence (PL) spectrum of In-doped ZnO hollow spheres composed of nanosheets networks and nanocones prepared by thermal evaporation process

To examine the vibrational and crystal properties, the as-prepared In-doped ZnO hollow spheres were examined by Raman-scattering. Figure 3.5.6 shows the typical Raman-scattering spectrum of In-doped ZnO hollow spheres. According to the group theory, with the wurtzite hexagonal phase, the ZnO belongs to C^4_{6v} space group. At the Γ point of the Brillouin zone, it predicts the presence of different optic modes: $\Gamma = A_1 + 2B_1 + E_1 + 2E_2$ in which A_1, E_1, and E_2 modes are Raman active. Among these, the E_2 modes are Raman active only while the A_1 and E_1 are also infrared active [**179**]. The observed Raman-scattering spectrum exhibits several peaks at 334 cm^{-1}, 381 cm^{-1}, 439 cm^{-1} and 582 cm^{-1}. The most dominated and strong peak appeared at 439 cm^{-1} attributes the Raman-active optical-phonon E_2 mode which is a characteristic peak of wurtzite hexagonal ZnO**[339]**. The appearance of short and suppressed peak at 582 cm^{-1} can be assigned as E_{1L}.

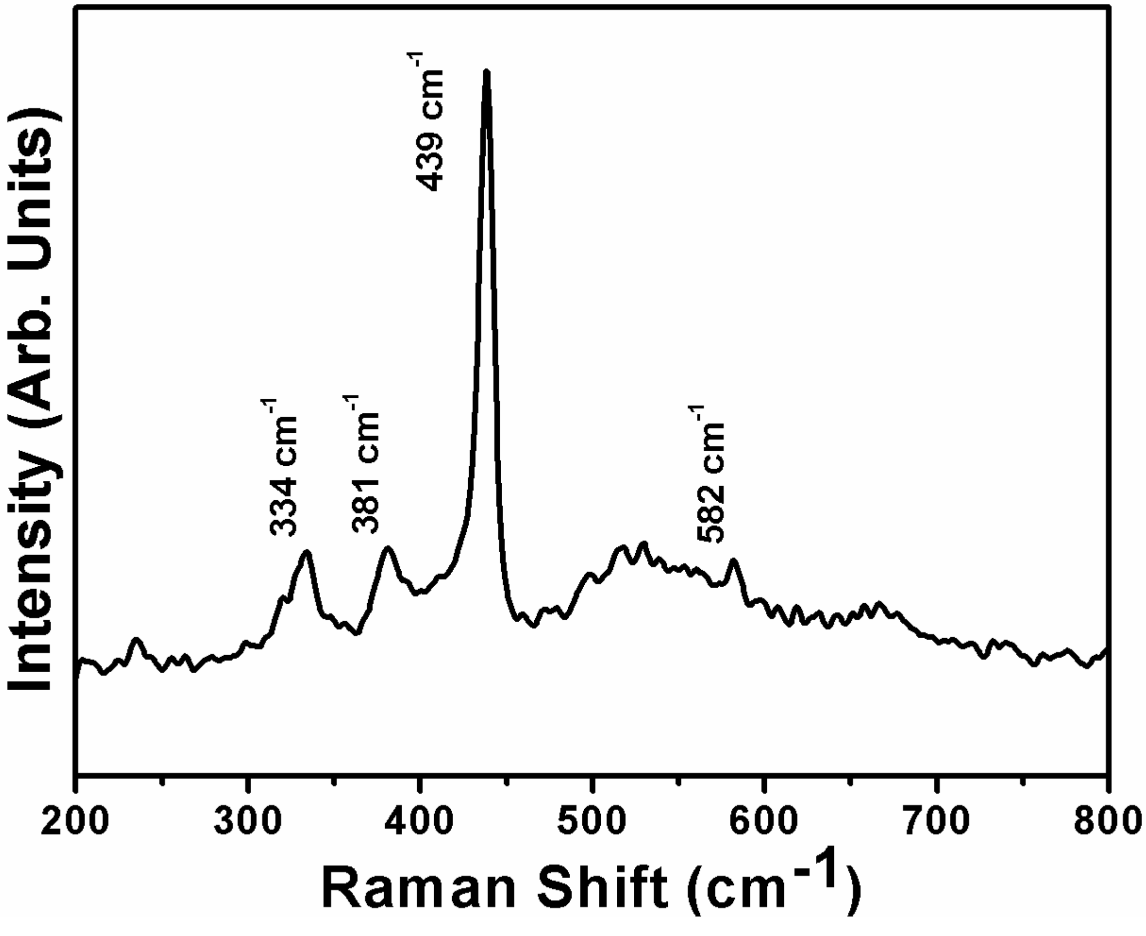

Figure 3.5.6. Raman-scattering spectrum of In-doped ZnO hollow spheres composed ofnanosheets networks and nanocones prepared by thermal evaporation process

This is reported that E_{1L} peak is originated due to the structural defects and impurities in the lattices of ZnO. As the In is doped into the lattices of ZnO, hence E_{1L} is expected in the Raman-scattering spectrum. The origination of two short peaks at 334 cm^{-1} and 381 cm^{-1} can be referred as $E_{2H} - E_{2L}$ (multi phonon) and A_{1T} modes, respectively. Finally, due to the presence of highest intensity optical-phonon E_2 mode in the observed Raman spectrum, it can be concluded that the prepared In-doped ZnO hollow spheres possess well-crystallinity.

3.5.4. Conclusion

In summary, In-doped ZnO hollow spheres composed of NS networks and nanocones were prepared on Si (100) substrate by facile thermal evaporation process using metallic zinc and indium powders in the presence of oxygen. The detailed compositional and morphological characterizations revealed that the grown products are In-doped ZnO and possess hollow spheres composed of NS networks and nanocones. The structural characterization confirmed that the prepared materials exhibiting well-crystallinity with the wurtzite hexagonal phase. A strong deep level emission and a suppressed UV emission was observed from the room-temperature PL spectrum of as-prepared In-doped ZnO hollow spheres which substantiate that the prepared materials can be used for various applications such as field emissive display technology, etc. Finally, it was also observed that doping of In in ZnO play an important role for the formation of NS networks and nanocones on the surfaces of hollow spheres, however, the pure ZnO hollow spheres show smooth and clean surfaces.

Section 3.6: Low-temperature synthesis of α-Fe_2O_3 hexagonal nanoparticles for environmental remediation and smart sensor applications

Section 3.6 demonstrates the successful synthesis and characterizations of α-Fe_2O_3 hexagonal nanoparticles and their effective utilization for the degradation of hazardous RhB dye and smart chemical sensor applications. The as-synthesized materials were characterized by various analytical techniques which revealed that the prepared nanoparticles are well-crystalline, possessing hexagonal shape, grown in high-density and well matched with the rhombohedral α-Fe_2O_3structures. The as-synthesized α-Fe_2O_3nanoparticles were used as efficient photocatalyst for the photocatalytic degradation of RhB-dye under light illumination which showed substantial degradation (~ 79%) of RhB-dye in 140 min. The considerable photo-degradation of RhB-dye was due to the unique morphology of the synthesized nanoparticles which might import the effective electron/hole separation and might generate the large number of oxy-radicals. Moreover, the synthesized α-Fe_2O_3nanoparticles were utilized as efficient electron mediators for the fabrication of 4-nitrophenol chemical sensor in aqueous media. The fabricated chemical sensor exhibited a high-sensitivity ∼ 367.6 $nA.mM^{-1}.cm^{-2}$and experimental detection limit of ~1.56 mM, with linearity in the range of 1.56 – 12.5 mM and correlation coefficient (R) of ∼0.99963. The obtained results demonstrated that the simply synthesized α-Fe_2O_3nanoparticles can effectively be used as efficient photocatalyst for the photocatalytic degradation of organic dyes and effective electron mediators for the fabrication of highly sensitive chemical sensors in aqueous medium.

3.6.1. Introduction

The residues of clothes and papers coloring industries are continuously accelerated the water pollution. The coloring includes several hazardous organics compounds which cause the serious environmental problems to human health and the aquaticmedium due to their toxicity and the carcinogenic effect [**342-344**]These harmful dyes are majorly mineralized by the heterogeneous catalytic process including photocatalytic and chemical oxidation processes [**342-344**].The photocatalytic decomposition by semiconductors nanomaterials is recently gained the most promising method for the decomposition/degradation of organic dyes in water to less harmful chemicals [**345,346**]. The metal oxides semiconductors are popularly employed as photocatalysts for the photocatalytic degradation of organic dyes owing to their wide band gap and high photosensitive nature [**347-349**]. The advance research is needed to develop efficient photocatalyst for the effective dye remediation.

On the other hand, the excess usage of the toxic chemicals as reacting species in most of the industries increases the environmental pollution [**249, 274**]. Among various chemicals, the phenolic compound, 4-nitrophenol (4NP) is extensively used as intermediates in various manufacturing industries of pharmaceuticals, analgesics, pesticides, dyes, and processing of leather [**350,351**]. Recently, 4NP is listed in the Environmental Protection Agency List of Priority Pollutants due to its high toxicity to the environment and human [**352-354**]. Therefore, a rapid and fast environmental monitoring system or device is required to detect and quantify the concentration of hazardous 4NP chemical for avoiding the water pollution and untoward effects on human health. In this regards, recently, a solution processed Ce-doped ZnO nanorods based chemical sensor for the detection of phenol derivatives called hydroquinone have been fabricated and reported in the literature [**355**]. J. Li et al. recently fabricated graphene oxide-based GC electrode based electrochemical sensor for the efficient detection of 4NP chemical. Therefore, the metal oxides semiconductors such as TiO_2, ZnO, SnO_2 and Fe_2O_3 could be the appropriate materials for the photocatalytic degradation of organic dyes and smart sensing electrode for chemical sensor.

Among them, iron oxide (α-Fe_2O_3, hematite) is recently receiving extensive attention as promising photocatalyst candidate due to its narrow band gap (2.0–2.2 eV) which could collect up to 40% of the solar spectrum energy, stability in most aqueous solutions and good magnetic properties [**356**]. Because of its excellent properties, to name a few, bio-compatible, thermodynamically stable, environmental friendly, low-synthesis cost, and so on, the α-Fe_2O_3 nanomaterials display the promising applications in several fields such as water splitting [**357**], sensors [**358**], Li-ion batteries and supercapacitors [**359**], photovoltaic [**360**], biomedical applications, etc. Recently, the utilization of α-Fe_2O_3 nanomaterials as photocatalyst has received great attention, especially for the degradation of harmful dyes and pollutants [**361**]. Importantly, it was examined that the performances of photocatalytic reactions are greatly influenced by particle size, shape and crystallinity of α-Fe_2O_3 nanomaterials [**362**]. The architectural aspects are still open to develop advance and efficient α-Fe_2O_3 nanomaterials for high performance photocatalytic reactions and highly sensitive system for the detection of hydroquinone chemical. Several efforts have been made to synthesize α-Fe_2O_3 nanostructures via sol-gel process [**363**], hydrothermal approach [**364**], and chemical precipitation [**365**], high energy ball milling [**366**] and so on.

In this paper, α-Fe_2O_3 hexagonal nanoparticles were synthesized, characterized and utilized as efficient photocatalysts for the degradation of hazardous RhB dye and as effective electron mediators for the fabrication of highly sensitive 4NP chemical sensors in aqueous medium.

3.6.2. Experimental Details

3.6.2.1. Synthesis of α-Fe_2O_3 hexagonal nanoparticles

α-Fe_2O_3 hexagonal nanoparticles were synthesized by facile hydrothermal process using iron chloride hexahydrate ($FeCl_3.6H_2O$) and hexamethylenetetramine (HMTA). In a typical reaction process for the synthesis of α-Fe_2O_3nanoparticles, 0.05M $FeCl_3.6H_2O$ was mixed with 0.03M HMTA in 50ml DI water under vigorous stirring. Subsequently, few drops of $NH_3.H_2O$ was added in the resultant solution to make the solution of pH=11 and stirred for 30min. After stirring, the resultant solution was loaded into a Teflon-lined stainless steel autoclave, sealed it and heated up to 130°C for 3h. After completing the reaction, the autoclave was naturally cool at room-temperature and finally dark brown product was obtained which was washed with DI water and ethanol sequentially. The obtained product was dried at 60°C for 2h. The synthesized products were examined in terms of their morphological, structural, photocatalytic and sensing properties.

3.6.2.2. Characterizations of as-synthesized α-Fe_2O_3 hexagonal nanoparticles

The as-synthesized α-Fe_2O_3 hexagonal nanoparticles were characterized in terms of their morphological, structural and optical properties. The general morphologies of as-synthesized nanoparticles are examined by FESEM while the detailed morphological investigations were done by TEM equipped with high-resolution TEM (HR-TEM). The crystallinity and crystal phases were examined by the XRD. The elemental and chemical compositions of as-synthesized α-Fe_2O_3 hexagonal nanoparticles were examined by EDS and FTIR spectroscopy, respectively. The scattering properties of as-prepared nanoparticles were examined by Raman-scattering spectroscopy.

3.6.2.3. Photocatalytic decomposition of Rhodamine B using as-synthesized α-Fe_2O_3 hexagonal nanoparticles

The photocatalytic degradation of RhB dye was carried out in a three neck pyrex flask reactor using α-Fe_2O_3nanoparticles as photocatalyst under UV illumination of xenon arc lamp (300W, Hamamatus: L 2479). For the photocatalytic degradation of RhB dye, 10ppm dye solution was prepared in 100ml DI water in which 0.15g photocatalyst (α-Fe_2O_3nanoparticles) was added and the resultant mixture was purged with Ar gas under continuous stirring. Consequently, the obtained suspension was equilibrated for 30min to stabilize the absorption of RhB dye over α-Fe_2O_3nanoparticles prior to the light exposure. The photocatalytic degradation of the RhB dye was estimated by measuring the absorbance of dye solution in the presence of photocatalyst exposed at different time intervals (10min). The absorbance was measured by UV-vis. Spectrophotometer. The degradation rate of RhB dye was estimated according to the following equation [**145,146**]**:**

$$\textbf{Degradation rate (\%)} = (C_o\text{-}C/C_o) \times 100 = (A_o\text{-}A/A_o) \times 100$$

Where C_o represents the initial concentration, C the variable concentration, A_o the initial absorbance, and A the variable absorbance.

3.6.2.4. Fabrication and characterization of 4-nitrophenol chemical sensor by I-V technique

For the fabrication of 4-nitrophenol chemical sensor, the glassy carbon electrode (GCE) was modified by using α-Fe_2O_3 hexagonal nanoparticles and used as working electrode. Prior to the modification, the surface of GCE was polished with alumina and thoroughly rinsed with DI water. To modify the electrode surface, slurry of α-Fe_2O_3 hexagonal nanoparticles were made by mixing an appropriate composition of nanoparticles and conducting agent (butyl carbital acetate). Finally, a small amount of the slurry was casted on GCE (surface area 0.0316 cm^2) surface, and then the modified electrode was dried in electric oven at 60 ± 5 ºC for 4h. To investigate the sensor analytical performance, I-V technique was used as mentioned in the reported literature [**355**]. For *I-V* measurements; Zahner electrochemical workstation was used in which the α-Fe_2O_3 hexagonal nanoparticles/GCE was used as a working electrode while Pt wire was employed as a counter electrode. The current response was measured from 0.0 to 0.9 V while the time delaying were 1.0 seccond. For all the measurements, the amount of 10.0 mL

PBS was kept constant. A wide concentration range (1.56 mM- 50 mM) was used for the concentration studies. All the sensing experiments were carried out at room-temperature.

3.6.3. Results and discussion

3.6.3.1. Morphological, structural and compositional properties of α-Fe_2O_3 hexagonal nanoparticles

The morphological and structural properties of as-synthesized iron oxide product was examined by FESEM and TEM and demonstrated in Fig. 1. Fig. 1(a) and (b) exhibit the typical FESEM images which reveal that the products are nanoparticles, prepared in large quantity and possessing hexagonal shape. The typical sizes of the nanoparticles are in the range of ~30 ± 10nm. The clear morphologies of as-prepared nanoparticles were examined by TEM which reveals that the prepared material possesses well-defined hexagonal nanoparticles which are grown in high-density (Fig. 3.6.1(c)). The TEM image is fully consistent with observed FESEM images. The detailed structural properties of as-prepared nanoparticles were examined by high-resolution TEM (HRTEM) which confirms the high-crystalline nature of as-synthesized nanoparticles. The HRTEM image exhibits the well-defined lattice fringes which are separated by 0.266nm and hence can be indexed to the (014) plane of the rhombohedral α-Fe_2O_3 structure.

The elemental compositions of as-prepared α-Fe_2O_3nanoparticles was examined by EDS and shown in Fig. 3.6.2(a). The EDS spectrum revealed that the as-synthesized nanoparticles are composed of iron and oxygen. Moreover, no peak related with any impurity or other element is found in the spectrum which confirmed that the synthesized nanoparticles are pure iron oxide without any significant impurity. The crystallinity and crystal phases of as-prepared nanoparticles were investigated by XRD in the range of 10-70°.

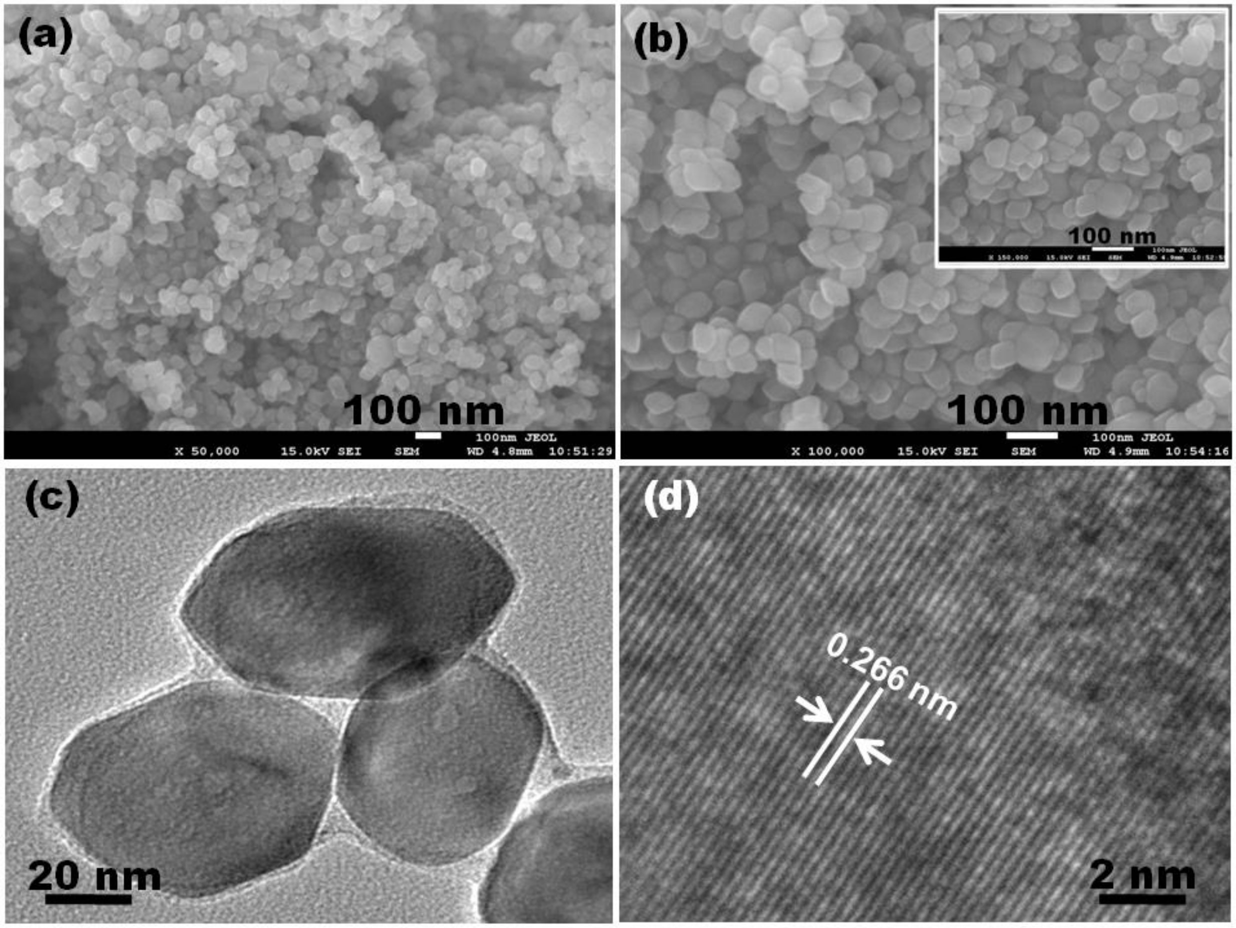

Figure 3.6.1. Low (a) and (b) high-magnification FESEM images, (c) Low and (d) high-resolution TEM images of as-synthesized α-Fe_2O_3 hexagonal nanoparticles

Several well-defined diffraction reflections are seen in the observed XRD pattern which is well matched to the rhombohedral α-Fe_2O_3structures (JCPDS 84-0311). Due to sharp diffraction reflections, it can be concluded that the synthesized nanoparticles are well-crystalline. Except of rhombohedral α-Fe_2O_3 phase, no other reflection related with any impurity was observed in the pattern which confirms that the as-synthesized products are pure and well crystalline. The chemical composition of as-synthesized α-Fe_2O_3 nanoparticles was examined by FTIR measurement, carried out at room-temperature in the range of 430-4000cm^{-1} (Fig.3.6.2(c)). Three well-defined absorption bands have been observed in the FTIR spectrum at 469, 575, and 3442cm^{-1}. The appearance of two sharp absorption bands at 469cm^{-1} and 575cm^{-1} are due to the formation of Fe-O bonds which clearly confirmed the formation of iron oxide crystals [**367**]. The presence of vary short band at 3442 cm^{-1} is mainly because of the surface hydroxyl and O-H stretching mode which generally appeared when the FTIR measurements are done at room-temperature. Importantly, except Fe-O, no other significant absorption peak was seen in the spectrum which confirmed that the synthesized nanoparticles are highly pure iron oxide without any impurity.

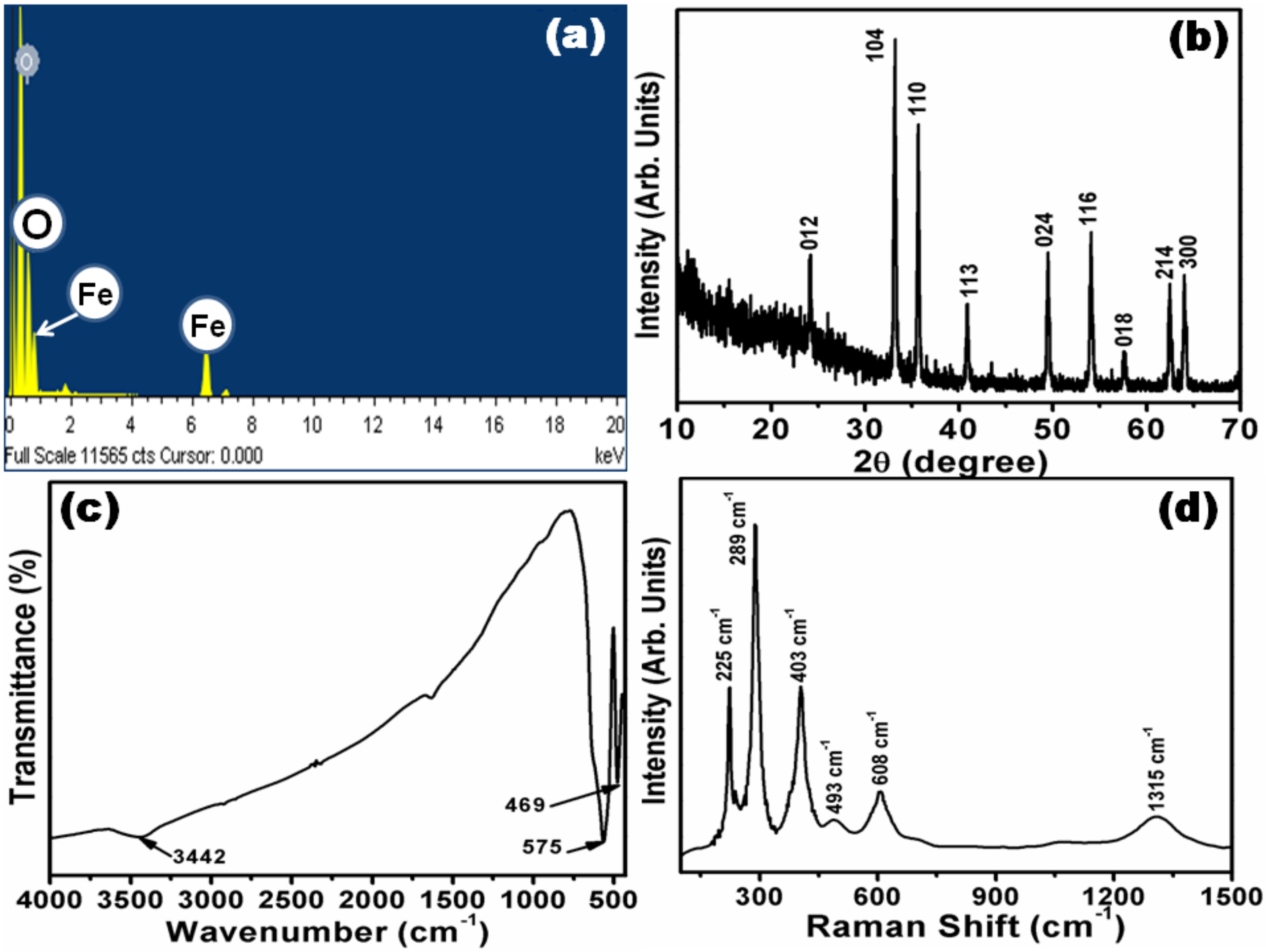

Figure 3.6.2. (a) EDS spectrum, (b) XRD pattern, (c) FTIR spectrum and (c) Raman-scattering of as-synthesized α-Fe_2O_3 hexagonal nanoparticles

Further to check the crystallinity, purity and scattering properties, the as-synthesized α-Fe_2O_3 nanoparticles were examined by Raman-scattering at room-temperature (Fig. 3.6.2 (d)). The α-Fe_2O_3 (hematite) belongs to D^6_{3d} crystal space group and group theory predicts seven phonon lines in the Raman spectrum [**368**]. Several well defined peaks at 225, 289, 403, 493, 608, and 1315cm^{-1}were observed in the Raman-scattering spectrum which confirmed that the synthesized nanoparticles are pure α-Fe_2O_3. The peaks appeared at 225 and 608cm^{-1} are assigned as Raman-active A_{1g}(1) and A_{1g}(2) modes, respectively. The appearances of other well-defined peaks at 289, 403, and 493cm^{-1} are related with Raman-active E_g modes. A small and suppressed peak appeared at 1315cm^{-1} are related with the second harmonic vibration mode.

3.6.3.2 Photocatalytic degradation of Rhodamine B using α-Fe_2O_3 hexagonal nanoparticles

The as-synthesized α-Fe_2O_3 nanoparticles were used as an efficient photocatalyst for the photocatalytic degradation of RhB dye under UV-light irradiation. The degraded RhB-dye over synthesized α-Fe_2O_3 nanoparticles was measured by UV-Vis absorption spectra of centrifuged dye solution in every 10min time interval, as shown in Fig. 3.6.3(a). The relative intensity of absorbance in UV-Vis spectra is analyzed to estimate the %degradation of RhB dye. The strong absorbance at 554 nm in UV-Vis has been observed by the degraded RhB-dye under UV light irradiation. The relative intensity of absorbance was continuously decreasing with increasing the exposure time of UV-light irradiation, indicating the continuous degradation of RhB-dye over the surface of synthesized α-Fe_2O_3 nanoparticles. It is estimated that the synthesized α-Fe_2O_3 nanoparticles substantially degraded the RhB dye by ~ 79% in 140min.

Fig. 3.6.3(b) shows the plot of degradation rate versus time interval, and depicts the gradual increase of RhB-dye degradation rate under UV-light irradiation. Noticeably, a negligible degradation rate of RhB-dye is seen when photocatalytic reaction is performed under UV-light irradiation without α-Fe_2O_3 nanoparticles, confirms that degradation of RhB dye proceeds over the surface of α-Fe_2O_3 nanoparticles. Similar patterns have been observed in the plot of the variation in the relative concentration (A/A_o) versus time interval (Fig. 3.6.3(c)) for the degradation of RhB-dye over the surface of synthesized α-Fe_2O_3 nanoparticles under UV-light irradiation. Fig. 3.6.3(d) presents the pie chart of RhB-dye degradation which is evidenced that the most of RhB dye degradation is seen in 70 min over the surface of synthesized α-Fe_2O_3 nanoparticles. Thus, these results confirm the efficient RhB-dye degradation under UV-light illumination by synthesized α-Fe_2O_3 nanoparticles.

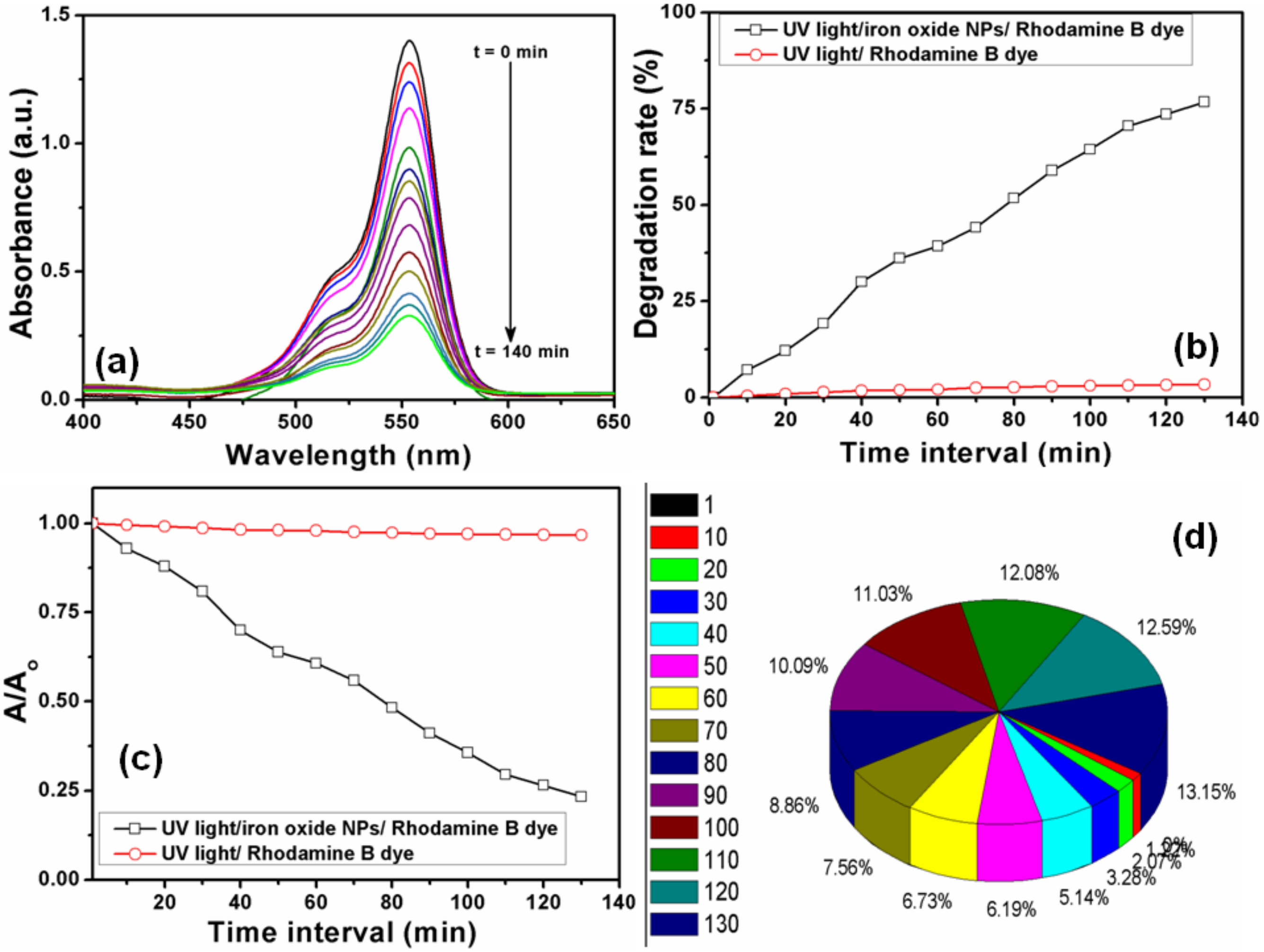

Figure 3.6.3. (a) UV–Vis absorbance spectra of decomposed RhB dye solution by light over as-synthesized α-Fe_2O_3 hexagonal nanoparticles, (b) degradation rate (%) and (c) extent of decomposition (A/Ao) of RhB dye with respect to time intervals, (d) pie-diagram for the photocatalytic degradation of as-synthesized α-Fe_2O_3 hexagonal nanoparticles

Figure 3.6.4 exhibits a schematic of RhB-dye degradation over the surface of α-Fe_2O_3 hexagonal nanoparticles under UV light illumination. Generally, the RhB-dye degradation could be explained by the separation of electron–hole ($\bar{e}$–h^+) pairs between the conduction (CB) and valence bands (VB) and high surface area of synthesized α-Fe_2O_3 nanoparticles. Moreover, during the separation of ($\bar{e}$–h^+) pairs, the formation of oxy-radicals such as hydroxyl (OH•)and superoxide (O_2•, HO_2•) are usually determined the degradation of organic dyes under light irradiation [**369**] which are generated on the surface of semiconductors [**268].**The following steps are involved for the generation of oxy-radicals during the photo-degradation of RhB-dye [**370**];

$$\alpha\text{-}Fe_2O_3 + h\upsilon \rightarrow \alpha\text{-}Fe_2O_3^{*}\ (\bar{e}\text{–}h^{+}) \tag{3.6.1}$$

$$h^{+} + H_2O \rightarrow \bullet OH + H^{+} \tag{3.6.2}$$

$$\bar{e} + O_2 \rightarrow O_2^{-} \tag{3.6.3}$$

$$O_2^{-} + H^{+} \rightarrow HO_2\bullet \tag{3.6.4}$$

$$O_2^{-} + RhB \rightarrow RhB^{+}\bullet\ \text{-}O_2 \tag{3.6.5}$$

$$\bullet OH + RhB^{+}\bullet \rightarrow CO_2 + H_2O \tag{3.6.6}$$

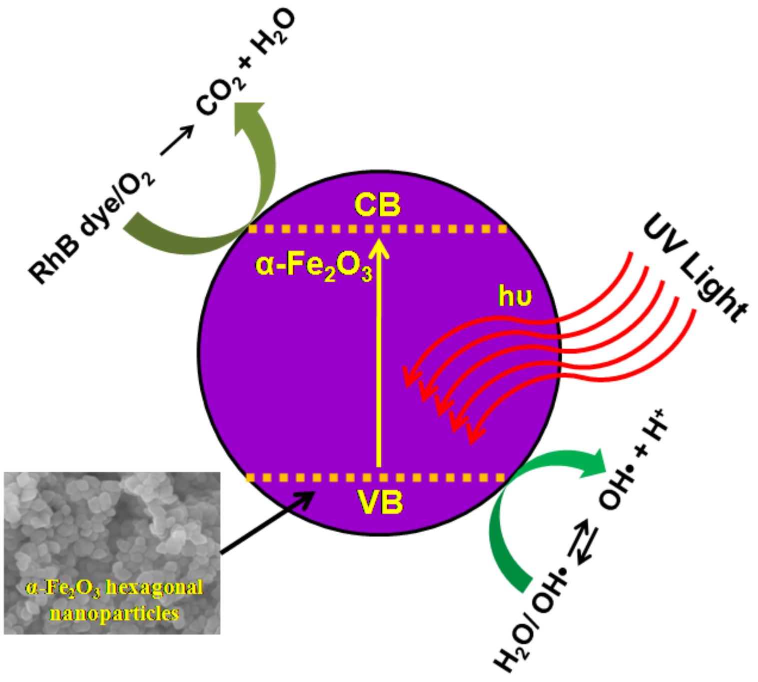

Figure 3.6.4. A schematic of RhB dye degradation over the surface of as-synthesized α-Fe_2O_3 hexagonal nanoparticles under UV light illumination

From the above steps, the high surface area of synthesized α-Fe_2O_3 nanoparticles sufficiently produces the active oxygen species {O_2, O_2^-, HOO•/•OH} which are significantly responsible for high degradation of RhB-dye into less harmful organics. Therefore, the synthesized α-Fe_2O_3 nanoparticles with high surface exhibits the high degradation of RhB-dye under UV-light irradiation due to generation of RhB^+•and oxyradicals on the surface of synthesized α-Fe_2O_3 hexagonal nanoparticles.

3.6.3.3. 4-Nitrophenol chemical sensor application of α-Fe_2O_3 hexagonal nanoparticles

The current (I)–voltage (V) measurements of the fabricated 4NP chemical sensor are performed to evaluate the sensing properties such as sensitivity, detection limit and correlation coefficient. The fabricated 4NP chemical sensor is composed of α-Fe_2O_3 hexagonal nanoparticles electrode as working electrode and Pt wire as counter electrode in 0.1M PBS. From Fig. 3.6.5 (a), a large increment in current is detected after addition of 4NP in PBS, whereas a low current is observed by sensor without 4NP chemical, which suggests that α-Fe_2O_3 hexagonal nanoparticles based electrode is highly active to 4NP chemical. Fig. 3.6.5(b) shows a series of the *I–V* curves of the fabricated 4NP chemical sensor with α-Fe_2O_3 hexagonal nanoparticles based electrode to investigate the detail sensing behavior and parameters. The fabricated 4NP chemical sensor presents a continuous increase in current upon the incremental addition of 4NP with the concentrations range from ∼1.56 mM – 50 mM. The continuously increased current might arise from the formation of large number of ions and the heightening in the ionic strength of the solution with the addition of 4NP. A plot of calibrated current versus 4NP concentrations (Fig. 3.6.5(c)) is drawn to estimate the sensitivity of the fabricated 4NP chemical sensor. It is seen that the calibrated current linearly increases as increasing the 4NP concentrations from 1.56 mM – 50 mM. High reproducible sensitivity of ~ 367.6 $\mu A.M^{-1}.cm^{-2}$ and good experimental detection limit of ~ 1.56 mM with correlation coefficient (R) of ∼0.99963 is attained by the fabricated 4NP chemical sensor with α-Fe_2O_3 hexagonal nanoparticles based electrode. A good linearity by the fabricated 4NP chemical sensor with α-Fe_2O_3 hexagonal nanoparticles based electrode is achieved in the range of ∼1.56 mM – 12.5mM.. The high sensitivity of 4NP chemical sensor might be attributed to the highly active surface of α-Fe_2O_3 hexagonal nanoparticles based electrode which might have large number of oxygenated species over the surface of α-Fe_2O_3 hexagonal nanoparticles. In this regards, Fig.

3.6.6 exhibits the mechanistic illustration of fabricated 4NP chemical sensor with α-Fe_2O_3 hexagonal nanoparticles based electrode. In electrochemical sensor, the oxygenated species are initially adsorbed on the α-Fe_2O_3 hexagonal nanoparticles based electrode after dipping into PBS in electrochemical system. Afterwards, the ionic species such as O^{2-} and O^{-} are formed after gaining the electrons from the conduction band of α-Fe_2O_3 hexagonal nanoparticles [**371, 372**].

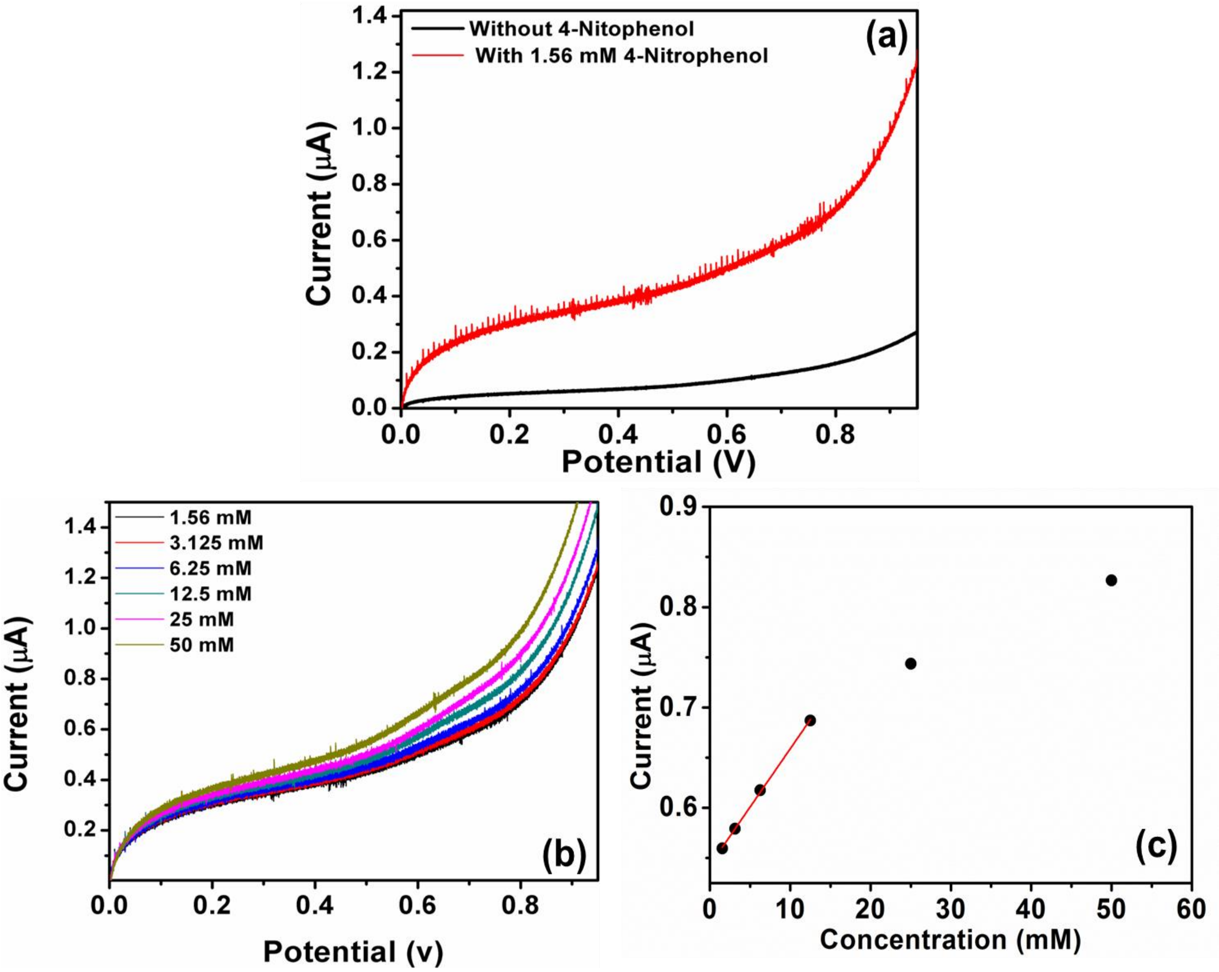

Figure 3.6. 5. (a)Typical *I-V* responses of α-Fe_2O_3 hexagonal nanoparticles modified GCE in 10 ml, 0.1 M PBS solution, (Black line) without 4 nitro-phenol and (red line) with 4-nitro-phenol (1.56 mM); (b) I-V response for various concentrations of 4 nitro-phenol (from 1.56 mM ~ 50 mM) and (c) calibration curve

These ionic species react with 4NP chemicals and converts into 4-nitroso phenol which again extradites electron to the conduction band of in presence of α-Fe_2O_3 hexagonal nanoparticles. This phenomenon is significantly increased the current and decreased the resistance of α-Fe_2O_3 hexagonal nanoparticles based electrode due to fast conduction of electrons during the sensing measurements. The multiple *I*–*V* measurements are performed for three consecutive weeks to investigate the reproducibility and the stability of fabricated 4NP chemical sensor with α-Fe_2O_3 hexagonal nanoparticles based electrode. No significant drop is observed in the sensing parameters, indicating the long term stability of the fabricated 4NP chemical sensor and high stability of α-Fe_2O_3 hexagonal nanoparticles based electrode.

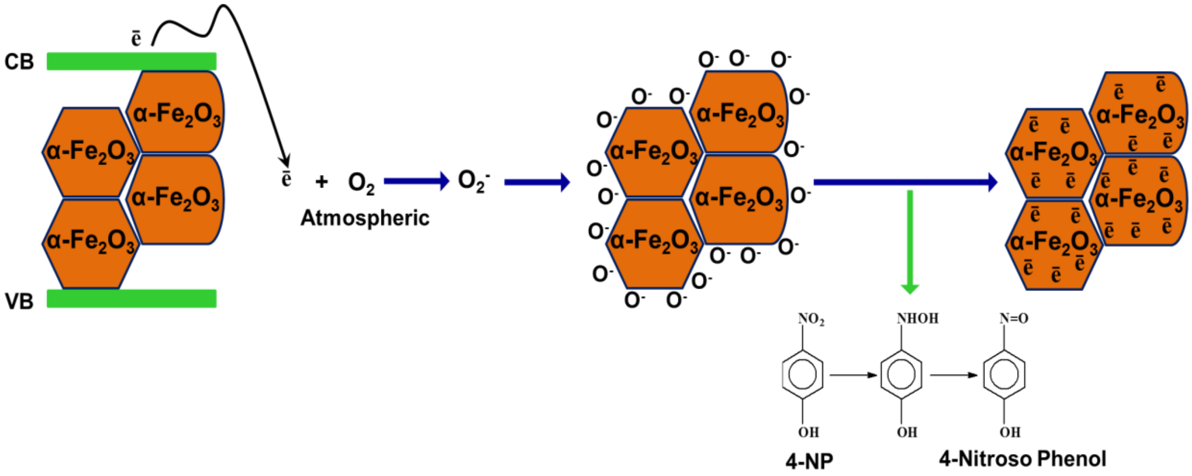

Figure. 3.6.6. (a) Schematic representation of 4 nitro-phenol chemical sensor fabricated based on I-V technique using α-Fe_2O_3 hexagonal nanoparticles modified GC electrode as working electrode; (b) chemical reaction describing the sensing mechanism

The fabricated 4NP chemical sensor exhibited better sensitivity and low-experimental detection limit as compared to those phenol based chemical sensors reported in the literature fabricated based on nanomaterials based electrodes. Table 3.6.1 exhibits the comparison summary of the performances of 4-NP chemical sensors fabricated based on the utilization of various nanomaterials as electron mediators. It is apparent from the table 3.6.1 that the fabricated 4-NP chemical sensor based on α-Fe_2O_3 hexagonal nanoparticles exhibits better sensitivity and lower experimental detection limit which confirmed that the fabricated sensor is promising candidate for the effective detection of 4-NP. The sensing properties and parameters are comparable to reported literatures, as summarized in table 3.6.1. Finally the high adsorption ability through the surface of α-Fe_2O_3 hexagonal nanoparticles results the efficient electro-catalytic activity towards 4NP chemical and exhibits the high sensitivity of the fabricated 4NP chemical sensor.

Table 3.6.1. The comparison summary of the performances of 4-NP chemical sensors fabricated based on the utilization of various nanomaterials as electron mediators.

Materials	Limit of detection	Linearity	Correlation coefficient (R^2)	Sensitivity	Ref.
Pt/PEDOT-PB[a]	8.23μM	2 to 100μM	0.99108	0.116μA/μM	[**373**]
LiTCNE/GCE[b]	7.5 nmol/L	27-23200 nmol/L	-	3.057 nA.nmol^{-1}.cm^{-2}	[**374**]
Carbon nanotube modifiedelectrode	4.0 × 10^{-7}	2.0 μM-4.0 mM	-	-	[**375**]
HRP-TiO_2nanotube[c]	2×10^{-7}M	0.8–130μM	0.993	0.19μA/μM	[**376**]
α-Fe_2O_3 hexagonal nanoparticles/GCE	**1.56 mM**	**1.56 – 12.5 mM**	**0.99963**	**367.6 nA.mM^{-1}.cm^{-2}**	**This work**

[a] poly(3,4-ethylenedioxythiophene) (PEDOT)/Prussian blue/polyazulene
[b] lithiumtetracyanoethylenide/glassy carbon electrode
[c] HRP = Horseradish peroxidase.

3.6.4. Conclusion

In summary, α-Fe_2O_3 hexagonal nanoparticles are synthesized by simple solution methods and applied as photocatalyst for the photocatalytic degradation of hazardous RhB-dye and as efficient electron mediator for the fabrication of effective 4-nitrophenol chemical sensor. By detailed morphological and compositional studies, it was confirmed that the as-synthesized α-Fe_2O_3 hexagonal nanoparticles possess well-crystalline, hexagonal disk shape and grown in high-density.The as-synthesized α-Fe_2O_3nanoparticles were used as efficient photocatalyst and exhibit a substantial degradation (~79%) of RhB-dye in 140 min which was mainly due to specific morphologies of as-synthesized as it imports the effective electron/hole separation for the generation of the large number of oxy-radicals which contribute in the degradation process. The fabricated 4NP chemical sensor based on α-Fe_2O_3 hexagonal nanoparticles shows a high and reproducible sensitivity of ~ 367.6 μA.M^{-1}.cm^{-2} and low-detection experimental limit of

~1.56 mM with correlation coefficient (R) of ∼0.99963. This work demonstrates that simply prepared α-Fe_2O_3 nanomaterials can efficiently be used as a photocatalyst for the photocatalytic degradation of organic pollutants and as effective electrode materials for the fabrication of highly sensitive sensor for the detection of hazardous and toxic chemicals.

CHAPTER-4 OVERALL CONCLUSION

In recent years, numerous intensive reseacrh efforts in the field of nanotechnology has shown great potentials. There have been significant improvements for the synthesis of desired inorganic nanomaterials and their several potential applications are presented by the scientists and reported in the literature. The development of nanomaterials help us to move towards a bright and comfortable future. These materials offer more precise methods of addressing the several unsolved problems and needs of the mankind. There are endless possibilities for improved devices, structures and materials if understanding can be developed for assembly at small structures. Nanotechnolgy has reached to the level of leading science with fundamental and research prospects in all basic cognitive sciences.An important feature of the nanotechnology is to bridge the gap between the atomic and molecular scale of fundamental sciences and the microstructural scale of engineering and manufacturing. Accordingly, a wide interdisciplinary knowledge is to be explored and linked for the benefit of mankind. It will lead to an understanding as well as to the fabrication of novel high technological devices. The product of nanotechnology is not itself a product, but it goes into something , for example, in a computer that becomes a product.

The overall conclusions of our work as presented in the previous chapter is presented here systematically as

A brief introduction of metal oxide nanostructures, their various synthetic methods and the properties of targeted metal oxides, i.e. undoped and doped ZnO and iron oxide have been presented in chapter 1. In addition to this, the utilization of prepared metal oxide nanomaterials for sensing, photovoltaic and photocatalytic applications are also demonstrated in this chapter. Finally, the chapter 1 describes the objective and importance of the thesis.

The prepared metal oxide nanomaterials were mainly synthesized by two techniques, i.e. hydrothermal and thermal evaporation processes and characterized in detail in terms of their morphological, structural, compositional, optical and electrical properties. Further, the prepared metal oxide nanomaterials were used for the fabrication of various high efficient sensing, photovoltaic (dye-sensitized solar cells) and photocatalytic applications. These all details are mentioned in chapter 2.

The main results and discussion of the obtained research results are demonstrated and discussed in chapter 3. This chapter is divided into several sections and each section exhibited the synthesis, properties and specific application of targeted metal oxide nanomaterials. The growth, characterization and ammonia chemical sensing applications of well-crystalline ZnO nanopencils were demonstrated in section 3.1. The ZnO nanopencils were grown via facile and simple hydrothermal process using commonly used laboratory chemicals. Importantly, due to well-crystallinity and higher surface area of the synthesized ZnO nanopencils; the fabricated sensor offers ultra-high sensitivity towards the efficient detection of liquid ammonia. The fabricated liquid ammonia chemical sensor exhibited ultra-high sensitivity of ~26.58 μA cm^{-2} mM^{-1} and very low experimental detection limit of ~ 5nM.

Section 3.2 demonstrates the hydrothermal synthesis of well-crystalline ZnO balls made of intermingled nanocrystalline NS and their use as effective anode photo-anode materials to fabricate efficient DSSCs. The detailed characterizations revealed that the prepared ZnO balls are possessing well-crystalline wurtzite hexagonal phase and exhibited good optical properties. Moreover, the fabricated DSSCs exhibited an overall light-to-electricity conversion efficiency of 2.1 % with a short-circuit current of 6.28 mA/cm^2, open-circuit voltage of 0.659 V and fill factor of 0.51. The obtained results revealed that simply synthesized ZnO nanomaterials can efficiently be used for the fabrication of high-efficient dye-sensitized solar cell applications.

Using simple and facile hydrothermal approach, Ag-doped ZnO nanoflowers were synthesized and characterized in detail which revealed that the prepared nanomaterials are well-crystalline and exhibiting good optical properties. Moreover, the synthesized Ag-doped ZnO nanoflowers were used as supporting matrixes for the fabrication of phenyl hydrazine chemical sensors. The fabricated phenyl hydrazine chemical sensor exhibited high-sensitivity of ~557.108 ± 0.012 μA.cm^{-2}.mM^{-1} and experimental detection limit of ~ 10 nM with correlation coefficient (R) of 0.97712. The details of Ag-doped ZnO nanoflowers and their efficient phenyl hydrazine sensor are presented in section 3.3.

Section 3.4 describes the Ce-doped ZnO nanorods for the detection of hazardous chemical; hydroquinone. The Ce-doped ZnO nanorods were prepared by simple and facile hydrothermal process and characterized in detail which confirmed the well-crystallinity of the prepared nanorods. The prepared Ce-doped ZnO nanorods were used to fabricate an efficient, robust, and highly sensitive with low-experimental detection limit hydroquinone chemical sensor. The fabricated hydroquinone chemical sensor exhibited a high and a reproducible sensitivity of ~10.218±0.01 mA.cm^{-2}.mM^{-1} with experimental detection limit of ~10 nM.

The growth and characterizations of In-doped ZnO hollow spheres composed of NS networks and nanocones are presented in section 3.5. The In-doped ZnO hollow spheres composed of NS networks and nanocones were grown on Si (100) substrate and examined in terms of their morphological, compositional, structural and optical properties. The detailed morphological studies revealed that the synthesized products are hollow spheres composed of NS networks and nanocones and grown in high-density. The observed structural properties exhibited well-crystallinity and wurtzite hexagonal phase for the grown materials. The room-temperature PL spectrum showed a broad band in the visible region with a suppressed UV emission and hence due the enhancement in the green emission, the prepared materials exhibits a great interest in the area of ZnO phosphors, such as field emissive display technology, etc.

Finally, section 3.6 demonstrated the successful synthesis and detailed characterization of α-Fe_2O_3 hexagonal nanoparticlesfor environmental remediation and smart sensor applications. The synthesized nanoparticles were synthesized by facile hydrothermal process and examined in detail using various analytical tools. The detailed characterizations studies revealed that the prepared nanoparticles are well-crystalline, possessing hexagonal shape, grown in high density and exhibiting good optical properties. The prepared α-Fe_2O_3 hexagonal nanoparticles were used as efficient material for the fabrication of 4-nitrophenol chemical sensor and as effective photocatalyst for the photocatalytic degradation of highly hazardous RhB dye. The fabricated 4-nitrophenol chemical sensor based on α-Fe_2O_3 hexagonal nanoparticles shows a high and reproducible sensitivity of ∼ 367.6 $\mu A.M^{-1}.cm^{-2}$ and experimental detection limit of ~1.56 mM with correlation coefficient (R) of ∼0.99963. Moreover, the prepared nanoparticles exhibiteda substantial degradation (~79%) of RhB-dye in 140 min which was mainly due to specific morphologies of as-synthesized as it imports the effective electron/hole separation for the generation of the large number of oxy-radicals which contribute in the degradation process.

Finally, it is concluded that the presented thesis has explored the successful synthesis, characterization and applications of undoped and doped ZnO and α-Fe_2O_3nanostructures, prepared by two simple techniques, i.e. hydrothermal and thermal evaporation process. By detailed studies presented in this thesis, it is obvious that the simply synthesized metal oxide materials can efficiently be used for various effective sensing, photovoltaic and photocatalytic applications. Even though we have targeted only two metal oxide nanomaterials, from their synthesis to potential applications, for this thesis but it is my personal belief that due to the excellent properties, the metal oxide class of nanomaterials will be used for wide applications. Finally, I hope that the work presented in this thesis has contributed in some or other way in the synthesis, characterization and potential applications of some undoped and doped ZnO and α-Fe_2O_3nanostructures.

References

[1]. C. N. R. Rao, A. Muller, A. K. Cheetham, The Chemistry of Nanomaterials: Synthesis, Properties and Applications Willey, Weinheim (2004).

[2]. A. K. Bandyopadhyay, Nano Materials: in Architecture, Interior Architecture and Design, New Age International, New Delhi (2008).

[3]. J. D. Meindl, Q. Chen and J. A. Davis, Science 293 (2001) 2044.

[4]. C. M. Leiber, Sci. Am. 58 (2001).

[5]. P. Yang, MRS Bull. 30 (2005) 85.

[6]. D.C. Coffey and D. S. Ginger, Nature Materials 5 (2006) 735.

[7]. M. Muccini, Nature Materials 5 (2006) 605.

[8]. K. Nomura, H. Ohta, A. Takagi, T. Kamiya, M. Hirano and H. Hosono, Nature 432 (2004) 488.

[9]. J. L. G. Fierro, Metal Oxides: Chemistry and Applications, CRC Press, Florida (2006).

[10]. V. E. Henrich, P. A. Cox, The Surface Chemistry of Metal Oxides, Cambridge University Press, Cambridge, UK (1994).

[11]. C. Noguera, Physics and Chemistry at Oxide Surfaces, Cambridge University Press, Cambridge, UK (1996).

[12]. A. R. José, F.-G. Marcos, Synthesis, Properties, and Applications of Oxide Nanomaterials, Willey, New Jersey (2007).

[13]. Y. Y. Wu, H. Q. Yan, M. Huang, B. Messer, J. H. Song, P. D. Yang, Chem. Eur. J. 8 (2002) 1261.

[14]. C. N. R. Rao, F. L. Deepak, G. Gundiah, A. Govindaraj, Prog. Solid State Chem. 31 (2003) 5.

[15]. Z. R. Dai, Z. W. Pan, Z. L. Wang, Adv. Func. Mater. 13 (2003) 9.

[16]. D. V. Bavykin, J. M. Friedrich, F. C. Walsh, Adv. Mater. 18 (2006) 2807.

[17]. C. Nutzenadel, A. Zuttell, D. Chartouni, G. Schmid, L. Schlapbach, Eur. Phys. J. D 8 (2000) 245.

[18]. G. C. Bond, C. Louis, D. T. Thompson, Catalysis by Gold, Imperial College Press, London (2006).

[19]. Z. Wang, X.-F. Qian, J. Yin, and Z. Zhu, Journal of Solid State Chemistry. 177 (2004) 2144.

[20]. L. E. Greene, M. Law, J. Goldberger, F. Kim, J. C. Johnson, Y. Zhang, R. J. Saykally, and P. Yang, Angew. Chem. Int. Ed. 42 (2003) 3031.

[21]. F. Bai, P. He, Z. Jia, X. Huang, and Y. He, Mater. Lett. 59 (2005) 1687.

[22]. B. Liu, and H. C. Zheng, J. Am. Chem. Soc. 126 (2004) 8124.

[23]. H. Jiang, T. Herricks, and Y. Xia, Nano Lett. 2 (2002) 1333.

[24]. H.-H. Lin, C.-Y. Wang, H. C. Shih, J.-M. Chen, and C.-T. Hsieh, J. Appl. Phys. 95 (2004) 5889.

[25]. G. Boschloo and A. Hagfeldt, J. Phys. Chem. B 105 (2001) 3039.

[26]. X. M. Liu and X. G. Zhang, Electrochimica Acta 49 (2004) 229.

[27]. Y.-N. Nuli, S.-L. Zhao, and Q.-Z. Qiu, Journal of Power Sources 114 (2003) 113.

[28]. Z. R. Dai, Z. W. Pan, and Z. L. Wang, J. Phys. Chem. B 106 (2002) 902.

[29]. G. Gundiah, A. Govindaraj, C. N. R. Rao, Chem. Phys. Lett. 351 (2002) 189.

[30]. Y. G. Wang, A. Z. Jin, and Z. Zhang, Appl. Phys. Lett. 81 (2002) 4425.

[31]. S. Papaefthimiou, G. Leftheriotis and P. Yianoulis, Ionics 4 (1998) 321.

[32]. Y. J. Xing, Z. H. Xi, X. D. Zhang, J. H. Song, R. M. Wang, J. Xu, Z. Q. Xue, and D. P. Yu, Appl. Phys. A 80 (2005) 1527.

[33]. K. Frohlich, R. Luptak, E. Dobrocka, K. Husekova, K. Cico, A. Rosova, M. Lukosius, A. Abrutis, P. Pisecny, and J. P. Espinos, Mater. Sci. in Semicond. Proces. 9 (2006) 1065.

[34]. D. H. Park, S. T. Lim, and S. J. Hwang, Electrochimica Acta 52 (2006) 1462.

[35]. W. H. Zhang, and J. S. Zhao, Journal of Molecular Structure 789 (2006) 177.

[36]. S.Y. Bae, H.W. Seo and J.H. Park, J. Phys. Chem. B 108 (2004) 5206,

[37]. Y.J. Chem, J.B. Li, et al, J. cryst. Growth 245 (2002) 163.

[38]. J.M. Wu, H.C. Shih, W.T. Wu, Y.K. Tseng and I.C. Chen, J. Cryst. Growth 281 (2005) 384.

[39]. Z.R. Dai, J.L. Gole, J.D. Stout and Z.L. Wang, J. Phys. Chem. B 106 (2002) 1274.

[40]. L. Dai, X.L. Chen, et al., Appl. Phys. A Mater. Sci. Process. 75 (2002) 687.

[41]. P.C. Chang, Z.Y. Fan, W.Y. Tseng, A. Rajagopal, J.G. Lu, Apply. Phys. Lett. 87 (2005) 2221002.

[42]. X. Wen, S. Wang, Y. Ding, Z.L. Wang and S. Yang, J. Phys. Chem. B 109 (2005) 215.

[43]. J.Zhou, L. Gong, et al., Apply. Phys. Lett. 87 (2005) 223108.

[44]. Y. Xia, P. Yang, Y.G. Sun, Y.Y. wu, B. Mayers et al., Adv. Mater. 15 (2003) 353.

[45][175]. A. Umar and Y.B. Hahn, nanotechnology 17 (2006) 2174.

[46].[174] A. Umar and Y.B. Hahn, Apply. Phys. Lett. 88 (2006) 173120.

[47]. A. Sekar, S.H. Kim, A. Umar and Y.B. Hahn, J.Crystal. Growth 277 (2005) 471.

[48]. A. Umar, S.H. Kim, Y.S. Lee, K.S. Nahm and Y.B. Hahn, J.Crystal. Growth 282 (2005) 131.

[49]. A. Umar , S. Lee, et al., J.Crystal. Growth 277 (2005) 479.

[50]. A. Umar, S. Lee, Y.H. Im and Y.B. Hahn, Nanotechnology 16 (2005) 2462.

[51]. A. Umar, S.H. Kime, Y.H. Im and Y.B. Hahn, Superlatt. Micrsostruc. 39 (2006) 238.

[52]. J. Zhou, Y. Ding, et al., Adv. Mater. 17 (2005) 2107.

[53]. J.Q. Hu, X.L. Ma, et al., J. Phys. Chem. B 106 (2002) 3823.

[54]. H.W. Kim and N.H. Kim, Appl. Phys. Mater. Sci. Process. 81 (2005) 763.

[55]. Q. Zhao, X. Xu, h. Zhang, Y. Chen, J. Xu and D. Yu, Appl. Phys. A Mater. Sci. Process. 79 (2004) 1721.

[56]. W. I. Park, D. H. Kim, S.-W. Jung, and G.C. Yi, Appl. Phys. Lett. 80 (2002) 4232.

[57]. B.P. Zhang, N.T. Binh, Y. Segawa, K. Wakatsuki and N. Usami, Appl. Phys. Lett. 83 (2003) 1635.

[58]. W. Lee, H.G. Sohn and J.M. Myoung, Mater. Sci. Forum 449 (2004) 1245.

[59]. J. Su, M. Gherasimova, et al., Appl. Phys. Lett. 87 (2005) 183108

[60]. T.T. Kang, X. Liu, R.Q. Zhang, W.G. Hu, G. Cong, F.Zhao and Q. Zhu, Appl. Phys. Lett. 89 (2006) 071113.

[61]. J.B. Baxter, E.S. Aydil, Appl. Phys. Lett. 86 (2005) 053114.

[62]. B.Liu and H.C.Zeng, J.Am. Chem. Soc. 125 (2003) 4430.

[63]. M. Guo, P. Diao and S.M. Cai, J. Solid State Chem. 178 (2005) 1864.

[64]. M.H. Cao, Y.H. Wang, et al., J. Nanosci. Nanotechnol. 4 (2004) 824.

[65]. J.Zhang, Z.G. Liu, et al., J.Crystal. Growth 280 (2005) 99.

[66]. D.S. Zheng, S.X. Sun, et al., J. Phys. Chem. B 109 (2005) 16439.

[67]. K.B. Zhou, X. Wang, et al., J. Catal. 229 (2005) 206.

[68]. Z.Y. Yuan and B.L. Su, Colloids Surf. A Physicochem. Eng. Aspects 241 (2004) 173.

[69]. G. Cao, “Nanostructures & Nanomaterials: Synthesis, Properties & Applications”, Imperial College Press, London (2004).

[70]. F.E. Kruis, H. Fissan, A. Peled, J. Aerosol Sci. 29 (1998) 511.

[71]. R. Strobel, S.E. Pratsinis, J. Mater. Chem. 17 (2007) 4743.

[72]. S. Iijima, Nature 354 (1991) 56.

[73]. C.B. Murray, D.J. Norris, M.G. Bawendi, J. Am.Chem. Soc. 115 (1993) 8706.

[74]. X.G. Peng, L. Manna, W.D. Yang, J. Wickham, E. Scher,A. Kadavanich, A.P. Alivisatos, Nature 404 (2000) 59.

[75]. A. Henglein, Chem. Rev. 89 (1989) 1861.

[76]. A.P. Alivisatos, J. Phys. Chem. 100(13) (1996) 226.

[77]. C. Burda, X. Chen, R. Narayanan, M.A. El-Sayed, Chem. Rev. 105 (2005) 1025.

[78]. G.A. Ozin, Chem. Commun. (2000) 419.

[79]. G.M. Whitesides, B. Grzybowski, Science 295 (2002) 2418.

[80]. W. Lu, C.M. Lieber, Nature Mater. 6 (2007) 841.

[81]. R.S. Wagner and W.S. Ellis, Apply. Phys. Lett. 4 (1964) 89.

[82]. R.S. Wagner, W.C. ellis, S.M. Arnold and K.A. Jackson, J. Appl. Phys. 35 (1964) 2993.

[83]. Y.Wu and P. Yang, J. Am. Chem. Soc. 123 (2001) 3165.

[84]. H.M. Smith and A.F.Turner , Appl. Opt. 4 (1965) 147.

[85]. R. Kelly and A. Miotello, in: Pulsed Laser Deposition of Thin Films (New York: Wiley), (1994) 55.

[86]. A. Miotello and R. Kelly, Appl. Phys. A 69 (1999) S67.

[87]. D.B. Geohegan, Pulsed Laser Deposition of Thin Films ed D H Chrisey and G K Hubler (1994) (New York: Wiley).

[88]. H. Sankur, W.J. Gunning, J. DeNatale and J.F. Flintoff , (1989).

[89]. I. Ohkubo, Y. Matsumoto, T. Hasegawa, K. Ueno, K. Itaka, P. Ahmet, T. Chikyow, M. Kawasaki and H. Koinuma , Japan. J. Appl. Phys. 2(40) (2001) L1343.

[90]. P.R. Willmott, P. Manoravi P and K. Holliday , Appl. Phys. A 70, (2000) 425.

[91]. S.R. Shinde, S.D. Kulkarni, A.G. Banpurkar, R. Nawathey-Dixit, S.K. Date, S.B. Ogale , J Appl Phys 88, (2002) 1566.

[92]. A. Harano, K. Shimada, T. Okubo, M. Sadakata, J Nanoparticle Res. 4 (2002) 215.

[93]. T. Makimura , T. Mizuta, K. Murakami . Jpn. J. Appl. Phys. 41 (2002) L144.

[94]. F.K.III. Urban, A. Hosseini-Tehrani, P. Griffiths, A. Khabari, Y.W. Kim, Petrov I. J Vac. Sci. Techno.l B 20 (2002) 995.

[95]. T. Karabacak, A. Mallikarjunan, et al., . Appl. Phys. Lett. 83 (2003) 3096.

[96]. L.M Cao, Z. Zhang et al., Adv. Mater. 13 (2001) 1701.

[97]. L.M. Cao, K. Hahn et al., Appl. Phys. Lett. 80 (2002) 4226.

[98]. A.P. Weber, M. Seipenbusch, G. Kasper, J. Phys. Chem. A 105 (2001) 8958.

[99]. E.F. Rexer, D.B. Wilbur, J.L. Mills, R.L. DeLeon, J.F. Garvey. Rev. Sci. Instrum, 71 (2000) 2125.

[100]. C.J. Brinker, G.W. Scherer, Sol-Gel Science, Academic Press, Inc.: New York, (1990).

[101]. L.L. Hench, J.K. West, Chem. Rev. (Wash- ington, D.C.), 90 (1990) 33.

[102]. B. O'Regan, J. Moser, M. Anderson, M. Grȧtzel, J. Phys. Chem . 94 (1990) 8720.

[103]. R. Kaur, A.V. Singh et al., J. Non-Cryst. Solids, 32 (2006) 2565.

[104]. Y.W. Chen, Y.C. Liu, et al., J. Chem. Phys. 123 (2005) 134701.

[105]. X.Y. Wang, X.Y. Wang, et al., J. Power Sources 140 (2005) 211.

[106]. H. Xu, D.H. Qin, Z. Yang, H.L. Li, Mater. Chem. Phys. 80 (2003) 524.

[107]. M. Zhang, Y. Bando and K. Wada, J. Mater. Sci. Lett. 20 (2001) 167.

[108]. J.H. Yang, G.M. Liu, L. Jun, Y.F. Qiu, S.H. Yang, Appl. Phys. Lett. 90 (2007) 103109.

[109]. C.S. Rout, S.H. Krishna, et al., Chem. Phys. Lett. 418 (2006) 586.

[110]. C.K. Xu, G.D. Xu, et al., Solid State Commun. 122 (2002) 175.

[111]. C.K. Xu, X.L. Zhao, et al., Solid State Commun. 125 (2003) 301.

[112]. C.K. Xu, G.D. Xu and G.H. wang, J. Mater. Sci. 38 (2003) 779.

[113]. J.H. Liang, C. Peng, X. Wang, et al., Inorg. Chem. 44 (2005) 9405.

[114]. A. Vantomme, Z.Y. Yuan, G.H. Du and B.L. Su, Langmuir, 21 (2005) 1132.

[115]. L.H. Thompson, L.K. Doraiswamy, Ind. Eng. Chem. Res. 38 (1999) 1215.

[116]. N.A. Dhas and A. Gedanken, Chem. Mater. 9 (1997) 3159.

[117]. R. Vijaykumar, Y. Diamant and A. Gedanken, Chem. Mater. 12 (2000) 2301.

[118]. H. S. Nalwa, Handbook of nanostructured materials and nanotechnology, Academic Press (2000).

[119]. K. Byrappa and M. Yoshimura: Handbook of Hydrothermal Technology (Noyes Publications/William Andrew Publishing LLC, U.S.A. 2001).

[120]. M . O'Donoghue, A guide to Man-made Gemstones. Great Britain: Van Nostrand Reinhold Company. (1983) 40. ISBN 0-442-27253-7.

[121]. Instrument Database:JEOL - JSM-6480LV, (2007), Retrieved March 15,2011 from http://www. speciation. net/Appl/Techniques /technique.html?id=47.

[122]. Energy Dispersive X-ray Spectroscopy (EDS), John Goodge, University of Minnesota-Duluth, Retrieved March 15, 2011 from http://serc. carleton. edu/research _education/geochemsheets/eds.html

[123]. J.R. Fryer, Chemical applications of Transmission Electron Microscopy, Academic press, San zdiego (1979).

[124]. Y.Ding, and Z.L. Wang, J. Phys. Chem. B. 108 (2004) 12280.

[125]. Rao, C.N.R.: Transition metal oxides. Annu. Rev. Phys. Chem. 40 (1989) 291.

[126]. Rao, C.N.R., Raveau, B.: Transition metal oxides. VCH Publishers Inc., New York (1995).

[127]. B. O'Regan and M. Gratzel, Nature 353 (1991) 737.

[128]. M. Gratzel, Inorg. Chem. 44 (2005) 6841.

[129]. Y. Chiba, A. Islam, Y. Watanabe, R. Komiya, N. Koide and L. Han, Jpn. J. Appl. Phys. Part 2 45 (2006) L638.

[130]. H.-J. Koo, Y.J. Kim, Y.H. Lee, W.I. Lee, K. Kim and N.-G. park, Adv. Mater. 20 (2008) 195

[131]. N.-G. park,and K. Kim, Phys. Stat. Sol. (a) 205 (2008) 1895.

[132]. D. Kanjilal, S. Chopra, M.M. Narayanan, I.S. Iyer, V. Jha, R. Joshi and S.K. Datta, Nucl. Instr. And Meth. A 238 (1993) 97.

[133]. J.F. Ziegler, J.P. Biersack and U. Littmark, in Stopping and Ranges of Ions in Matter (Pergamon, New York (1985) 46.

[134]. K. Lal, Real Structure of Real Crystals, PINSA, 64/A(5) (1998) 609.

[135]. Z.G. Pinsker, Dynamical Scattering of X-rays in Crystals, Springer – Verlag, Berlin (1978).

[136]. B.W. Batterman and H. Cole, Rev. Mod. Phys. 36 (1964) 681.

[137]. D. B. Williams, C. B. Carter; Transmission Electron microscopy: A text book for Materials Science, Plenum press (1996).

[138]. L. D. Landu, E. M. Lifshitz; Electrodynamics of continuous media, Butter- Worth and Heinmann (1998).

[139]. D. Cullity; Elements of X-ray diffraction, Addition-Wesley (1956).

[140]. R. Jenkins, R. L. Synder; Introduction to X-ray powder diffractometry, JonWiley & Sons (1996).

[141]. A. G. Jackson;Handbook of crystallography for electron microscopist and others, Springer-Verlag (1991).

[142]. M.J. Pelletier, Ed. Blackwell. Analytical application of Raman Spectroscopy, Oxford (1999).

[143]. I.R. Lewis, H.G.M. Edwards, Eds, Handbook of Raman Spectroscopy: From the Research Laboratory to the Process Lines, Marcel Dekker, New York (2001).

[144]. A. Umar, A. Al-Hajry, Y. B. Hahn and D. H. Kim, Electrochimica Acta 54, 5358-5362 (2009)].

[145]. S. A. Khayyat, M. Abaker, Ahmad Umar, M. O. Alkattan, N. D. Alharbi, S. Baskoutas, J. Nanosci. Nanotechnol. 12 (2012) 8453.

[146]. L.X. Zhang, P. Liu, Z.X. Su, Polym. Degrad. Stab. 91 (2006) 2213.

[147]. A. Sutti, C. Baratto, G. Calestani, C. Dionigi, M. Ferroni, G. Faglia, G. Sberveglieri, Sens. Actuators B 130 (2008) 567.

[148]. G. Korotcenkov, Sens. Actuators B 107 (2005) 209.

[149]. B. T. Marquis, J. F. Vetelino, Sens. Actuators B 77 (2001) 100.

[150]. A. L. Kukla, Y. M. Shirshov, S. A. Piletsky, Sens. Actuators B 37 (1996) 135.

[151]. G. Ballun, F. Hajdu, G. Harsanyi, G., IEEE 26th Int. Spring Sem. Elect. Tech. (2003) 471.

[152]. Y. S. Lee, B. S. Joo, N. J. Choi, J. O. Lim, J. S. Huh, D. D. Lee, Sens. Actuators B 93 (2003) 148.

[153]. S. Christie, E. Scorsone, K. Persaud, F. Kvasnik, Sens. Actuators B 90 (2003) 163.

[154]. Z. Jin, Y. Su, Y. Duan, Y., Sens. Actuators B 72 (2001) 75.

[155]. C. Y. Shen, C. L. Hsu, K. C. Hsu, J. S. Jeng, Jpn. J. Appl. Phys. 44 (2005) 1510.

[156]. C. Y. Shen, C. P. Huang, K. C. Hsu, J. S. Jeng, IEEE Int. Ultrason. Ferroelec. Freq. Control, (2004) 546.

[157]. S. B. Khan, M. M. Rahman, E. S. Jang, K. Akhtar, H. Han, Talanta 84 (2011) 1005.

[158]. B. Karunagaran, P. Uthirakumar, S. J. Chung, S. Velumani, E. K. Suh, Mater. Charact. 58 (2007) 680.

[159]. H. Nanto, T. Minami, S. Takata, J. Appl. Phys. 60 (1986) 482.

[160]. M. Y. Faizah, A. Fakhru'l-Razi, R. M. Sidek, A. G. Liew Abdullah, Int. J. Eng. Tech. 4 (2007) 106.

[161]. D. Haridas, K. Sreenivas, V. Gupta, Sens. Actuators B 133 (2008) 270.

[162]. H. E. L. Hernandez, C. S. Perez, A. G. J. Valenzuela, Opt. A: Pure Appl. Opt. (2010) 10.

[163]. M. M. Rahman, A. Jamal, S. M. Faisal, J. Nanoparticle Research (2011) doi:10.1007/s11051-011-0301-7.

[164]. S. B. Khan, M. Faisal, M. M. Rahman, A. Jamal, Talanta 85 (2011) 943.

[165]. M. M. Rahman, A. Jamal, M. Faisal, Appl. Mater. Interfaces 3 (2011) 1346.

[166]. M. Faisal, M. M. Rahman, A. Jamal, A. Umar, Materials Letters 65 (2011) 1400.

[167]. S. Khan, M. Faisal, M. M. Rahman, A. Jamal, Science of the Total Environment 409 (2011) 2987.

[168]. L. Schmidt-Mende, J. L. MacManus-Driscoll, Mater. Today 10 (2007) 40.

[169]. A. Umar, M. M. Rahman, S. H. Kim, Y. B. Hahn, Chem. Commun. (2008) 166.

[170]. M. M. Rahman, A. Umar, K. Sawada, Sens. Actuators B 137 (2009) 327.

[171]. R. Wahab, Y. S. Kim, D. S. Lee, J. M. Seo, H. S. Shin, Sci. Adv. Mater. 2 (2010) 35.

[172]. J. Wu, D. Xue, Sci. Adv. Mater. 3 (2011) 127.

[173]. R. A. Laudise, A. A. Ballman, J. Phys. Chem. 64 (1960) 688.

[174]. A. Umar, Y. B. Hahn, Appl. Phys. Lett. 88 (2006) 173120.

[175]. A. Umar, Y. B. Hahn, Nanotechnology 17 (2006) 2174.

[144]. A. Umar, A. Al-Hajry, Y. B. Hahn, D. H. Kim, Electrochimica Acta 54 (2009) 5358.

[176]. A. Al-Hajry, A. Umar, Y. B. Hahn, D. H. Kim, Superlatt. Microstruct. 45 (2009) 529.

[177]. R. A. Nyquist, R. O. Kagel, ‘Infrared spectra of Inorganic Compounds’; Academic Press, Inc.: New York, London, (1971) 220.

[178]. C. A. Arguelo, D. L. Rousseau, S. P. S. Porto, 1969. Phys. Rev. 181 (1969) 1351.

[179]. J. M. Calleja, M. Cardona, Phys. Rev. B 16 (1977) 3753.

[180]. Y. H. Yang, C. X. Wang, B. Wang, Z. Y. Li, J. Chen, D. H. Chen, N. S. Xu, G. W. Yang, J. B. Xu, Appl. Phys. Lett. 87 (2005) 183109.

[181]. S. G. Ansari, Z. A. Ansari, H. K. Seo, G.S. Kim, Y. S. Kim, G. Khang, H. S. Shin, Sens. Actuators B 132 (2008) 265.

[182]. A. O. Dikovska, G. B. Atanasova, N. N. Nedyalkov, P. K. Stefanov, P. A. Atanasov, E. I. Karakoleva, A. T. Andreev, Sens. Actuators B 146 (2010) 331.

[183]. A. Umar and Y. B. Hahn, “Metal Oxide Nanostructures and Their Applications”, American Scientific Publishers (ASP), Los Angeles, USA (2010).

[184]. R. Mohan, G.-S. Kim, and S.-J. Kim, Sci. Adv. Mater. 6 (2014) 336.

[185]. L. Yuan and G. Zhou, Mater. Focus 1 (2012) 222.

[186]. H. Usui and H. Sakaguchi, J. Nanoeng. Nanomanuf. 3 (2013) 311.

[187] . M. Ding, D. Zhao, B. Yao, and X. Xu, Sci. Adv. Mater. 6 (2014) 197.

[188]. S. Yu, Z. Cao, and H.-Q. Su, J. Nanoeng. Nanomanuf. 4 (2014) 23.

[189]. K. Namratha, K. Byrappa, J. Bai, V. R. Rai, D. Ehrentraut, I. A. Ibrahim, and M. Yoshimura, Mater. Focus 2 (2013) 136.

[190]. K. Li, C. Zhang, and D. Xue, J. Nanoeng. Nanomanuf. 4 (2014) 33.

[191]. M. Gusatti, C. E. M. Campos, D. A. R. Souza, V. M. Moser, N. C. Kuhnen, and H. G. Riella, J. Nanosci. Nanotechnol. 13 (2013) 8307.

[192]. P. S. Badgujar, S. S. Arbuj, J. M. Mali, S. B. Rane, and U. P. Mulik, J. Nanoeng. Nanomanuf. 4 (2014) 65.

[193]. C. Zhang, S. Zhou, K. Li, S. Song, and D. Xue, Mater. Focus 2 (2013) 11.

[194]. S. C. Singh, J. Nanoeng. Nanomanuf. 3 (2013) 283.

[195]. S. S. Arbuj, N. Rumale, A. Pokle, J. D. Ambekar, S. B. Rane, U. P. Mulik, and D. P. Amalnerkar, Sci. Adv. Mater. 6 (2014) 269.

[196] A. Kumar, S. Rahman, S. N. Kazim, Z. A. Ansari, and S. G. Ansari, Mater. Focus 2 (2013) 148.

[197]. V. N. Singh, G. Partheepan, and A. Kumar, J. Nanoeng. Nanomanuf. 3 (2013) 276.

[198]. D. A. Dinh, K. N. Hui, K. S. Hui, J. Singh, P. Kumar, and W. Zhou, Rev. Adv. Sci. Eng. 2 (2013) 259.

[199.]. B. B. Sapkota and S. R. Mishra, J. Nanosci. Nanotechnol. 13 (2013) 6588.

[200]. A.-I. Danciu, V. Musat, T. Busani, J. V. Pinto, R. Barros, A. M. Rego, A. M. Ferraria, P. A. Carvalho, R. Martins, and E. Fortunato, J. Nanosci. Nanotechnol. 13 (2013) 6701.

[201]. T. Singh and J. Singh, Rev. Adv. Sci. Eng. 2 (2013) 313.

[202]. G. R. Chaudhary, P. Saharan, A. Umar, S. K. Mehta, and S. Mor, Sci. Adv. Mater. 5 (2013) 1886.

[203]. N. Aste, R. S. Adhikari, and L. C. Tagliabue, Rev. Adv. Sci. Eng. 2 (2013) 179.

[204]. R. Saikia, P. K. Kalita, and P. Datta, Energy Environ. Focus 2 (2013) 91.

[205]. K. Li, J. Shao, and D. Xue, Mater. Focus 2 (2013) 461.

[206]. K. Chen and D. Xue, J. Nanoeng. Nanomanuf. 4 (2014) 71.

[207]. A. L. Donne, A. Scaccabarozzi, S. Tombolato, S. Binetti, M. Acciarri, and A. Abbotto, Rev. Adv. Sci. Eng. 2 (2013) 170.

[208]. X. LI, L. Zhang, H. Song, and L. Chou, Energy Environ. Focus 2 (2013) 1.

[209]. S. G. Ansari, F. T. Zehra, and Z. A. Ansari, J. Nanoeng. Nanomanuf. 3 (2013) 131.

[210] K. Li, H. Li, P. Yan, Y. Zhang, and D. Xue, Rev. Adv. Sci. Eng. 2 (2013) 216.

[211]. K. Fan, R. Li, J. Chen, W. Shi, and T. Peng, Sci. Adv. Mater. 5 (2013) 1596.

[212]. X.-Y. Cheng, Z.-J. Zhou, Z.-L. Hou, W.-H. Zhou, and S.-X. Wu, Sci. Adv. Mater. 5 (2013) 1193.

[213]. S.-J. Yuan, Z.-J. Zhou, Z.-L. Hou, W.-H. Zhou, R.-Y. Yao, Y. Zhao, S.-X. Wu, and D. Xue, Sci. Adv. Mater. 5 (2013) 927.

[214].J. Qin, G. Zhang, J. Liang, H. Xia, Y. Xing, and W. Sun, Sci. Adv. Mater. 6 (2014) 140.

[215]. M. Motlak, N. A. M. Barakat, M. S. Akhtar, A. M. Hamza, A. Taha, O.-B. Yang, and H. Y. Kim, Energy Environ. Focus 2 (2013) 217.

[216]. C. R.-García, R. Jiménez, J. P.-Carvajal, A. B.-Murcia, M. Darder, P. Aranda, D. C.-Amorós, and E. R.-Hitzky, Sci. Adv. Mater. 6 (2014) 150.

[217]. J. Kong, Y.-L. Zhou, W.-H. Zhou, Z.-J. Zhou, and S.-X. Wu, J. Nanoeng. Nanomanuf. 4 (2014) 1

[218]. M. Gratzel, Nature 414 (2001) 338.

[219]. M. K. Nazeeruddin, P. Pechy, T. Renouard, S. M. Zakeeruddin, R. H.-Baker, P. Compte, P. Liska, L. Cevey, E. Costa, V. Shklover, L. Spiccia, G. B. Deacon, C. A. Bignozzi, and M. Gratzel, J. Am. Chem. Soc. 123 (2001) 1613.

[220]. M. Durr, A. Bamedi, A. Yasuda, and G. Nelles, Appl. Phys. Lett. 84 (2004) 3397.

[221]. A. E. Suliman, Y. Tang, L. Xu, Solar Energy Materials & Solar Cells 91 (2007) 1658.

[222]. K. Keis, E. Magnusson, H. Lindstrom, S.-E. Lindquist, A. Hagfeldt, Solar Energy Materials & Solar Cells 73 (2002) 51.

[223]. C. Y. Jiang, X. W. Sun, G. Q. Lo, and D. L. Kwong, J. X. Wang, Appl. Phy. Lett. 90 (2007) 263501.

[224]. S. Wu, H. Han, Q. Tai, J. Zhang, B. L. Chen, S. Xu, C. Zhou, Y. Yang, H. Hu, and X.-Z. Zhao, Appl. Phy. Lett. 92 (2008) 122106.

[225]. A.-J. Cheng, Y. Tzeng, Y. Zhou,. M. Park, T. Wu, C. Shannon, D. Wang, and W. Lee, Appl. Phy. Lett. 92 (2008) 092113.

[226]. C. Bauer, G. Boschloo, E. Mukhtar, A.Hagfeldt, J. Phys. Chem. B 105 (2001) 5585.

[227]. Q. Zhang, T. P. Chou, B. Russo, S. A. Jenekhe, and G. Cao, Angew. Chem. Int. Ed. 47 (2008) 2402.

[228]. T. P. Chou, Q. F. Zhang, G. E. Fryxell, and G. Z. Cao, Adv. Mater. (Weinheim, Ger.) 19 (2007) 2588.

[229]. E. Hosono, S. Fujihara, I. Honma, and H. S. Zhou, Adv. Mater. (Weinheim, Ger.) 17 (2005) 2091.

[230]. J. B. Baxter and E. S. Aydil, Appl. Phy. Lett. 86 (2005) 53114.

[231]. M. Law, L. Greene, J. Johnson, R. Saykally, and P. Yang, Nature Mater. 4 (2005) 455.

[232]. A. A.-Hajry, J. Nanosci. Nanotechnol. 10 (2010) 994.

[233]. D.-I. Suh, S.-Y. Lee, T.-H. Kim, J.-M. Chun, E.-K. Suh, O.-B. Yang and S.-K. Lee, Chemical Physics Letters, 442 (2007) 348.

[234]. A. Umar, M. S. Akhtar, S. H. Kim, A. Al-Hajry, M. S. Chauhan, and S. Chauhan, Sci. Adv. Mater. 3 (2011) 695.

[235]. A. Umar, M. S. Chauhan, S. Chauhan, R. Kumar, G. Kumar, S. A. A.-Sayari, S. W. Hwang, A. A.-Hajry, J. Colloid Interface Science 363 (2011) 521.

[236]. L. Wu, Y. Wu, Lu Wei, Physica E28, 76 (2005).

[237]. A. Cheng, Y. Tzeng, Y. Zhou, M. Park, T-H. Wu, C. Shannon, D. Wang, and W. Lee, Appl. Phys. Lett. 92 (2008) 92113.

[238]. V. Ramamurthy, and K. S. Schanze, “Semiconductor Photochemistry and Photophysics” (CRC, Boca Raton) Vol. 10 (2003).

[239]. P. Balraju, P. Suresh, M. Kumar, M. S. Roy, G. D. Sharma, Journal of Photochemistry and Photobiology A: Chemistry 206 (2009) 53.

[240]. A. Umar, Y.B. Hahn, Ed. “Metal Oxide Nanostructures and Their Applications”, Part IV, American Scientific Publisher, USA, 2010

[241]. N. Rastakhiz, A. Kariminik, V.S. Nejad, S. Roodsaz, Int. J. Electrochem. Sci. 5 (2010) 1203.

[242]. S. Chitravathi, B.E. Kumara Swamy, U. Chandra, G P. Mamatha, B S. Sherigara, J. Electroanal. Chem. 645 (2010) 10.

[243]. L. Tang, G.M. Zeng, Y.H. Yang, G.L. Shen, G.H. Huang, C.G. Niu, W. Sun, J.B. Li, Int. J. Environ. Anal. Chem. 85 (2005) 111.

[244]. Z.S. Yang, W.L Wu, X. Chen, Y.C. Liu, Anal. Sci. 24 (2008) 895.

[245]. D. Afzali, H.K. Maleh, M.A. Khalilzadeh, Environ. Chem. Letters, 9 (2010) 375.

[246]. S.G. Ansari, Z.A. Ansari, R. Wahab, Y.S. Kim, G. Khang, H.S. Shin, Biosens. Bioelectron. 23 (2008) 1838.

[247]. P. Gouma, Sci. Adv. Mater. 3 (2011) 787.

[248]. G.N. Dar, A. Umar, S.A. Zaidi, S. Baskoutas, S.W. Hwang, M. Abaker, A. Al-Hajry, S.A. Al-Sayari, Talanta, 89 (2012) 155.

[249]. K.I. Choi, J.H. Lee, Sci. Adv. Mater. 3 (2011) 811.

[250]. A. Khan, S.N. Khan, W.M. Jadwisienczak, Sci. Adv. Mater. 2 (2010) 572.

[251]. B. Haghighi, S. Bozorgzadeh, Talanta 85 (2011) 2189.

[252]. H. Zeng, J. Cui, B. Cao, U. Gibson, Y. Bando, D. Golberg, Sci. Adv. Mater. 2 (2010) 336.

[253]. Z. Zhang, Y. Yuan, Y. Fang, L. Liang, H. Ding, L. Jin, Talanta 73 (2007) 523.

[254]. R. Ding, J. Liu, J. Jiang, X. Ji, X. Li, F. Wu, X. Huang, Sci. Adv. Mater. 2 (2010) 396.

[255]. S.K. Mohanta, D.C. Kim, B.H. Kong, H.K. Cho, W. Liu, S. Tripathy, Sci. Adv. Mater. 2 (2010) 64.

[256]. J. Zhong, S. Muthukumar, Y. Chen, Y. Lu, H.M. Ng, E.L. Garfunkel, Appl. Phys. Lett. 83 (2003) 3401.

[257]. C. Ronning, P.X. Gao, Y. Ding, Z.L. Wang, D. Schwen, Appl. Phys. Lett. 84 (2004) 783.

[258]. J.S. Jie, G.Z. Wang, X.H. Han, Q.X. Yu, Y. Liao, G.P. Li, J.G. Hou, Chem. Phys. Lett. 387 (2004) 466.

[259]. L.P. Zhu, M.J. Zhi, Z.Z. Ye, B.H. Zhao, Appl. Phys. Lett. 88, (2006) 113106.

[260]. R.C. Wang, C.P. Liu, J.L. Huang, S.J. Chen, Appl. Phys. Lett. 88 (2006) 023111.

[261]. S. H. Kim, A. Umar, Y.K. Park, J.H. Kim, E.W. Lee, Y.B. Hahn, J. Alloys Compds. 479 (2009) 290.

[262]. H. Chen, J. Qi, Y. Huang, Q. Liao, Y. Zhang, Acta Phys. -Chim. Sin. 23 (2007) 55.

[263]. S. Liu, C. Li, J. Yu, Q. Xiang, Cryst. Eng. Comm, 13 (2011) 2533.

[264]. Y. Lai, M. Meng, Y. Yu, Appl. Cat. B: Environ. 100 (2010) 491.

[265]. X. Li, Y. Wang, J. Alloys Compds. 509 (2011) 5765.

[266]. S.W. Dian, W.Y. Lian, Chin. J. Vac. Sci. Technol. 27 (2007) 309.

[267]. F.X. Hui, L. He, M.X. Hong, Y. Wen, Nanosci. Nanotechnol. 6 (2009) 61.

[268]. R. Chakravarty, C. Periasamy, Sci. Adv. Mater. 3 (2011) 276.

[269]. L.S. Roselin, R. Selvin, Sci. Adv. Mater. 3 (2011) 251-258.

[270]. Y.H. Ni, X.W. Wei, J.M. Hong, Y. Ye, Mater. Sci. Eng. B 121 (2005) 42.

[271]. M.S. Chauhan, R. Kumar, A. Umar, S. Chauhan, G. Kumar, S.W. Hwang, A. Al-Hajry, J. Nanosci. Nanotech. 11 (2011) 4061.

[272]. C. Ren, B. Yang, M. Wu, J. Xu, Z. Fu, Y. lv, T. Guo, Y. Zhao, C. Zhu, J. Hazard. Mat. 182 (2010) 123.

[273]. S. Mujumdar, Mat. Sci. Poland, 27 (2009) 123

[274]. G. Busca, S. Berardinelli, C. Resini, L. Arrighi, Technologies for the removal of phenol from fluid streams: A short review of recent developments, J. Hazard. Mater. 160 (2008) 265.

[275]. F. Xiaoqin, T. O. Kiang, T. M. Siu, Metal Oxide Barium Strontium Titanate Thin Films for Electrical Immunosensing Applications, Sci. Adv. Mater. 3 (2011) 763.

[276]. G. W. Ho, Gas Sensor with Nanostructured Oxide Semiconductor Materials, Sci. Adv. Mater. 3 (2011) 150.

[277]. L.W. Perelo, Review: In situ and bioremediation of organic pollutants in aquatic sediments, J. Hazard. Mater. 177 (2010) 81.

[278]. H. Zhang, L. Wang, Z. Tan, Z. Li, G. Ding, Z. Jiao, P. Gu, Preparation of SnO2 Nanoparticles by Hard Template Method for High Selectivity Gas Sensors. J. Nanosci. Nanotechnol. 11 (2011) 11023.

[279]. S. K. Mehta, K. Singh, Ahmad Umar, G. R. Chaudhary, S. Singh, Well-Crystalline α-Fe2O3 Nanoparticles for Hydrazine Chemical Sensor Application. Sci. Adv. Mater. 3 (2011) 962.

[280]. L. Tang, G. Yu, W. Si, Y. Ou, L. Qiao. Pd-Ag Alloy Dendritic Nanowires: Fabrication and Application in Hydrogen Sensor, J. Nanosci. Nanotechnol. 11 (2011) 10255.

[281]. D.K. Pandey, N. Mishra, P. Singh, Pesticide Biochem. Physiol. 83(2005) 82.

[282]. G.C. Jagetia, K.S. Lakshmy Menon,V. Jain, Toxical. Lett. 121 (2001) 15.

[283]. A.A. Hathoot, Int. J. Electrochem. Sci. 7 (2012) 251.

[284]. S. Wang, D. Du, Sensors2 (2002) 41.

[285]. I.R.W.Z. de Oliveira, R.E.M.d. Osorio, A. Neves, I.C. Vieira, Sens. Actuators B 122 (2007) 89.

[286]. Bo Kong, T. Yin, X. Liu, W. Wei , Anal. Lett. 40 (2007) 2141.

[287]. J. Li, C.-Y. Liu, C. Cheng, Electrochim. Acta 56 (2011) 2712.

[288]. I. Matsubara, W. Shin, N. Izu, M. Nishibori, T. Itoh, Sci. Adv. Mater. 3 (2011) 853.

[289]. W. Jin, W. Chen, Y. Lu, C. Zhao, Y. Dai, J. Nanosci. Nanotechnol. 11 (2011) 10834.

[290]. G. M. Kale, Sci. Adv. Mater. 3 (2011) 879.

[291]. S.M. Sze, Semiconductor Sensors, Wiley, New York, 1994.

[292]. Y. Qiu, S. Yang, Adv. Funct. Mater. 17 (2007) 1345.

[293]. F. Sheng, C. Xu, J. Guo, G. Zhu, Q. Chen, Sci. Adv. Mater. 3 (2011) 709.

[294]. J. Tu, X. Li, N. Li, R. Wang, W. Geng, Q. Yuan, Y. Cao, T. Zhang, J. Nanoeng. Nanomanuf. 2 (2012) 41.

[295]. M. A. Kanjwal, F. A. Sheikh, N. A. M. Barakat, X. Li, H. Y. Kim, I. S. Chronakis, Co3O4, ZnO, J. Nanoeng. Nanomanuf. 1 (2011) 196.

[296]. X.J. Huang, Y.K. Choi, Sens. Actuators B 122 (2007) 659.

[297]. Z. Zheng, J. Nanoeng. Nanomanuf. 2 (2012) 60.

[298]. B.C. Yadav, R. Srivastava, C.D. Dwivedi, P. Pramanik, Actuators B 131 (2008) 216.

[299]. C.S. Lao, P.X. Gao, R.S. Yang, Y. Zhang, Y. Dai, Z.L. Wang, Chem. Phys. Lett. 417 (2006) 358.

[300]. J. Singh, S.S. Patil, M.A. More, D.S. Joag, R.S. Tiwari, O.N. Srivastava, Appl. Surf. Sci. 256 (2010) 6157.

[301]. M. Abaker, A. Umar, S. Baskoutas, G.N. Dar, S.A. Zaidi, S.A. Al-Sayari, A. Al- Hajry, S.H. Kim, S.W. Hwang, J. Phys. D: Appl. Phys. 44 (2011) 425401.

[302]. Y. Fan, Z. Li, J. Nanoeng. Nanomanuf. 2 (2012) 123.

[303]. Z. Jing, J. Wang, F. Li, L. Tan, Y. Fu, Q. Li, J. Nanoeng. Nanomanuf. 2 (2012) 133.

[304]. G.N. Dar, A. Umar, S.A. Zaidi, S. Baskoutas, S.H. Kim, M. Abaker, A. Al-Hajry, S.A. Al Sayari, Sci. Adv. Mater. 3 (2011) 901.

[305]. R.C. Wang, H.Y. Lin, Sens. Actuators B 149 (2010) 94.

[306]. V. Kobrinsky, E. Fradkin, V. Lumelsky, A. Rothschild, Y. Komem, Y. Lifshitz, Sens. Actuators B 148 (2010) 379.

[307]. I.S. Hwang, S.J. Kim, J.K. Choi, J. Choi, H. Ji, G.T. Kim, G. Cao, J.H. Lee, Sens. Actuators B 148 (2010) 595.

[308]. L.A. Patil, A.R. Bari, M.D. Shinde, V. Deo, Sens. Actuators B 149 (2010) 79.

[309]. N. Palomera, M. Balaguera, S. K. Arya, S. Hernández, M. S. Tomar, J. E. Ramírez-Vick, S. P. Singh, J. Nanosci. Nanotechnol. 11 (2011) 6683.

[310]. W. Hao, M. Sun, H. Xu, T. Wang, J. Nanosci. Nanotechnol. 11 (2011) 10649.

[311]. A.A. Ibrahim, G.N. Dar, S.A. Zaidi, A. Umar, M. Abaker, H. Bouzid, S. Baskoutas, Talanta 93 (2012) 257.

[312]. W. Liang, B.D. Yuhas, P. Yang, Nano Lett. 9 (2009) 892.

[313]. S. Anandan, M. Miyauchi, Phys. Chem. Chem. Phys. 13 (2011) 14937.

[314]. Y.S. Chen , T.Y. Tseng,J. Nanosci. Nanotechnol. 8 (2008) 4514.

[315]. J. Lang, Q. Han, J. Yang, C. Li, X. Li, L. Yang, Y. Zhang, M. Gao, D. Wang, J. Cao, J. Appl. Phys. 107 (2010) 074302.

[316]. M. El Jouad, M.A. Lamrani, Z. Sofiani, M. Addou, T. El Habbani, N. Fellahi, K. Bahedi, L. Dghoughi, A. Monteil, B. Sahraoui, S. Dabos, N. Gaumer, Opt. Mater. 31 (2009) 1357..

[317]. M. Yousefi, M. Amiri, R. Azimirad, A.Z. Moshfegh, J. Electroanal. Chem. 661 (2011) 106.

[318]. C. Ge, C. Xie, S. Cai, Sci. Engg: B 137(2007) 53.

[319]. H. Du, J. Ye, J. Zhang, X. Huang, C. Yu, J. Electroanal. Chem. 650 (2011) 209.

[320]. Z. Jiang, Z. Guo, B. Sun, Y. Jia, M. Li, J. Liu, Sens. Actuators B 145 (2010) 667.

[321]. T. M. Milao, V. R. de Mendonça, V. D. Araújo, W. Avansi, C. Ribeiro, E. Longo, and M. I. Bernardi, Sci. Adv. Mater. 4 (2012) 54.

[322]. Ahmad Umar, Nanoscale Res. Lett. 4 (2009) 1004.

[323]. M. Law, L. E. Greene, J. C. Johnson, R. Saykally and P. Yang, P. Nat. Mater. 4 (2005) 455.

[324]. Service, R. F. Science 276 (1997) 895 .

[325]. Ryu, Y. R.; Zhu, S.; Budai, J. D.; Chandrasekhar, H. R. ; Miceli, P. F.; White, H. W. J. Appl. Phys. 88 (2000) 201.

[326]. Wang, A.; Dai, J.; Cheng, J.; Chudzik, M. P.; Marks, T. J.; Chang, R. P. H.; Kannewurf, C. R. Appl. Phys. Lett. 73 (1998) 327.

[327]. Wang, Z.L.; Song J.H. Science, 312 (2006) 242.

[328]. Wang, X.D.; Song, J.H.; Liu, J.; Wang, Z.L. Science, 316 (2007) 102.

[329]. Wang, Z.L. Materials Today, 10 (2007) 20..

[330]. Rizwan Wahab, Sourabh Dwivedi, Ahmad Umar, Surya Singh, I. H. Hwang, Hyung-Shik Shin, Javed Musarrat, Abdulaziz A. Al-Khedhairy, and Young-Soon Kim, J. Biomed. Nanotechnol. 9 (2013) 441.

[331]. Kulvinder Singh, Ahmad Umar, Arun Kumar, G. R. Chaudhary, Sukhjinder Singh, and S. K. Mehta, Sci. Adv. Mater. 4 (2012) 994.

[332]. Prachi Joshi, Soumyananda Chakraborti, Pinak Chakrabarti, Surinder P. Singh, Z. A. Ansari, M. Husain, and Virendra Shanker, Sci. Adv. Mater. 4 (2012) 173.

[333]. S. P. Chang, C. W. Li, K. J. Chen, S. J. Chang, C. L. Hsu, T. J. Hsueh, H. T. Hsueh, Sci. Adv. Mater. 4 (2012) 1174.

[334]. Q. Liao, Y. Huang, Z. Qin, Z. Zhang, J. Qi, Y. Zhang, L. Xia, J. Nanosci. Nanotechnol. 12 (2012) 775.

[335]. R. I. Badran, A. Umar, S. Al-Heniti, A. Al-Hajry, T. Al-Harbi, J. Alloy. Comp. 508 (2010) 375.

[336]. S. A. Khayyat, M. Abaker, Ahmad Umar, M. O. Alkattan, N. D. Alharbi, S. Baskoutas, J. Nanosci. Nanotechnol. 12 (2012) 8453.

[337]. Y. Huang, Y. Zhang, Y. Gu, X. Bai, J. Qi, Q. Liao, and J. Liu, J. Phys. Chem. C, 111 (2007) 9039.

[338]. S. Y. Bae, C. W. Na, J. H. Kang, J. Park, J. Phys. Chem, B, 109 (2005) 2526.

[339]. H. Algarni, M. M. El-Gomati, and M. S. Al-Assiri, Sci. Adv. Mater. 4 (2012) 961.

[340]. D.M. Bagnall, Y.F. Chen, Z. Zhu, T. Yao, S. Koyama, M.Y. Shen, and T. Goto, Appl. Phys. Lett. 73 (1998) 1038.

[341]. Zhang, K. Li, S. Song, D. Xue, Sci. Adv. Mater. 4 (2012) 1148.

[342]. M.R. Hoffmann, S.T. Martin, W. Choi, D.W. Bahnemann, Chem. Rev. 95 (1995) 69;

[343]. A. Khan, Niyaz. A. Mir, M. M. Haque, M. Muneer, and C. Boxall, Sci. Adv. Mater. 5 (2013) 160;

[344] .Yunqing Zhu, Xie Quan, Fengjiao Chen, Xinfei Fan, and Yujie Feng, Sci. Adv. Mater. 4 (2012) 1191.

[345]. R. Kumar, G. Kumar, A. Umar, Mater. Lett. 97 (2013) 100.

[346]. C. Cao, C. Hu, W. Shen, S. Wang, J. Wang, H. Liu, Y. Xi, Sci. Adv. Mater. 5(2013) 796.

[347]. S. A. Khayyat, M.S. Akhtar, A. Umar, Mater. Lett. 81 (2012) 239.

[348]. C. Chen, H. Chen, J. Shi, J. Yu, Sci. Adv. Mater. 5 (2013) 896.

[349]. C. Jin, C. Xing, F. Wang, W. Shen, Sci. Adv. Mater. 5 (2013) 663.

[350]. H. Yin, Y. Zhou, S. Ai, X. Liu, L. Zhu, L. Lu, Microchim. Acta 169 (2010) 87.

[351]. M. Castillo, R. Domingues, M.F. Alpendurada, D. Barcelo, Anal. Chim. Acta 353 (1997) 133.

[352]. E. Lypczynska-Kochany, Chemosphere 22 (1991) 529.

[353]. Hava Ozay, Sci. Adv. Mater. 5 (2013) 575.

[354]. M. Abaker, G. N. Dar, Ahmad Umar, S. A. Zaidi, Ahmed A. Ibrahim, S. Baskoutas, and A. Al-Hajry, Sci. Adv. Mater. 4 (2012) 893.

[355]. G.N. Dar, A. Umar, S.A. Zaidi, A. A. Ibrahimd, M. Abaker, S. Baskoutas, M.S. Al-Assiri, Sensors and Actuators B: Chemical, 173 (2012) 72.

[356]. D.K. Zhong, J.W. Sun, H. Inumaru, D.R. Gamelin, J. Am. Chem. Soc. 131 (2009) 6086.

[357]. Cesar I, Kay A, Gonzalez Martinez J A, Grätzel M,. Journal of the American Chemical Society 128 (14) (2006) 4582.

[358]. Li X, Wei W, Wang S, Kuai L, Geng B. Nanoscale. 3 (2) (2011) 718.

[359]. Chen J S, Zhu T, Yang X H, Yang H G, Lou X W. Journal of the American Chemical Society, 132 (38) (2010) 13162.

[360]. Yu Hou et al. Nat Commun. 4 (2013) 1583.

[361]. Z. Zhang, M. F. Hossain, T. Takahashi, Appl. Catal. B: Environ. 95 (2010) 423.

[362]. Zhou X, Yang H, Wang C, Mao X, Wang Y, Yang Y, Liu G. J. Phys. Chem. C, 114 (40) (2010) 17051.

[363]. C. R. Gong, D. R. Chen, X. L. Jiao, Q. L. Wang, J. Mater. Chem. 14 (2004) 905.

[364]. C. J. Jia, L. D. Sun, Z. G. Yan, L. P. You, F. Luo, X. D. Han, Y. C. Pang, Z. Zhang, C. H. Yan, Angew. Chem., Int. Ed. 44 (2005) 4328.

[365]. X. Q. Su, B. Yan, Mater. Chem. Phys. 93 (2005) 552.

[366]. L. L. Wang, J. S. Jiang, Physica B 390 (2007) 23.

[367]. L.Chen, J. Zhang, Sci. Adv. Mater. 4 (2012) 859.

[368]. S.P.S. Porto, R.S. Krishnan, J. Chem. Phys. 47 (1967) 1009.

[369]. D. Tassalit, A.N. Laoufi, F. Bentahar, Sci. Adv. Mater. 3 (2011) 944.

[370]. V. Mirkhani, S. Tanngestaninejad, M. Moghadam, M.H. Habibi,A. Rostami Vartooni, J. Iran. Chem. Soc. 6 (2009) 578.

[371]. P.P. Sahay, S. Tewari, S. Jha, M. Shamsuddin, J. Mater. Sci. 40 (2005) 4791.

[372]. F. Hellegouarch, F. Arefi-Khonsari, R. Planade, J. Amouroux, Sens. Actuators B 73 (2001) 27

[373]. S. Lupua, C. Lete, M. Marin, N. Totir, P. C. Balaure, Electrochim. Acta 54 (2009) 1932

[374]. R. S. Luz, F. S. Damos, A. B. Oliveira, J. Beck, L. T. Kubota, Talanta 64 (2004) 935.

[375]. L. Luo, X. Zou, Y. Ding, Q. Wu, Sens. Actuators B 135 (2008) 61.

[376]. A.K.M. Kafi, A. Chen, Talanta 79 (2009) 97.

List of Publications

2013

[15] Sang Hoon Kim, Ahmad Umar, M. S. Akhtar, **G. N. Dar**, A. Al-Hajry, "ZnO balls made of intermingled nanocrystalline nanosheets for photovoltaic device application" **Sci. Adv. Mater. 6, xx-xx (2014)**

[14] Ahmad Umar, M. S. Akhtar, **G.N.Dar**, M. Abaker,A. Al-Hajry, S. Baskoutas, "Visible-light-driven photocatalytic and Chemical Sensing Properties of SnS_2 nano-flakes",**Talanta, 114, 183-190 (2013).**

[13] S. H. Kim, **G. N. Dar**,Ahmad Umar*, "Growth of In-Doped ZnO Hollow Spheres Composed of Nanosheets Networks and Nanocones: Structural and Optical Properties",**Journal of Nanoscience and Nanotechnology,13, 4639-4644 (2013).**

2012

[12] M. Abaker**, G. N. Dar**, Ahmad Umar, S. A. Zaidi,Ahmed A. Ibrahim, S. Baskoutas, A. Al-Hajry, "CuO nanocubes based highly sensitive 4-Nitrophenol Chemical Sensor",**Sci. Adv. Mater. 4, 893-900 (2012)**

[11] **G. N. Dar**, Ahmad Umar, S. A. Zaidi,Ahmed A. Ibrahim, S. Baskoutas, "Ce-doped ZnO nanorods for the detection of hazardous chemical",**Sensors and Actuators B: Chemical,173, 72-78 (2012).**

[10] O. Al-Dossary, Ahmad Umar,* A. A. Al-Harbi, S. A. Zaidi, **G. N. Dar**, "$La_{0.7}Sr_{0.3}MnO_3$ Nanoparticles based Ultra-high sensitive Ammonia Chemical Sensor",**J. Nanosci. Nanotechnol. 12, 6368-6373 (2012).**

[9] Ahmed A. Ibrahim, **G. N. Dar**, Shabi Abbas Zaidi, Ahmad Umar, S. H. Kim, H. Bouzid, S. Baskoutas, "Growth and properties of Ag-Doped ZnO nanoflowers for highly sensitive phenyl hydrazine chemical sensor application",**Talanta, 95, 257-263(2012)**

[8] Ahmad Umar, Faten Al-Hazmi, **Ghulam Nabi Dar**, S. A. Zaidi, Reem M.Al-Tuwirqi, Fowzia Alnowaiserb, Ahmad A Al-Ghamdi, S. W. Hwang "Ultra-sensitive ethanol sensor based on rapidly synthesized $Mg(OH)_2$ hexagonal nanodisks", **Sensors and Actuators B: Chemical, 166-167, 97-102(2012).**

[7] **G.N. Dar**, Ahmad Umar, Shabi Abbas Zaidi, S. Baskoutas, S.W. Hwang, M. Abaker, A. Al-Hajry, S.A. Al-Sayari, “Ultra-high sensitive ammonia chemical sensor based on ZnO nanopencils”,**Talanta 89, 155-161 (2012).**

[6] Faten Al-Hazmi, Ahmad Umar, G. N. Dar, A. A. Al-Ghamdi, S. A. Al-Sayari, A. Al-Hajry, S. H. Kim, Reem M.Al-Tuwirqi, Fowzia Alnowaiserb, Farid El-Tantawy, “Microwave Assisted Rapid Growth of Mg(OH)$_2$ Nanosheet Networks for Ethanol Chemical Sensor Application”,**Journal of Alloys and Compounds, 519, 4-8 (2012).**

2011

[5] **G. N. Dar**, Ahmad Umar, Shabi Abbas Zaidi, S. Baskoutas, S. H. Kim, M. Abaker, A. Al-Hajry and S. A. Al-Sayari, “Fabrication of High-Sensitive Non-Enzymatic Glucose Biosensor based on ZnO Nanorods”,**Sci. Adv. Mater. 3, 901-906 (2011).**

[4] M. Abaker, Ahmad Umar*, S. Baskoutas, **G. N. Dar**, S. A. Zaidi, S. A. Al-Sayari, A. Al-Hajry, S. H. Kim and S. W. Hwang, “Highly Sensitive Ammonia Chemical Sensor Based on α-Fe$_2$O$_3$nanoellipsoids”,**Journal of Physics D: Applied Physics 44, 425401 (2011).**

[3] M. Abaker, Ahmad Umar*, S. A. Al-Sayari, **G. N. Dar**, M. Faisal, S. H. Kim and S. W.Hwang, “Growth and photocatalytic properties of Sb-doped ZnO nanoneedles by hydrothermal process”,**AIP Conference Proceedings, 1370, 121 (2011).**

[2] S. H. Kim, Ahmad Umar*, S. W. Hwang, H. Al-Garni, M. Abaker, S. A. Al-Sayari,**G. N. Dar**, A. Al-Hajry, “Growth of branched In-doped ZnO nanowires: Structural and Optical Properties”,**AIP Conference Proceedings, 1370, 142 (2011).**

[1] M. Abaker, Ahmad Umar, S. A. Al-Sayari, **G. N. Dar**, M. Faisal, S. H. Kim, and S. W. Hwang, "Growth and photocatalytic properties of Sb-doped ZnO nanoneedles by hydrothermal process", **AIP Conference Proceedings, 1370, 121-127(2011).**